UNIVERSITÉ DU LUXEMBOURG

PhD-FSTC-2014-02

The Faculty of Sciences, Technology and Communication

DISSERTATION

Defense held on 28/01/2014 in Luxembourg

to obtain the degree of

DOCTEUR DE L'UNIVERSITÉ DU LUXEMBOURG

EN PHYSIQUE

by

David Regesch

PHOTOLUMINESCENCE AND SOLAR CELL STUDIES OF CHALCOPYRITES
COMPARISON OF CU-RICH VS. CU-POOR AND POLYCRYSTALLINE VS. EPITAXIAL MATERIAL

Dissertation defense committee

Dr Susanne Siebentritt, dissertation supervisor
Professor, University of Luxembourg

Dr Ludger Wirtz, Chairman
Professor, University of Luxembourg

Dr Roland Scheer, Vice Chairman
Professor, Martin-Luther-Universität Halle-Wittenberg

Dr Heinz Kalt
Professor, Karlsruhe Institute of Technology

Dr Alex Redinger
University of Luxembourg

CONTENTS

CHAPTER

ONE

INTRODUCTION

Within the last 30 years, the chalcopyrite $Cu(In,Ga)Se_2$ received a lot of attention because of its suitable properties for thin film solar cell applications. The early work was carried out mainly at the Bell Laboratories, where the first $CuInSe_2$ solar cell with an efficiency of 12% was produced [1]. Within the last years, an intense research concentrated on $Cu(In,Ga)Se_2$ thin films and pushed the record efficiencies of small laboratory scale cells constantly upwards to the current record of 20.8% [2] and to 19.6% for $5x5cm^2$ sub-modules [3].
Today, $Cu(In,Ga)Se_2$ thin films are not only limited to research labs any more and modules are available for the installation on the rooftops of electrical consumers. The commercially available modules with polycrystalline $Cu(In,Ga)Se_2$ thin films show efficiencies of 15.7% [4]. Nevertheless, modules with a single junction and a comparable absorber thickness based on thin epitaxial GaAs [5] show efficiencies of up to 24.1% [4]. The huge difference is due to better electrical properties of the epitaxial material, when compared to the polycrystalline counter part and is also observed for silicon based solar cells [6].
In contrast to GaAs and silicon based cells, the polycrystalline $Cu(In,Ga)Se_2$ material outperforms the epitaxial devices. On lab scales, the highest reported efficiency for epitaxial devices is only 8.5% [7]. However, there is no fundamental reason to assume that single crystalline $Cu(In,Ga)Se_2$ solar cells should not outperform their polycrystalline counterparts. In fact, the first efficient $CuInSe_2$ device reaching 12% was based on a single crystalline absorber, albeit a bulk crystal [1]. Efforts to prepare single crystalline $Cu(In,Ga)Se_2$ cells have been limited so far because the industrial application is based on the polycrystalline material.
Chalcopyrites are well known to form a stable phase at significant deviations from the stoichiometric point ranging from Cu-poor ($[Cu]/([Ga]+[In]) < 1$) to Cu-rich ($[Cu]/([Ga]+[In]) > 1$) compositions [8, 9]. The role of the copper content on the material properties were investigated before by Hall and PL studies [10]. The results indicate an improvement of several material properties of Cu-rich absorbers. For example, an increase of the charge carrier mobility [11], a decrease of the defect concentration [12], and an increased excess charge carrier concentration under illumination [13] are observed. However, the overall effective influence of the Cu-excess during the growth on the general absorber and device quality has not been investigated in detail.

The aim of this work is to investigate the difference of the epitaxial and the polycrystalline material. Therefore, the first part (section 3) concentrates on the influence of the composition for both material types. The second part concentrates on the preparation and the analyses of solar cells with single crystalline absorbers (section 4) to clarify the differences in the achieved efficiencies for solar cell devices.

The comparison of polycrystalline and epitaxial material is performed on the bare absorbers by means of photoluminescence (PL) measurements at room temperature (section 3). Therefore, the PL set-up at the Laboratory for Photovoltaics (LPV) was extended within this work to perform calibrated PL measurements. Quantitative measurements allow the determination of the quasi-Fermi level splitting of the bare absorber layer (section 2.5.3). The quasi-Fermi level splitting is of importance, since it gives the maximum achievable open circuit voltage in the solar cell without finishing the device and indicates the quality of the absorber layer. Thereby, the direct comparison of epitaxial and polycrystalline material and the dependence on the compositions is possible.

The epitaxial material used for the solar cells is grown by metalorganic vapour phase epitaxy (MOVPE) on a GaAs substrate layer. Before my arrival, the MOVPE system at LPV was used to grow pure $CuInSe_2$ and $CuGaSe_2$. Therefore, a part of this work concentrates on the development of a growth process for $Cu(In,Ga)Se_2$ material. By balancing the $[Ga]/([Ga]+[In])$ ratio, the lattice mismatch between the GaAs substrate and the $Cu(In,Ga)Se_2$ absorber can be minimized and the induced strain within the grown film is minimized ensuring samples of a very high quality. Thereby, the number of dislocations within the film are reduced coming along with a longer lifetime for the minority carriers and better transport properties in the device.
At LPV, epitaxial solar cells were not produced so far, so that the production path for building devices had to be developed as well. The growth process and the characterization of the first epitaxial $Cu(In,Ga)Se_2$ based solar cells produced in Luxembourg are discussed in chapter 4.

CHAPTER

TWO

BACKGROUND AND LITERATURE

This chapter provides some background information about the chalcopyrite Cu(In,Ga)Se_2 used in this work. First, the crystal structure and the resulting electronic properties are summarized before explaining the principles of hetero-epitaxial growth which is important in this work. Afterwards, the physical background of the characterisation methods used for the analysis shown in the results are highlighted. One focus is the interaction of light with semiconductors, which is important for the operation of a solar cell and especially for photoluminescence measurements used in the first part of the results. Furthermore, the fundamental principles of a solar cell are discussed and the characterisation techniques providing the most important parameters are explained.

2.1. Chalcopyrites

The name chalcopyrite originates from the abundant mineral $CuFeS_2$ first discovered in 1725 [14]. In the 1970s the first synthesis of $CuInSe_2$ in combination with a n-type CdS layer showed the first indication, that chalcopyrites may be used as solar cells [15, 16]. Common for all chalcopyrites is the tetragonal crystal structure, as described in the following, concentrating on Cu(In,Ga)Se_2.

2.1.1. Crystal structure

$CuIn_{1-x}Ga_xSe_2$ belongs to the group of chalcopyrite materials, described with the formula $CuBC_2$ where $B = In, Ga$ and $C = Se, S$. The crystal structure is commonly described as a derivative of the sphalerite structure known from II-VI compounds [18] (also known as zinc blende) by substituting the bivalent cation by a monovalent copper (1+) and a trivalent In^{3+} or Ga^{3+} cation. Therefore, the periodicity is doubled in one direction compared to the primary cubic structure (figure 2.1). The modification comes along with a tetragonal distortion ($\eta = \frac{c}{2a} \neq 1$, where a and c are the lattice constants) and a displacement (u) of the anions from the ideal tetrahedral side. The tetragonal distortion is due to a different bond length between the anion and the two different cations [19] caused by other bond strengths between the $Cu - C$ and the $B - C$ [16]. The lattice constants can be determined from X-ray diffraction measurements and show a dilated unit cell along the c-axis for $CuInSe_2$ with $\eta = 1.005$ and a compressed unit cell for $CuGaSe_2$

Figure 2.1.: ***Crystal structure*** *- Unit cell of the chalcopyrite crystal structure Cu(In,Ga)Se_2 [17].*

with $\eta = 0.982$. The values were calculated using the equation in table B.1, which was derived by averaging the available data from the literature (see section 2.2.1 for details). The different bond lengths cause also the anion displacement, which is $u = 0.25$ for ZnSe. An estimation of the displacement can be calculated with the bond lengths $R_{\mathrm{Cu,C}}$, $R_{\mathrm{B,C}}$, and the lattice constant a:

$$u = \frac{1}{4} + \frac{R_{\mathrm{Cu,C}}^2 - R_{\mathrm{B,C}}^2}{a^2}. \tag{2.1}$$

For $CuInSe_2$, the bond lengths are $R_{\mathrm{Cu,C}} = 2.484$Å, $R_{\mathrm{B,C}} = 2.586$Å [20] and the displacement of Se is found to be $u = 0.23$. On the other hand, the displacement in $CuGaSe_2$ was calculated to be $u = 0.264$ [21].
The tetragonal distortion and the anion displacement modify the electronic structure compared to the related zinc blende type as shown in the next section 2.1.2.
While the ternaries $CuInSe_2$ and $CuGaSe_2$ are suitable to study fundamental properties, the alloy $CuIn_{1-x}Ga_xSe_2$ is typically used in solar cell application (with $x \approx 0.3$ [22]) taking advantage of the band gap dependence on x (in the following also abbreviated as GGI referring to the gallium and indium content [Ga]/([Ga] + [In])). Concerning the crystal structure, several studies report about the lattice constants for different GGIs as disscused later in section 2.2.1 (figure 2.5).

2.1.2. Electronic structure

Similar to the crystal, the electronic structure is also related to ZnSe. Figure 2.2a illustrates the conduction band and a three-fold degenerated valence band at the centre of the Brillouin zone (Γ-point) of an artificial semiconductor with a ZnSe like structure, but without the spin-orbit coupling.
Due to the anion displacement u for $CuInSe_2$ and $CuGaSe_2$, this structure is distorted leading to different electrical fields within the crystal. The so called crystal field splitting Δ_{CF} leads to a splitting of the valence band into a non-degenerated and a two-fold

degenerated energy level compared to ZnSe. Because of a positive Δ_{CF} in $CuInSe_2$ and a negative one in $CuGaSe_2$, the two levels are inverted when compared to each other. The interaction of the electron spin with its angular momentum leads to an additional splitting. The so called spin-orbit coupling (Δ_{SO}) leads to an additional splitting of the valence band levels resulting in three fundamental band gaps. Cu(In,Ga)Se_2 is a direct semiconductor.

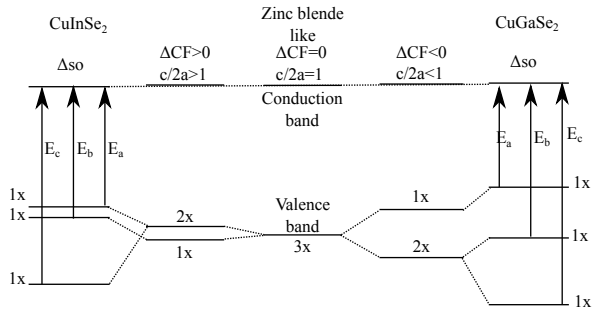

(a) The band diagram of $CuInSe_2$ and $CuGaSe_2$ derived from ZnSe (without spin-orbit coupling). According to [23].

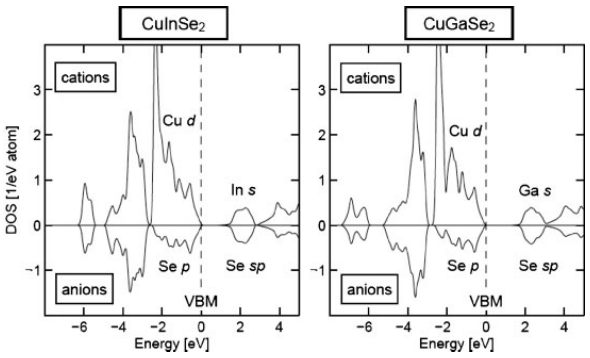

(b) The calculated density of states for $CuInSe_2$ and $CuGaSe_2$ [24].

Figure 2.2.: ***Electronic structure of $CuInSe_2$ and $CuGaSe_2$*** *- left side: The band structure of pure $CuInSe_2$ and $CuGaSe_2$ derives from the one of the zinc blende structure. The lifting of the degeneracy (shown as 3x, 2x, and 1x) of the valence band is due to additional contributions of the spin-orbit coupling and the crystal field splitting leading to three fundamental band gaps at the Γ point [23]. right side: Calculated density of states. [24]*

In the 1970 [25–27], electro reflectance, photoluminescence, and x-ray photo emission measurements were carried out on chalcopyrites to deduce the electrical nature of the material.
It was shown, that the electronic structure close to the valence band edge is mainly influenced by the hybridization [28] of the Cu d and the Se p orbitals. This is in agreement with theoretical calculations, as shown in figure 2.2b. The calculations suggest further that the conduction band is mainly determined by the $B^{III} - s$ and a Se-sp like states. The Cu-d-Se-p hybridization forms an anti bonding valence band maximum implying a weak bond between the Cu and the Se atoms [24].

Defects

The three different species forming the Cu(In,Ga)Se_2 unit cell allow the formation of various types of defects, while the concentration obviously depends on the composition and the growth conditions. Four types of defects may be present:

1. The misalignment of several atoms in a crystal leads to the formation of dislocation or line defects. One differentiates two types of dislocations: screw and edge dislocations. Because of a small lattice mismatch to the substrate, these dislocations can be formed during epitaxial growth (section 2.2).

2. An array of dislocations is also known as a planar defect, for example stacking faults. Also at a grain boundary, the orientation of the crystal changes abruptly, which causes an array of dislocations. Stacking faults are caused by a change in the ordering of the atomic layers in the crystal [29].

3. A three dimensional defect structure within the crystal can be caused by inclusions of another material or by a hole within the material, also known as voids.

4. Point defects arise at lattice positions (or at interstitial) in the unit cell structure (intrinsic and extrinsic defects). Intrinsic defects determine the doping of Cu(In,Ga)Se_2 and are therefore very important for solar cell applications [24]. They further act as recombination centres.

Point defects can seperated into three subgroups:

1. **Vacancies**, for instance abbreviated as V_{Cu}, describing an unoccupied (Cu) position in the lattice.

2. An **interstitial** is an atom on a position within the crystal which is normally not occupied. Interstitials are usually denoted as Cu_i. In this case a copper atom on an interstitial lattice position.

3. An atom located on a site which is normally occupied by another species is called **antisite**, e.g. copper on an indium position Cu_{In}. In this example the copper atom is located at the position usually occupied by an indium atom.

According to the first theoretical calculations [30] and to the review [24], it is very likely to form point defects in Cu(In,Ga)Se_2. For $CuInSe_2$ ($CuGaSe_2$), the point defects with the lowest formation enthalpies are the copper vacancy V_{Cu} and the cation antisites Cu_{In} (Cu_{Ga}) and In_{Cu} (Ga_{Cu}). However, the situation is more complicated, since experiments revealed, that $CuInSe_2$ can either exhibit a p-type or n-type character [31,32], depending on the growth conditions. The n-type semiconductor is observed for $CuInSe_2$ grown under copper and selenium poor conditions [32]. On the other hand, there are no experimental evidences for a n-type character of $CuGaSe_2$, which was always found to be p-type. These experimental observations are in agreement with theoretical calculations [33, 34]. For $CuGaSe_2$, the p-type character is due to a very low formation energy of the V_{Cu}^{-} which may become positive (exothermic) with an increasing Fermi energy and acts as an acceptor [34]. In $CuInSe_2$, the formation of the intrinsic In_{Cu}^{2+} double donor under selenium poor conditions results in a net n-type doping [33]. If this positively charged donor is formed, two free electrons are released leading to an increase in the Fermi level. Simultaneously, as mentioned before, the formation enthalpy for V_{Cu}^{-} will decrease and the formation of copper vacancies gets more probable.
The prediction of which defect is formed is rather difficult, since the formation enthalpy ΔH of a defect depends first on the chemical potential of the species (the growth conditions) [30]. Furthermore ΔH depends on the Fermi level, which itself depends on the charge carrier densities. Since the carrier densities are also influenced by the charge state of a defect [24, 30, 35], a complex interplay has to be accounted for.
The calculation are still a matter of debate [36–39]. Since Pohl's calculations [39] are based on a bigger supercells with 216 atoms (compared to 64 in [38]), a short summary of

the recent finding is based on this work. The lowest formation energy in $CuInSe_2$ are found for the antisite In_{Cu} (donor), the vacancy V_{Cu} (acceptor), the antisite Cu_{In} (acceptor), and the interstitial Cu_i (donor) and is analogue for $CuGaSe_2$. While previous calculations attributed the effect of doping and self-compensation to In_{Cu} (Ga_{Cu} for $CuGaSe_2$) and V_{Cu} [33] the present computation reveals, that depending on the growth conditions, Cu_{In}, Cu_{Ga}, and Cu_i may substantially contribute to the doping and compensation [39].
With an increasing doping concentration, the formation of defect complexes gets more likely. For example, in $CuInSe_2$ large concentrations of In_{Cu}^{2+} and V_{Cu}^{1-} may be present and form a complex $(In_{Cu}^{2+} + 2V_{Cu}^{-})^0$. This neutral defect complex can explain the wide excistance region of $CuInSe_2$ grown under copper deficient conditions [24].
The combination of Hall, photo-, and cathodo-luminescence measurements on samples grown under Cu-excess revealed the existence of a shallow donor D with an activation energy of $E_{act} = 10(12)$ meV for $CuInSe_2$ ($CuGaSe_2$). Furthermore, several acceptor ionization energies could be identified: $E_{A1,act} = 40(60)$ meV, $E_{A2,act} = 60(100)$ meV and $E_{A3,act} = 100(140)$ meV. The $A3$ acceptor is observed for more or less every Cu-rich growth condition. On the other hand, the $A1$ defect vanishes while the $A2$ appears with increasing Cu excess [24]. According to [39], the donor D can be most likely assigned to In_{Cu} or the copper interstitial Cu_i, the shallowest acceptor $A1$ to the copper vacancy.

Electrical properties and GGI

The similarities and differences in the electronic structure between the ternaries $CuInSe_2$ and $CuGaSe_2$ were pointed out above. Since the second part of this work concentrates on epitaxial $CuIn_{1-x}Ga_xSe_2$ based solar cells with different GGIs, a composition dependent summary of the previous discussion is depicted in figure 2.3. Shown are the energy gap and the position of the valence and conduction bands according to [40]. The donor and the three acceptors are depicted as well. It is to say, that continuous change for an increasing GGI could be confirmed experimentally for the $A1$ acceptor [24].
The band gap follows the dependence of the composition as specified in [41]. The values for the ternaries and the equation used to calculate the properties are summarized in table B.1.

The band gap energy in dependence of the composition can be calculated with the equation [41]

$$E_g(x) = 1.035 + 0.389x + 0.264x^2 \tag{2.2}$$

where x describes the gallium content in $CuIn_{1-x}Ga_xSe_2$.

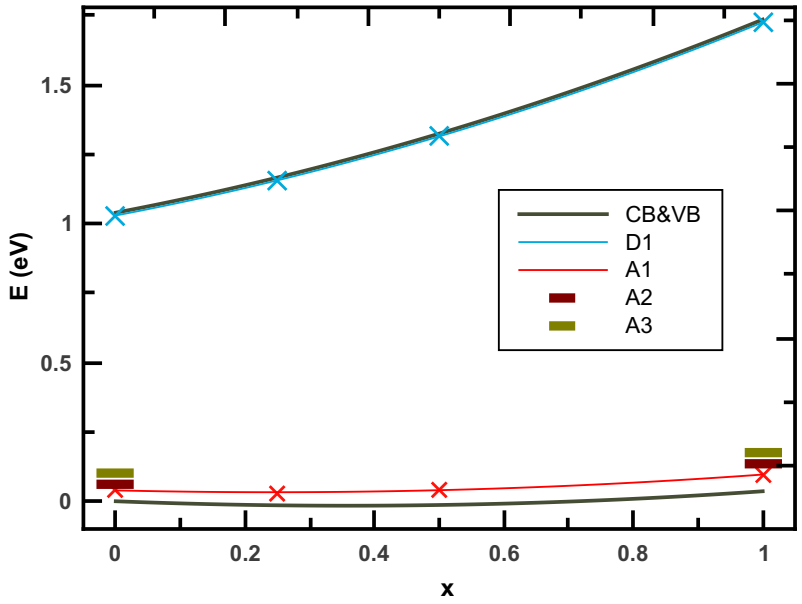

Figure 2.3.: ***Electronic properties for Cu(In,Ga)Se$_2$*** *- Overview of electronic properties for Cu(In,Ga)Se$_2$. Depicted are the conduction- and the valence band (and thus the band gap) and the most common defects.*

2.2. Hetero-epitaxial growth

A main task in this work is the development and optimization of a process for a device fabrication of epitaxial Cu(In,Ga)Se$_2$ based solar sells. The important issues for the growth of hetero-epitaxial absorber material are summarized in the following. The term epitaxy derives from the Greek words "epi" (above) and "taxis" (in order) and refers to the deposition of a material onto a single crystalline substrate. If the overlayer and the substrate are the same material the growth is called homo-epitaxy. If they differ from each other it is described as hetero-epitaxy. Epitaxy is usually used to grow single crystals with a very high purity and quality. For this purpose special attention needs to be paid to two issues: the lattice mismatch at growth temperature and the thermal expansion coefficient. Both points are described, before discussing the hetero-epitaxial growth in section 2.2.1.

1. The lattice constants of the substrate and the overlayer generally differ from each other. If the substrate is much thicker than the overlayer, the magnitude of the lattice mismatch for the substrate with a lattice constant a_s and the layer with a lattice constant a_l is usually expressed as [42]:

$$f = \frac{a_s - a_l}{a_l}. \tag{2.3}$$

This mismatch leads to strain inside the layer manifesting itself in the deformation of the layer's unit cell. Depending on the sign of f, the layer exhibits compressive strain for $f < 1$ and tensile strain for $f > 1$. Either way the strained solid contains an additional energy term, the strain energy per unit volume. This term increases

linearly with the layer thickness until it exceeds the energy necessary to form a structural defect (dislocation) which reduces the strain step wise.

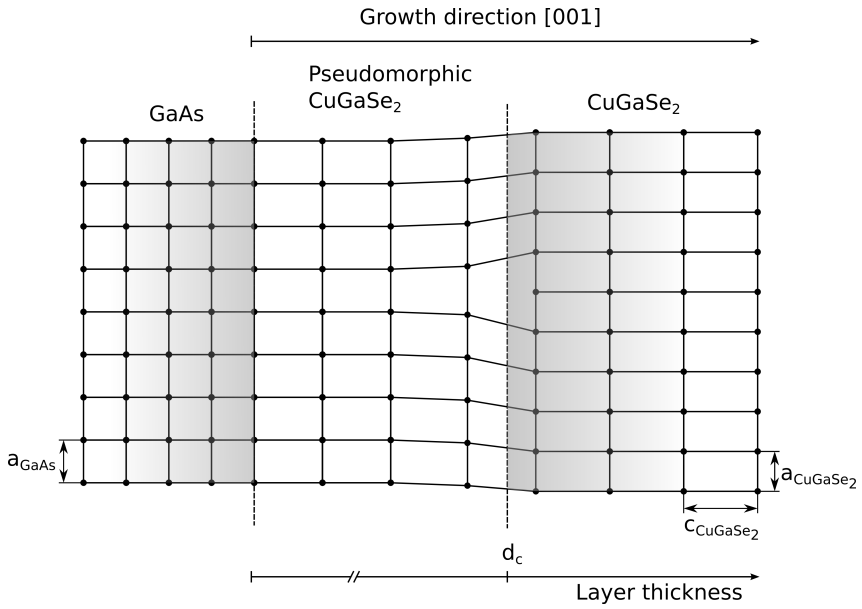

Figure 2.4.: ***Schematic view of hetero-epitaxial growth of $CuGaSe_2$ on GaAs*** *- First, the $CuGaSe_2$ adapts to the lattice constant of GaAs and grows pseudomorphic. When it gets energetically more favourable, the strain energy is reduced by the formation of dislocations. Afterwards, the $CuGaSe_2$ grows relaxed with lattice constants equals to an independent single crystal. [43]*

When a material is grown on a substrate with a slightly different lattice constant, the material will first adopt to the lattice constant of the substrate and the unit cell of the material is distorted. With an increasing distance from the substrate, the distortion decreases until the unit cell exhibits the same dimension as the pure material would have. As long as the lattice constant of the material differs from the undistorted unit cell, the growth is called pseudomorphic growth. Afterwards, the layer starts to grow relaxed. Figure 2.4 illustrates the situation and the transition from the pseudomorphic growth to a relaxed growth after the formation of a dislocation. Note that the figure is a schematic picture, since misfit dislocations are located at the interface to the substrate and not illustrated.

The critical thickness specifying the transition to a relaxed growth is found to be inversely proportional to the lattice mismatch at growth temperature. For III-V semiconductor, the empirical relation of

$$d_c \approx \frac{0.8nm}{f(T_{growth})} \tag{2.4}$$

was found [44].

2. Normally, the formation of the desired material requires a sufficiently high temperature in the order of a couple of hundred degrees Celcius. Therefore, the thermal

expansion coefficients of both material should be as close as possible. Otherwise additional strain will be induced during the cooling down to room temperature. This strain may cause the formation of cracks through the whole layer for tensile strain.

Obviously, the substrate's surface has to be clean to allow an epitaxial growth and to avoid any contamination of the layer to be grown. Additionally, the growth temperature should be below the decomposition temperature of the substrate. Indeed, for the growth of Cu(In,Ga)Se_2 on GaAs ($T > 470°C$) the desorption of arsenic leads to an abundance of gallium (see section 2.3.3).

Property	x=0	x=0.5	x=1.0	GaAs
a(Å)	5.7871	5.699	11.63	5.652 [45], 5.654 [46]
c(Å)	11.63	11.324	11.018	c=a
$\alpha_a(10^{-6}K^{-1})$	10.65	11.9	13.1	5.7 [47],6.9 [48, 49]
$\alpha_c(10^{-6}K^{-1})$	8.15	6.7	5.2	$\alpha_a = \alpha_c$
$\epsilon_{\parallel,a}$ (%) T=300K/800K	-2.3/-2.5	-0.8/-1.0	0.7/0.4	-
$\epsilon_{\parallel,c}$ (%) T=300K/800K	-2.7/-2.9	$\approx$ 0/-0.2	2.6/2.6	-
d_a (nm) T=800K	31	73	197	-
d_c (nm) T=800K	27	410	30	-

Table 2.1.: *Summary of structural parameters of Cu(In,Ga)Se_2* *- Summary of material properties of $CuIn_{1-x}Ga_xSe_2$ for x=0, 0.5 and 1 and GaAs. Depicted are calculated values for the lattice constants a and c, and the thermal expansion coefficient along the a (α_a) and c a (α_c) axis following the equation in table B.1. The equation for the lattice constants were determined by fitting linear equations to the data found in literature. The calculated values for the strain ϵ (equation (2.6)) along the a- and the c-axis and the estimated thickness of the pseudomorph layer (equation (2.4)) are based on the extrapolated values. $\epsilon_{\parallel,a}$ corresponds to the strain along the a axis, assuming that the Cu(In,Ga)Se_2 unit cell grows such, that the a-axis is parallel to the substrate; $\epsilon_{\parallel,c}$ assumes that the c axis is parallel to the surface. The strain at the growth temperature was calculated with the lattice constants at room temperature considering the respective thermal expansion (equation (2.5)).*

2.2.1. Chalcopyrite grown on GaAs

The Cu(In,Ga)Se_2 layers in this work were grown on GaAs (001). The lattice constants and the thermal expansion coefficients for selected GGIs are given in table 2.1. Figure 2.5 depicts the development of the lattice constants a and c for the alloy Cu(In,Ga)Se_2 with respect to the GGI and for GaAs . The linear relation was extrapolated using a linear fit to the data (vertical and horizontal symbols) available in literature (compare table B.1). The solid lines represent the constants at room temperature and the dashed lines at the growth temperature. The values at growth temperature are calculated using the thermal expansion coefficients:

$$a(T) = a + a\alpha_a(T - T_{room}). \tag{2.5}$$

This equation was applied to the linear extrapolation based on the values for the thermal expansion coefficient given in table 2.1. For the ternaries, the lattice constant a is closer than $0.5c$ to the value for GaAs . Indeed, if the ternaries are grown on GaAs (001), the

c-axis of both, $CuInSe_2$ [50] and $CuGaSe_2$ [43] grows perpendicular to the surface of the substrate. This is in agreement with the smaller difference between a_{CuInSe_2} and the lattice constant GaAs when compared to $0.5c_{CuInSe_2}$ (figure 2.5). The same holds for $CuGaSe_2$.

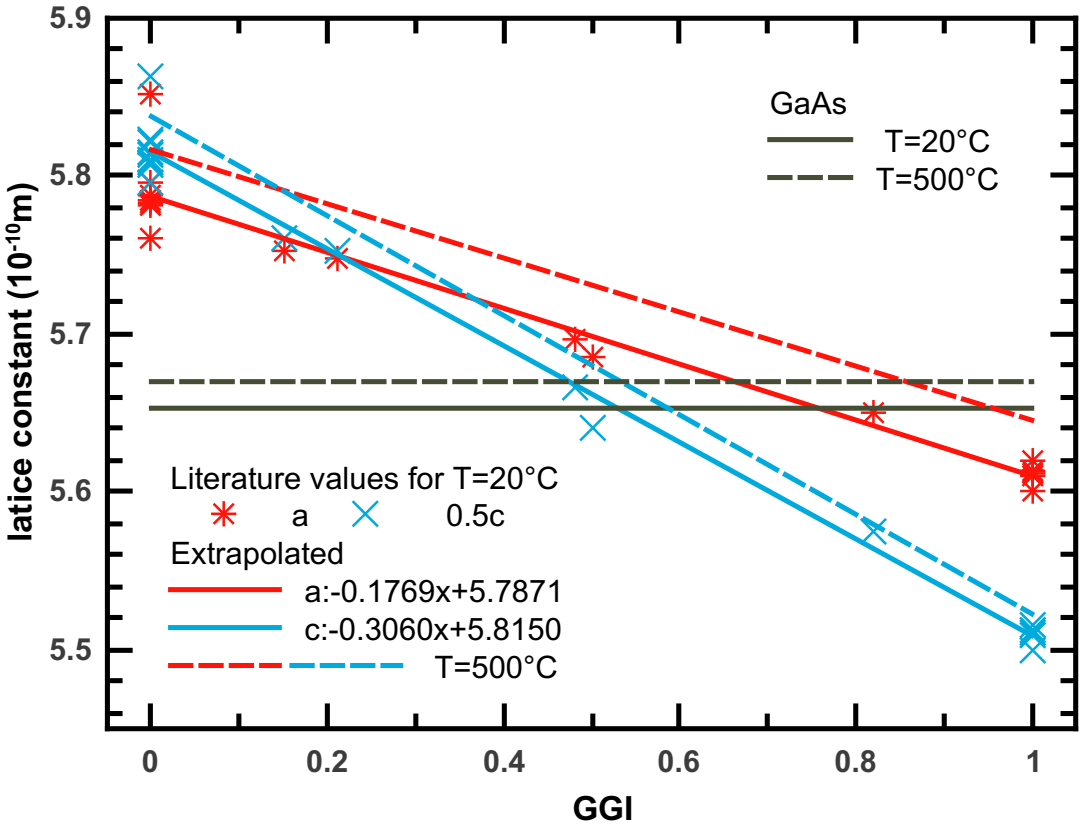

Figure 2.5.: ***Lattice constant in dependence of the composition*** *- Depicted are literature values of the lattice constants a (star) and 0.5c (crosses) for $CuIn_{1-x}Ga_xSe_2$ in dependence of the compositions. The solid line is a linear fit to these data (equation depicted for lattice constant at room temperature). The lattice constant of GaAs is shown as the solid gray line. The dashed lines represent the lattice constants at 500 °C and were calculated with the thermal expansion coefficients given in table 2.1. Data (the star for the lattice constant a and the cross for $0.5c$) following [51–70] and [45, 46, 49] for GaAs .*

The induced strain parallel to the substrate surface during the pseudomorphic growth is given by

$$\epsilon_{\parallel,x} = \frac{x_{str} - x}{x}. \tag{2.6}$$

Depending on the growth direction, x is either the relaxed lattice constant a or c; the index *str* refers to the strained constant. If the c-axis is perpendicular to the surface $x_{str} = a_{GaAs}$ and for the parallel case $x_{str} = 2a_{GaAs}$. As calculated in table 2.1, the smallest strain for the ternaries is achieved for a c-axis perpendicular to the surface. Nevertheless, there is a region ($0.2 < [Ga]/([Ga] + [In]) < 0.7$), where the growth parallel to the surface is favourable (see section 4.2.1). Almost no strain due to a lattice mismatch can be achieved for $x \approx 0.5$, if the c-axis grows parallel to the surface, such that two unit cells of GaAs form the interface to the $CuIn_{1-x}Ga_xSe_2$.

The equations (2.3), (2.4), and (2.5) can be used to determine the critical thickness, up to which a pseudomorphic growth is expected (table 2.1). It has to be pointed out, that this value is a rough estimation, because the actual degree of relaxation depends also on the growth procedure [42]. Furthermore, residual strain may be present and the cooling process may create additional stress [42, 71].
One should keep in mind, that the strain can influence the electrical properties, such as the band gap or the band bending at the interface. For example, tight-binding calculation for $CuGaSe_2$ predict the change in the band gap for different c/a ratios [17, 43, 72]. It was found, that the pseudomorphic $CuGaSe_2$ on GaAs (001) can lower the band gap by almost 70 meV [72].
For $CuInSe_2$ strain may be observed as well. However, in contrast to $CuGaSe_2$, the c-axis is only slightly stretched relatively to the relaxed axis and almost no change for the band gap due to residual strain is expected when grown on GaAs (001) (thus, the c-axis is perpendicular to the surface of the substrate) [17].

2.2.2. X-ray diffraction

A powerful tool for structural investigation is based on the diffraction of x-rays inside a crystal since these wavelengths are in the order of the inter atomic distances. A brief overview of the principle is given before applying it to the grown samples.
The periodicity of a crystal leads to an elastic scattering of x-rays directed onto the solid. The waves may interfere constructively if the path difference for reflections between neighbouring planes is a integral multiple n of the wavelength λ as illustrated in figure 2.6 and reflected in the equation

$$2d_{hkl}sin\theta = n\lambda. \tag{2.7}$$

The reflections diffracted at two different lattice planes with the distance d_{hkl} to each other can be detected in dependence of the angle θ. Equation (2.7) is called Bragg's law and determines only the position θ of the reflex. The intensity is computable by the

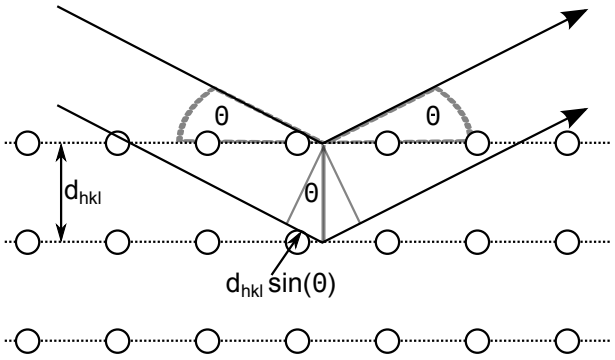

Figure 2.6.: ***X-ray diffraction technique*** *- X-ray diffraction of two rays at neighbouring lattice planes. Constructive interference is observable if the path difference of the diffracted waves $2d_hklsin\theta$ is equal to an integral number of the wavelength*

structure factor. Since the intensity is only interesting if many peaks are observed, it is not used in this discussion. Nevertheless it should be mentioned, that strain inside the

film broadens the peak. The samples investigated in this work grow with a c-axis parallel or perpendicular to the surface of the GaAs . Either way, only one diffraction plane is visible. The position of the diffraction peaks for a tetragonal system are given by

$$sin\theta = \frac{\lambda}{2a}\sqrt{h^2 + k^2 + \frac{a^2}{c^2}l^2} \tag{2.8}$$

where h, k, and l are the Miller indices of the respective lattice planes. For the cubic system GaAs equation (2.8) is still valid and the quotient a/c is one.

XRD provides an indirect measure for a strained growth process (section 2.2.1). Due to the relaxation process mentioned above, dislocations occur in the grown film, which influences the peak shape of the reflected waves. A perfect crystal will produce very narrow peaks in the diffraction pattern, since the crystal does not change within the volume which is probed by the incoming beam. Therefore, the perfect crystal has a very big coherence volume resulting in a coherent diffraction pattern [73]. Dislocations reduce the coherence volume and a broadening of the peaks in the XRD pattern is observed.

2.3. Growth process

Metalorganic vapor-phase epitaxy (MOVPE) is one possibility to grow samples according to the previously described hetero-epitaxy (section 2.2). It is frequently used in semiconductor fabrication processes, because of the controllable growth conditions, a very high quality and purity, and well defined interfaces for multi layer systems. An organic compound acts as the carrier material, which decomposes in a reactor at high temperatures releasing the metal atom to be deposited. This section aims to explain the basic principle and the important parameters for epitaxy of Cu(In,Ga)Se_2 with a high quality as used in this work.

2.3.1. The principle

Figure 2.7 shows the scheme of a typical MOVPE system[1]. It highlights the two most important parts of the system: the gas cabinet where the raw materials are stored and the partial pressures are adjusted and the reactor where the actual growth process takes place:

Gas cabinet

The used system operates with either nitrogen or hydrogen. While nitrogen is used in the hibernation mode (standby) and for cleaning purposes only, hydrogen acts as the carrier gas during the process. The metalorganic precursors are stored in stainless steel containers (bubblers) which then again are stored in a water bath with a defined temperature. The constant temperature ensures a steady partial pressure of the metal organic inside the container. The Cu source is stored in an oven, since the operation temperature is 65 °C. Mass flow controllers define the flux through the sources and through a bypass, as

[1] Within this work the AIX 200 manufactured by Aixtron was used

shown in figure 2.7.
By adjusting the H_2 flux through the bubbler (source), where the material's vapour pressure is taken up, the molar fluxes of the metalorganic source materials can be controlled. A second mass flow controller (push) is necessary, to allow comparable flow velocities between different runs. This is achieved by keeping the sum of both fluxes (source and push) through the pressure controllers always constant. For instance, if the gas flux through the indium bubbler (the "source" pressure) is increased, the flux through the "push" mass flow controller is decreased accordingly. After adjusting the gas flows precisely, a well defined amount of all metalorganic is guaranteed. Finally, the bypass above the boubbler is used when the precursor is not needed or if the machine is in the hibernation mode.
A regulator valve (dashed boxes in figure 2.7) pipes the gas mixture to either the vent line, which is connected to the exhaust, or into the reactor line (Run MO). These two lines allow the abrupt switching of the sources and allows for instance the growth of very abrupt interfaces, when different materials are deposited onto each other. It can further be used to stabilize the flow by guiding the gas mixture through the vent line before being piped through the line to the reactor. An exception is the copper vapour, which flows through a separate line (the dopant line) and joins directly at the entrance to the reactor. To avoid deposition of the metal organic precursor in the line, the whole Cu supply chain is heated up to 70 °C.

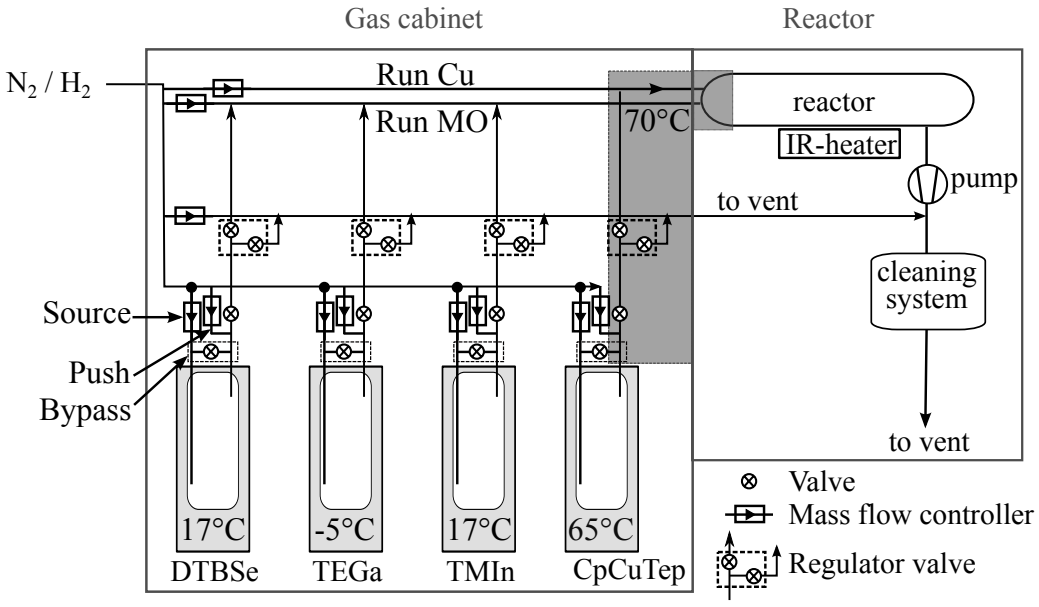

Figure 2.7.: ***Schematic illustration of the MOVPE*** *- Schematic view of the MOVPE system.*

Reactor

The reactor consists of two glass tubes. The liner, a rectangular shaped tube optimized for a laminar flow of the gas mixture and a protecting outer round pipe, which surrounds the liner. The substrate is placed on a graphite block within the liner, the so-called susceptor and can be rotated with a gas foil rotation system (a rotating disc driven by a flow of gas) to achieve better homogeneity. This is of interest, because the Cu precursor

tends to decompose before the other materials immediately after entering the liner. By rotating the substrate, a homogeneous deposition is ensured. An infrared heating system below the linear is used to control the growth temperature inside the reactor chamber. A thermocouple inside the graphite block monitors the temperature inside the system.
Of course, the deposition is not limited to the substrate only so that the liner and the susceptor block have to be cleaned after a while. Both can be removed and cleaned. While the liner can be cleaned in concentrated HNO_3, the susceptor has to be cleaned manually by polishing with a soft piece of paper.
The working pressure during the growth process (inside the liner) is typically 50 mbar achieved by a pump behind the reactor. The pumped gas is cleaned by a filter system, before exhausted into the environment. Special care has to be taken, that no oxygen is inside the whole system, since the precursor material reacts exothermically with it.
Therefore, to avoid any contamination inside the reactor, a glove box is connected to the gas cabinet. The water and oxygen contamination is typically below 0.1 ppm and allows a clean pre- and post- processing within the dry nitrogen atmosphere. Furthermore, it avoids the possible leakage of toxic material from the reactor and the GaAs dust into the lab environment.

2.3.2. Controlling the growth process

The growth process is a very sophisticated process and can fill several textbooks like [42, 71, 74]. In the following, the most important issues for the operation are discussed.

Precursor

A common feature of chemical vapor-phase techniques is the transport of the host atom in the gas phase to the substrate. A thermal dissociation takes place in the reactor near the surface of the heated substrate. The most important requirements for a proper precursors ensuring an efficient growth are [42]:

1. The stability should be such, that on one hand the entire decomposition at the growth temperature is guaranteed. Furthermore, it should not decompose at much lower temperatures compared to the other precursors in the system. On the other hand, the long-term storage should not be hampered due to a too low stability.

2. A sufficient material flux is achieved, if the vapour pressure is high. Therefore, the volatility should be as high as possible to avoid a low growth rate due to insufficient amounts of the raw materials.

3. A liquid phase is desired because the vaporisation rate does not change with time. The rate depends on the surface area, which changes for solid precursors while being used. Liquids ensure, due to the constant area, a steady state and reproducible flow.

In general, most sources have the form MX_n, where M represents the metal and X_n alkyls like methyl (CH_3). The decomposition can be controlled by choosing a suitable organic ligand X_n since the bond strength depends on it. The precursors found to be best suited for Cu(In,Ga)Se_2 are shown in figure 2.8 and their names are:

- Cyclopentadienyl-Copper-Triethylphosphine (CpCuTEP), $C_5H_5CuP(C_2H_5)_3$
- Triethylgallium (TEGa), $(C_2H_5)_3Ga$
- Trimethylindium (TMIn), $(CH_3)_3In$
- Ditertiarybutylselenium $(DTBSe), ((CH_3)_3C)_2Se$

A detailed discussion about the material properties and the issues with a proper copper source can be found in [17].

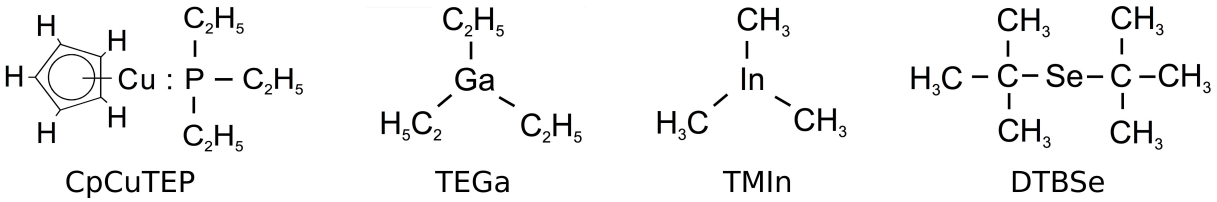

Figure 2.8.: ***Precursor used in the MOVPE process*** *- Chemical structures of the metalorganic source materials [17].*

2.3.3. Growth process

The growth process itself is a sophisticated procedure and involves many gas phase reactions, surface reactions, and hydrodynamical aspects. Already the decomposition itself is a rather complicated mechanism. Since the MOVPE is extensively used and well studied[2] for the fabrication of some III-V semiconductors such as GaAs, it can be used to draw some analogy. For example, the gallium precursor Triethylgallium decomposes following the reaction mechanism [76]:

$$Ga(C_2H_5)_3 \longrightarrow Ga(C_2H_5)_2 + C_2H_5 \longrightarrow Ga(C_2H_5) + 2(C_2H_5) \longrightarrow Ga + 3(C_2H_5) \quad (2.9)$$

The left hand side describes the state before entering the reactor, the two reaction steps in the middle occur within the reactor before the single Ga atom is incorporated into the GaAs crystal. The remaining $3(C_2H_5)$ is pumped to an exhaust.
The crucial parameter for the growth is the partial pressure of each metalorganic precursor (MO) inside the reactor, since it is directly proportional to the amount of the raw material available for the growth. The partial pressure is determined by

$$p_{mo} = p_r \frac{Q_s}{Q_{tot}} \frac{p_v(T)}{p_{bub} - p_v(T)} \quad (2.10)$$

where Q is the volume flow through the (s)ource and the (tot)al gas flow through the reactor. p represents the pressure inside the (r)eactor, the (bub)bler, and the (v)apor pressure of the source material at a given temperature T [42]. For the ternaries $CuInSe_2$ [50] and $CuGaSe_2$ [43] it was shown, that the [Cu]/[In] and [Cu]/[Ga] ratio in the deposited film depend linearly on the ratio of the partial pressures. Both compounds require a

[2]The elementary processes for the growth of GaAs includes 60 species, more than 200 reactions in the gas phase, and a total of 19 species and more than 100 mechanisms at the surface [42, 75].

selenium overpressure preventing the re-evaporation of the selenium [77,78]. For $CuInSe_2$ a selenium overpressure is further needed to avoid the possible n-type character observed for a lack of selenium [79]. While the overpressure for $CuGaSe_2$ is $p_{Se}/(p_{Cu} + p_{Ga}) \approx 9$, it is $p_{Se}/(p_{Cu} + p_{In}) \leq 25$ for $CuInSe_2$ [17] and a value in between for $CuIn_{1-x}Ga_xSe_2$. Once the appropriate amounts of MOs are flowing through the reactor with the heated substrate, the growth with the desired composition starts. The process can be divided into several steps, as indicated in figure 2.9a [42,71,74]:

1. The decomposition of the MOs is observed as soon as the temperature is sufficient to overcome the dissociation energy. A process similar to reaction (2.9) starts for the MOs.
2. Near the substrate, a vertical diffusion onto the growth surface appears.
3. The adsorption of the reactants takes place.
4. Further decomposition processes might still occur and the desorption of the remaining organic compounds takes place.
5. A diffusion process on the surface takes place until
6. the incorporation into the crystal is observed. A desorption process of already deposited elements might occur as well, if the temperature is too high.

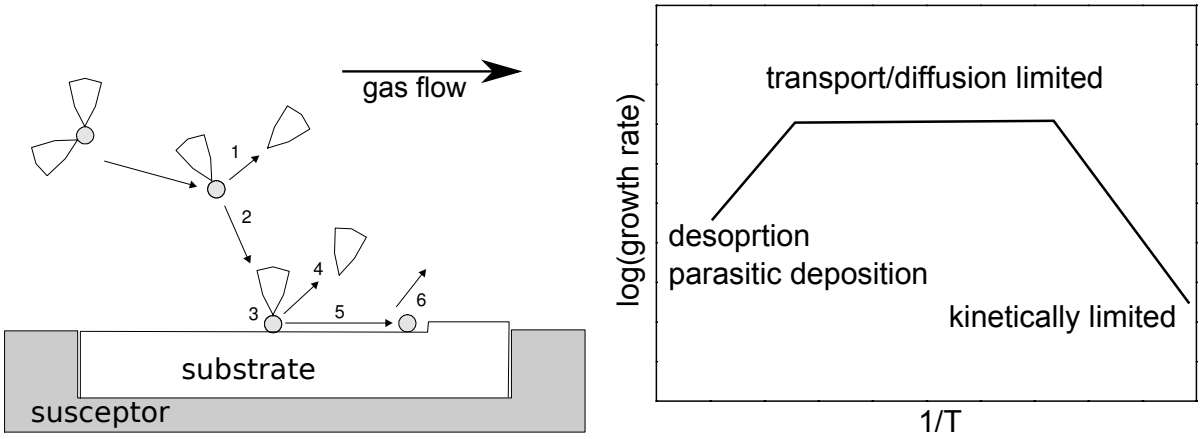

(a) Principle of the growth process inside the reactor. After [80].

(b) Limitations of the growth rate in dependence of the temperature. After [80].

Figure 2.9.: ***MOVPE growth process*** *- Schematic illustration of the growth process inside the reactor inside the MOVPE system and a schematic drawing of the limiting factors for the growth process. The growth mechanism inside the reactor can be divided into different phases: (1) the decomposition of the MOs, the diffusion (2) of the partly decomposed MOs, the adsorption (3) of the reactants on the surface followed by further decomposition processes (4). The metal diffuses (5) on the surface before it incorporates (6) into the grown crystal.*

All processes including the adsorption, the growth, and the desorption are also called interface reaction. The slowest of these processes limits the final growth rate. As schematically

shown in figure 2.9b, three growth regions can be specified: a kinetically driven, a diffusion dominated, and a desorption limited process.

Kinetically limited growth at low temperatures, an exponential relation between the temperature and the growth rate is observed. This indicates a thermally activated processes. With an increasing temperature T, the number of decomposed molecules increases and the growth rate is characterised by a certain activation energy E_a of the pyrolysis: $R \propto exp(-\frac{E_a}{k_b T})$. The word pyrolysis describes the thermochemical decomposition of material.

Transport limited process Once the temperature is sufficient to allow a fast separation of the carrying molecules from the metal, the transport to the surface is the limiting factor. The diffusion process towards the substrate depends only weakly on the temperature, so that the growth rate is almost constant over a wide temperature range. The process is called transport- or diffusion limited growth.

Desorption dominated process If the temperature is too high, the decomposition of the MOs starts closely after the reactor entrance leading to a parasitic deposition at the reactor walls before reaching the substrate. Additionally, the desorption of already deposited atoms on the substrate gets more likely. As a result, the growth rate decreases again. Especially for the copper precursor, the temperature should not be too high, since the dissociation energy is low, compared to the other MOs. The decomposition starts already at $T_{initial} = 80$ °C [81], while the decomposition of the gallium precursor starts at $T_{initial} = 225$ °C, indium at $T_{initial} = 250$ °C [82], and selenium at $T_{initial} = 300$ °C [83].

Since the highest growth rate is not sensitive to slight temperature variation in the transport limited region, it is desired to limit the reactor temperature to this region. The range for a transport limited growth process with the system used at LPV is between $500 - 550$ °C [17].
As pointed out in literature, the diffusion of gallium from the GaAs substrate into the Cu(In,Ga)Se_2 layer cannot be avoided [84, 85]. Due to the decomposition of the GaAs when the temperature is increased, arsenic desorbs [86, 87] and releases gallium which diffuses into the Cu(In,Ga)Se_2 layer [84]. The desorption of As and the incorporation of Ga into a metal film was demonstrated to occur already at T = 420 °C [88].
For Cu(In,Ga)Se_2 it was found, that the diffusion depends on the [Ga]/([Ga] + [In]) ratio and argued, that Ga diffuses on metal vacancies on either the Cu or the In sublattice [85]. The diffusivity of gallium in dependence of the [Cu]/[In] ratio exhibits a minimum around the [Cu]/[In] $\approx$ 1 and increases for lower and higher ratios [85]. For [Ga]/([Ga] + [In]) < 0.25 (in the bulk) a gallium gradient within the first ≈ 120 nm was found. For [Ga]/([Ga] + [In]) ≥ 0.38 a layer ($25 - 50$ nm) of pure $CuGaSe_2$ was measured prior to a similar gradient for smaller GGIs [50].

Besides the temperature dependent desorption of arsenic, the interface is affected as well. The formation of voids is more likely for increasing temperatures and can be suppressed consequently by lowering the temperature [13]. Figure 2.10 shows the effect of the growth temperature for the interface between $CuInSe_2$ grown on GaAs (100) [89]. The used system and the process are comparable to the MOVPE system used in this work.

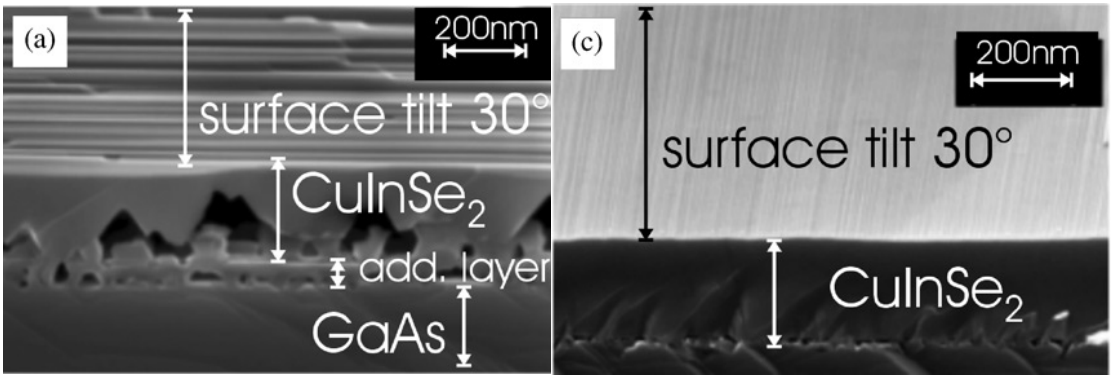

Figure 2.10.: ***Interface between GaAs and $CuInSe_2$*** *- The interface between GaAs and $CuInSe_2$ as found in literature [89]. The $CuInSe_2$ layer was grown on GaAs (100) with a MOVPE process similar to the one used in this work. The interface on the left hand side was observed at a growth temperature of* $\mathrm{T} = 570\ ^{\circ}\mathrm{C}$*; the sample on the right was grown at* $\mathrm{T} = 500\ ^{\circ}\mathrm{C}$*. Although the lower growth temperature shows a smoother interface compared to the higher temperature, a small layer of voids between the GaAs and the $CuInSe_2$ is visible.*

For a growth temperature of $\mathrm{T} = 570\ ^{\circ}\mathrm{C}$ (left hand side of figure 2.10), big pyramidal voids at the interface are observed. The voids almost extend up to the surface. A reduced temperature ($\mathrm{T} = 500\ ^{\circ}\mathrm{C}$; right hand side) reduces the voids significantly. Nevertheless, a small layer of voids between the GaAs and the $CuInSe_2$ is still visible. A further reduction of the temperature showed the presence of polycrystalline grains throughout the film [89].

2.4. Interaction of photons and semiconductors

2.4.1. Macroscopic description

The interplay between light and a semiconductor can be described with three magnitudes (figure 2.11): the reflectivity (R_f), the transmission (T) and the absorptivity (A). These values depend on the photon energy (E_{ph}) and are related to each other by equation (2.11). The value represents the percentage of photons being reflected, absorbed and transmitted, respectively.

$$R_f(E_{ph}) + T(E_{ph}) + A(E_{ph}) = 1 \quad (2.11)$$

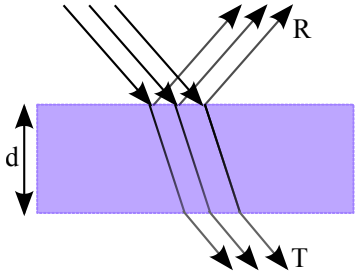

Figure 2.11.: ***Optical processes in solids*** *- Scheme of optical processes observed in a semiconductor.*

Obviously, the different layers in a solar cell device require the optimisation of the different properties. While the window layer demands a high transmission within a wide spectral range, the absorptivity should be the dominating term in the absorber layer to maximize the number of available charge carriers (compare section 2.6.3). Naturally, the reflectivity is meant to be as small as possible.

The magnitude T is used in the simulation presented in section 4.10.
The relative quantities allow the derivation of more meaningful values, such as the sample thickness[3] or the absorption coefficient [91, 92]. In this work, α was determined from the absorptivity using two methods: a direct determination by means of the photoluminescence spectra at room temperature and an optical model describing the absorption coefficient. First, the low energy side of the photoluminescence peak at room temperature is determined by the absorptivity. The usage of equation (2.12) leads to the absorption coefficient near the band gap and is explained more in detail in section 2.5.4.

$$A(E) = (1 - R_f(E))(1 - e^{-\alpha(E)d}) \tag{2.12}$$

In this work, the sample thickness d was determined from scanning electron microscope (SEM) measurements.
The absorption coefficient is crucial for any solar cell application and closely linked to the emission spectra of semiconductors. A detailed discussion is given in the next section 2.4.2.

2.4.2. Absorption coefficient

In the macroscopic picture, the absorption coefficient α can be defined by the Beer-Lambert law [93–95]:

$$I(E, x) = I_0 exp(-\alpha(E)x). \tag{2.13}$$

The radiation intensity I at the position x inside a medium is given by an exponential decay depending on the position and the absorption coefficient α. In other words, α describes the inverse extinction length. It defines the penetration depth for a photon with a certain energy E_{ph} into a medium as the inverse of the absorption coefficient. Figure 2.13 illustrates the calculated absorption coefficient (left axis) and the resulting penetration depth (right axis) for $Cu(In,Ga)Se_2$.

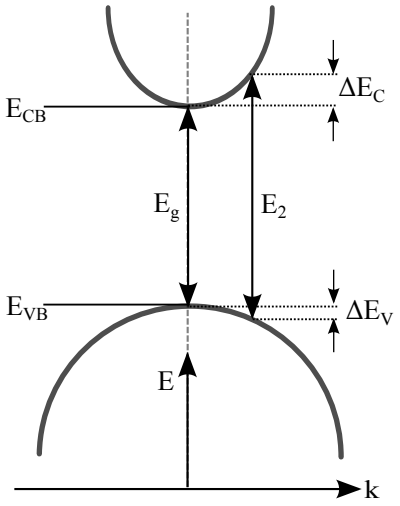

Figure 2.12.: ***Parabolic valence and conduction band*** *- Schematic illustration of different transition processes in a direct semiconductor.*

Since the absorption process itself is closely related to the (photo)luminescence process in a semiconductor, it is worth to get an overview of the microscopical picture for a direct semiconductor. In general, the energy of the photon is absorbed by a (quasi) particle within a crystal, such as charge carriers or phonons. Since the presence of charge carriers within the conduction band is crucial for the operation of a solar cell, the discussion is limited to the generation of an electron-hole pair. Then, the absorption of radiation is the transition of a charge carrier from an (i)nitial state $|i\rangle$ to a (f)inal state $|f\rangle$, the indices i

[3] E.g., Swanepoel showed, that the absorption coefficient (α), the refractive index (n), and the sample thickness (d) can be deduced by only measuring the transmission. [90]

and f refer to lower and upper energy, e.g. from the Cu-d/Se-p band (the valence band $E < 0$) to the In-s/Se-sp band for a $CuInSe_2$ sample (figure 2.2b). Obviously, the photon energy has to be at least as high as the energy difference of the involved states ($E_{ph} \geq E_g$ for the mentioned band-to-band transition). Figure 2.12 illustrates two possible transitions within the $E(k)$ diagram.
In the semi-classical one electron approximation, the interchange of energy between a photon and an electron is described by the (classical) vector potential $\vec{A}$ attributed to the photon and the momentum $\vec{p}$ of the quantum mechanically treated (Bloch) electrons. By applying the time dependent perturbation theory, the Schrödinger equation can be solved [93, 96][4]. The result is typically summarized in a transition rate (Fermi's Golden rule):

$$W_{i,f} = \frac{2\pi}{\hbar} |\langle i| \vec{H_{pe}} |f\rangle|^2 \delta(E_i - E_f - E_{ph}). \tag{2.14}$$

The Hamiltonian $\vec{H_{pe}}$ describes the electron-photon interaction, the indices represent the **i**nitial and the **f**inal state and E_{ph} is the photon energy. The total transition probability W_{if}^{total} from the valence band to the conduction band (compare figure 2.12) can be gathered by summing up all transitions for all initial and final states. Since a transition can only occur, if the initial state is occupied and the final state is empty, each transition $W_{i,k}$ has to be multiplied with the Fermi-Dirac distribution representing the probability of occupied and empty states within the valence and the conduction band. The total transition probability is directly related to the absorption coefficient [93].

Assuming a two band model with different effective masses describing the parabolic shape of each bands, the total transition probability can be calculated with the joint density of states [93]. The absorption coefficient is than

$$\alpha(E) \propto (\frac{2\mu}{\hbar^2})^{3/2} \sqrt{\frac{E - E_g}{E}} \tag{2.15}$$

where μ is the reduced mass of the electron and the hole system. Equation (2.15) only holds for a perfect system with two bands. In reality, the shape of $\alpha(E)$ differs in different energy regimes.

For illustration purposes, the differences in the absorption coefficient can be divided into 4 parts (figure 2.13):

1. Transitions near the band gap (chapter 3): The transition near the band gap as derived within the effective mass theory (equation (2.15)) and is fairly well described with the square root law.

2. Electronic structure far above the band gap. While the optical properties are very similar for $CuIn_{1-x}Ga_xSe_2$ for not too high energies, differences are observed for higher energies E $\gtrsim$ 3 eV. They are not discussed in this work but are described in reference [23].

[4] Neglecting the quadratic term of the vector potential A for low light intensities and the term rising from $\vec{p}$ acting on $\vec{A}$ (due to a negligible photon momentum p) the Hamiltonian $\vec{H} = (\vec{p} + e\vec{A})^2/2m_0 + V(\vec{r}) = \vec{p}^2/2m_0 + e/2m_0(\vec{p}\vec{A} + \vec{A}\vec{p}) + e/2m_0\vec{A}^2 + V(\vec{r})$ can be separated. Then, the photon-electron interaction can be treated separately $H_{pe} = \frac{e}{2m_0}\vec{A}\vec{p}$. [93]

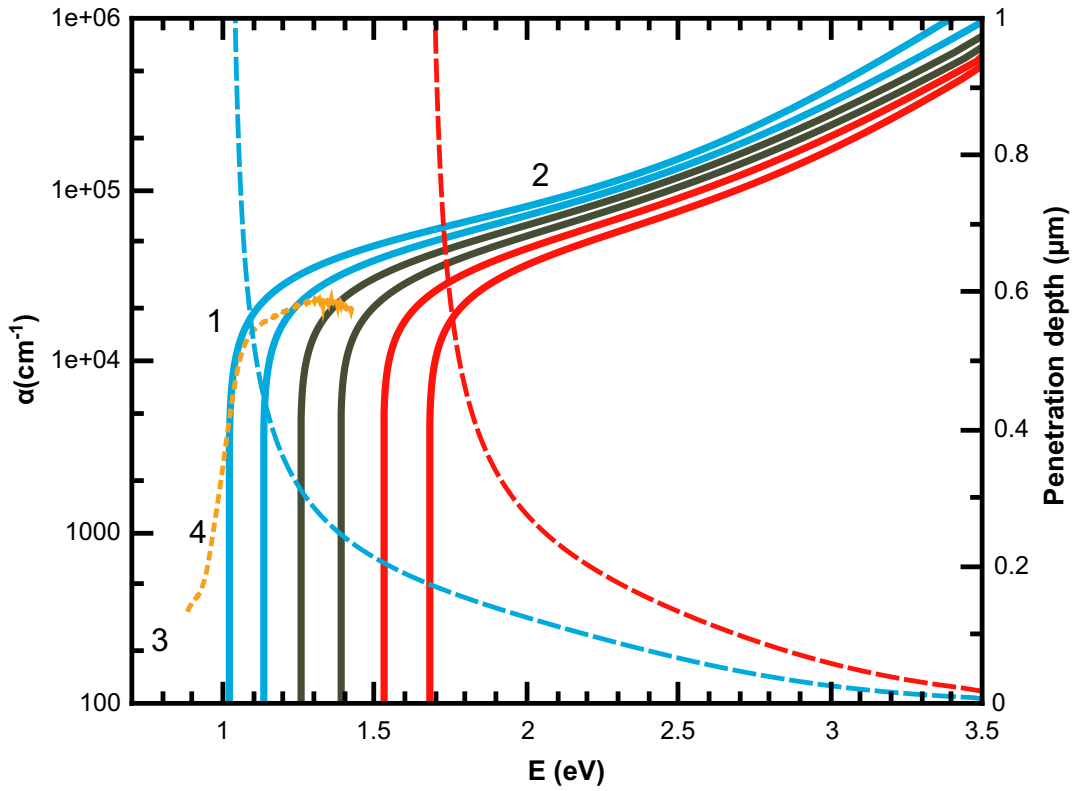

Figure 2.13.: ***Absorption coefficient*** *- Model for the absorption coefficient(left axis) in Cu(In,Ga)Se_2 for different GGIs. Up to $= 3\ \mathrm{eV}$, the absorption spectra are very similar. The penetration depth for the ternaries(dashed lines) is related to the right axis. The dashed orange line shows the measured absorption coefficient of a polycrystalline $CuInSe_2$ layer measured in the home lab. The numbers the different parts in the absorption coefficient influenced by band-to-band transitions (1), transitions far above the band gap (2), defect related (3) transitions (only symbolic), and the Urbach tailing (4). More details about the regions are described in section 2.4.2. Data for α after [35] calculated with equation* (2.17).

3. Defect related absorption. Transition from or to a localized defect state may occur for energies far below the band gap [97].

4. Band tail (Urbach-Martienssen) related absorption (chapter 3): the so called Urbach-Martienssen tailing describes variations from the square root behaviour closely below the band gap [98–101]. The tailing can be caused by band gap fluctuations, disorder in the crystal, optical phonons, impurities and native defects[5]. In any case, the additional interactions are responsible for an extension of the density of state and allow transitions from or into these states. The derivation from the ideal approximation can be described with an exponential function

$$\alpha(E) = \alpha_u e^{-\frac{(E_0-E)}{E_u}} \tag{2.16}$$

where E_u and α_u depend on the measured sample [103][6].

To describe the band gap related transitions and the absorption coefficient for higher energies, equation

$$\frac{\alpha_0}{E}\sqrt{E-E_g} + \alpha_1 \exp\left(\frac{E-E1}{B1}\right) \tag{2.17}$$

can be used, with the absorption coefficient α_0, the band gap energy E_g, the temperature T. The parameter α_1, $E1$, and $B1$ describe the high energy region. For $CuIn_{1-x}Ga_xSe_2$, the absorption behaviour is very similar (figure 2.13). The change towards higher energies corresponds the changing band gap. The values $E1$ and $B1$ differ only slightly and can be calculated with the equation given in table B.1. The equation was extrapolated on the bases of the values given in [35].

Obviously, the absorption coefficient can be used to determine the band gap as described later (section 2.5.4 and 3.2.2).

Impressively, one process inverse to the absorption process, derives automatically from the quantum mechanical treatment [96, 97] and is called "stimulated emission". The photon of a certain energy can induce the transition to a final state lower in energy compared to the initial state. The created photon has the same properties as the photons of the incident beam. In contrast to the stimulated emission, the spontaneous emission occurs independently of an external electromagnetic field and is an intrinsic property of any semiconductor.
A semiconductor in its thermal equilibrium shows a steady generation of electron-hole pairs (ehp) due to a finite temperature ($T > 0K$) balanced by the recombination of these ehp due to a finite lifetime of the charge carriers. This rate is known as the spontaneous emission rate R_{sp} and is closely related to the absorption coefficient discussed above via the Roosbroeck Shockley relation [105]

$$R^0_{sp} = \frac{n^2}{\pi^2\hbar^3c^2}\frac{\alpha(E)E^2}{e^{\frac{E}{k_BT}}-1} = Bn_0p_0. \tag{2.18}$$

[5]The higher the impurity density, the more pronounced the tailing [102]

[6]Sometimes, the Urbach energy is described by using the steepness parameter $\sigma(T) = k_BT/E_u$. The parameter σ depends weakly on the temperature, since for instance the lattice vibrations are temperature dependent. Shioda et al measured the temperature dependence of the absorption coefficient for $CuInSe_2$ and determined the steepness parameter as a function of the composition. A decreasing Urbach energy with the [Cu]/[In] ratio was observed [104].

Here, B is the recombination constant. The spontaneous emission rate can be understood as a generalisation of the radiation from a black body. An ideal black body absorbs and emits photons of all energies. Since a semiconductor only absorbs photons with energies higher than the band gap, the emission is limited by the same restriction. Thus, the absorption coefficient in (2.18) accounts for these limitation. Photoluminescence experiments benefit from the spontaneous emission rate in non-equilibrium, as described in the next section.

2.5. Photoluminescence

The spontaneous emission rate is important, since the inverse determines the radiative lifetime of the charge carrier $\tau = 1/R_{sp}$. It can be easily described with an material specific constant B and the intrinsic carrier concentration $n_i^2 = n_0 p_0$:

$$R_{sp}^0 = B n_i^2. \tag{2.19}$$

After the creation of additional eh pairs, the semiconductor is no longer in a thermal equilibrium and the spontaneous emission rate is modified to:

$$R_{sp} = R_{sp}^0 \frac{np}{n_i^2} - R_{sp}^0 \tag{2.20}$$

Since the recombination rate is directly related to the radiative lifetime, it can be used to estimate the life time in $Cu(In,Ga)Se_2$ to $\tau_{\text{rad}} \approx 10^{-6}$ s using the calculated absorption spectra in figure 2.13. The method is used in [35].

2.5.1. The basic principles

Assuming a semiconductor in a thermal equilibrium (in the dark) suddenly exposed to a photon flux Φ_{ph}. Then, the general principle of a PL experiment can be divided into four steps:

1. The **creation** of an electron-hole pair (ehp) by **absorbing** a photon (section 2.4.2). Obviously, the photon energy has to be at least as high as the energy difference between the involved states, e.g. $E_{ph} > E_g$ for band-to-band transitions. Right after the excitation ($\Delta t \approx 10^{-14}$ s [106]), the electrons energy distribution reflects the spectral distribution of the exciting photon flux (figure 2.14).

2. The **relaxation** of the previously excited ehp (figure 2.14). The excited charge carriers lose rapidly ($\Delta t \approx 10^{-12}$ s [106]) their energy due to thermal relaxation processes, such as the interaction with the lattice, until a new energetical distribution is reached. The new distributions are given by the density of states and require two quasi-Fermi levels to describe the electron and hole distribution. These new distributions are completely independent of the spectral shape of the excitation flux. This is a fundamental difference compared to other interactions like Raman or Brillouin scattering, where the excitation energy is important for the process itself. This is way a monochromatic excitation can be used to perform measurements equivalent to the photon flux from the sun, as explained later in section 3.1.

3. The **radiative recombination** of the relaxed ehp. After the relaxation process, the charge carriers are distributed close to the band edges (see figure 2.16a) from where radiative and non-radiative recombination processes can occur. The radiative recombination leads to the emission of a photon with an energy $E_{emit} = E_i - E_f$ according to difference of the involved energy levels.

4. The **escape** of the emitted photon from the sample. By the radiative recombination, a photon is created within the material, propagating spherically in the crystal (assuming an optically isotropic medium). This photon can interact again with the surrounding and thus might lead to another absorption process or to the stimulated emission process. As long as the quasi-Fermi level splitting is small compared to the band gap, the stimulated emission process can be neglected [96]. Nevertheless, a portion of the emitted photons will reach the surface and leave the crystal.

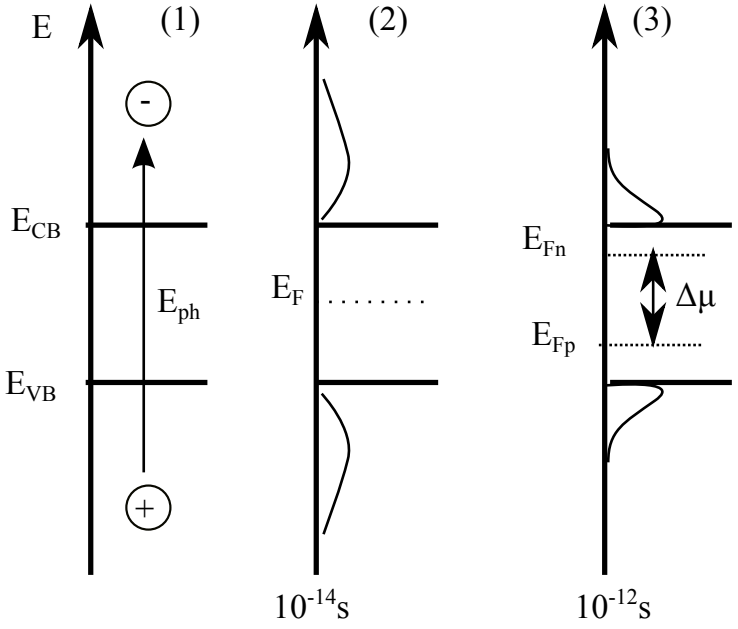

Figure 2.14.: ***Illustration of the absorption process in PL experiments*** *- (1) shows the absorption of one photon with an energy E_{ph}. Usually, many photons are absorbed and the charge carrier distributions reflects (after $\Delta t \approx 10^{-14}$ s) the spectral distribution of the exciting photon flux (2). The distribution can be described wit one Fermi leve. After $\Delta t \approx 10^{-12}$ s relaxation processes (3), a new distribution is observed and described by two quasi-Fermi levels, one for the electrons and one for the holes. According to [106].*

By analysing the emitted photons, many material properties can be derived. Figure 2.15 summarizes the most common transitions that can be observed in photoluminescence (PL) measurements, while the dominating recombination path depends on the temperature. Band-to-band transitions are the dominating process at room temperature and defect or exciton related transitions are usually visible at lower temperatures.
Since the spontaneous recombination rate is proportional to the absorption behaviour (equation (2.18) and (2.20)), the above considerations in section 2.4.2 for the absorption coefficients transfer directly to the spontaneous recombination rate. Again, the probability for a transition from an initial to a final state traces back to Fermi's golden rule (2.14).

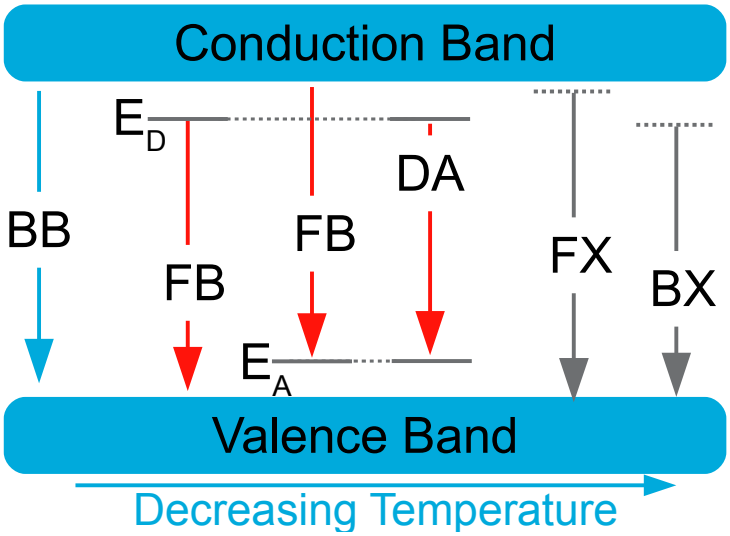

Figure 2.15.: ***Common transitions observed in luminescence measurements*** *- The dominating transition depends on the temperature.*

If the probability for a state being occupied is given by P_i, the spontaneous emission rate is given by:

$$R_{sp} \propto W_{i,f} P_i (1 - P_f). \tag{2.21}$$

The number of recombinations per unit time depends on the number of occupied states $n(E_u)$ in the upper energy and on the number of the unoccupied states in the lower level. It is given by the product of probability P and the density of states D respectively. The number of states may describe a discrete energy state (for impurities) or a distribution (e.g. bands). By finding an appropriate description for the involved states, equation (2.21) can be used to derive precise descriptions for any transition depicted in 2.15. For band-to-band and defect related transitions this is shown elaborately in [96]. Real life conditions aggravate a proper description, since the defect distributions are generally unknown or a mixture of bulk and surface states. Nevertheless, it turned out that a phenomenological description is sufficient, to derive defect and exciton related properties, as briefly shown below. Band-to-band transitions are discussed more in detail in section 2.5.3.

2.5.2. Defect spectroscopy

Within this work, defect spectroscopy based on PL was carried out to confirm the absorber's compositions, since the characteristic PL fingerprints can be used to determine the composition [9, 107]. These measurements are typically carried out at temperatures of $T \leq 10$ K where defect related transitions are dominating. Besides, the PL efficiency[7] is higher, since non-radiative recombinations are usually suppressed. The identification of each transition by changing either the excitation intensity or the temperature and the determination of activation energy is summarized in [9, 17]. Thus, the description is limited to a brief description of the transition characteristics. In general, the nature of a transition can be identified by changing the excitation intensity and the temperature.

[7] The PL efficiency is the ratio of the radiative and the total lifetime.

The change of the peak position and corresponding area is characteristic for the most important transitions. The change of the PL yield with the excitation intensity can be generally described with

$$Y_{PL}(\Phi_{exc}) = \Phi_{exc}^{k} \tag{2.22}$$

where k is the characteristic parameter. The temperature dependence follows the general equation

$$Y_{PL}(T) = 1/\left(1 + T^{3/2} C \exp\left(\frac{-E_{act}}{k_B T}\right)\right) \tag{2.23}$$

and can be used to determine the activation energy of the involved defect.
The parameter k in equation (2.22) and the change of the position of the emission peak maximum when performing an intensity dependent measurement can be used to specify the origin of the transition (discussed below). The position can be described with the empirical equation $E_{max}(\Phi_{exc}) = E_{PL}(\Phi_0) + \beta log_{10}(\frac{\Phi_{exc}}{\Phi_0})$ where the parameter β is also characteristic for the transition. For excitonic transitions $\beta = 0$ and $1 < k < 2$. For defect related transitions $k < 1$. β is zero for Free-to-Bound transitions, a few meV per decade for weakly compensated material and > 10 meV per decade in the case of strong compensated semiconductors [9].

Excitonic transitions

Excitonic transitions are typically observed at low temperatures. The electrically neutral quasi particle (the exciton) consists of an electron-hole pair which is held together by their Coulomb interaction. The maximum of the PL emission is at $E_{max,free} = E_{band} - E_{Coulomb}$. If an exciton is bound to a defect, the maximum is given by the so called "Hayne's rule" [108] $E_{max,bound} = E_g - E_{BE}$ where $E_{BE} = A + BE_{defect}$, where A and B depend on the ionization state of the impurity and the effective masses of the host crystal [109][8]. The line shape of the free exciton is given by an Lorentzian function [110]. Exciton related transitions are useful, because their position can be used to determine the band gap or for instance the valance band splitting in $CuInSe_2$ measured on single crystals [111] or in $CuGaSe_2$ [9]. A bound exciton, or say the constants A and B provide information about the charged state of the defect they are bound to.

Donor-Acceptor transitions

Transitions from one defect state (or a distribution) to another within the band gap are typically called donor-acceptor transitions. The transition process requires two neutral defects as an initial state. An optical transition returns the semiconductor to an equilibrium state, schematically illustrated by the reaction $D^0 + A^0 \rightarrow E_{ph} + D^+ + A^-$. The oppositely charged defects lead to an additional Coulomb energy which is transferred to the emitted photon. This results in an emission peak at $E_g - E_A - E_D + E_{coul}(r_{DA})$. The Coulomb action in the donor-acceptor case depends on the spatial distance r_{DA} between the involved defects. Since both defects are localized, the transition involves a tunnelling step determining the contribution of the Coulomb interaction. While the peak shape is described theoretically in [112], the analysis is usually based on an empirical equation [9].

[8] Hayne's rule may be transformed to $E_{BE} = CE_{defect}$ for a charged defect and to $E_{BE} = CE_{defect} + E_{FE}$ for a neutral defect with the binding energy E_{FE} of the free exciton.

Donor-acceptor transitions deliver information about the defect ionization energies and may be used to correlate the Coulomb energy to a defect concentration [17]. The transition process can involve the interaction with phonons within the sample leading to an additional peak lower in intensity and shifted by the characteristic energy of the involved phonon.

Free-to-Bound transitions

Transitions involving a free carrier with a hole trapped at an acceptor are typically referred to as Free-to-Bound transitions (or via a donor). The emission maximum is reduced by the binding energy of the defect E_{defet} with respect to the band gap. The peak shape depends on the impurity density. For lower concentrations it is well described by Eagles law [113] $I_{PL} \propto \sqrt{E-(E_g-E_{defect})}e^{(\frac{-(E-(E_g-E_{defect}))}{k_BT})}$. With increasing impurity concentration, an overlap of the impurities' wave functions gets more likely. Finally, the formation of an impurity band is observed and reflected in the broadening of the emission peak.

Band-to-Band transitions

Transitions between two bands, say the conduction and the valence band, tend to dominate at higher temperatures, where most of the shallowed defects are ionized and excitons are not observable[9]. Since measurements at room temperature are excessively used within this work, the emission peak at room temperature is discussed more in detail in section 2.5.3.

2.5.3. Band-Band transitions

As pointed out by Bebb and Williams [96], it is possible to determine an equation describing the band-to-band transition with the transition matrix and a detailed analysis of the density of states.
Nevertheless, the same result can be derived with a thermodynamical treatment of radiation, as introduced by Würfel [106, 114]. Würfel pointed out, that the emission of luminescent radiation is a quasi equilibrium problem, if a chemical and thermal equilibrium among the charge carriers in the conduction and in the valence band exists separately[10]. Than, the emission is closely related to the thermal radiation for a black body as described by Kirchhoff's and Planck's law [106, 115]. Due to the electronic structures of semiconductors, photons with lower energies are simply transmitted through the material. This is reflected in Planck's generalized law, derived similar to Planck's derivation. The differences are an additional therm for the emissivity (absorptivity) and the usage of two different Fermi levels. The absorptivity (or emissivity) depends on the photon energy and accounts for the restricted absorption of photons. The different Fermi levels consider the non-equilibrium situation and describe the charge carrier distributions for holes and electrons respectively. If E_{FC} is the Fermi-level for the electrons and E_{FV} the Fermi-level

[9] Excitons usually exhibit small binding energies and are only visible for $k_BT \leq E_{FE}$ where E_{FE} is the binding energy of the free exciton.
[10] This is typically the case unless the lifetime of the excitations is very short.

for the holes, the spontaneous emission rate derives to [106]

$$R_{sp} = A(E)\frac{c_0}{n}D_\gamma(E)\frac{E^2}{exp(\frac{E-(E_{FC}-E_{FV})}{k_BT})-1}. \tag{2.24}$$

Here, $A(E)$ denotes the absorptivity (related to the absorption coefficient with equation (2.12)) and $D_\gamma = \frac{\Omega n^3}{4\pi h^3 c_0^3}$ is the density of states for photons in a solid angle Ω in a medium where n denotes the refractive index. A black body in the sense of Kirchhoff's definition [106] absorbs any photon independent of its energy ($A(E) = 1$). In a thermal equilibrium, one Fermi level is sufficient to describe the charge carrier distributions. In this case, $E_{FC} - E_{FV} = 0$ and equation (2.24) merges to Planck's equation.
For a Lambertian sample surface (section 2.4.2), the detected photon flux outside of the material is given by [106, 116]

$$Y_{PL}(E) = \frac{\Omega}{4\pi c_0^2 \hbar^3}\frac{A(E)E^2}{exp(\frac{E-\mu}{k_BT})-1}, \tag{2.25}$$

if assuming a homogeneous illumination ($\mu \neq 0$), a homogeneous material, and flat Fermi levels. The surface is assumed to be a Lambertian surface [117, 118]. μ is the quasi-Fermi level splitting and is defined as $E_{FC} - E_{FV} = \mu$.
An illustration of the charge carrier distribution for different quasi-Fermi levels is shown in figure 2.16a and the corresponding PL emission spectra are depicted in2.16b. Figure 2.16a illustrates three different Fermi levels E_{FC} for electrons in the conduction band and assumes one value for the holes in the valence band. This situation may refer to a p-type semiconductor excited with three different intensities or to three slightly different materials illuminated with the same excitation flux and exhibiting different non-radiative recombination rates. For simplicity reasons, only one constant E_{FV} is assumed. The grey line represents the density of states and the filled areas the occupied states with respect to the corresponding quasi Fermi level. The emission peak in figure 2.16b was calculated following equation (2.25) requiring the knowledge of the absorptivity (equation (2.12)). The absorptivity (related to the right axis) was calculated using the absorption coefficient for a direct semiconductor (equation (2.15)), for an arbitrary value of reflectivity ($R_f = 0.05$) and, a sample thickness of 2 µm. The low energy side is determined by the absorption behaviour around the band gap. On the other hand, the high energy slope is given by the Boltzmann approximation and determined by the temperature and the quasi-Fermi level splitting. The peak height is very sensitive to changes in the quasi-Fermi level splitting[11]. In the example, an increase of around 8% in the quasi-Fermi level splitting from 0.75 eV to 0.81 eV leads to a difference in the peak height in one order of magnitude.
The knowledge of the quasi-Fermi level splitting is important, since it gives an upper limit for the achievable open circuit voltage in a solar cell by only measuring the bare absorber [106, 120].

2.5.4. Evaluation

As discussed later, it is possible to calculate the absorptivity by modelling the absorption coefficient and use a fitting procedure to determine the quasi-Fermi level splitting as

[11] Of course, the intensity is also very sensitive to the temperature, as discussed in [119]

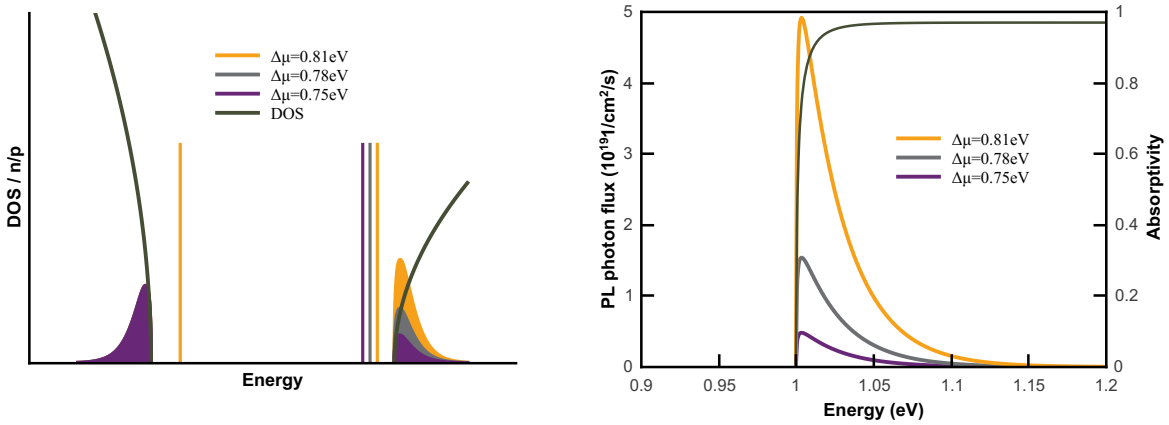

(a) Illustration of the occupied states (coloured area) related to quasi-Fermi level splitting (vertical lines).

(b) Simulated PL emission peaks for different quasi-Fermi level splittings and the absorptivity (grey).

Figure 2.16.: ***Schematic for the PL emission peak*** *- Illustrating the relation (left) between the density of state (gray lines) and the occupied states (coloured area) and the PL emission peak(right). Note that the occupied states (coloured area) cannot extend the DOS. For illustration purposes, the area is bigger than the DOS (in the conduction band)*

described in section C.2. The model can be easily applied to Cu-rich $CuInSe_2$ samples but shows limitations for Cu-poor samples. Nevertheless, an alternative evaluation process can be applied in any case and used to determine the quasi-Fermi level splitting, the temperature, and the band gap E_g. The path is explained in [119, 121] and can be briefly summarized in two steps:

1. When concentrating on the high energy side (Boltzmann approximation) of the emission peak with energies above the band gap $E > E_g + 0.1$ eV [119], the absorptivity can be assumed to be $A(E) \approx 1$. Additionally, the "-1" in the denominator in equation (2.25) can be neglected and transformed to $ln(\frac{Y_{PL}(E)}{CE^2}) = -\frac{E-\mu}{k_B T}$ as shown in 2.17a. A linear extrapolation (grey lines in figure 2.17a) gives the quasi-Fermi level splitting μ and the temperature T

2. The knowledge of μ and T allows the determination of the absorptivity by inserting both values back into equation (2.25). The extracted absorptivity is shown in figure 2.17b. Since the absorption behaviour close to the band gap is determined by the band gap itself and the Urbach tailing (section 2.4.2), both values can be determined in the second step. An experience based approach using the absorptivity indicates that the band gap is related to the energetic position where $A(E_g) = 1/e$ [119] (section 2.5.4). Alternatively, after deriving the absorption coefficient $\alpha(E)$ by means of equation (2.12), The band gap can be deduced by $\alpha(E)^2 * E$ to eliminate the square root in equation (2.15). The intercept with the energy axis of a linear fit to the linear regime gives the band gap.

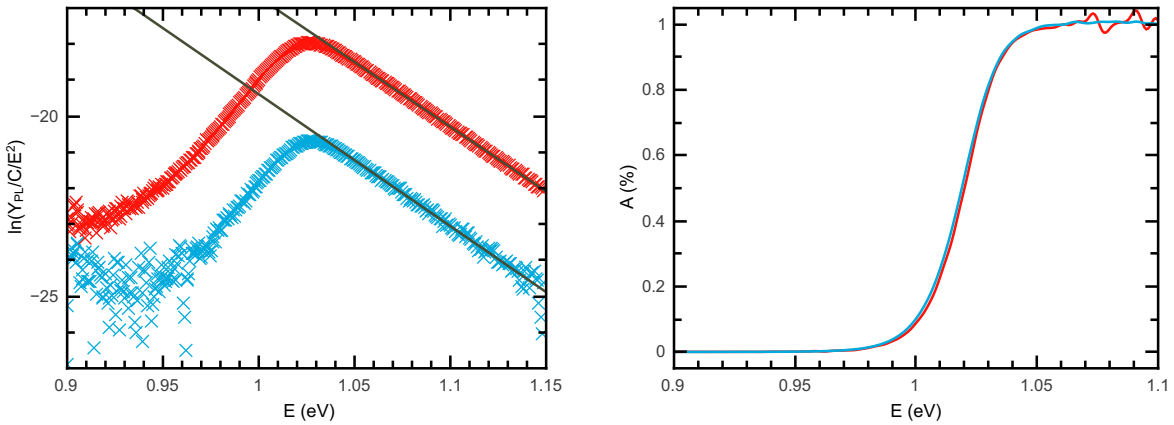

(a) The linear curves show the evaluation allowing the determination of the quasi-Fermi level splitting, red represents a higher quasi-Fermi level splitting.

(b) Illustrating the deduced absorptivity near the band edge. The plot is suitable to determine the optical band gap: $A(E_g) = e^{-1}$. Note, that the absorptivity is independent of the excitation intensity.

Figure 2.17.: ***Illustration of the evaluation procedure*** *- Examples of two PL spectra recorded at room temperature measured for one same sample excited with excitation intensities equivalent to one (blue) and five (red) times AM1.5. The determination of the quasi-Fermi level splitting is shown on the left and the resulting absorptivity on the right.*

2.6. Solar cells

This section deals with the charge transport within semiconductors, in particular in a pn junction, the electrical properties of solar cells, and what kind of experiments reveal details of the solar cell characteristics.

2.6.1. Charge carrier transport in semiconductors

Figure 2.18 shows a schematic band diagram in one dimension of a semiconductor under illumination introducing the important energy levels used in the following with respect to a reference level $E = 0$. The electro statical potential φ accounts for possible space charges within the semiconductor and an external electrical field. The electron affinity χ gives the difference from the electro statical potential to the conduction band maximum E_{CB} and the valence band maximum E_{VB} is given by adding the band gap energy E_g. A position dependence of E_g or χ may arise due to a change in composition with the position z in the material. Finaly, the quasi-Fermi levels are illustrated as dotted lines, describing the electro-chemical potential of the electrons and holes, respectively. The electro-chemical potential itself consists of two contributions: First, the chemistry of the material in form of the electron affinity which depends only on the material. Second, the "reduced chemical potential" which depends only on the particle densities (n and p) and the density of states in the CB and VB (N_C and N_V). According to figure 2.18 the Fermi levels for electrons and holes are given by

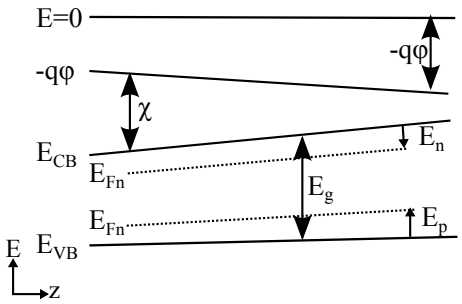

Figure 2.18.: ***General case of the band diagram of a semiconductor*** *- Schematic band diagram of a semiconductor. Note that q may have a positive or negative sign (according to [35]).*

$$E_{Fn}(z) = -q\varphi(z) - \chi(z) - E_n(z) \tag{2.26}$$

$$E_{Fp}(z) = -q\varphi(z) - \chi(z) - E_g(z) + E_p(z). \tag{2.27}$$

The transport equation for electrons (and holes) describing the current density within the device can then be traced back to the position dependent change of the quasi-Fermi levels

$$J_n(z) = \mu_n n(z)\frac{dE_{Fn(z)}}{dz} = \mu_n n(z)(-q\frac{d\varphi(z)}{dz} - \frac{d\chi(z)}{dz} - \frac{dE_n(z)}{dz}) \tag{2.28}$$

with the charge carrier density n, the electron mobility μ_n, and z the position inside the semiconductors (holes by analogy with an additional term for the band gap energy). With the definition in figure 2.18, electrons are moving in the direction of a decreasing E_{Fn} and holes to an increasing value of E_{Fp}.

A proper description of the carrier transport has to take recombination and generation processes into account. As mentioned in the section about defect spectroscopy (2.5.2), recombination processes (and thus also generation processes) from one band to another or transitions involving a defect level in the band gap may occur in a semiconductor. The

continuity equation for electrons and holes accounts for this generation and recombination processes and is given for electrons by

$$\frac{\delta n(z)}{\delta t} = G_n(z) - R_n(z) + \frac{1}{q}\frac{dJ_n(z)}{dz} \tag{2.29}$$

where G_n is the generation rate and R_n the recombination rate for electrons. Both rates may differ for electrons and holes from each other, if the transition process occurs via a trap state.
Finally, the Poisson equation links the electrostatic potential $\varphi(z)$ to the charge density $\rho(z)$

$$\frac{d^2\varphi(z)}{dz^2} = -\frac{\rho(z)}{\epsilon} \tag{2.30}$$

where ϵ is the dielectric constant. Intuitively, the position dependent charge density can be calculated by summing up the electron and hole density and the additionally ionized defects

$$\rho(z) = q(p(z) - n(z) + N_D^+(z) - N_A^-(z) \tag{2.31}$$

The transport, the continuity, the Poisson, and the space charge equation ((2.28)-(2.31)) build a set of coupled differential equations allowing the calculation of the charge transport within a semiconductor or within a junction. An analytical solution is generally not possible and either a device simulation software should be used or further approximations are necessary.

2.6.2. Heterojunction

Assuming a p-type semiconductor (with its Fermi level close to the valence band) and an n-type semiconductor (with its Fermi level close to the conduction band) are brought together, a new thermal equilibrium with only one Fermi level is adapted. Thus, mobile charge carriers are transferred across the interface balancing the different charge carrier concentrations. In the case of a p-type absorber and an n-type window layer, electrons from the window and holes from the absorber will flow across the junction and form a depletion region near the junction. Within the depletion approximation, which assumes that all impurity atoms are completely ionized and that free carriers can be neglected in the depletion region, the width of the region is controlled by the neutrality condition

$$-qN_{A,a}w_a \pm qN_{IF} + qN_{D,w}w_w = 0 \tag{2.32}$$

where w_a is the space charge width in the absorber, and w_w the width within the window layer. The N_{IF} accounts for possible positive (+) or negative (−) charges at the interface. Figure 2.19 illustrates the situation of a heterojunction formed by two semiconductors. The space charge widths are indicated on the z-axis, where $z = 0$ marks the position of the interface. Due to differences in the material properties (the band gaps and electron affinities), a conduction (ΔE_C) and a valence band offset (ΔE_V) appear at the interface. The potential drop across the junction, the so called built in voltage V_{bi}, is given by the conduction band offset, the absorber's band gap, and the reduced quasi-Fermi levels ($E_{p,a} = E_{Fp} - E_{V,a}$ for holes in the absorber and $E_{n,w} = E_{C,w} - E_{Fn}$ for electrons in the window layer) far away from the junction

$$eV_{bi} = E_{g,a} - E_{p,a} - E_{n,w} + \Delta E_C. \tag{2.33}$$

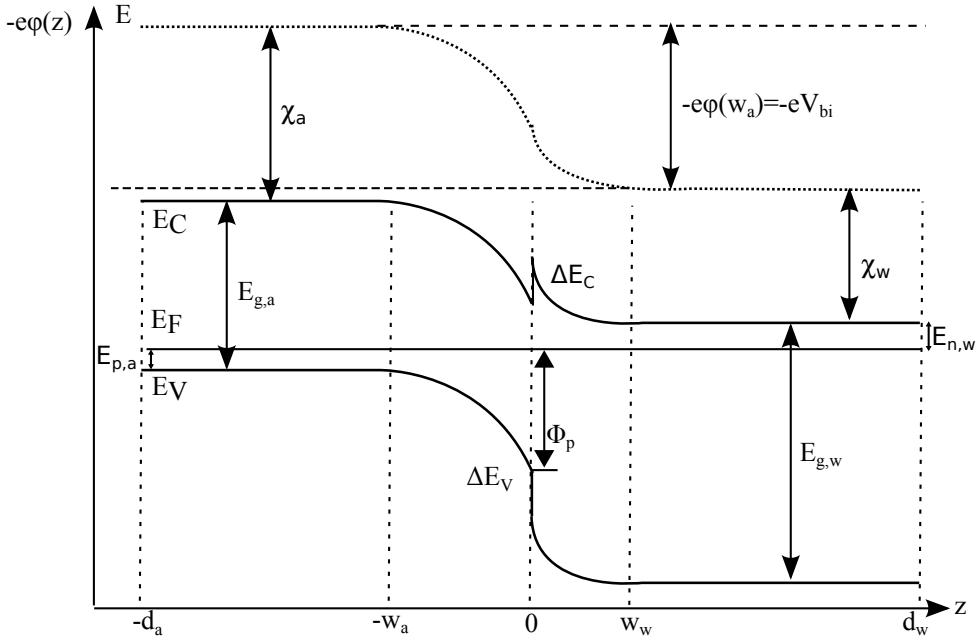

Figure 2.19.: ***Schematic band diagram of a heterostructure*** *- Illustration of the heterostructure formed between a p-type and an n-type semiconductor with different band gaps and electron affinities. The indices a and w refer to the absorber and the window layer.*

An applied voltage V will modify the potential difference between the two sides and the voltage drop across the junction is modified to $(V_{bi} - V)$. Additionally, the depletion width will be modified. It can be calculated by combining the charge neutrality condition (equation (2.32)) and the Poisson equation (2.30) and is given by [35]

$$w_a(V) = +\frac{s\epsilon_a N_{IF}}{\Omega} + \sqrt{\frac{\epsilon_a \epsilon_w N_{D,w}}{N_{A,a}} \left(\frac{2\Omega}{q}(V_{bi} - V) - N_{IF}^2 \right)} \tag{2.34}$$

$$w_w(V) = -\frac{s\epsilon_w N_{IF}}{\Omega} + \sqrt{\frac{\epsilon_a \epsilon_w N_{A,a}}{N_{D,w}} \left(\frac{2\Omega}{q}(V_{bi} - V) - N_{IF}^2 \right)} \tag{2.35}$$

with $\Omega = \epsilon_a N_{A,a} + \epsilon_w N_{D,w}$. Equation (2.34) describes the extension into the absorber and (2.35) into the window layer. The possible interface charges are accounted for by $s = -1$ for a negative and $s = +1$ for a positive charge density at the interface. The first positive sign in combination with the index a describes the width inside the absorber layer and the negative sign (with index w) gives the extend into the window layer. Thus, the space charge width increases under a reverse bias and decreases under forward bias.
For an asymmetric n^+p junction ($N_{D,w} >> N_{A,a}$) without interfaces, the width extents only in the p-type layer and is simplified to [35]

$$w_a(V) = \sqrt{\frac{2(V_{bi} - V)\epsilon_a}{qN_{A,a}}}. \tag{2.36}$$

The commonly used structure of Cu(In,Ga)Se_2 based solar cells contains an addition buffer layer. This leads to a slight modification of the above discussion, since another n-type layer

is introduced between the absorber and the window layer. The resulting modifications of the above equation are discussed for instance in [35]. However, the principle remains the same.

2.6.3. Principle of a solar cell

A solar cell is a device which transforms the energy of light into electrical energy. The cells discussed in this work are based on a heterojunction described above. Photons with a sufficiently high energy are absorbed and electron-hole pairs are generated. These charge carriers may then either recombine or be collected at the contacts. The collection is ensured by a separation of both charge carrier types due to a gradient of the electrochemical potential (as indicated in the transport equation (2.28)). Under illumination, two quasi-Fermi levels are present, so that gradients in the Fermi level for electrons describes the electron current and the Fermi level for holes the hole current.

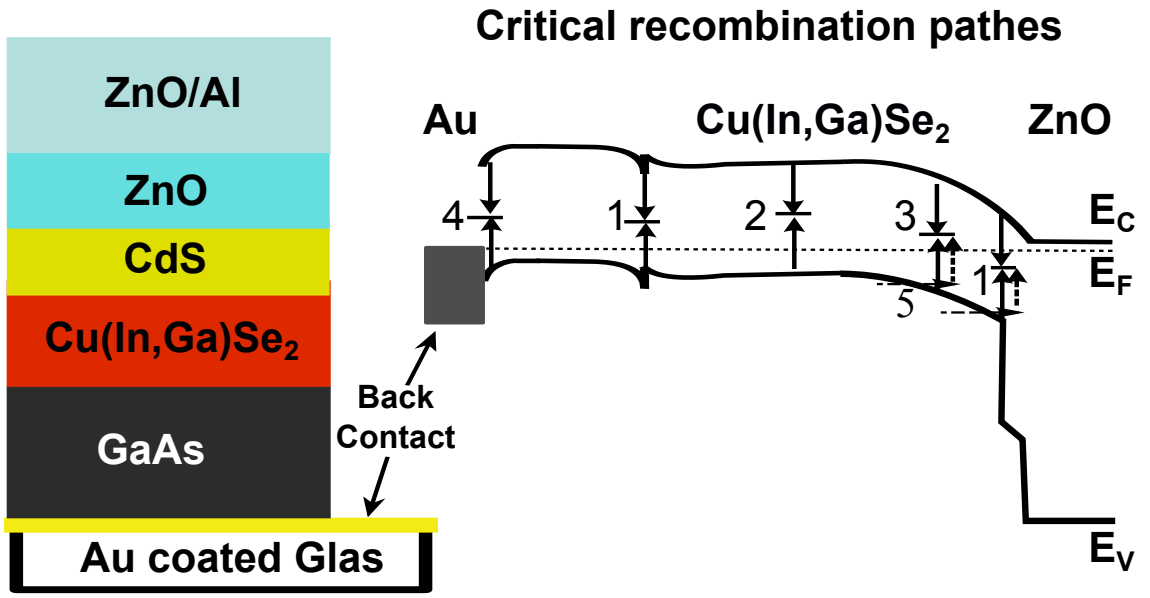

Figure 2.20.: ***Schematic drawing of an epitaxial Cu(In,Ga)Se$_2$ solar cell*** *- Left: Schematics of the epitaxial device used in this work. Details about the deposition are described in section 4.3. Right: Cartoon of the band structure highlighting the most critical recombination paths inside the device. Illustrated are recombinations at the interfaces (1), in the quasi neutral zone (2), in the space charge zone (3), and at the back contact (4). Tunnelling enhanced recombination process at the interface and in the space charge region are indicated by (5).*

In Cu(In,Ga)Se$_2$ based devices (figure 2.20), the electrons (minority carrier) move towards the pn-junction and holes to the back contact. The photo current is determined by the minority charge carriers, which is usually limited by recombination processes in the bulk of the absorber, in the space charge region, at the interface(s), or at the back contact. The critical recombination paths are highlighted in figure 2.20.

Diode currents

Information about the dominating recombination paths can be deduced by measuring the current voltage characteristics of the solar cell. In the dark, a biased solar cell exhibits a voltage dependent diode current. While almost no current flow is observed under reverse bias conditions, an exponential increase under a forward bias is observed. Under illumination, an additional photo current is observed and the total current can be written as a sum of both

$$J_{light}(V) = J_{diode}(V) - J_{ph}(V). \tag{2.37}$$

If the photo current J_{ph} does not depend on the voltage, the current is simplified to $J_{light}(V) = J_{diode}(V) + J_{SC}$, where J_{SC} is the short circuit current, and is called shifting approximation. In practice, solar cells based on heterostructures show all recombination processed mentioned above in parallel (right hand side in figure 2.20), so that the total diode current J_{diode} is the sum of currents from different regions within the cell, e.g. the space charge region or the quasi neutral zone. Generally, each contribution can be described with an exponential equation [35]

$$J_{diode}(V) = J_0 \left(\exp\left(\frac{eV}{Ak_BT}\right) - 1\right) \text{ with } J_0 = J_{00}\exp\left(\frac{-E_{\text{act}}}{Ak_BT}\right). \tag{2.38}$$

Here, T is the temperature, J_0 is the saturation current density and A the diode quality factor, describing the voltage dependence of the current. The saturation current can further be attributed to a characteristic activation energy E_{a} and a reference current density J_{00}. The dominating recombination path may change with the applied voltage. For instance, a small saturation current and a small diode factor will lead to a low current density at low voltages and to high currents at higher voltages. On the other hand, a big J_0 and a bigger A for another recombination path may result in a higher current at low and a smaller contribution at high voltages. Thus, changes in the diode factor of the total current may occur, since the recombination mechanisms in the different zones (figure 2.20) exhibit characteristic diode quality factors, e.g $A = 1$ in the quasi neutral region (QNR, (2) in figure 2.20) and $A = 2$ in the space charge region (SCR, (3) in figure 2.20). A detailed discussion about the different characteristics for the reference current density and the diode quality factor within the different regions can be found elsewhere [35].

Current voltage characteristics

A thin film solar cell can be described with an equivalent circuit of electrical components. The so called one diode model (figure 2.21) assumes, that the current voltage characteristic can be approximated by a diode, a resistor parallel (R_{sh}) to the diode representing a possible shunt, and a resistor in series (R_S).
The current voltage characteristic of a solar cell under illumination can then be described by an implicit function accounting

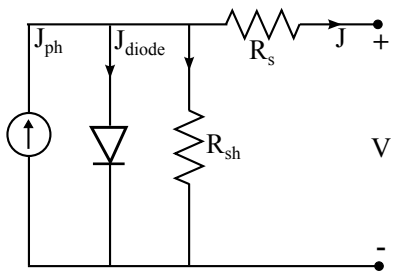

Figure 2.21.: *Equivalent circuit of the one diode model* - *Equivalent circuit illustrating the one diode model. The direction of the current is given within the 4th quadrant of a V-J plot.*

for electrical loss mechanisms within the device [35]

$$J_{light}(V) = J_0 \left(\exp\left(\frac{q(V - J_{light} * R_S)}{Ak_BT} \right) - 1 \right) + \frac{V - J_{light} R_S}{R_{sh}} + J_{SC}\eta_{ec}(V) \tag{2.39}$$

where J_0 is the saturation current density for the recombination under illumination, J_{SC} is the short circuit current and η the voltage dependent external collection function. If the series resistance is small and the parallel resistance high, η_{ec} links the short circuit current to the photo current J_{ph} in equation (2.37) by

$$J_{ph}(V) = J_{SC}\eta_{ec}(V). \tag{2.40}$$

Before discussing the collection function more in detail (section 2.6.5), the important parameters which can be extracted from the current-voltage characteristics are introduced. Characteristic parameters are the open circuit voltage V_{OC} (V(J=0)) and the short circuit current J_{SC} (J(V=0)) and the fill factor (FF). FF can be calculated with

$$FF = \frac{V_{mp} J_{mp}}{V_{OC} J_{SC}} \tag{2.41}$$

where the index mp describe the point with the maximum power output (maximum power point). The conversion efficiency of a solar cell is than given by

$$\eta = \frac{FF J_{SC} V_{OC}}{P_{\text{sun}}} \tag{2.42}$$

where P_{sun} is the incident solar power density. Usually, the efficiency is measured at room temperature with an illumination equivalent to an AM1.5g spectrum [122], to allow a comparison with other devices. Measuring the temperature dependence of the IV curve can reveal further information.

2.6.4. Temperature dependent current voltage analyses

Temperature dependent measurements are useful, since they allow the determination of the dominating recombination path, which may be in the bulk or at the interface. The distinction is possible, since the diode currents from different regions in the device depend on the temperature (equation (2.38)). A practical approach describing the temperature dependence of the open circuit voltage (where J=0) is given by [35]

$$qV_{OC} = E_a + Ak_BTln(\frac{-J_{SC}\eta(V_{OC})}{J_0} - \frac{V_{OC}}{J_0 R_{sh}}). \tag{2.43}$$

Since the shunt resistance is high in a reasonable cell ($> 10^3\ \Omega\text{cm}^2$), the last term in the ln can be neglected. E_a is the activation energy of the dominating recombination path. It is obtained by plotting V_{OC} versus the temperature and given by the intercept with the ordinate at T=0K of a line fitted to the data. If bulk recombination is the prevalent one, the activation energy approximates the absorbers band gap energy. In case of dominating interface recombinations, it leads to smaller energies compared to the band gap and is

related to the interface band gap or to ϕ_p (figure 2.19 in section 2.6.2). The interface band gap is the distance from the lowest conduction band to the highest valence band of two materials.
Additionally, the temperature dependence of the diode quality factor A for a decent solar cell can reveal more information about the location of the dominating recombination path. On one hand, recombinations can be classified with respect to the involved particles

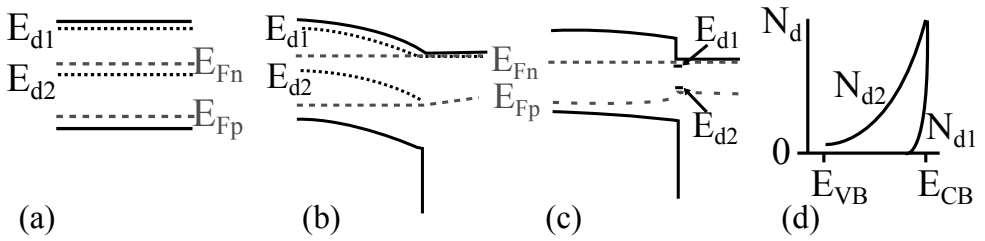

Figure 2.22.: ***Defect related recombination via defect states in a solar cell*** *- Defect related recombination via defect states in the QNR (a), the SCR (b), and at the IF (c) of an absorber/window heterostructure. A defect distribution is illustrated in (d). According to [35].*

absorbing the recombination energy: photons (radiative recombination), electrons (Auger recombination), and phonons (phonon recombination). On the other hand, an alternative classification differentiates band-to-band transitions and defect related transitions. For decent chalcogenide material, it turned out that defect related transitions (Shockley-Read-Hall recombination [123,124]) determine the diode current [35]. Therefore, a more careful discrimination for the diode quality factor is advised, since the defect distribution can influence A.
If the dominating path is located in the QNR ((a) in figure 2.22), the diode quality factor is expected to be $A_{QNR} = 1$ [35]. For an applied forward bias V with $qV >> k_BT$ it can be shown, that the quality factor does not depend on the temperature [35]. It is one for a single defect level and a defect distribution $N_d(E)$.
The defect distribution is assumed to follow an exponential function decaying into the band gap with its maximum N_{d0} at the conduction band edge (d) in figure 2.22)

$$\frac{dN_d(E)}{N_{d0}} = \frac{exp(\frac{-(E_C-E)}{k_BT^*})dE}{k_BT^*} \tag{2.44}$$

where the decay is described with the characteristic energy k_BT^*. An example is depicted in figure 2.22.
If the dominating recombination path is in the SCR ((b) in figure 2.22), the quality factor can be derived to be $A_{SCR} = 2$ for a single energy level in the middle of the band gap which is independent of the temperature. If a defect distribution as given in equation (2.44) is present, the diode factor shows a dependency on the temperature and has to be modified to $A_{SCR}(T) = 2/(1 + \frac{T}{T^*})$. An additional correction term may be necessary, if the device exhibits an enhanced recombination due to tunnelling. In this case, the diode factor reads $A_{SCR,tunnel}(T) = 2/(1 + \frac{T}{T^*} - \Sigma)$ with $\Sigma = \frac{E_{00}^2}{3(k_BT)^2}$ where E_{00} is the characteristic tunnelling energy [35, 125].
A device dominated by interface recombinations ((c) in figure 2.22) with a single defect

level exhibits a diode factor independent of the temperature $A_{IF} = 1/(1-\Theta)$ where the correction term depends on the doping densities of the absorber and the window layer $\Theta = \epsilon_a\epsilon_0 N_{A,a}/(\epsilon_a\epsilon_0 N_{A,a} + \epsilon_w\epsilon_0 N_{D,w})$. Again, the above defect distribution adds a temperature dependence: $A_{IF} = 1/(1-\Theta+\frac{\Theta}{T^*})$ [35]. Tunnelling enhanced interface recombinations influence the quality factor similar to the case of recombinations in the SCR: $A_{IF} = 1/((1-\Theta)(1-\Sigma))$ (single defect) and $A_{IF} = 1/((1-\Theta)(1-\Sigma)+\frac{\Theta}{T^*}))$.

As seen later (section 4.4), the epitaxial cells analysed in this work cannot be described with the one diode model and the proper determination of the diode quality factor is difficult. In general, diode factors greater than two can be explained by tunnelling mechanism (indicated as (5) in figure 2.20). Based on the observation of Riben and Feucht [126] a device which is dominated by tunnelling mechanisms can be identified with a temperature dependent diode quality factor, which is proportional to the inverse of the temperature

$$A \propto \frac{1}{T}. \tag{2.45}$$

2.6.5. Quantum efficiency measurements

While the IV measurement yields information on the total value of the short circuit current density, the measurement of the quantum efficiency (QE) can reveal more details about the collection length and current loss mechanisms. If a bias dependent measurement is performed, the space charge width of the device can further be derived.
The external quantum efficiency (EQE) is defined as the ratio of minority carriers and the number of incident photons electons(λ)/photons(λ) for a certain wavelength λ. The EQE can be written in a differential form [35]

$$EQE(\lambda, V) = -1/q\frac{dJ_{ph}(\lambda, V)}{dj_\gamma(\lambda)} \tag{2.46}$$

where $j_\gamma(\lambda)$ is the incident photon flux density at a given wavelength. Equation (2.46) describes the wavelength dependent current response of the device. Thus, the photo current J_{ph} can be expressed in these quantities by the integration [35]

$$J_{ph}(V) = -q\int_0^\infty \frac{dj_\gamma(\lambda)}{d\lambda} EQE(\lambda, V)d\lambda \tag{2.47}$$

and gives a possibility to calculate the photo current by measuring the EQE. The knowledge of the external collection function to determine the photo current, as described above (equation (2.40)), is not required, since it is contained within the measurement.

Typically, the collection function of the absorber is close to unity within the SCR and declines exponentially with the diffusion length in the QNR [35]. If w_a is the width of the SCR and $L_{n,a}$ is the electron diffusion length, an effective collection length can be defined as

$$L_{eff} = w_a + L_{n,a}. \tag{2.48}$$

As pointed out before, the space charge width depends on the applied voltage and increases under a reverse bias (equation (2.36) in section 2.6.2). Therefore, the collection function

must change and will affect the EQE as well.
The dependency was used by Gärtner [35, 127] approximating the shape of the EQE as

$$EQE(\lambda, V) = T(\lambda)\,(1 - R(\lambda))\left(1 - \frac{\exp(-\alpha_a\,(\lambda)\,w_a\,(V))}{1 + \alpha_a(\lambda)L_{n,a}}\right). \tag{2.49}$$

Here, T is the transmission of the window and the buffer layer and R the reflectivity of the solar cell. α_a describes the absorption coefficient of the absorber. The EQE approaches unity for short wavelengths with $\alpha_a(\lambda)w_a(V) >> 1$ and does not depend on the voltage [35]. On the other hand, when applying a bias voltage to the device, the change in the SCR width will influence the EQE for long wavelengths. A further simplification of (2.49) concentrates on the high wavelength region and allows the determination of the effective collection length L_{eff} defined above [128, 129]:

$$EQE\,(\alpha_a(\lambda)) = K(1 - \exp(-\alpha_a(\lambda)L_{eff}) \tag{2.50}$$

where K is a constant accounting for the losses due to the absorption in the window and buffer layer and the reflectivity of the cell.

Set-Up at LPV

Figure 2.23 illustrates the principle of the technique as it is used in the home laboratory. A monochromator selects the desired wavelength from two light sources, which is then guided to the sample to be measured. The different light sources are optimized to cover the whole spectrum from the ultra violet to the infrared with a sufficiently high intensity. The spot diameter is in the order of 2 mm. Because of the low signal response from the sample, the current is measured with a lock-in amplifier. The required reference point signal for the amplifier is given by a chopper behind the monochromator. The contacts of the solar cell are connected to a potentiostat which first amplifies the current before the signal reaches the lock-in system. Additionally, a DC bias voltage can be applied to the device. The whole system is controlled by a computer program which automatically calibrates the system with the known current response of a Si and an InGaAs diode.

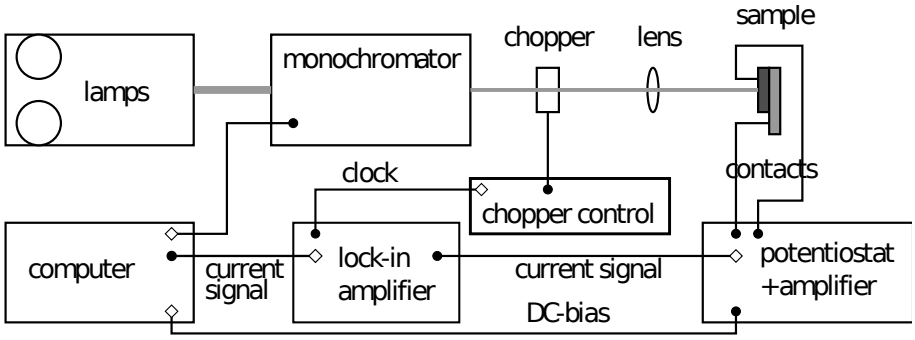

Figure 2.23.: ***Set-up for QE measurement*** *- The optical path of the light monochromatic light beam is shown in gray. The sample is connected to a potentiostat amplifying the signal from the sample before entering into the lock-in amplifier and beeing recorded by a computer. The amplifier uses the chopper as a clock signal. [130]*

2.6.6. Capacitance measurement

The measurement of the capacitance as a function of voltage is a widely used technique to determine the doping concentration and the built in voltage of a device. The capacitance can be determined by applying an AC voltage to a pn-junction and measuring the resulting admittance Y. The capacitance is then the imaginary part of the admittance

$$C = \frac{Im(Y)}{\omega} \tag{2.51}$$

where ω is the angular frequency of the AC voltage. In the specific case of a pn-junction with a highly doped window layer and without deep defects in the absorber, the space charge width is given by equation (2.36). For the specific case, the alternating voltage leads to a constant charging and discharging process of the defect levels located at the boundaries of the SCR. The capacitance can be expressed as the change of charges with the changing voltage and in analogy with the charges on the plates of a capacitance, it is

$$C = \frac{dQ}{dV} = \frac{\epsilon_a A}{w_a} \tag{2.52}$$

with the area A of the solar cell, the space charge width w_a and the dielectric constant of the absorber. If an additional external DC voltage is applied to the device, the SCR is modified (see equation (2.34)) and the capacitance will change accordingly:

$$C = \sqrt{\frac{qA^2\epsilon_a N_A}{2(V_{\mathrm{bi}} - V)}}. \tag{2.53}$$

A transformation yields the Mott-Schottky plot, reflected in

$$\frac{1}{C^2} = \frac{2}{\epsilon_a N_A q A^2}(V_{\mathrm{bi}} - V). \tag{2.54}$$

Thus, by changing the external voltage, the determination of the doping concentration and the built in potential becomes possible.

2.6.7. Band alignment

The band offsets within a pn-junction play an important role for the electrical properties of the device. For example, the built in voltage (equation (2.33)) is influenced by the conduction band offset and changes accordingly the width of the space charge region. A non-optimized band alignment can further hamper the charge transport due to induced potential barriers or an increase in recombination at the interface. While the band offsets for the pn-junction in Cu(In,Ga)Se_2 devices is well studied [9, 35], the following section mainly concentrates on the additional interface to the GaAs substrate. Later, the discussion will be used in the simulation part (section 4.10) showing the calculations for epitaxial devices.
Band offsets can be determined experimentally, e.g. by photoemission spectroscopy (PES) or by capacitance measurements [9, 131] or calculated, e.g. by self-consistent electronic structure calculations [35]. Referring to the interface between GaAs and Cu(In,Ga)Se_2,

experimental data and theoretical calculations can be found in literature. However, as seen later, the values differ slightly and are compared below.
In general, the experimental determination of valence band offsets (VBO) is rather difficult, since various circumstances can falsify the result. For instance, to determine the VBO between two materials A and B by means of PES, the core levels of the bare material A are measured first. Then, thin layers of different thicknesses of material B are deposited and the change of the core levels are measurement again. The comparison of the energy levels allows the determination of the valence band offset. During the growth the interdiffusion of species from material A to B or vice versa might occur, which can falsifies the result.
Another difficulty for $Cu(In,Ga)Se_2$ is the presence of ordered defect compounds (ODC) such as $CuGa_3Se_5$ in $CuGaSe_2$. A ODC phase may falsify the results as well. For example, when going from a Cu-poor to a Cu-rich composition of $CuGaSe_2$, the valance band maximum may shift up to ≈ 0.5 eV [132].

An experimental approach [133] studies the band offsets between $CuGaSe_2$ and $CuAlSe_2$ grown on GaAs using PES. The samples were grown with metalorganic vapour phase epitaxy on a GaAs (001) substrate and are directly comparable with this work. The authors specify a valence band offset of $\Delta E_V = -0.3$ eV when going from the GaAs to $CuGaSe_2$. With a band gap energy of $E_{g,GaAs} = 1.4$ eV for GaAs, the conduction band offset follows to be $\Delta E_C = 0$ eV.

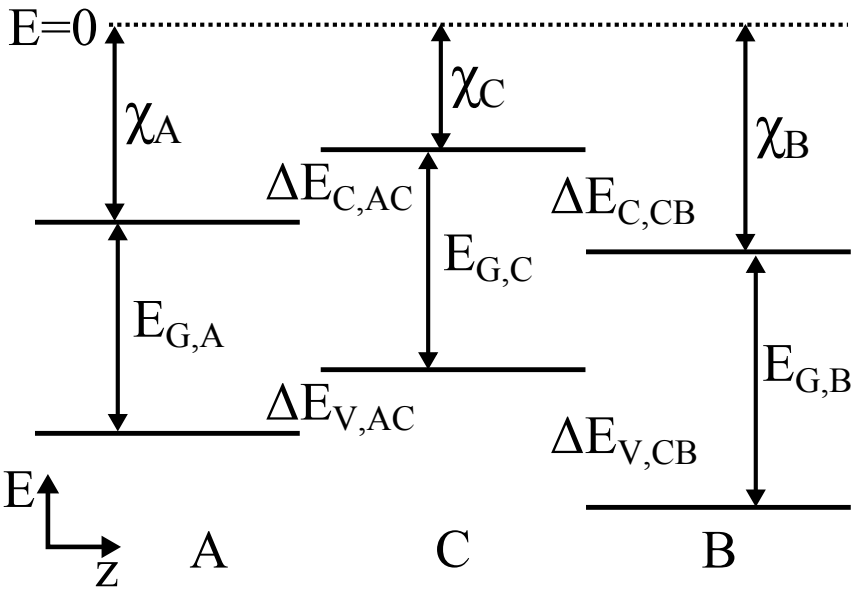

Figure 2.24.: ***Transitivity rule*** *- Illustration of the transitivity rule. The band offsets between two semiconductor A and B can be calculated with the transitivity rule, if the offset of A and B are known with respect to a third semiconductor C.*

The so called transitivity rule [134, 135] helps to derive a comparison and is illustrated in figure 2.24. The rule states, that the offset between two semiconductors A and B can be deduced, if the offset to a third material C is known for A and B, respectively: $\Delta E_v^{AB} = \Delta E_v^{AC} - \Delta E_v^{BC}$.

ΔE_{VB}	ΔE_{CB}	Method	Reference
-0.3	0.0	directly measured (ΔE_{VB})	[133]
0.0	+0.3	transitivity rule	[136, 137]
-0.4	-0.1	IFIGs	[131]
$\approx +0.1$	+0.4	transitivity rule	via $CuInSe_2$ [40, 138]

Table 2.2.: *Valence band discontinuity between GaAs and $CuGaSe_2$* *- Summary of different valence band offsets found in or deduced from the literature. The last row was determined based on measurements of $CuInSe_2$ and ZnSe and then transferred to $CuGaSe_2$ allowing a direct comparison.*

In this case A is GaAs, B is $CuGaSe_2$ and the reference C is ZnSe. By means of PES, the valence band discontinuity between $CuGaSe_2$ and ZnSe were determined to be $\Delta E_V = -0.6$ eV and the offset of the conduction band calculated to be$\Delta E_C = +0.4$ eV [136]. On the other hand, the VBO between GaAs and ZnSe was determined (by PES as well) in [137]. Here, the offset is determined in dependence of the interface composition $\frac{Ga}{As}$ and is for a stoichiometric surface $\Delta E_V = -0.6$ eV when going from the ZnSe to the GaAs and $\Delta E_V \approx -0.7$ eV for $\frac{Ga}{As} \approx 1.5$. Thus, the VBO is $\Delta E_V \approx 0$ eV between GaAs and $CuGaSe_2$ and the CBO calculated to be $\Delta E_C = +3$ eV.

The valence band offset between $CuInSe_2$ and ZnSe was also determined with PES measurements [138]. The results showed a VBO when going from $CuInSe_2$ to ZnSe of $\Delta E_V = -0.7$ eV. According to the transitivity rule, the valence band offset between GaAs and $CuInSe_2$ is then $\Delta E_V = +0.1$ eV resulting in a CB offset of $\Delta E_B = -0.3$ eV for $CuInSe_2$. Since the change of the band maxima for $CuIn_{1-x}Ga_xSe_2$ are known [40], a direct comparison to $CuGaSe_2$ is possible. The band offset between $CuInSe_2$ and $CuGaSe_2$ were found to be $E_V = 0.04$ eV and $E_V = 0.7$ eV [40]. Therefore, the offsets between GaAs and $CuGaSe_2$ read $\Delta E_V = +0.14$ eV resulting in a CB offset of $\Delta E_B = +0.4$ eV.

Finally, the interface-induced gap state (IFIGs) model [131] was applied to $Cu(In,Ga)Se_2$ before [9, 35, 131]. The IFIGSs model relies on a material specific energy level across the interface, the so called charge-neutrality level or branch-point energy. At the interface of two semiconductors, the electronic states determined by the bulk are modified and additional interface states are formed at the interface. These new states are also known as virtual gap states and are within the band gap of the bulk material. The branch-point energy is then defined as the energy level where the character of the virtual gap state changes from VB-like (donor like) to CB-like (acceptor like) [131]. The difference of the branch-point energies of two semiconductors 1 and 2 is directly related to the valance band offset by $\Delta E_{VB} = W_{BP,1} - W_{BP,2}$. Applied to GaAs and $CuGaSe_2$, the valence band offset reads $\Delta E_V = -0.4$ eV [131].

In summary, the valence band offset between $CuGaSe_2$ and GaAs is between $\Delta E_V = -0.4$ eV and $\Delta E_V = +0.1$ eV (table 2.2). In combination with the band gap, the conduction band maximum can be calculated (figure 2.24). For the simulation performed with SCAPS [139], the electron affinity has to be adjusted according to the conduction band, as described in section 4.10. For different GGIs, the band maxima can be calculated according to the equation given in table B.1 (compare figure 2.3). The band discontinuities for the common polycrystalline cells were discussed in literature. A summary of the used values is given in the simulation section 4.10.

CHAPTER

THREE

QUASI-FERMI LEVEL SPLITTING IN $CUINSE_2$ FILMS

This chapter summarizes the results of the PL experiments carried out at room temperature with a series of polycrystalline and epitaxial $CuInSe_2$ samples featuring a range of composition of [Cu]/[In] $\approx 0.8 - 1.7$. Since the set-up is used for all measurements, it is described in the beginning. The measured spectra were analysed as shown in section 2.5.4 and are discussed in section 3.2 and 3.3.

3.1. Methodology

3.1.1. Set-up

Within this work, the available set-up at LPV was extended to allow intensity calibrated measurements. To improve the collection of photons emitted from the sample, lenses had to be exchanged. The new lenses have an anti reflecting coating in the spectral range of interested around 1 eV. A new spectrally calibrated light source was introduced ensuring a spectrally correction. The new intensity calibration was established by using the available laser systems. The correction is described more in detail in section 3.1.2.
All measurements were carried out with the extended self-made set-up schematically shown in figure 3.1. The set-up uses a confocal geometry, meaning that one lens (2) is used to focus the excitation onto the sample and to collect the emitted photons from the sample. An advantage of this configuration is the efficient collection of the emitted signal, since the position of the sample holder coincidences with the focal point of this lens (lens 2 in figure 3.1). The excitation was realized using the green laser line ($\lambda = 514.5$ nm) of an argon ion laser (green line in figure 3.1). To avoid a high excitation density on a tiny spot (due to the focusing onto the sample), a beam widener was introduced (the combination of lens (1) and (2)). The optical path of the excitation is illustrated in figure 3.1 where the position of lens (1) is chosen such that the focal point (circle) of this lens and the one next to the sample (lens (2)) fall together. Thus, the beam widener acts as a Keplerian telescope as described in [140] where the optical path of a Gaussian beam is explained more in detail. The widening ensures a homogeneous excitation reflected in the parallel beam at the sample's position in figure 3.1. The beam size was chosen to be bigger than the detected area and the diffusion length of the charge carriers in $CuInSe_2$. The diffusion length in $CuInSe_2$ depends on the [Cu]/[In] ratio and is between 1.6 µm

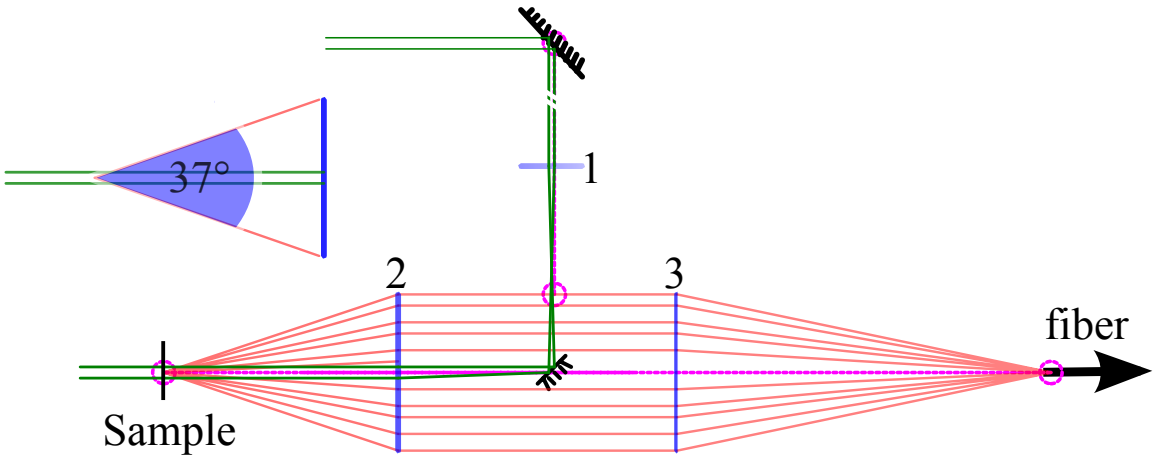

Figure 3.1.: ***Schematic view of the PL set-up*** *- Optical path for the confocal set-up used for the PL measurements. Mirrors (black) and lenses (blue) were used to ensure a big excitation spot on the sample and to guide the emitted photons to a fiber connected to the spectrometer. Therefore, the focal points of the lenses (1) and (2) were chosen such that they act as a Keplerian telescope and thus as a beam widener. Note that the exciting laser beam (green) is parallel at the measuring position. The sample's position is at the focal position of the lens (2), ensuring an efficient collection of the PL signal (red lines) and parallel light beams on the right hand side of lens (2). The focal point of lens (3) guides the photons to the fiber connected to the spectrometer.*

for Cu-poor and ≈ 3 µm for Cu-rich material [141]. Finally, the emitted photons were collected and coupled into a fiber optic guiding the signal to the spectrometer (Shamrock SR-303i-B from the company Andor). The spectrometer is equipped with a Si camera for the visible spectral range and an InGaAs detector for higher wavelengths.
The beam size at the samples position was determined with a CCD camera. The physical dimensions of the active area on the chip allows the transformation from pixel to a physical length. Thereby the determination of the area and thus the power density of the excitation source is possible. This is crucial to ensure comparable excitations by allowing the calculation of a photon flux and thus the specification of a sun equivalent. Figure 3.2 illustrates the calibration function for the excitation, where this flux is plotted against the power indicated on the control unit of the laser. The right axis (logarithm) translates the flux into the equivalent of suns assuming a semiconductor with a band gap of $E_g = 1$ eV. The translation is done my means of the AM1.5g spectrum [122]. The integral $\int_{E_g}^{\infty} AM1.5(E)dE$ over the AM1.5g spectrum determines the number of absorbable photons (see appendix C.1).

3.1.2. Correction function

To separate the reflected excitation signal from the actual emission spectrum, the usage of additional filters is necessary[1]. These filters may show different transmission characteristics and can modify the spectrum emitted from the sample. Additionally, the detectors

[1] In fact, many facts determine the measured spectra. More optical compounds such as grey filters or colour filters might be in the optical path or gases in the ambient air, for instance water vapour [142] may absorb the emitted photons and thus falsify the data.

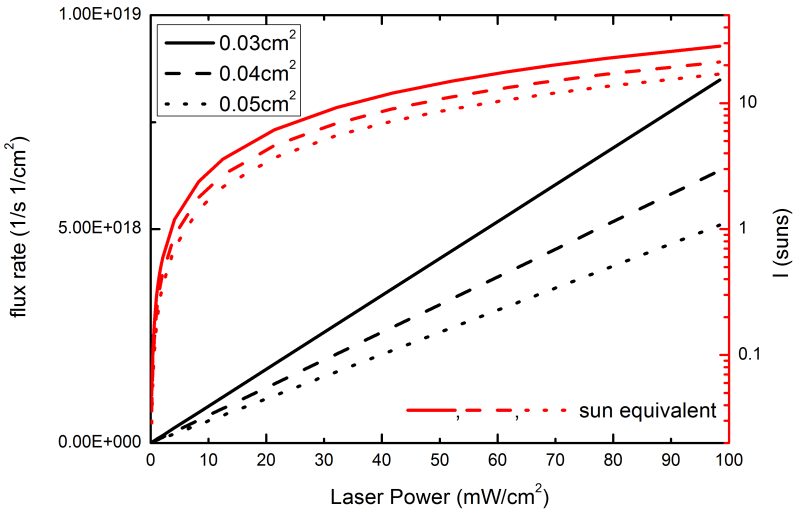

Figure 3.2.: ***Calibration of the excitation*** *- The calibration function for measuring equivalent to x-suns. The abscissa shows the laser power on the control panel of the laser. Measuring the power at the sample position within the set-up and by knowing the diameter of the laser beam the photon flux density at the sample position can be determined. The equivalent sun(s) are given on the right axis.*

show a wavelength dependent sensitivity. To take the transmission characteristics of the optical components, the sensitivity of the detector, and other spectral distortion into account, the raw measurement has to be corrected spectrally. Measuring the spectrum of a known reference light source allows the determination of a wavelength dependent correction function. By applying this correction function to the recorded emission spectra of a sample, all set-up related (spectral) errors are eliminated. The unit of the intensity measured in the detector is still arbitrary. The spectral correction is illustrated in figure 3.3 where the measured reference spectrum (red line) of the calibration lamp (dotted red line) is shown. If $f_{\mathrm{exp}}(\lambda)$ is the measured spectrum of a known spectrum $f_{\mathrm{cal}}(\lambda)$, the spectral correction function $c(\lambda)$ is given by

$$c(\lambda) = \frac{f_{\mathrm{cal}}(\lambda)}{f_{\mathrm{exp}}(\lambda)}. \tag{3.1}$$

To determine absolute values of the quasi-Fermi level splitting and the temperature (section 2.5.4)[2], an additional intensity correction is necessary. The spectral correction has to be scaled to convert the arbitrary unit into a meaningful power density.

The scaling factor was determined by means of the laser line with a known power density[3]. Therefore, the laser peak was measured and spectrally correcting by applying the spectral correction function given by equation (3.1) (blue peak in figure 3.3). If the photon flux from the laser is given by ϕ and the maximum of the spectrally corrected

[2]Note that the absorption behaviour can be determined without knowing the absolute value of emitted photons.

[3]As described above, the area of the laser spot was determined with a CCD camera. The power was determined with a power meter.

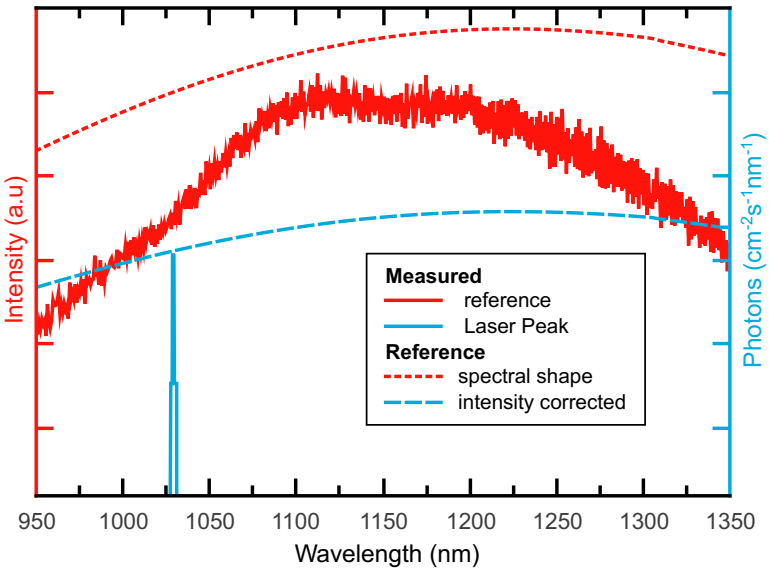

Figure 3.3.: ***Absolute correction function*** *- The schematic plot illustrates the spectral and intensity correction. The spectral shape of a known reference light source (dotted line) can be used to correct the measured reference (red line). The spectral corrected data can be scaled to an absolute value by multiplying the data with an additional factor. Note that depicted laser (blue line) is the second order peak to illustrate the principle. The correction factor was determined with the main peak at $\lambda = 514$ nm. The spectrally and intensity corrected reference measurement is shown as the dashed blue line.*

peak by p_{max}, the scaling factor is calculated by $s = \frac{\phi}{p_{max}}$. Then, the absolute intensity is given by

$$c_{abs}(\lambda) = c(\lambda)s \tag{3.2}$$

The dashed blue line in figure 3.3 shows spectrally and intensity corrected reference spectrum. To minimise the error, several laser peaks with different photon fluxes (compare figure 3.2) should be measured and averaged.

3.1.3. Lambertian surface

As pointed out before, the validity of Planck's generalized law (equation (2.25)) is delimited by various assumptions (see chapter 2.5.3). One of these assumptions is the existence of a Lambertian surface (section 2.4.2), meaning that the angular dependence of the intensity with respect to the surface normal follows a cosine law described by Lambert's emission law [117,118]. Since the evaluation of the performed PL experiments within this work rely on (2.25) it is worthwhile to revise the angular dependence of the emitted photons. Exemplary, a Cu-poor and a Cu-rich sample for both material types (polycrystalline and the epitaxial) were measured. The schematic set-up for the measurement is depicted in figure 3.4a, where the sample is mounted above the fixed rotation centre of a rotatable arm. The arm is equipped with a fiber optics connected to the same spectrometer as used in the later measurements and described in section 3.1.1. The distance between the surface and the fiber was approximately 4 cm. The incident laser beam was parallel to the sample's surface normal. The intensity was chosen such that a compromise between

a reasonable count rate and the measurement time was found for the different samples, respectively. To compare the different measurements, the peaks where normalized to the highest measured signal for one sample.

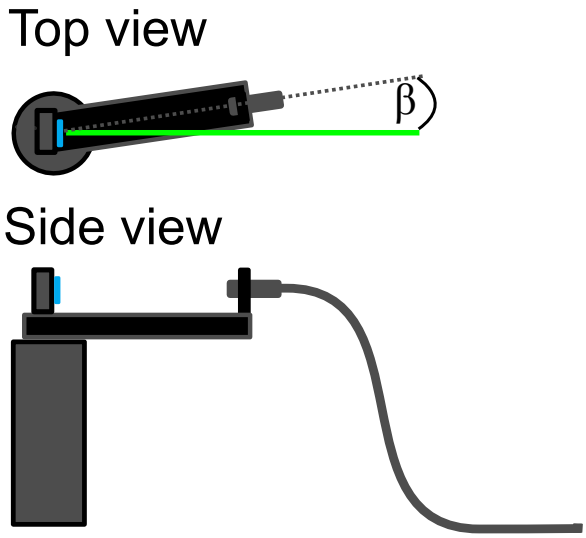

(a) Schematic view of the set-up to measure the angular dependence of the emitted signals. The green line represents the incident laser beam.

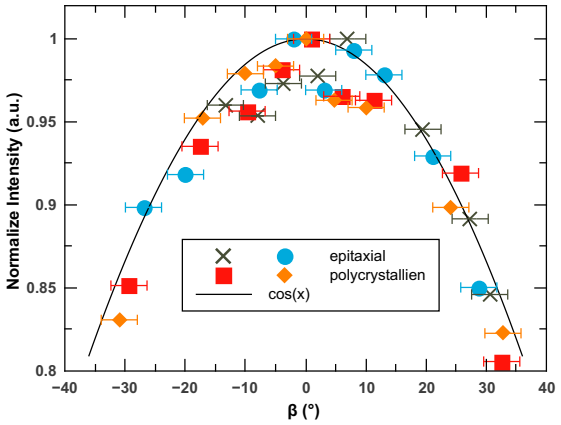

(b) Normalized maxima of the recorded spectra in dependence of the measuring angle (symbols). The angle is illustrated in the set-up on the left hand side. The line represents the shape according to Lambert's emission law.

Figure 3.4.: ***Angular dependence of emitted photons for $CuInSe_2$*** *- Set-up (left) used to validate the Lambertian surface and the measured intensity distribution(right).*

Figure 3.4b summarizes the angular dependence of the peak maximum normalized to the highest value, respectively. The argumentation is limited to the maximum height, since neither the position on the sample nor the excitation intensity was changed. Thus, the peak height is directly proportional to the quasi-Fermi level splitting of each absorber. The solid line in figure 3.4b represents the expected dependence for a Lambertian surface. The measured intensities are in reasonable agreement with the theoretical curve. Thus, one can conclude, that the $CuInSe_2$ samples behave like a Lambertian surface and the assumption for equation (2.25) is valid.

3.2. Influence of Cu excess during the growth

The following part concentrates on the influence of Cu excess during the growth of the absorber layers. The influence will be discussed in terms of the quasi-Fermi level splittingand the absorption behaviour near the band edge. In the beginning the composition dependence of the quasi-Fermi level splitting is examined, since this value is compulsory for the calculation of the absorption behaviour.
Two sample series of $CuInSe_2$ are investigated: an epitaxial and a polycrystalline one. The epitaxial samples where grown as described in chapter 2.3. The polycrystalline samples were grown on a molybdenum coated soda lime glass substrate in a molecular beam

epitaxy (MBE) chamber. The elements were co-evaporated following a modified three-stage process [143, 144]. For the Cu-poor films the full three-stage process with different durations of the third step was used. On the other hand, Cu-rich films were prepared by varying the duration of the second stage without the third step.
All samples were measured, the spectra corrected (section 3.1.2) and evaluated as described in section 2.5.4 (compare section D).

3.2.1. Quasi-Fermi level splitting

The dependence of the quasi-Fermi level splitting on the absorber's composition is depicted in figure 3.5 for the polycrystalline samples (blue circles) and for the epitaxial ones (red diamonds). In general, both series exhibit the same trend: an increase of the quasi-Fermi level splitting with an increasing [Cu]/[In] ratio. Nevertheless, the epitaxial material exhibits in general $\approx 50 - 100$ meV higher values compared to the polycrystalline ones.

The epitaxial series shows an almost linear correlation between [Cu]/[In] $\geq$ 0.8

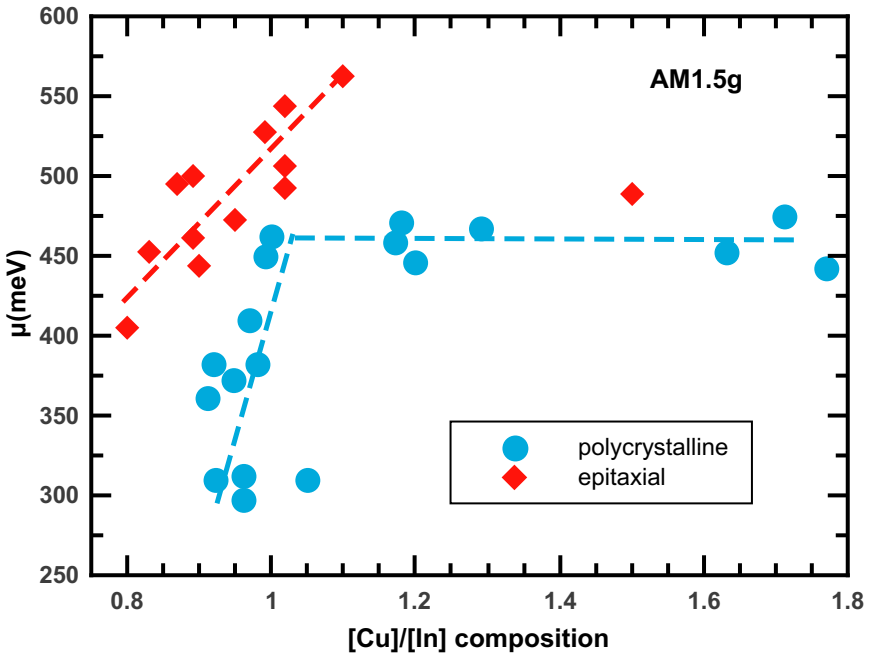

Figure 3.5.: ***Quasi-Fermi level splitting of epitaxial and polycrystalline $CuInSe_2$*** *- The quasi-Fermi level splitting for epitaxial (red diamond) and polycrystalline (blue circles) $CuInSe_2$ samples in dependence of their composition. The excitation was equivalent to AM1.5g (see section 3.1.1).*

and [Cu]/[In] $\leq$ 1.1 starting at $\approx$ 405 meV up to $\approx$ 570 meV. However, the value for [Cu]/[In] $\approx$ 1.5 does not follow this trend. The significantly lower value of 490 meV is probably related to a different surface structure. Due to the high Cu excess, it is very likely to form Cu_xSe crystals on top of the surface [13, 84]. This additional compound modifies the reflection behaviour, may introduce non-radiative recombination regions, and the emitted photons from $CuInSe_2$ can be scattered. Thus, the emission rate outside the

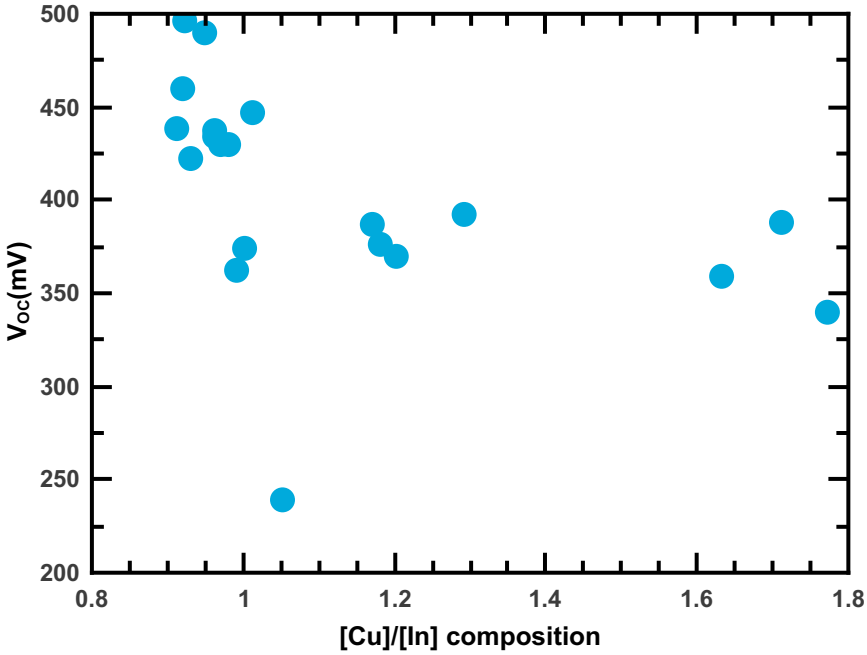

Figure 3.6.: ***Open circuit voltage for polycrystalline $CuInSe_2$*** *- Open circuit voltage of cells made from polycrystalline absorbers of the same growth process as the samples shown in figure 3.5.*

sample is reduced.
On the other hand, the polycrystalline series exhibits a step like behaviour around the stoichiometric point. First, the increase for [Cu]/[In] < 1 can be approximated by a linear behaviour, levelling off for samples grown with a higher Cu supply. Only one point at [Cu]/[In] $= 1.05$ does not follow this trend and shows a minor quality compared to the higher values of the neighbouring compositions. This is most likely related to this particular growth process.
Since the quasi-Fermi level splitting limits the maximum achievable open circuit voltage (section 2.5.3), it is interesting to compare the measured values with the V_{OC} of the final devices. Unfortunately, it was not possible to create pure $CuInSe_2$ based epitaxial solar cells, which is why the following discussion is limited to the polycrystalline samples.

Correlation with V_{OC}

During one process, four different films can be grown at once with an identical composition. While several absorbers are used to perform different characterisation techniques, one is used to make solar cell devices. Figure 3.6 shows the measured V_{OC} of the finished devices for the above discussed absorbers respectively. Compared to the measurements of the quasi-Fermi level splitting on the bare absorbers, the opposite trend is observed: The V_{OC} decreases until slightly above the stoichiometric point and levels off for [Cu]/[In] ≥ 1.2. As indicated already above, the outlier ([Cu]/[In] $= 1.05$) deviates from this trend. The deviation can be attributed to a minor absorber quality and could be observed before. This indicates that the determination of the quasi-Fermi level splitting before finishing the complete device is a suitable tool to sort out absorber layers with a

minor quality and thus saving time and resources.
Besides the general contradicting trend (compared to the quasi-Fermi level splitting in figure 3.5), the values differ significantly. While μ shows values of ≈ 300 meV for the lowest [Cu]/[In] ratios, the V_{OC} rises up to 0.5 V. This difference is related to the ageing of the absorber material, which is especially severe for Cu-poor compositions. As discussed later more in detail (section 3.3), the absorber's quality is significantly reduced when exposed to air and can be recovered with an etch in KCN. Since an etch in KCN is the standard procedure in the lab when making solar cells, the increase is related to the refreshing etch. The contradicting trends in the V_{OC} and the quasi-Fermi level splitting leads to the conclusion, that the samples grown under Cu excess have in principle a higher potential. The quasi-Fermi level splitting of the bare absorbers reveals ≈ 100 meV higher values than the measured V_{OC}. Thus, the generally observed trend for worse performing Cu-rich $CuInSe_2$ [145] cannot be explained by a minor absorber quality of samples grown under Cu excess. A fundamental difference between Cu-rich and Cu-poor compositions is a higher doping level and a widening of the surface band gap. It is believed that the enlargement of the band gap is accompanied with a bigger valence band offset to the CdS layer which is beneficial for the type inversion at the pn-junction [145]. In combination with the generally observed higher doping concentrations, the interface recombinations for Cu-rich samples are significantly higher and can explain the difference between the higher quasi-Fermi level splitting and the lower V_{OC}. The discussion about the difference between Cu-poor and Cu-rich absorbers and the different situation at the interface is continued in chapter 3.3.

3.2.2. Absorption

Knowing the quasi-Fermi level splitting (and the temperature), the absorption behaviour near the band gap can be deduced (section 2.5.4) and therefore the optical band gap and the Urbach energy. The absorption coefficient can be calculated by means of equation (2.12), if the sample thickness d and the reflectivity R_f are known. For the evaluation the reflectivity was assumed to be $R_f = 0$ since the reflectivity in $Cu(In,Ga)Se_2$ within the band gap region is low enough that it does not modify the values for the quasi-Fermi level splitting significantly [119] (compare section C.2). The calculated absorptivity spectra are depicted in figure 3.7 where the red colour indicates the Cu-rich and the blue the Cu-poor side. A clear trend is observed, namely a shift to higher energies with an increasing [Cu]/[In] -ratio. A more detailed analysis is given in the following.

Band gap

In the following, the absorptivity (1) (section 2.5.4) and the absorption coefficient (2) (equation (2.15)) are used to determine the band gap.
The first method is illustrated in figure 3.7 and shows the absorptivity for the epitaxial (left) and the polycrystalline (right) samples. The green line indicates the position, where the absorptivity drops to e^{-1} so that the intercept with the absorptivity gives the position of the band gap. Figure 3.8 shows the second method using the absorption coefficient, and depicts the squared absorption coefficient deduced from the absorptivity. The green dashed line shows an exemplary linear fit in the linear regime. In this case, the band gap

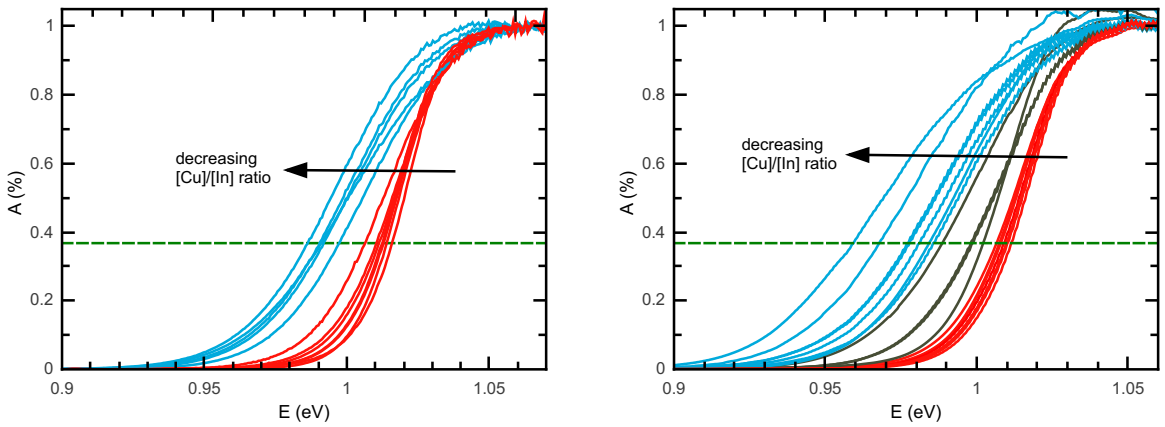

(a) Epitaxial $CuInSe_2$ *(b) Polycrystalline $CuInSe_2$*

Figure 3.7.: *Absorptivity for epitaxial and polycrystalline $CuInSe_2$* *- Calculated absorptivity for $CuInSe_2$ absorber layer with different compositions: Cu-poor (blue), Cu-rich (red), and around the stoichiometric point (grey). The dashed green line represents $A = e^{-1}$ as an indication for the band gap. The spectra are deduced from PL measurements at room temperature and determined as described in section 2.5.4*

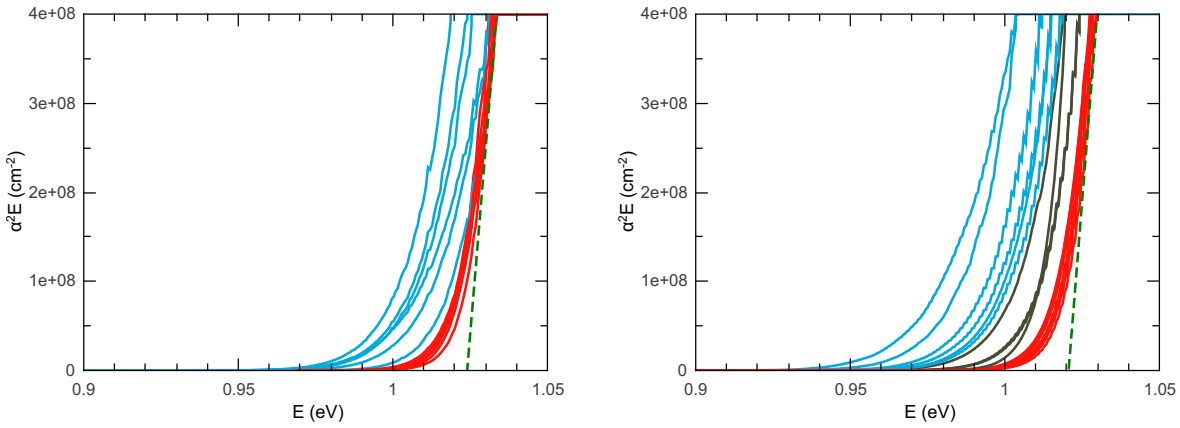

(a) Epitaxial $CuInSe_2$ *(b) Polycrystalline $CuInSe_2$*

Figure 3.8.: *Absorption coefficient for epitaxial and polycrystalline $CuInSe_2$* *- Absorption coefficient α for $CuInSe_2$ absorber layer with different compositions: Cu-poor (blue), Cu-rich (red), and around the stoichiometric point (grey). The absorption coefficient was derived from the absorptivity shown in figure 3.7 with equation (2.12). The absorption coefficient is plotted as $\alpha(E)^2 E$ in dependence of the energy to determine the band gap energy. The straight line (green) indicates the region dominated by the square root behaviour of the absorption coefficient.*

is given by the intercept with the energy axis.

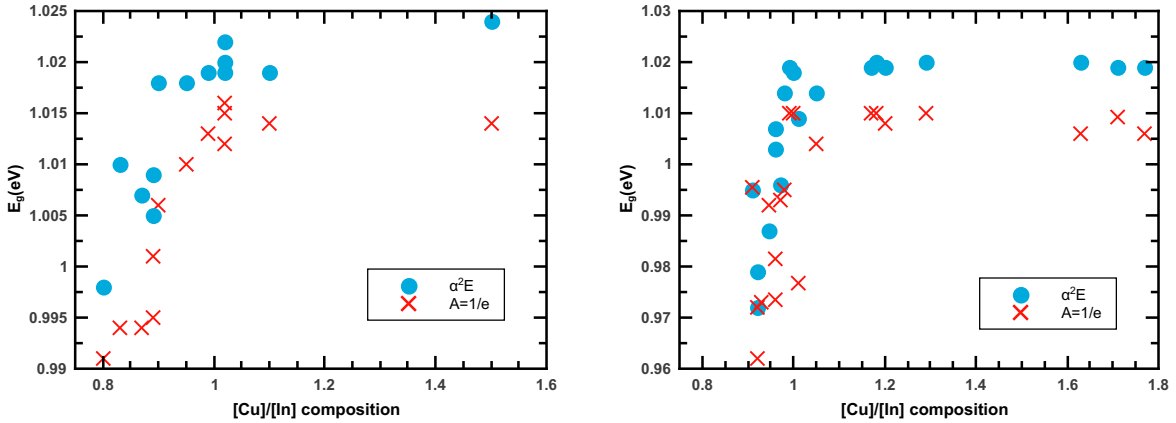

(a) Epitaxial $CuInSe_2$ *(b) Polycrystalline $CuInSe_2$*

Figure 3.9.: *Composition dependence of the band gap for $CuInSe_2$* *- The composition dependence of the band gap for epitaxial (left) and polycrystalline (right) $CuInSe_2$ with different [Cu]/[In] ratios determined with different methods.*

The results of the composition dependent optical band gap determined via the PL measurement are depicted in figure 3.9b (polycrystalline) and 3.9a (epitaxial) where the red crosses were determined using method (1) and the blue circle with method (2).
Either way, both sample types show an almost identical shape, namely a constant increase up to a composition of [Cu]/[In] = 1.0 and levelling off afterwards. In the polycrystalline case, the levelling off occurs at $E_g \approx 1.01$ eV (method (1)) or following method (2) at $E_g \approx 1.02$ eV. Although the values for samples with [Cu]/[In] > 1 are comparable for both types, the polycrystalline material shows slightly lower values on the Cu-poor side down to $E_g = 0.96$ eV and $E_g = 0.97$ eV for the lowest [Cu]/[In]-ratios, while the epitaxial counter part reaches values down to $E_g \approx 0.99$ eV. The reason for the difference might be related to strain within the epitaxial film. Tight-binding calculations applied to $CuGaSe_2$ showed a dependence of the band gap on the ratio a/c of the lattice constants [17, 43, 72]. Therefore, it is likely that the epitaxial Cu-poor samples were slightly strained.
The two methods to determine the band gap lead to slightly different values. Obviously, the usage of the absorption coefficient seems to be more reliable, since it is identical to the literature value of $E_g = 1.02$ eV [41, 146, 147] since it is rather clear to find the linear region arising from the transformation from a square root behaviour to a linear shape by squaring the absorption coefficient. The absorptivity method is slightly hampered by the influence of the Urbach tailing. However, a clear distinction between the Urbach tailing dominated part and the band gap related part is clearly possible.
The increasing band gap with an increasing [Cu]/[In] ratio can be explained with improved theoretical calculations. Self-consistent band structure calculations predicted a pronounced dependence of the band gap on the anion displacement parameter (section 2.1.1. Indeed, huge differences in the displacement parameters had been observed while the band gap remained unchanged [148]. This indicates, that the theoretical calculations in the past overestimated the influence by neglecting an other band gap stabilizing effect.

GW calculations explain this stability for $CuInSe_2$ by a feedback mechanism [148, 149]: if a distortion of the lattice occurs, the variation of the anion displacement affects the size of the band gap. However, this variation also acts upon the concentration of Cu vacancies, since the formation energy of this defect is modified by a shift of the valence-band maximum (VBM). As a result, the variation in the density of Cu vacancies induces a change in the band gap that counterbalances the initial change due to the distortion [148].

Urbach tailing

As discussed in section 2.4.2, the typical square root character of the absorption coefficient near band gap has to be extended by an exponential function describing the Urbach tailing for a proper description below the band gap. By plotting the absorption coefficient logarithmically, a straight line reveals the region, where the Urbach tailing dominates the absorption. This can be seen in figure 3.10 showing the logarithm of the absorption coefficients for the known sample series. The colour indicates the composition: Cu-poor

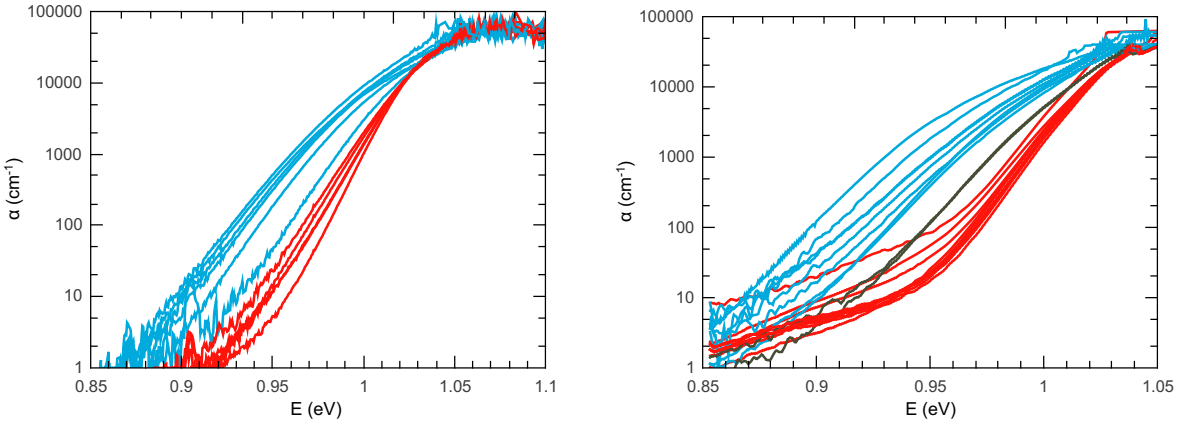

(a) Epitaxial $CuInSe_2$ *(b) Polycrystalline $CuInSe_2$*

Figure 3.10.: *Absorption coefficient for different [Cu]/[In]-ratios of $CuInSe_2$* *- The absorption coefficient of epitaxial (left) and polycrystalline (right) $CuInSe_2$ thin films derived from PL measurements.*

in blue and Cu-rich in red. For the polycrystalline material (figure 3.10b), the Cu-poor samples exhibit a more convex and the Cu-rich ones a more concave shape. Although this effect is significantly less pronounced for the epitaxial films, it is still visible. Another interesting feature is the appearance of an additional slope within the band gap ($E \leq 0.9$ eV) for the Cu-rich absorbers. As pointed out before (section 2.4.2), this region is related to transitions into localised states, namely defects.
By fitting the exponential function (2.16) within the linear region right below the previously determined band gap energy, the Urbach energy can be obtained. The results of the fitted Urbach energies are depicted in figure 3.11. The red diamonds and the blue circles show the Urbach energies for the epitaxial and the polycrystalline samples, respectively. Both kinds of absorbers are again very comparable: With an increasing [Cu]/[In] ratio, the Urbach energies decrease from ≈ 15 meV (16.5 meV for polycrystalline) until levelling out for [Cu]/[In] > 1.0 at ≈ 9 meV (11 meV). In general, the values are comparable to the ones measured on single crystals grown by a freezing method [104].

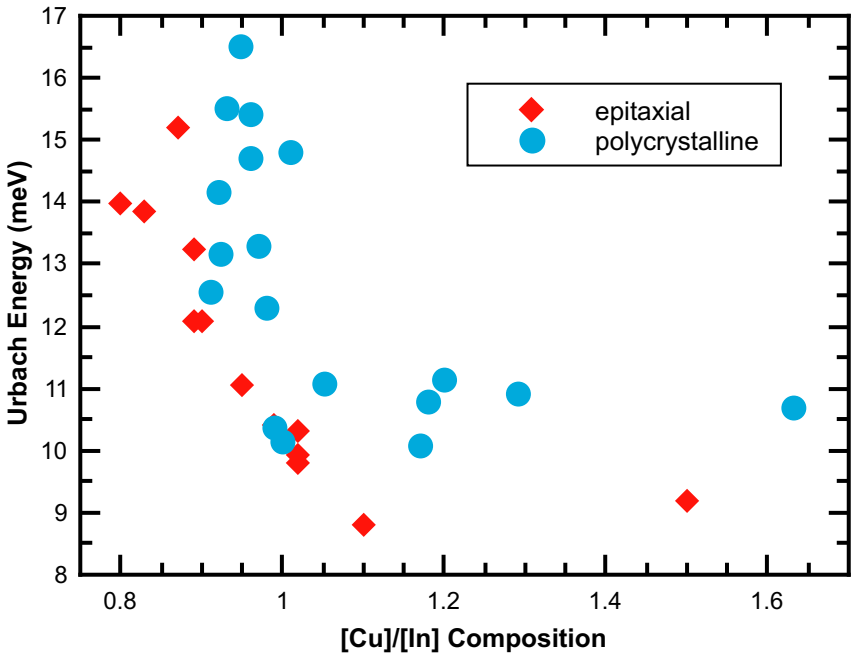

Figure 3.11.: ***Composition dependence of the Urbach energy for $CuInSe_2$*** *- Urbach energies for epitaxial(diamond) and polycrystalline(circle) $CuInSe_2$ thin film absorbers.*

3.3. Degradation of CISe

This section deals with absorber qualities of bare epitaxial and polycrystalline absorbers and their degradation. The influence of an etch in KCN, the effect of an additional CdS layer on top of the absorber, and a comparison of fresh and aged layers is given. The discussion concentrates on the quasi-Fermi level splitting, since it is interpreted as a measure of the absorber quality.
All measurements were performed with the same calibrated PL set-up and evaluated as described in section 2.5.4. For the evaluation of one time series, it is assumed that the temperature does not change with time while using the same excitation power. Thus, an average of the determined temperatures (section 2.5.4) for the first ten measurements was calculated and used as a constant parameter for each fit of a series. This path was chosen, since the first measurements showed the highest PL intensity resulting in a very smooth dataset. The excitation flux was set to five times AM1.5g (section 3.1.1). Before discussing the degradation and the passivation more in detail, the influence of a constant excitation flux is highlighted.

3.3.1. Illumination dependent effects

A constant illumination influences the degradation speed of freshly grown samples and refreshed absorbers[4]. This behaviour is known, e.g. in GaAs [150], CdTe/CdS [151], or in $Cu(In,Ga)Se_2$ [152]. To specify the difference between the ageing under constant illumination and in the dark, several spots on the same sample previously not exposed to

[4] As shown later, an etch in KCN refreshes a degraded $CuInSe_2$ absorber and compares with the freshly grown material.

any light were measured. The time dependent change of the quasi-Fermi level splitting of these measurements is shown in figure 3.12 for a polycrystalline Cu-poor (blue) and a Cu-rich (red) absorber.

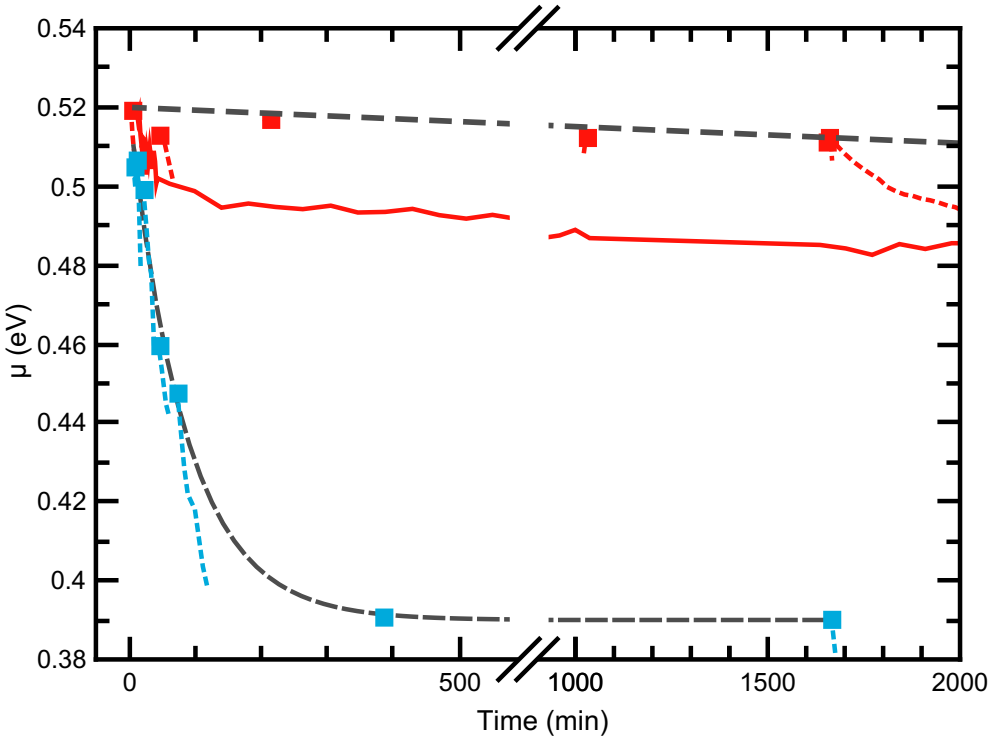

Figure 3.12.: ***Ageing in the dark and under illumination*** *- Comparison of a Cu-poor (red) and a Cu-rich (blue) $CuInSe_2$ thin film. The measurement was performed on different spots on the samples previously not exposed to light. The first measurement (squares) correspond to the "dark" state and the dotted lines to the degradation under illumination. The grey dashed lines are fits to the dark data points. The Cu-rich sample follows a linear, the Cu-poor an exponential decay.*

Two different states are depicted: 1) The red solid line corresponds to a freshly grown sample measured with a constant illumination right after leaving the growth chamber ($t = 0$). 2) the squares correspond to the first measurement on a spot not exposed to any light before. Here, $t = 0$ corresponds to the time after leaving the KCN solution of the recovery etch. The following dotted line were measured at the same position under constant illumination.

To highlight the difference to the previously dark spots the ”dark” points were fitted (dashed grey line) with a linear equation (Cu-rich) and an exponential function (Cu-poor). Although the decay in the dark is slower compared to the illuminated ones, both compositions show a decrease in the quasi-Fermi level splitting. Nevertheless, for the Cu-rich absorber, the degradation speed is significantly reduced. The drop of the quasi-Fermi level within one day is in the order of 10 meV. On the other hand, the Cu-poor samples exhibit a faster loss of around 120 meV.

Under constant illumination, the Cu-poor sample looses $\Delta\mu \approx 50$ meV in 60 min and only $\Delta\mu \approx 20$ meV in the dark (in the plot at t $\approx$ 100 min). In the same time of 60 min,

the Cu-rich absorber looses less then 1 meV in the dark and ≈ 6 meV(in figure 3.13a at t ≈ 1650 min).

3.3.2. Aged samples

Epitaxial and polycrystalline samples with different compositions were exposed to air for several months until they were considered as "aged". This aged state was determined and is shown in 3.13a (polycrystalline) and 3.13b (epitaxial) as the rectangles at $t < 0$. Here, the colour indicates the composition: blue for Cu-poor, red for Cu-rich, and grey for stoichiometric. The general trend is in agreement with the previous observations, namely an increase of the quasi-Fermi level splitting with the [Cu]/[In] ratio. It reads (table 3.1) $\mu \approx 400$ meV for [Cu]/[In] = 0.95, $\mu \approx 450$ meV for [Cu]/[In] = 1.05 and $\mu \approx 460$ meV for [Cu]/[In] = 1.2 on the polycrystalline side and $\mu \approx 460$ meV for [Cu]/[In] = 0.9 and $\mu \approx 490$ meV for [Cu]/[In] = 1.0 and $\mu \approx 500$ meV for [Cu]/[In] = 1.6 on the epitaxial side.

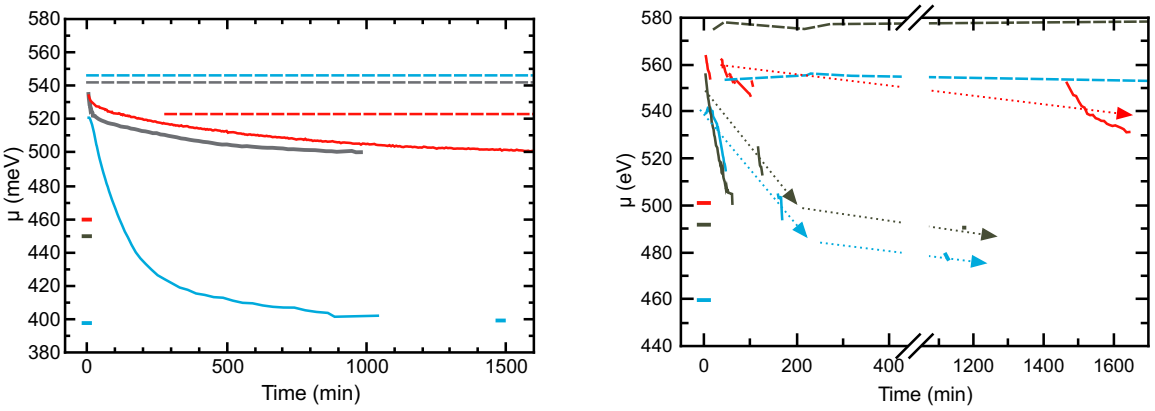

(a) Polycrystalline $CuInSe_2$ with different compositions: [Cu]/[In] = 0.95 (blue), [Cu]/[In] = 1.05 (grey), and [Cu]/[In] = 1.2 (red).

(b) Epitaxial $CuInSe_2$ with different compositions: [Cu]/[In] = 0.9 (blue), [Cu]/[In] = 1.0 (grey), and [Cu]/[In] = 1.6 (red). The dotted lines with an arrows act as a guide to the eye to highlight the degradation of the bare absorbers.

Figure 3.13.: ***Ageing behaviour of $CuInSe_2$*** *- Ageing behaviour of polycrystalline (left) and epitaxial (right) samples. Different colours represent different samples with different compositions. The solid lines show the change of the quasi-Fermi level splitting with respect to the time after an etch in KCN. The dashed lines show the time dependent change after the deposition of a CdS layer.*

In the following, each sample was etched just before starting the time dependent measurement. Thereby, the time between the etching process and the first measurement was about 3 min. Details of the etching process are described in section 4.3.
The time dependent change of the quasi-Fermi level splitting is shown in the solid coloured lines in figure 3.13. Here, $t = 0$ refers to the state immediately after the etch and reveals significantly higher quasi-Fermi level splitting when compared to the aged state (table 3.1). However, the extend of the refreshing effect decreases with an increasing

[Cu]/[In]-ratio. The Cu-poor samples show a much higher increase (≈ 120 meV for the polycrystalline and ≈ 80 meV for the epitaxial) compared to the Cu-rich ones (≈ 70 meV and ≈ 60 meV respectively).
For $t > 0$, all samples show the same trend: a decrease in the quasi-Fermi level splitting with time. For the polycrystalline samples (3.13a), the Cu-poor absorbers decrease much faster when compared to the Cu-rich ones and lose around 120 meV levelling off after 15 h. Thereby, the biggest change is observed within the first 4 h. On the other hand, the Cu-rich counter part loses only around 35 meV within 24 h without reaching the value of the quasi-Fermi level splitting of the aged state before the etch.
For the epitaxial samples (figure 3.13b), the trends for the lowest and the highest [Cu]/[In] ratio are comparable to the decay in the polycrystalline case. However, the differences are less pronounced: after 1100 min it is only around 60 meV compared to 120 meV and 10 meV compared to 30 meV for the Cu-rich case.

Nevertheless, the epitaxial case shows some differences: First, the curves exhibits gaps, usually followed by higher values afterwards. The gaps occur, because other samples were measured in the mean time. The higher values afterwards can be explained with a slightly different position on the sample, after remeasuring the same absorber again. The slightly different position was not exposed to a continuous illumination and explains the jump, as discussed previously when comparing the degradation under continuous illumination and in the dark in section 3.3.1. The difference is in the same order of magnitude. For example for the Cu-rich absorber (red) in figure 3.13b at the first gap around t $\approx$ 50 min, the first value right before and after the gap are almost identical. This compares to the Cu-rich case in section 3.3.1 showing also a minor change within the same Δt (figure 3.12).
The second difference shows the almost stoichiometric sample. Under continuous illumination, the decay is comparable to the Cu-poor composition, while it differs for the polycrystalline sample. The difference might be related to either inhomogeneities in the sample or due to the error related to the EDX measurements.
To allow a more detailed comparison of the measured samples, the time dependent change was fitted with an exponential decay function (equation (3.3)) where μ_0 represents the offset, A corresponds to the difference of the aged and the refreshed state and τ is the characteristic decay constant.

$$\mu(t) = \mu_0 + Ae^{-t/\tau} \tag{3.3}$$

The composition dependence of the decay time and the difference A for the polycrystalline samples under a continuous illumination is shown in figure 3.14 where the dashed lines act as a visual guide. The discussion is limited to the polycrystalline samples, since all

polycrystalline			epitaxial		
[Cu]/[In]	μ_{before}	μ_{after}	[Cu]/[In]	μ_{before}	μ_{after}
0.95	400	520	0.9	460	540
1.05	450	535	1.0	490	555
1.2	460	530	1.6	500	560

Table 3.1.: ***Comparison of the quasi-Fermi level splitting before and after an etch in KCN*** *- A comparison of the quasi-Fermi level splitting in meV of polycrystalline and epitaxial $CuInSe_2$ absorbers before and after the etch in KCN. The composition was determined by EDX measurements.*

of them were measured under illumination while the epitaxial ones were not and thus hampering a direct comparison. For [Cu]/[In] < 0.97 the decay constant is in the range of 30 min. A remarkable jump around the stoichiometric point is clearly visible, where the time constant increases suddenly to more than 600 min. On the other hand, the amount of decay (right axes) decreases with an increasing [Cu]/[In]−ratio from 120 meV and levelling out to 20 meV at stoichiometry. A further increase in the [Cu]/[In] ratio does not change A further. Thus, the decay is faster and more severe for Cu-poor absorbers than for Cu-rich absorbers.

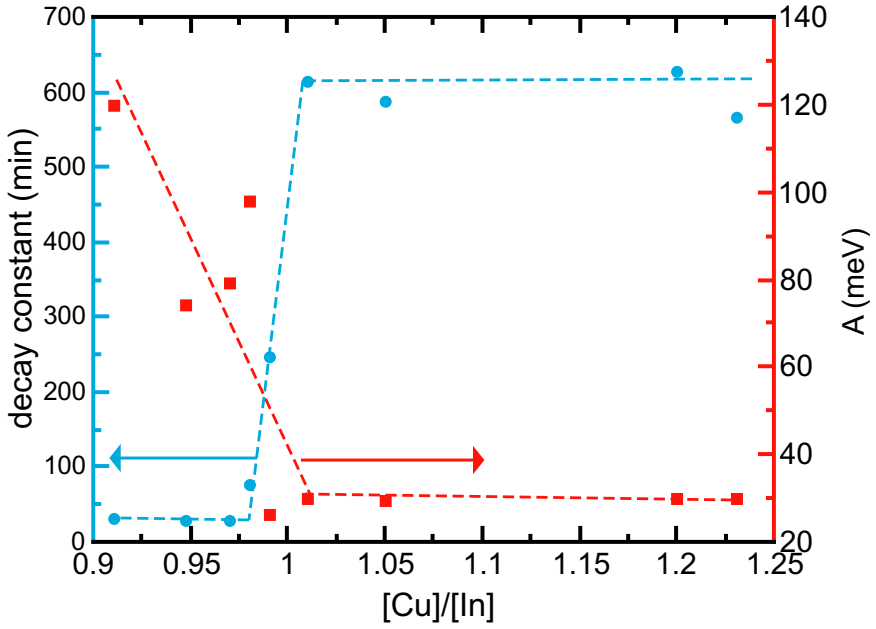

Figure 3.14.: ***Summary of fit parameter*** *- The determined decay constants and the amplitude are plotted in dependence of their composition for the polycrystalline samples.*

The observation can be explained with a different surface composition observed for different growth conditions [153]. Since "Cu-poor " means In-rich, there is more In at the surface. Thus, it is very likely to form mostly In_2O_3 as shown in [154, 155]. Since the Cu-rich material supplies less In, the oxidation is less pronounced.

If an oxidized surface creates new surface states providing the material with new non-radiative recombination centres, the measured PL signal will be reduced and thus a lower quasi-Fermi level splitting will be measured. This explains the measured difference in the degradation speed.

It was shown before that an etch in KCN removes Cu selenide [156], elemental Se [157] and Cu hydroxide [158]. So, one can conclude, that KCN removes In oxide as well, which explains the significant improvement of the absorber quality when an aged sample got etched in KCN.

As the epitaxial and the polycrystalline samples behave very similar, it can further be concluded that the degradation is rather independent of the Na content, since the epitaxial samples do not contain sodium. The reason for that lies in the soda lime glass, which is used for the growth of the polycrystalline material, leading to a Na diffusion from the

glass into the absorber. However, for the epitaxial samples GaAs is used as a substrate, which does not contain sodium. Then, it can be concluded that oxygen and not water is responsible for the oxidation, since the absorption of water at room temperature was only observed if the material contained Na [159].

Passivation

After the ageing experiment, all samples where etched again in KCN and a CdS buffer layer was deposited on top of the samples directly afterwards. The deposition process is described in section 4.3. After the deposition, the same PL measurements were performed again, also shown in figures 3.13 (dashed lines). Here, the same color represents the same sample. The plot reveals no change within the first 1500 min. Even after five months in the dark and even with continuous illumination no change in the quasi-Fermi level splitting was observed. Thus it can be concluded that the CdS layer passivates the absorber. Nevertheless, some observations have to be pointed out: For the polycrystalline samples, the Cu-poor absorbers exhibit the highest quasi-Fermi level splitting after the CdS deposition, which differs from the observation of the bare absorbers. In addition, they show the highest increase compared to the state directly after the etch. Although the quasi-Fermi level splitting for the stoichiometric sample (grey) is still higher compared to the freshly etched state, but lower than the Cu-poor sample. Then, a completely different behaviour is observed for the highest ratio of [Cu]/[In] = 1.2. The quasi-Fermi level splitting for Cu-rich samples after the CdS deposition is generally lower compared to Cu-poor ones and especially lower than the freshly etched state. This observation is very likely related to the interface between the $CuInSe_2$ and the CdS. It seems that the number of non-radiative interface recombinations increases drastically with an increasing [Cu]/[In] ratio, leading to a lower PL yield and thus to a lower quasi-Fermi level splitting. This is in agreement with the best performing cells with a Cu-poor composition [22, 160]. Due to the presence of an ODC phase at the surface, a widening of the surface band gap is observed. The enlargement of the band gap is accompanied with a bigger valence band offset to the CdS layer [145] which is beneficial for the type inversion at the interface. Moreover, temperature dependent I-V measurements (section 2.6.4) indicate that Cu-rich devices are dominated by a fundamentally different recombination behaviour when compared to the Cu-poor counter part [145]. The activation energy for Cu-poor $CuIn_{1-x}Ga_xSe_2$ devices follows the band gap for $x = [0, 1]$ and is thus dominated by bulk recombination. The activation energy for Cu-rich devices on the other hand indicates a device dominated by interface recombinations [145]. This agrees well with the observations for the quasi-Fermi level splitting after the CdS deposition introducing non-radiative recombination centres at the interface leading to a reduced quasi-Fermi level splitting.
Within this work, no additional structural or compositional examinations were performed to clarify the situation at the interface between the absorber and the CdS layer. Nevertheless, studies on $CuGaSe_2$ pointed out, that the deposition temperature of the CdS is important [161]. In this case, the crystal quality for a Cu-rich sample was poor at a deposition temperature of 60 °C. At 80 °C, the formation of Cu-S inclusions was observed. Surely, the used temperature of 67 °C is in between both temperatures but may not be optimal for Cu-rich absorbers.

3.3.3. Influence of CdS deposition

It is known, that an ammonia solution present in the CdS deposition process, etches group III oxides [162]. Therefore, the deposition process itself might also show a similar effect like the etch in KCN. To investigate the influence of the deposition itself, an aged polycrystalline absorber was quartered. As described above, the quasi-Fermi level splitting of the aged state was determined with PL measurements on each piece. Afterwards, three of the four parts were etched in KCN at different times before depositing the buffer layer, while the remaining piece was not treated. The same deposition bath was used for the set of four samples to ensure the comparability of the depositions. The results are shown

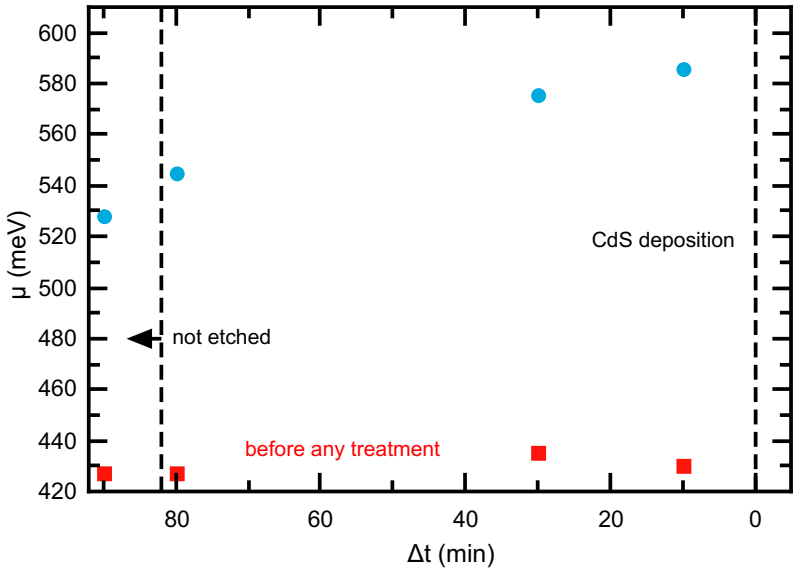

Figure 3.15.: ***Influence of CdS deposition*** *- Comparison of the CdS deposition with a prior etch in KCN* 10 min, 30 min *and* 80 min *before the deposition. The reference sample was not etched (left side). The sample was a polycrystalline* $CuInSe_2$ *sample with a composition of* $[Cu]/[In] = 0.9$.

in figure 3.15 displaying the quasi-Fermi level splitting of each piece before and after the CdS deposition. The squares reflect the aged state and the circles the measurement after the CdS deposition, while symbols above each other correspond to the same sample piece. The time indicated on the abscissa corresponds to the time between the etch and the CdS deposition, which itself was done at $t = 0$. The unetched piece is depicted on the left side of the plot.
All pieces show an almost identical aged state, which is expected since the used absorbers were homogeneous. In any case, it has to be pointed out, that the CdS deposition process itself refreshes the absorber layer. The untreated piece shows an increase of around 100 meV. Nevertheless, the gain can be even higher with a prior etch in KCN. The etch 80 min before the deposition leads to an additional increase of $10 - 20$ meV. The highest gain of around 50 meV compared to the untreated piece is observed for the KCN etch 10 min before the deposition of the buffer layer. Thus, one can state that the CdS deposition recovers the quality of aged absorbers to a large extend. Nevertheless, a KCN

etch immediately before the deposition recovers the quality of aged absorbers even more.

3.3.4. Fresh and aged

Since at least one improvement in the history of record efficiencies in $Cu(In,Ga)Se_2$ is based on an optimization of the process by minimizing the time between each step [22] it is reasonable to conclude that the absorber state with the highest quality is directly after the growth or after leaving the growth chamber. The previous discussions in 3.3 revealed that both, an etch in KCN, and the cleaning in an ammonia solution are able to refresh $CuInSe_2$ absorber layers. Certainly, it is not clear how the refresh compares to a freshly grown absorber.
To clarify the situation freshly grown samples where measured directly after the growth process. Figure 3.16 shows the ageing behaviour of two polycrystalline absorbers with a [Cu]/[In]-ratio of ≈ 1.2 (red), ≈ 1.0 (blue), and one epitaxial absorber of ≈ 0.9 (orange). The general behaviour is comparable to the case discussed above in figures 3.13a & 3.13b: A higher copper content exhibits a slower decline and a higher quasi-Fermi level splitting (red and blue). The higher splitting for the Cu-poor epitaxial sample can be explained, since it compares to the epitaxial behaviour discussed above. Figure 3.5 shows, that the quasi-Fermi level splitting for an epitaxial sample with a composition of [Cu]/[In] ≈ 0.9 can be higher compared to the Cu-rich polycrystalline case. The new information is shown after the axis break (solid lines) on the right hand side of figure 3.16. The curves were recorded two month after the first measurement. During this time all samples were exposed to ambient air and again, etched immediately before the experiment. All samples show almost identical values after the growth and directly after the etch. A comparable degradation speed under constant illumination is observed. However, the epitaxial sample exhibits a slightly smaller value.

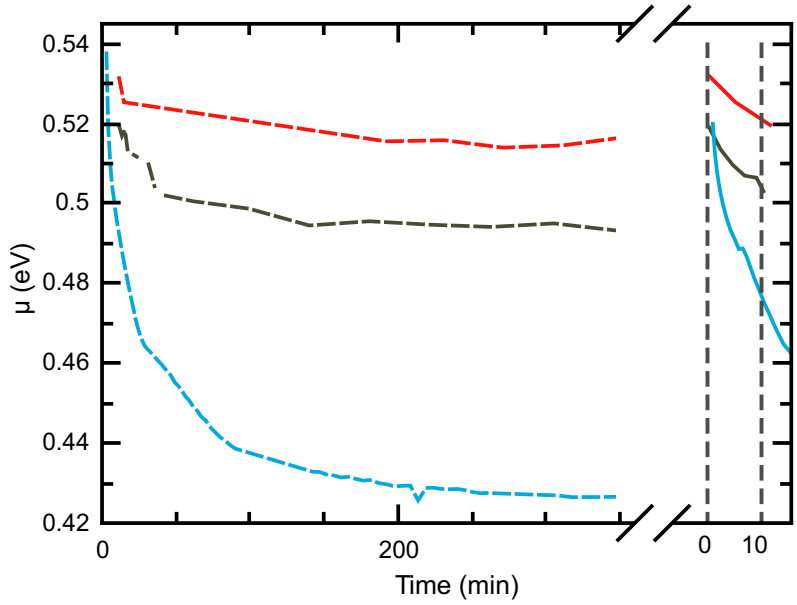

Figure 3.16.: ***Comparison of fresh and refreshed $CuInSe_2$ absorbers*** *- Depicted are two polycrystalline absorbers in red ([Cu]/[In] ≈ 1.2) and blue ([Cu]/[In] ≈ 1.0) and an epitaxial one in orange ([Cu]/[In] ≈ 0.9). The dashed lines are measured directly after leaving the growth chamber. The solid lines are measured after an etch in KCN .*

3.4. Summary

All results were derived from calibrated photoluminescence measurements at room temperature for polycrystalline and epitaxial $CuInSe_2$ absorbers with different [Cu]/[In] ratios. The measurement technique allows the determination of the quasi-Fermi level splitting and the analysis of the absorption behaviour near the band gap, which allows the determination of the band gap and the Urbach energy. This path was not carried out so far and the direct comparison of epitaxial and polycrystalline $CuInSe_2$ material was not done before. For doing so, the set-up (section 3.1.1) was extended to allow calibrated measurements for a quantitative determination of the quasi-Fermi level splitting (section 2.5.4).

3.4.1. Composition dependence of the quasi-Fermi level splitting, the band gap and the Urbach energy

The quasi-Fermi level splitting measured with an excitation flux equivalent to AM1.5g shows a clear dependence on the [Cu]/[In] ratio. Epitaxial and polycrystalline $CuInSe_2$ absorber layer with a Cu-poor composition exhibit lower values than the Cu-rich counter part. For both sample types, the quasi-Fermi level splitting increases with an increasing [Cu]/[In] ratio and levels off beyond the stoichiometric point. For polycrystalline material, the increase in the order of 150 meV, when the [Cu]/[In] ratio increases from [Cu]/[In] ≈ 0.9 to > 1.0. The epitaxial samples show a slightly lower increase of 100 meV for the same range of composition. However, the epitaxial material exhibits ≈ 100 meV higher values compared to the polycrystalline ones.

The band gap energies and the Urbach energy were derived from the absorption coefficient (section 2.4.2), which was deduced from the PL measurements after the determination of the quasi-Fermi level splitting. The determined band gap energies for polycrystalline material increase with an increasing [Cu]/[In] ratio from $E_g = 0.97$ eV ([Cu]/[In] $\approx$ 0.9) to $E_g = 1.02$ eV ([Cu]/[In] $\approx$ 1.0) (figure 3.9b. Similar to the quasi-Fermi level splitting, the band gap levels out for higher [Cu]/[In] ratios and compares well with the literature value of $E_g = 1.02$ eV [41, 147, 163]. Epitaxial samples exhibit a comparable value for [Cu]/[In] $\gtrsim$ 1 but a less pronounced decay to $E_g = 0.99$ eV for [Cu]/[In] $\approx$ 0.8 (figure 3.9a). The higher value can be explained with a slightly strained film.

It was shown, that a clear distinction between the band gap and the Urbach tailing is possible. The determined Urbach energies (figure 3.11) decrease with an increasing [Cu]/[In] ratio. Similar to the band gap energies, the values are levelling out for [Cu]/[In] $\gtrsim$ 1 at $E_u \approx 11$ meV for polycrystalline samples and at $E_u \approx 9$ meV for the epitaxial ones. For [Cu]/[In] < 1, the values increase to $E_u \approx 12.5 - 17$ meV ([Cu]/[In] = 0.9) for the polycrystalline samples and to $E_u \approx 14$ meV ([Cu]/[In] = 0.8) for the epitaxial layers. This indicates a lower defect formation within the crystals grown under Cu excess. For any sample it was possible, to distinguish between the band gap (band-to-band transitions) and the Urbach tailing by analysing the absorption coefficient.
The determined values by PL compare excellent with measurements based on the transmission revealing a similar increase in the band gap and a levelling out for Cu-rich samples for the band gap as well as the Urbach energies. [104].

3.4.2. Degradation

In general, the measured amount of degradation and the degradation time depends on the [Cu]/[In] ratio. Cu-poor absorbers decay faster and more severe than the Cu-rich counter part (figure 3.13a and 3.13b). The degradation speed depends on the illumination. Measuring under a continuous illumination, the decay is significantly faster than without (3.12). This is true for both, epitaxial and polycrystalline samples. Nevertheless, without illumination the loss for Cu-poor epitaxial samples within the first hour after being etched in KCN is only in the order of 15 meV and around 55 meV for the polycrystalline counterpart.
It was shown that the chemical bath deposition of CdS stops the decay. However, the observed quasi-Fermi level splitting after the passivation of Cu-poor $CuInSe_2$ is higher when compared to Cu-rich absorbers. This is most likely related to the interface between both layers. While the Cu-poor surface exhibits less non-radiative recombination centres, the interface for a Cu-rich surface seems to exhibit more centres leading to a lower PL yield and thus to lower values of the quasi-Fermi level splitting.
The examination of the CdS deposition itself (figure 3.15) revels that the chemical bath deposition cleans the surface to an extend of ≈ 100 meV. Nevertheless, a prior etch in KCN can further improve the gain up to ≈ 60 meV.
Time resolved PL measurements allow the determination of the radiative lifetime of the charge carriers. Since the lifetime is proportional to the number of radiative recombination, it is also proportional the measured PL intensity and thus to the quasi-Fermi level

splitting (section 2.5). As reported before, the lifetime measured on bare polycrystalline Cu(In,Ga)Se_2 films decreases, if the material is exposed to air [152] which is in agreement with the observed decay of the quasi-Fermi level splitting, when the bare absorber is exposed to air. Since no change in the lifetime was measured, after the deposition of a CdS layer, it was concluded that the CdS layer has a passivating effect [152]. The long term measurements of the quasi-Fermi level splitting over several months could confirm the passivation as well.
Finally, the comparison of the measured quasi-Fermi level splitting of freshly grown absorbers and the refreshing in KCN of the same samples after two months shows that the quasi-Fermi level splitting after the etching compares to the state directly after the growth (figure 3.16).

3.4.3. Epitaxial versus polycrystalline

In general, all PL experiments revealed that epitaxial samples exhibit the same trends in terms of the quasi-Fermi level splitting, the band gap and the Urbach tailing compared to their polycrystalline counter part. A significant change around the stoichiometric point was observed for all measurements: A preceding approximately linear increase (or decrease) for [Cu]/[In] $\lesssim 1$ is observed followed by an levelling out for higher ratios. According to that, the measured quasi-Fermi level splitting (figure 3.5) and the determined band gap (figure 3.9a) follow this increasing trend. The Urbach energies decrease (figure 3.11). While the values for the band gap do not differ significantly from polycrystalline absorbers, the differences in the quasi-Fermi level splitting and in the Urbach energies are more pronounced. The difference of $\Delta\mu \approx 100$ meV ([Cu]/[In] ≈ 1.1) is remarkable and clearly indicates a higher absorber quality. A reasonable explanation is the absence of grain boundaries in the epitaxial films reducing the amount of non-radiative recombination.
The Urbach energies for the epitaxial samples exhibit slightly lower value over the examined composition range. Nevertheless, the difference gets more severe for compositions below the stoichiometric point. While the Urbach energy is $E_u = 14$ meV for [Cu]/[In] $= 0.8$, values of up to $E_u = 16.5$ meV are observed for the polycrystalline case indicating a higher defect density in the polycrystalline material.
All results indicated, the epitaxial material has a better quality. Since the quasi-Fermi level splitting determines the maximum achievable open circuit voltage of a finished solar cell, one can suggest, that the usage of epitaxial Cu(In,Ga)Se_2 as the absorber layer in a solar cell should result in decent performing devices. However, the epitaxial devices reported in the literature never reached the performance of the polycrystalline counterpart [7, 11]. The highest reported efficiency is 8.5% for Cu(In,Ga)Se_2 grown on GaAs (111). Since the epitaxial material does not contain grain boundaries, it can help to understand there role in the polycrystalline devices. The lack of grain boundaries and the better absorber quality shown in this work motivates further investigate of epitaxial Cu(In,Ga)Se_2 base devices. Therefore, the following part concentrates on the production of epitaxial Cu(In,Ga)Se_2 absorber and the fabrication of devices.

CHAPTER

FOUR

EPITAXIAL SOLAR CELLS

The PL results showed (section 3.2) that the epitaxial absorber exhibits a better material quality in terms of the quasi-Fermi level splitting compared to the polycrystalline counter part. However, the highest reported efficiency for epitaxial Cu(In,Ga)Se_2 solar cells reach only 8.5% for material grown on GaAs (111) and 7.3% for a substrate orientation of (001) [7]. The efficiencies do not compare to the current polycrystalline record devices showing conversion efficiencies of 20.8% [2]. A fundamental difference is the lack of sodium, when growing the epitaxial devices. The presence of Na, either due to diffusion from the soda lime glass substrate or by an additional Na source, is known to increase the device efficiencies drastically by improving the V_{OC} and the fill factor [164, 165].
However, the first photovoltaic device based on $CuInSe_2$ single crystals did not contain Na and reached a power conversion efficiency of 12% [1] proving that efficiencies above 10% are possible even without Na. In contrast to the solar cells produced by Shay [1] who used a zone-refining technique[1], the later work concentrates on epitaxial Cu(In,Ga)Se_2 grown on a substrate. Due to the comparable lattice constant of GaAs, the absorber is typically grown on GaAs using molecular beam epitaxy [166] or metal organic chemical vapour deposition [7, 11]. As shown later by simulating the device with an additional substrate layer (section 4.10), the GaAs does not hamper the device. Therefore, it is interesting to clarify the causes of the inferior performance of epitaxial devices compared to polycrystalline ones. Additionally, the epitaxial devices do not contain grain boundaries, and might help to understand there influence on the device performance.
This chapter describes the growth process of the epitaxial absorber (section 4.1) and the measurements confirming a good quality (section 4.2). The production steps used in this work to produce epitaxial devices are illustrated (section 4.3). The analysis of the devices is based on (temperature dependent) IV, bias dependent quantum efficiency, and capacitance measurements and is presented afterwards (section 4.4).

[1] To purify the single crystal, a narrow region within the crystal is molten. By pulling the crystal though the heater, the molten zone moves along the crystal. The principle can be used to produce crack free single crystals with a very high purity and quality.

4.1. The growth process at LPV

The MOPVE at LPV is a computer controlled system. The software provides a recipe manager which allows to control each parameter digitally. The typical growth recipe for Cu(In,Ga)Se_2 samples is divided into three parts: the preprocessing (leak test and a cleaning step), the actual growth, and the cool down (after the growth process in, at first a H_2- and finally in a N_2 atmosphere). After ensuring the tightness of the reactor by performing a leak test, the H_2 carrier gas is switched on and the reactor pressure is set to 50 mbar. The bake out process is started and the reactor temperature is ramped up to 650 °C, which is meant to clean the reactor and the substrate surface. After 5 min, the temperature is decreased to the growth temperature.

State of the art for $CuInSe_2$ and $CuGaSe_2$

Depending on the desired film composition, the growth temperature is set to 470 °C for $CuInSe_2$ and 520 °C for $CuGaSe_2$. Besides, the bubbler flows are adjusted to the desired [Cu]/[In] or [Cu]/[Ga] ratio and piped though the vent line until a stable flow is achieved. The composition is adjusted by changing the partial pressures of In, Ga, and Se, while each recipe requiers an over pressure of selenium. While the over pressure for $CuGaSe_2$ is $p_{Se}/(p_{Cu} + p_{Ga}) \approx 9$, it is $p_{Se}/(p_{Cu} + p_{In}) \leq 25$ for $CuInSe_2$. After 3 min, the flux is redirected to the run line and the actual growth process starts. Depending on the growth rate and the desired the sample thickness, the process time is varied between 4 and 10 hours, before the flux is guided through the vent line again. The flux through the precursors is cut and the cool down under H_2 is initialized by switching off the heater. For T < 170 °C, the reactor atmosphere is switched back to N_2.

$CuIn_{1-x}Ga_xSe_2$

A main task in this work is the development and optimization of a process for a device fabrication of epitaxial Cu(In,Ga)Se_2 based solar sells. To grow Cu(In,Ga)Se_2 films, the growth temperature had to be adjusted and the selenium over pressure had to be adjusted according to the [Ga]/([Ga] + [In]) ratio. The starting temperature was chosen to be 500 °C, which turned out to work well for compositions between $0.3 < GGI < 0.65$ as shown in the next section. The selenium pressure turned out to be crucial for a smooth surface without inclusions, as seen later.
For all runs, the partial pressure of copper remained constant. To allow different [Cu]/([Ga]+[In]) ratios, only the partial pressures for indium and gallium where adjusted. Thereby, the pressure ratio corresponds to the desired [Ga]/([Ga]+[In]) composition. Accordingly, the magnitude of the partial pressures of In and Ga is used to control the growth conditions for Cu-poor or Cu-rich samples. Additionally, the selenium pressure ratio $\frac{p_{\mathrm{Se}}}{(p_{\mathrm{Cu}}+p_{\mathrm{Ga}}+p_{\mathrm{In}})}$ had to be adjusted to guaranty a comparable ratio for different runs.

4.2. Crystal quality

When growing the epitaxial Cu(In,Ga)Se_2 films, especially two issues were taken into account, the strain within the film and the interface to the GaAs substrate. The strain within the film has to be minimized since it influences the properties of a solar cell. Obviously, a smooth interface is required as well, to minimize the recombination rate at the interface. A measure for the defect concentration is the full width half maximum of the peaks in a x-ray diffraction pattern. One possible origin of the defects is related to the strain in the film. During the growth process, the strain tends to be minimized by introducing dislocations in the film (section 2.2). The XRD measurements are presented in the following. The interface was verified by means of SEM measurements and is described in section 4.2.2.

4.2.1. XRD

An overview of typical XRD patterns of Cu(In,Ga)Se_2 films grown on epitaxial GaAs (001) is depicted in figure 4.1. Exemplary, the normalized patterns of the ternaries $CuInSe_2$ (grey) and $CuGaSe_2$ (orange), and the GGIs of 0.44 (blue) and 0.65 (red) are depicted. A reference spectrum of GaAs is shown in green.
For any sample, the highest intensities in the peak structure at $2\theta \approx 66°$ originates from the (400) planes of the GaAs substrate. The peak consists of different contributions caused by the x-ray source: Radiation due to $Cu_{K\alpha 1}$ (highest intensity) and $Cu_{K\alpha 2}$ (slightly lower intensity compared to the main peak). Due to an aged x-ray source [167] or because of an insufficient filter after the source, some more parasitic lines are visible. The bump on the left side of the GaAs peak ($2\Theta = 65.8°$) is related to the $Cu_{K\alpha 3}$ line [167]. Additional the tungsten $W_{L\alpha 1}$ and $W_{L\alpha 2}$ line explain the reflection at $2\theta = 63.0°$ and $2\theta \approx 63.45°$.

The expected peak position for Cu(In,Ga)Se_2 of the (008) and the (400) reflection can be calculated according to equation (2.8) giving the position Θ in dependence of the wavelength of the used radiation source ($\lambda_{CuK\alpha 1} = 1.5406$Å), the indices (hkl), and the lattice constants. The constants a and c and their dependence on the composition x were calculated with the equation given in table B.1. The usage of equation (2.8) is justified, since the film thickness is around 1 µm. Therefore, one can assume, that a relaxed growth was ensured and the peak position is not influenced by strain effects.
The results are indicated above the XRD pattern in figure 4.1. The upper row (green) shows the positions for the (400) reflexes, the lower (black) illustrates the (008) positions. As pointed out in section 2.2.1 $CuInSe_2$ and $CuGaSe_2$ were found to grow with a c-axis perpendicular to the GaAs surface because of the smaller strain at the interface. Figure 4.1 confirms this: The observed peaks for $CuInSe_2$ (grey) and $CuGaSe_2$ (orange) can be attributed to the (008) planes, respectively. The slight shift of the expected value for $CuGaSe_2$ is most likely due to some remaining stress within the film [43].
The $CuIn_{1-x}Ga_xSe_2$ sample with x=0.65 (red) follows this trend. The peak at $2\Theta = 66.54°$ is clearly related to the (800) reflection caused by the $Cu_{K\alpha 1}$ radiation, as the calculated value illustrates. The second peak at $2\Theta = 66.81°$ is caused by the $Cu_{K\alpha 2}$ line. On the other hand, the $CuIn_{1-x}Ga_xSe_2$ samples with x=0.44 (blue) clearly corresponds to the (400) reflex at $2\Theta = 66.37°$ ($Cu_{K\alpha 1}$) and $2\Theta = 66.56°$ ($Cu_{K\alpha 2}$). In this case, the c-axis is parallel to the surface. Both compositions were grown at the same temperature of

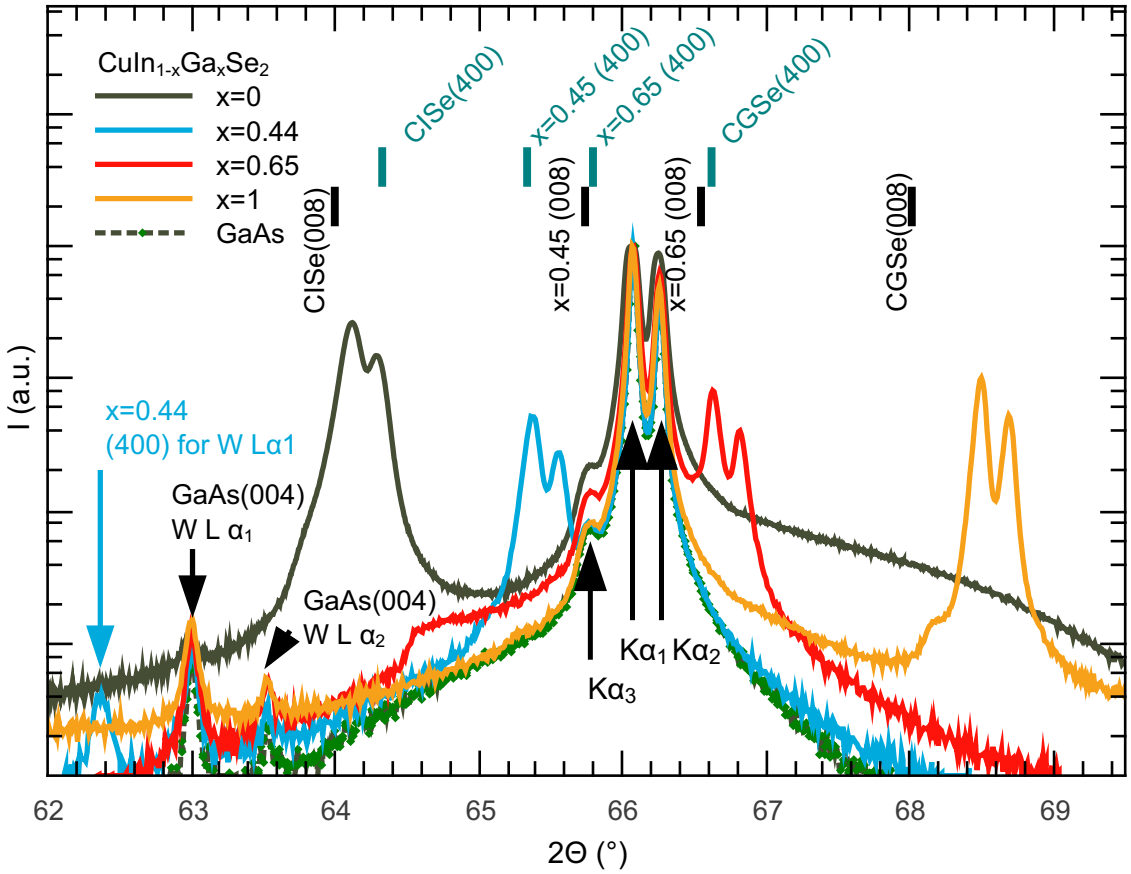

Figure 4.1.: *XRD measuremnts* - *Overview of selected XRD spectra for $CuIn_{1-x}Ga_xSe_2$ with x=0, 0.44, 0.65, and 1.0. The most pronounced peak is the (400) reflection of the GaAs substrate. The lines in the top represent the expected positions of the (400) and the (008) peaks of the $CuIn_{1-x}Ga_xSe_2$ for x=0, 0.44, 0.65, and 1. The peaks were calculated with equation (2.8) using the calculated lattice constants (compare section 2.2.1 and the table B.1 for the equation). The ternaries and the curve for x=0.65 exhibit the (008) reflection, while the (400) peak is visible for x=0.44. This indicates, that the latter crystal grows such, that the c-axis is parallel to the substrate's surface. The peaks at $2\Theta = 63.0°$ and $2\Theta = 63.5°$ are caused by $W_{L\alpha 1,2}$. The peak on the left side at $2\Theta \approx 62.4°$ is related to the (400) reflection of the sample with x=0.45 arising from $W_{L\alpha 1}$.*

T = 500 °C. Therefore, it is reasonable to assume, that T = 500 °C is suitable for composition around [Ga]/([Ga] + [In]) = 0.5.
Figure 4.1 reveals also a change in the full width half maximum (FWHM) of the Cu(In,Ga)Se_2 reflection. When comparing the different FWHM for $CuIn_{1-x}Ga_xSe_2$, a much broader peak for x=0 is observed. The different peak widths of the pure ternaries reflect the differences in the strain. A strained film will relax during the growth process by introducing dislocation in the crystal. Therefore a smaller coherence volume is present in the crystal, leading to a broadening of the peaks in the diffraction pattern. Coherence volume describes the volume inside the crystal producing a coherent diffraction pattern [73].
The values specified in table 2.1 show for the strain along the a-axis (at growth temperature) $\epsilon_{\parallel,a} = -2.5$ for $CuInSe_2$ and $\epsilon_{\parallel,a} = 0.4$ for $CuGaSe_2$. The reduced strain for $CuGaSe_2$ can be explained with the lower value $\epsilon_{\parallel,a} < \epsilon_{\parallel,c}$. Besides, the peak width decreases for an increasing GGI within the film, which is in agreement with the decreasing stress as calculated in table 2.1. A more detailed analysis is given in the next section.

Minimizing the strain

A growth temperature of 500 °C is suitable for compositions around [Ga]/([Ga] + [In]) = 0.5 as shown above. Nevertheless, the selenium pressure in the reactor influences the quality as well, as shown in the following. Figure 4.2 depicts three different films grown at 500 °C. The partial pressures in the reactor were adjusted such, that the pressure ratios $p_{\mathrm{Cu}}/(p_{\mathrm{Ga}} + p_{\mathrm{In})}$ and $p_{\mathrm{In}}/p_{\mathrm{Ga}}$ remain constant. Only the pressure ratio $\frac{p_{\mathrm{Se}}}{(p_{\mathrm{Cu}}+p_{\mathrm{Ga}}+p_{\mathrm{In})}}$ was change to 10 (sample S1, grey), 15 (S2, blue), and 20 (S3, red). The crosses represent the measured data point and the solid line shows the model (solid lines), fitted to the data.
The model has to account for the multiple reflexes from the GaAs and Cu(In,Ga)Se_2. Both materials exhibit at least a double (GaAs a triple) peak structure due to the three copper lines from the x-ray source. To account for the additional broadening of the signal from the sample due to the limited resolution of the machine, several Pseudo-Voigt functions were used[2] (see section D for details on the used program and the construction of models). The equation for the PSV is given by

$$I(x) = I_0 \left(\beta \exp\left(\frac{-2}{\pi} \frac{(x - x_0)^2}{(w/2)} \right) + (1 - \beta) \frac{1}{1 + \left(\frac{x - x_0}{w/2} \right)^2} \right) \tag{4.1}$$

where x_0 is the peak position, w the FWHM, and β determines the fraction of the Gaussian peak (first term) and the Lorentzian peak (second term). The model consists of the sum of five PSV functions, where the parameter β describes the resolution of the machine. β was determined by fitting three PSV functions to the three peaks caused by GaAs, where β was equal for the three functions. Assuming a constant broadening within the range of $65° \leq 2\Theta \leq 67°$, the determined β from the GaAs reference measurement was used to fit the Cu(In,Ga)Se_2 peaks as well. For a proper description of sample S1, an

[2] The Voigt profile is a peak shape commonly used in diffraction experiments. The peak is calculated by convoluting a Gaussian peak with a Lorentzian peak to account for different broadening mechanisms: a material related broadening and a machine related broadening. To minimize the calculation time, the Voigt profile can be approximated with the Pseudo-Voigt (PSV) function, combining both peak types with a scaling factor β (equation (4.1)).

additional Gaussian peak was used to describe the bump at $2\Theta \approx 65°$ (caused by the $Cu_{K\alpha 3}$ line). The determined values for the FWHM (w) are summarized in table 4.1 and read $w_{S1} = 0.092°$, $w_{S2} = 0.102°$, and $w_{S3} = 0.069°$. Sample S2 shows a slightly higher value compared to the other ones. This seems to be surprising, since lower values are observed for a higher and a lower selenium pressure. A comparison of PL measurements at room temperature can help to reveal the discrepancy. The normalized PL spectra from measurements at room temperature of the same samples (S1-S3) are depicted in figure 4.3.

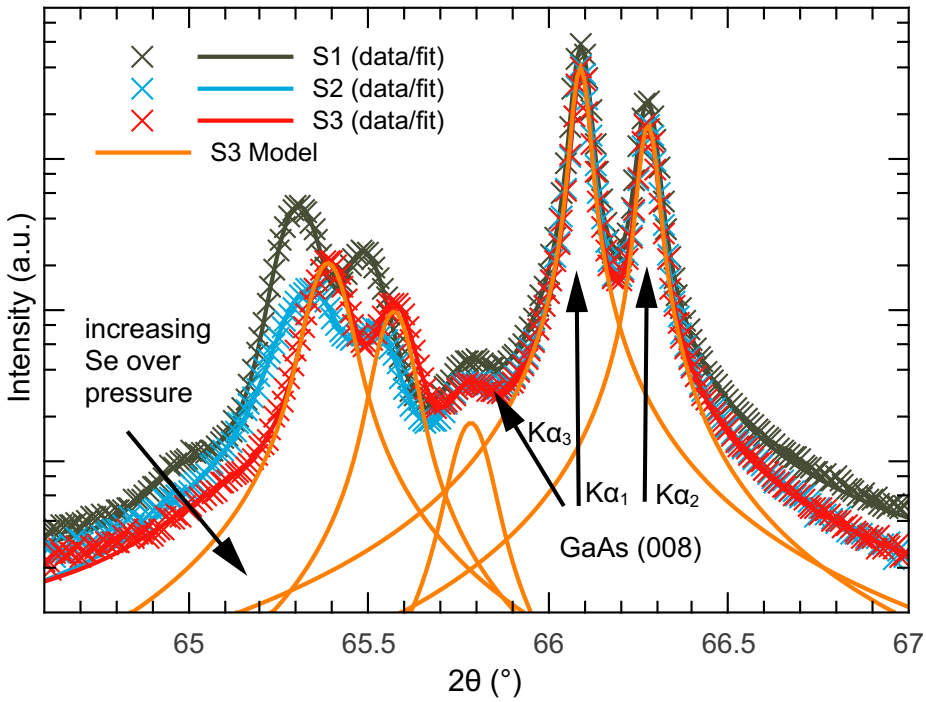

Figure 4.2.: ***XRD pattern for different selenium pressures*** *- The selenium pressure influences the growth visible in a reduced FWHM of the XRD peak an optimized growth. The data (crosses) were fitted with Pseudo-Voigt functions. The sum of these peaks is shown in the coloured solid lines (grey, blue, and red). For sample S3, the different peaks (orange lines) are depicted exemplary.*

First, when comparing the peak positions in the PL spectra, a small change in the band gap is observed (section 2.5). These positions are in agreement with the expected ones, since they are related to the band gap (section 2.5.3), because the band gap increases with an increasing GGI. Sample S1, with the lowest GGI exhibits the lowest band gap and the smallest value for the diffraction peak. Sample S2 shows a very broad shoulder on the low energy side, which differs significantly from S1 and S3. The wide extend to lower energies indicates the presents of either a gradient or an influence of the inclusions on the surface (see below). Therefore, the slightly bigger FWHM is most likely caused by the same effect and leads to an additional broadening which is not related to strain. From this it can be concluded, that the used selenium pressure influences the strain: An increase in the $\frac{p_{Se}}{(p_{Cu}+p_{Ga}+p_{In})}$ ratio leads to a reduction of the strain within the layer for $[Ga]/([Ga] + [In]) \approx 0.45$.

Sample	$\frac{p_{\mathrm{Se}}}{(p_{\mathrm{Cu}}+p_{\mathrm{Ga}}+p_{\mathrm{In}})}$	GGI[a]	CGI[b]	FWHM[c] (°)	position[d] (°)	E_g (eV)
S1	10	0.40	0.9	0.092	65.306	1.21
S2	15	0.47	0.92	0.102	65.533	1.25
S3	20	0.44	0.88	0.069	65.538	1.25

Table 4.1.: *XRD summary* - *Given are the determined FWHM and the peak positions according to the model shown in figure 4.2. The samples were grown with different selenium pressures in the reactor, while the ratios* $p_{Cu}/(p_{Ga} + p_{In}) = 0.88$ *and* $p_{In}/p_{Ga} = 1.47$ *were unchanged. The band gap was determined from PL measurements (figure 4.3) at room temperature.*

[a] [Ga]/([Ga] + [In]) determined using EDX
[b] [Cu]/([Ga] + [In]) determined using EDX
[c] The full width half maximum w of the Pseudo-Voigt peak shape described in the text.
[d] The position of the peak maximum x_0 of the Pseudo-Voigt peak shape for the $\mathrm{Cu}_{K\alpha 1}$ line.

Besides the defect density within the film, the surface morphology is influenced by the different selenium pressures as well. Figure 4.3 shows top view pictures obtained from SEM measurements for the samples S1, S2, and S3. Only sample S3 with the highest selenium pressure shows a surface without protrusions as it is known from $CuInSe_2$ and $CuGaSe_2$ [153]. On the other hand, a lower selenium pressure leads to the formation of inclusions on the surface.

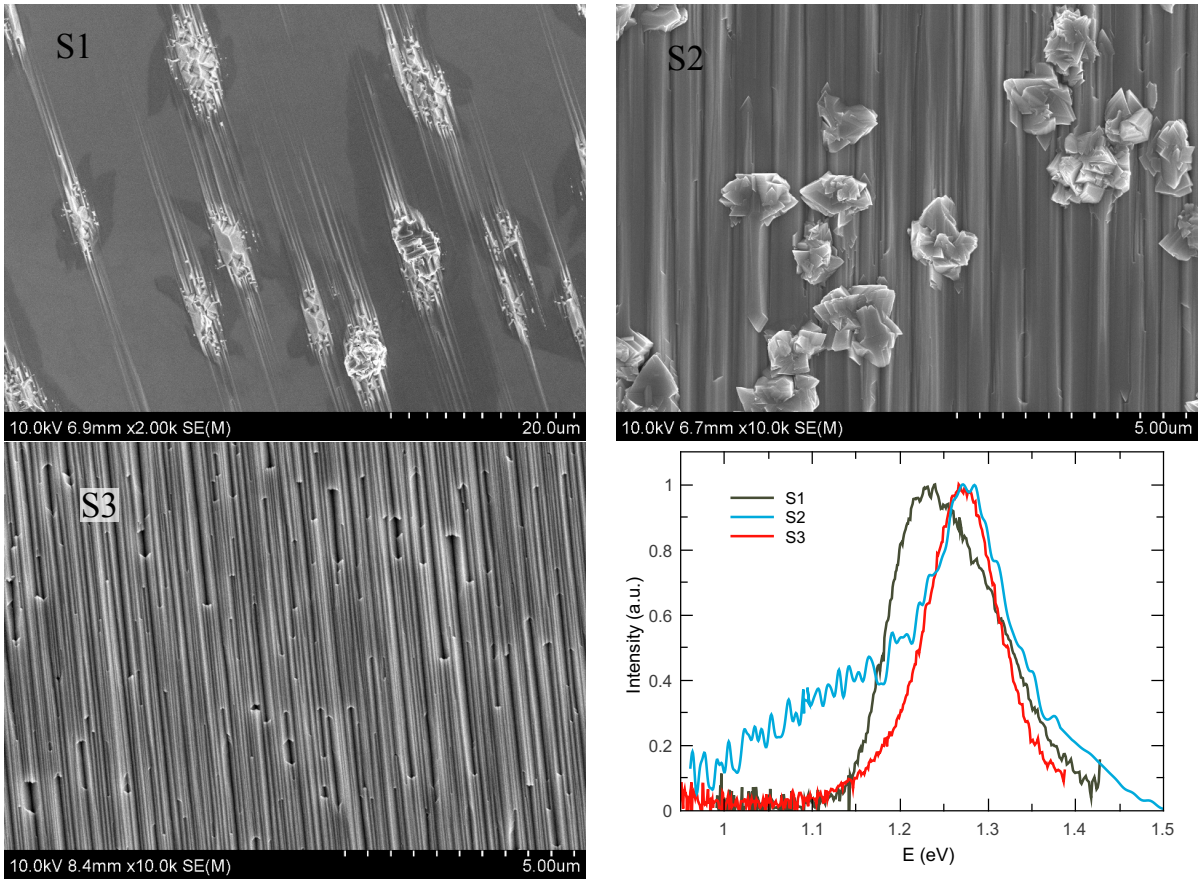

Figure 4.3.: *SEM pictures and PL spectra at room temperature for different selenium pressure* - *SEM pictures and PL spectra at room temperature for the samples S1, S2, and S3. A summary of the compositional properties is given in table 4.1. The SEM pictures show a flat surface for sample S3 with the highest selenium pressure during growth, which shows a facet like surface known for Cu-poor $CuInSe_2$ and $CuGaSe_2$ samples [153]. The highest density of these inclusions is observed for sample S2, which shows a broadening on the low energy side of the PL spectrum. S1 with a lower density and S2 with no inclusions show a typical peak shape measured at room temperature.*

4.2.2. Interface and surface morphology

A proper interface is crucial for the solar cell operation, since a non-ideal interface can significantly increase the recombination rate or pin the Fermi level. The most intuitive approach to verify a proper interface is a cross section measurement. Two representative measurements are depicted in figure 4.4 showing a Cu-poor sample with [Ga]/([Ga] + [In]) ≈ 0.3 and figure 4.5 with [Ga]/([Ga] + [In]) ≈ 0.45. It can be seen, that the interface between the GaAs and the absorber layer is very smooth and does not exhibit any unwanted voids for both compositions. This confirms, that the growth temperature of 500 °C works well for both ratios.

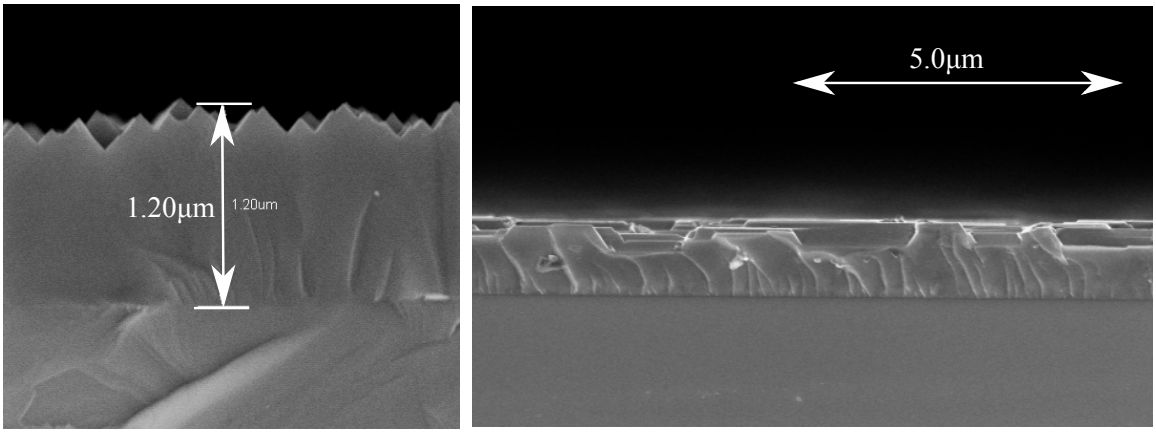

Figure 4.4.: ***SEM cross section of a Cu-poor Cu(In,Ga)Se$_2$ film*** *- Two sample with a slightly Cu-poor composition of [Cu]/([Ga] + [In]) ≈ 0.9 and a of [Ga]/([Ga] + [In]) ≈ 0.3.*

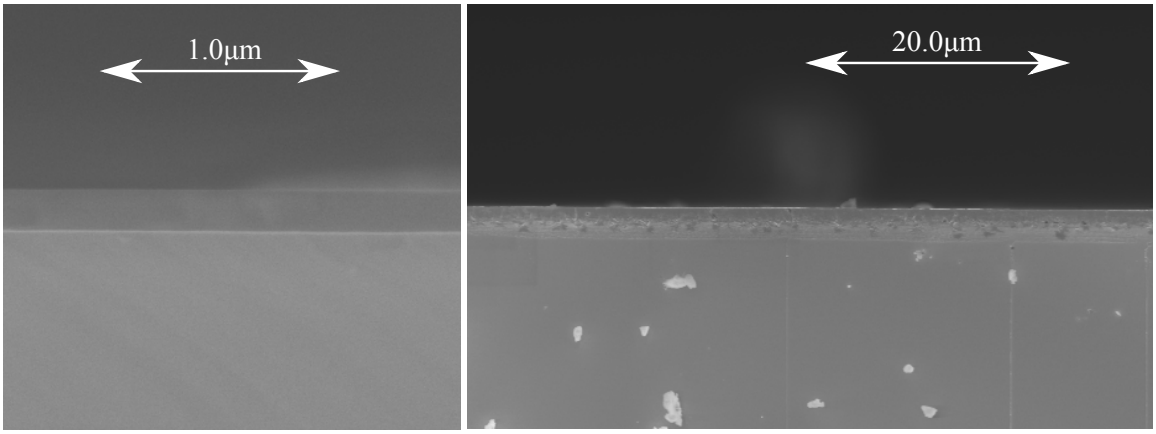

Figure 4.5.: ***SEM cross section of a Cu(In,Ga)Se$_2$ close to the stoichiometric point*** *- A cross section SEM picture of a Cu(In,Ga)Se$_2$ film with [Cu]/([Ga] + [In]) ≈ 1.0 and [Ga]/([Ga] + [In]) ≈ 0.5. No formation of voids was observed at a growth temperature of 500 °C. Depicted are two different samples.*

Two representative top views for a Cu-poor and a stoichiometric composition with [Ga]/([Ga] + [In]) ≈ 0.3 (figure 4.6a and 4.6b) reveals the known facet like structure [153] for compositions below the stoichiometric point and a rather smooth surface for a stoichiometric sample. Figure 4.6b is blurred since focusing on the very smooth surface is

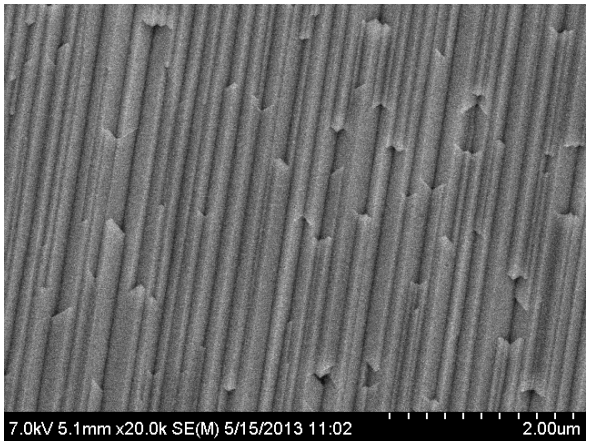

(a) A Cu-poor film showing the typical facet like structure.

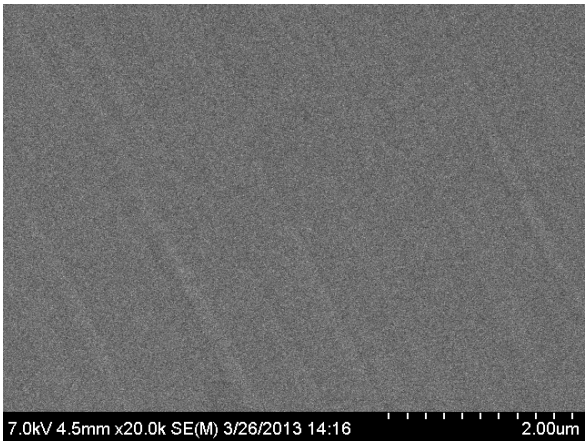

(b) A stoichiometric film with a smooth surface.

Figure 4.6.: ***SEM top view*** *- Two SEM top views of Cu(In,Ga)Se_2 with [Ga]/([Ga]+[In]) ≈ 0.3. Picture (a) is the top view of the same sample shown in figure 4.4 (left hand side).*

rather difficult. It is important to note, that the facets are not only observed for $CuInSe_2$ and $CuGaSe_2$. The structure was seen for [Ga]/([Ga] + [In]) ≈ 0.3 (figure 4.4) and for [Ga]/([Ga] + [In]) ≈ 0.5 and ≈ 0.6 (not depicted).

4.2.3. Summary of the crystal quality

For the first time, epitaxial Cu(In,Ga)Se_2 films were successfully grown at the Laboratory for Photovoltaics in Luxembourg. It was shown, that the modification of the growth temperature to 500 °C for $CuIn_{1-x}Ga_xSe_2$ films is suitable for compositions between $0.3 \leq x \leq 0.65$. The analysis of the XRD pattern reveals, that the c-axis of the unit cell grows for $x \geq 0.65$ perpendicular to the substrate's surface, when grown on GaAs (001). It could be shown, that a value of $x = 0.45$ leads to growth where the c-axis of the film is parallel to the surface of the substrate. This phenomenon can be explained with the strain in the Cu(In,Ga)Se_2 layer. Since the lattice mismatch for $x \approx 0.5$ is smaller, if the c-axis is parallel to the substrate, this orientation is energetically favoured.
The reduced strain causes less dislocations and is therefore visible in the full with half maximum w of the Cu(In,Ga)Se_2 related peaks in the XRD pattern. It was shown, that w can be reduced down to 0.069°. Additionally, it was shown, that the selenium overpressure influences the FWHM as well. Besides, the inclusion on the sample's surface can be suppressed by adjusting the over pressure to higher values. In the system at LPV, an overpressure of $\frac{p_{\mathrm{Se}}}{(p_{\mathrm{Cu}}+p_{\mathrm{Ga}}+p_{\mathrm{In}})=20}$ leads to a smooth surface for [Ga]/([Ga] + [In]) ≈ 0.5. SEM pictures confirmed, that the known characteristics of the facet like surface for Cu-poor $CuInSe_2$ and $CuGaSe_2$ [153] can be also observed for Cu(In,Ga)Se_2. The cross section picture revealed smooth interfaces between the GaAs and the Cu(In,Ga)Se_2 films, which can be explained with a reduced strain as well.

4.3. Making epitaxial devices

The typical devices as depicted in figure 2.20 with an epitaxial absorber layer were produced with the following procedure:

1. Commercially available epi-ready GaAs wafers from Wafer Technology Ltd. were used as a substrate. The heavily Zn doped material with a charge carrier density in the order of $5x10^{18}\mathrm{cm}^{-3}$, a thickness of 0.5 mm, and a diameter of 2 inches were introduced into the deposition system.

2. The Cu(In,Ga)Se_2 absorber layer was grown as described in section 2.3 up to a thickness of approximately 1 µm. Since the MOVPE system was never used to deposit the buffer or the window layer, the samples had to be taken out of the system[3]. Typically, only half of the wafer is used for the following steps to allow the usage of the available standard equipment, which is optimized for samples on squared glas pieces of one inch[2]. Since the precise cutting is rather difficult, variations of the device size cannot be avoided.

3. Before dipping the absorber into the chemical bath, the backside has to be protected to avoid any deposition of CdS on the back side. A CdS layer on the backside of the wafer would prevent an ohmic back contact. The fastest and most reliable method is to cover the back side with capton tape. By doing so, the variations of the wafer size can be handled easily. The dimensions of the wafer may vary, since parts might be used for different analysis techniques requiring another cutting step.

4. The CdS buffer layer was deposited in a chemical bath. To clean the sample surface exposed to air an etching step prior to the deposition was performed. Both processes, the etch and the CdS deposition are described below. The protecting capton tape on the back side resists both treatments and allows the usage of the same sample holder for the cleaning and the deposition step. Both processes, the etch and the CdS deposition, are also described in 3.3, where their influence on the quasi-Fermi level splitting is examined. There, it was shown, that the time between the etch and the deposition should be as short as possible in order to avoid a loss in the open circuit voltage. Based on these observations, the time between the etch and the CdS deposition was less than one minute.
   To avoid any damage in the CdS layer, it is useful to keep off the layer from any surface. Thus, the tape can be carefully removed by holding the wafer in one hand and using a scalpel to remove the tape with the other hand.

5. The window layer was deposited by an RF sputtering system[4]. As a first step, an 80 nm thick layer of i-ZnO was sputtered from a stoichiometric ZnO target in argon atmosphere. The 300 nm thick ZnO:Al layer was sputtered directly after from a ZnO/Al_2O_3 (2%wt) target in argon atmosphere.

[3] In general, the deposition of CdS and ZnO can be carried out in a MOVPE system. However, the testing of the appropriated precursors and the optimization of the growth process would have been too time consuming.

[4] Orion 8 manufactured by AJA int.

6. The front contacts are deposited by e-beam evaporation, through a grid-shape patterned mask dividing the absorber in 16 small solar cells per half of a wafer. A 10 nm thick layer of nickel is at first evaporated in order to prevent any oxidation (from the ZnO) and diffusion of the 2 µm thick layer of aluminium deposited right after. To allow an easy post processing, the mask should be placed such, that the contact grid is parallel to one of the crystallographic axis, to simplify the cutting process. The wafters are shipped with two small flat edges to identify the orientation. If the squared mask is placed such, that one side is parallel to one of the edges of the wafer, the separation of each cell is much easier.

7. Finally, the back side of the GaAs substrate was covered with a 200 nm thick gold layer ensuring an ohmic contact to the device.

The steps 4 to 6 are also used for the polycrystalline material. Since these samples are directly grown on the molybdenum, which is also used for the back contact, the final deposition of the gold layer is unnecessary. Besides, the usage of capton tape to protect the back side can be spared, since the molybdenum layer is protected by the glass substrate. In addition, the sample holder for the polycrystalline samples used for the CdS deposition is designed such, that the CdS cannot reach the back side of the glass.

Etching process

Before depositing the CdS buffer layer, each sample was etched for 150 s in a 10 wt. % aqueous KCN solution. The etch is a standard solution known to remove secondary phases without disturbing the $CuInSe_2$ matrix [168]. It is used for any solar cell produced in the laboratory and well established [169–171]. The solution is made by dissolving the needed amount of KCN-powder in the corresponding mass of deionized water: 22 g of KCN are introduced in 198 g of distilled water to get the solution. The time between the etch and the CdS deposition was less than one minute.

CdS deposition

The deposition of a CdS buffer layer is well known in the $Cu(In,Ga)Se_2$ community [172]. Following the established procedure, the buffer was deposited in a chemical bath. 50 mM thiourea solution was used as a sulfur source and a 2 mM solution of cadmium sulfate as a cadmium source within a 1.5 mM solution of ammonium hydroxide as described in [173]. The deposition follows the process parameter used at LPV for the polycrystalline devices. Thus, the deposition time was 5 min and carried out at 67 °C resulting in a thickness of approximately 50 nm. The temperature is achieved by a heated water bath around the beaker where the deposition takes place. The growth rate depends on the temperature and the pH of the solution [161].

While polycrystalline cells can be scratched easily to separate one sample into several smaller cells after the production steps described in the beginning of this section, the epitaxial material is much more fragile and tends to break in many pieces. Due to the

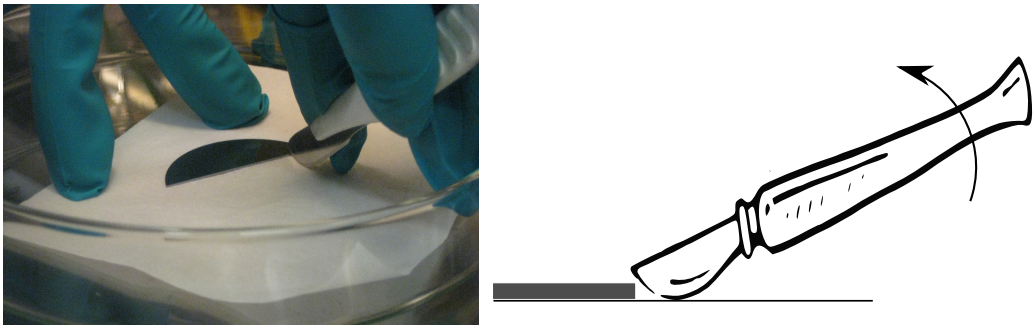

Figure 4.7.: ***Preparation of small devices of epitaxial solar cells*** *- The picture illustrates the cutting method used to prepare the small devices. The tip of a scalpel is placed a few millimeter above the sample and perpendicular to the edge. By winding the knife courageously the sample breaks along the crystallographic axes. For testing purposes, only a quarter of a wafer is used for the deposition process. In this case, the cutting is performed on the pure GaAs wafer. To prepare the small test cells (see the right hand side in figure 4.8), the separation of each cell is done after the deposition of all layers, the buffer and the window, the grid and the back contact (see the description in the beginning of section 4.3). Scalpel from [174].*

MOVPE process a small stripe at the edges (see the left hand side of figure 4.8) tends to be slightly different in composition compared to the main area. Furthermore, the shunt resistivity is much higher, if the wafer edges are still present when measuring the final cell. This is most likely related to a reduced thickness in this area or to the coverage of the CdS. Thus, the edges have to be removed in a first step. Next, each cell has to be separated from the others ensuring that no electrical contact exists between them. The cutting process is done using the first millimetres of the tip of a scalpel. In doing so, it is important to place the scalpel parallel to one of the crystallographic axis and unroll the tip on top of the device to initiate the breaking of the crystal along the axis. The principle of the cutting process is illustrated in figure 4.7.
After all cells are separated from each other, one still has to implement an easily accessible back contact. All available measurement set-ups require a back contact accessible from the top. Therefore, the gold backside of each sample was glued with a conductive silver paste on top of a gold coated glass slice (see the right hand side in figure 4.8).
The separation of the cells requires practice and some experience. During the cutting of the cells of the first batch, many samples were destroyed or unusable, e.g. if the break cuts the long ”fingers” of the grid (the thin white stripes in figure 4.8) very close to the dots used for the electrical characterisation, the photo active area is too small. This is one reason, why only four samples of the first batch are analysed in the next sections. The second reason is, that only samples with an efficiency of $\eta > 3.0\%$ were considered worse to be analysed. For the second batch, the cutting process was much more successful, but due to the lower GGI, no reasonable efficiency was achieved (section 4.9).

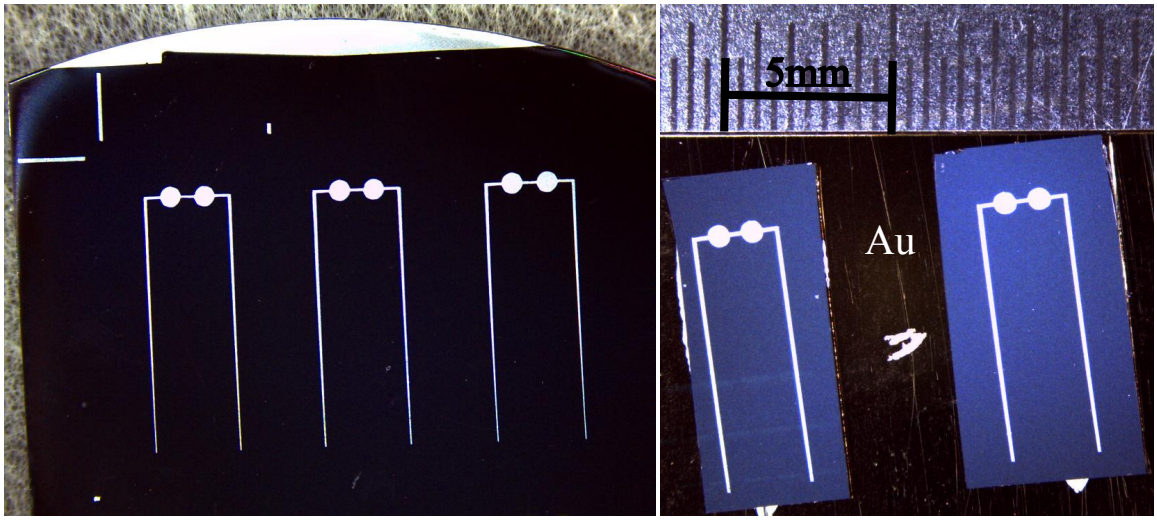

Figure 4.8.: ***Photo of epitaxial solar cells*** *- Left: Picture of a wafer after the deposition of the absorber, the buffer, and the window layer. The front contact is deposited using a squared mask leading to the deposition of aluminium visible in the upper part of the wafer. Right: Cut solar cells glued with a conductive silver paste on top of a glas substrate coated with gold.*

4.4. Characterization of epitaxial devices

The following sections summarize the electrical characterization performed on the first epitaxial devices. Two batches of samples were produced, one with a $[Ga]/([Ga]+[In]) = 0.4-0.5$ and a second with a lower $[Ga]/([Ga]+[In]) \approx 0.3$. Unfortunately, the second batch did not result in efficient cells ($\eta \leq 3\%$ and mostly below 1%). Thus, the main evaluation focuses on the first batch. The second batch will be presented briefly afterwards. In the following, the IV characteristics and their temperature dependence, the EQE and voltage dependent capacitance measurements are presented.

4.5. Current voltage analysis

The current - voltage (IV) characteristic was measured with the set-up available in the lab. The illumination source was a cold mirror halogen lamp providing a light spectrum closer to AM1.5g, when compared to a normal halogen source. The lamp was adjusted in height, until the measurement of the short circuit current (J_{sc}) of a calibrated reference solar cell delivered the certified value of J_{sc}. Hereby, the incident photon flux above the band gap of the reference cell onto the surface of the solar cells is ensured to be close to AM1.5g.
A four probe measurement was used to minimise the effect of contact resistances. A computer controlled current-voltage measure unit was used to apply a voltage and to measure the current of the device. The temperature dependent measurements were performed with a similar set-up, where the sample is placed into a cryostat. Here, the height of the illumination source was adjusted until the measured short circuit current corresponded to the previously measured one with the standard set-up. Thus, the comparability and the right illumination power density was ensured.

The single diode equation (2.39) was used to determine the diode factor and the shunts directly, where the external collection function was assumed to be independent of the voltage $\eta_{ec}(V) = 1$. For well behaving devices, it was easily possible to fit the implicit equation (2.39), for worse performing cells not, as described later. The fit was done with an algorithm implementing the orthogonal distance regression [175] available in the python library scipy [176, 177] (see in the appendix D).
As seen later, most of the IV curves of the analysed devices do not show the typical shape which can be easily described with the one diode model, This is due to the presence of a small kink as seen later. Nevertheless, the one-diode model was used as shown in the following: A comparison of two implicit fits is shown in figure 4.9a with a linear axis; figure 4.9b shows the absolute values of the current shifted by J_{SC} in log-plot. Exemplary, the grey crosses show the measured data at T=300K (sample A under illumination). The blue curve was fitted within the limits $-0.5 < V < 0.33$V. On the other hand, the red curve was fitted over the whole measured range. However, the data points within the grey area (figure 4.9b) were not considered. When comparing both fits, the determined

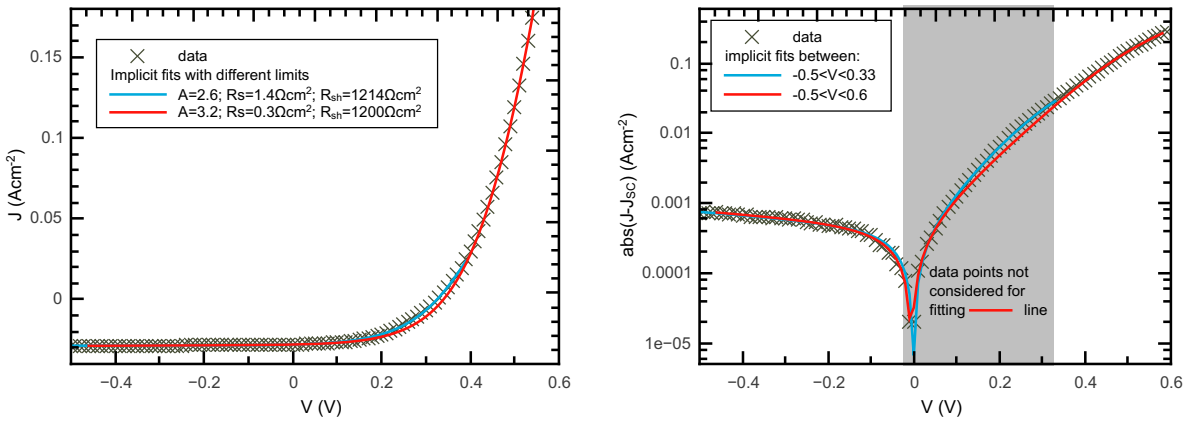

(a) Linear plot of determined IV curves

(b) Logarithmic plot of the absolute of the determined IV curves shifted with J_{SC}

Figure 4.9.: *Comparison of evaluation methods* *- Exemplary illustration comparing the two used fitting procedures methods. The data (cross) were fitted with the implicit diode equation* (2.39)*. The blue curve was obtained by limiting the fit within the voltage range $-0.5 < V < 0.33$V. Te red curve used the whole voltage range, however, the data points in the grey area were not considered.*

diode factors differ from each other. While the red curve show a value of $A = 2.6$, the blue curve leads to a higher value of $A = 3.2$. While the shunt resistance is comparable, $R_{shunt} = 1214\ \Omega cm^2$ (red) and $R_{shunt} = 1200\ \Omega cm^2$ (blue), the series resistance differs slightly: $R_{s,blue} = 1.4\ \Omega cm^2$ ($R_{s,red} = 0.3\ \Omega cm^2$). The later discussion about the temperature dependent change of the diode parameters is based on the second method: fitting the whole measured data range and excluding the data points around the kink. Therefore, the absolute values of the diode factor should be seen as an upper limit. since they are generally greater than $A > 2$. Both methods, the limited fitting range and the broader limits with excluding data points, exhibit the same trends and the discussion is not hampered.

Room temperature

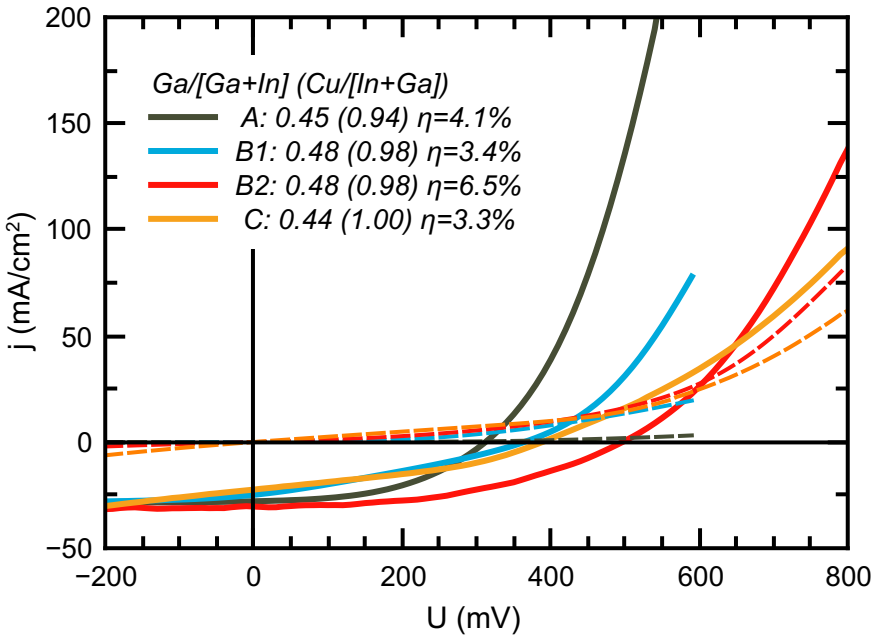

Figure 4.10.: ***Overview of the first epitaxial solar cells*** *- Depicted are the IV curves at room temperature for the absorbers analysed more in detail in this section. The colour indicates the sample measured under illumination (solid lines) and in the dark (dashed lines).*

Figure 4.10 depicts the IV curves measured at room temperature for the compositions [Ga]/([Ga] + [In]) = 0.45 and [Cu]/([Ga] + [In]) = 0.94 (grey, sample A), [Ga]/([Ga] + [In]) = 0.48 and [Cu]/([Ga] + [In]) = 0.98 (blue, sample B1 and red, sample B2), and [Ga]/([Ga] + [In]) = 0.44 and [Cu]/([Ga] + [In]) = 1.00 (orange, sample C). The set of samples are the best performing absorbers from the first batch of epitaxial solar cells fabricated in Luxembourg. Although more absorbers were produced, the discussion is limited to these four samples, since many were destroyed during the preparation procedure (see section 4.3). Besides, only cells with an efficiency of $\eta > 3\%$ were fully characterised (temperature dependent IV, EQE, and capacitance measurements).
The first batch was grown with a [Ga]/([Ga] + [In]) between 0.4 and 0.5 since the lattice mismatch within this area is expected to be small (see section 2.2 and 4.2) ensuring the growth of an unstrained layer and thereby minimizing the number of dislocations within the film. At the same time, the [Cu]/([Ga]+[In]) was aimed at to be grown under Cu-poor conditions.
The characteristic solar cell properties are summarized in table 4.2. Although all devices were processed the same why, the two different absorbers with identical composition show quite different device characteristics. While one exhibited the highest efficiency of 6.5% within this work, the other showed slightly more than half of this value. This is mostly due to a low shunt resistance for sample B1 (compare table 4.3). Sample C also suffers from a low shunt resistance. It should be mentioned, that the highest achieved efficiency of 6.7% is not depicted, since no temperature dependent measurements are available. Nevertheless, the open circuit voltage of $V_{OC} = 0.505$V and the short circuit current

Sample	CGI/GGI	η (%)	V_{OC} (V)	J_{SC} ($\frac{\mathrm{mA}}{\mathrm{cm}^2}$)	FF	ZnO
A	0.94/0.45	4.1	0.31	28	46	LPV
B1	0.98/0.48	3.4	0.37	25	30	LPV
B2	0.98/0.48	6.5	0.50	30	45	HZB
C	1.00/0.44	3.3	0.38	22	37	LPV
Record device [7]						
on GaAs (111)	-/0.3	8.5	0.46	31.6	58	-
on GaAs (001)	-/0.3	7.3	0.48	24.8	61	-
on GaAs (110)	-/0.3	6.4	0.42	27.7	55	-

Table 4.2.: ***Solar cell parameters at room temperature*** *- Summary of the typical solar cell parameters for the devices depicted in figure 4.10. The absorber thickness was* $\mathrm{d} \approx 1\ \mu\mathrm{m}$*. The bottom part compares the epitaxial record device found in literature [7]. The ZnO was either deposited at LPV or at the Helmholtz Zentrum Berlin (HZB).*

($\mathrm{J_{SC}} = 31\ \frac{\mathrm{mA}}{\mathrm{cm}^2}$) are comparable to the most efficient sample discussed here (table 4.2). The higher fill factor of 46 is due to the slightly higher values of V_{OC} and J_{SC} and a slightly lower series resistance of 0.9 $\Omega\mathrm{cm}^2$ (compared to 1.5 $\Omega\mathrm{cm}^2$).
The highest reported efficiency for epitaxial Cu(In,Ga)Se_2 solar cells (with a [Ga]/([Ga]+[In]) $\approx$ 0.3) reaches 8.5% for material grown on GaAs (111) and 7.3% for a substrate orientation of (001) (table 4.2) [7]. When focusing on the comparable substrate orientation of (001), the performance of the the best device is close to the reported record of 7.3% conversion efficiency. The observed V_{OC} and the short circuit current measured in this work are even higher than the record device. However, a higher V_{OC} is expected because of the higher gallium content leading to an increased band gap. Nevertheless, the fill factor is smaller, which is most likely related to the presence of a kink, as seen later. While the reported shunt resistance under illumination is in the same order of magnitude, the measured series resistance in this work is only half of the reported record device (table 4.3).

Sample	CGI/GGI	$R_{s,illu}$	$R_{s,dark}$	$R_{sh,illu}$	$R_{sh,dark}$
A	0.94/0.45	0.5	68	1000	3800
B1	0.98/0.48	1.9	14.5	200	300
B2	0.98/0.48	1.5	5.5	400	1800
C	1.00/0.44	1.9	3	37	37
Record device [7]					
on GaAs (111)	-/0.3	3	-	330	-
on GaAs (001)	-/0.3	3	-	500	-
on GaAs (110)	-/0.3	3	-	250	-

Table 4.3.: ***Comparison of resistances at room temperature*** *- Summary of resistances in* $\Omega\mathrm{cm}^2$ *at room temperature illustrating the huge differences between measurements in the dark and under illumination. The resistances were determined with a linear fit around* 0 V *for the shunt resistance, and around the highest measured voltage for the series resistance. The bottom part compares the available data for the epitaxial record device found in literature [7].*

Figure 4.10 shows huge differences between the illuminated (solid) and the dark (dashed) measurements. First, all samples exhibit a cross over and a deviation from the shifting approximation (section 2.6.3). If the IV curve measured under illumination crossed the one measured in the dark, the situation is referred to as cross over. Shifting approximation describes the situation, when the current under illumination is shifted by a constant offset, namely the short circuit current. Since the external collection function was assumed to be $\eta_{ec}(V) = 1$ to allow the usage of the one diode model (as described in the beginning of this chapter), the shifting approximation was assumed for the later evaluation.

There are several explanations for both effects [35]:

Cross over A cross over may be observed, if an electron barrier ϕ is present in the dark and significantly reduced under illumination. Examples for a barrier ϕ vanishing under illumination are a CdS layer with a high doping concentration [178] or a high density of acceptors in the absorber close to the interface to the CdS [179].

The first case was shown for $CuInSe_2$ and CdS [178]: a high doping concentration in the buffer layer will shift its conduction band maximum (CBM) down. As soon as the energy level of the CBM approaches the value of the conduction band in the bulk of the $CuInSe_2$ absorber layer, the barrier for the electrons (a spike in the conduction band when going from the $CuInSe_2$ layer to the CdS) is increased. Under illumination, the photo current generated in the absorber is partially blocked (resulting in a kink in the IV curves when being simulated [179]). Under illumination (with blue light in the case of [178]), the concentration of free electron and holes may change significantly. Deep defect levels can be filled with holes. If the holes have a sufficiently long lifetime in this defect state, the concentration of electrons in the conduction band is increased and the electron barrier is reduced.
The second case of a high acceptor density in the absorber results in a large negative charge in the acceptor states. This leads to a large potential drop over the buffer and forms a barrier for the electrons [35]. Under illumination, the acceptors can be filled with photo generated holes from the buffer layer, which reduces the acceptor charge and therefore the electron barrier [35, 179].
In both situation, the diode current is larger under illumination and a cross over is observed.

Shifting approximation Possible reasons for a violation of the shifting approximation are a voltage dependent collection function, an illumination dependent shunt path, or changes of the dominating diode current [35]. A shunt path can also be induced by conducting dislocations, creating a shunt between the GaAs and the CdS buffer.

First, the voltage dependence of the SCR width, interface recombinations and photo current barriers result in a voltage dependent collection function (section 2.6). As seen later more in detail, the devices are indeed dominated by interface recombinations (section 4.6.1), at least one photo current barrier is present (section 4.6.2), and (partly) small changes in the space charge width are observed (section 4.7).

Second, a shunt path may be present, which is not or less pronounced in the dark. Nevertheless, if photoconductive material is present in the device, an additional or more pronounced shunt path may be observed.

Finally, the origin of the diode current may change under illumination.

4.6. Temperature dependent analysis

The temperature dependent measurements are shown in figures 4.11 to 4.14. The left hand side depicts the measurement in the dark while the right hand side illustrates the measurements under illumination.

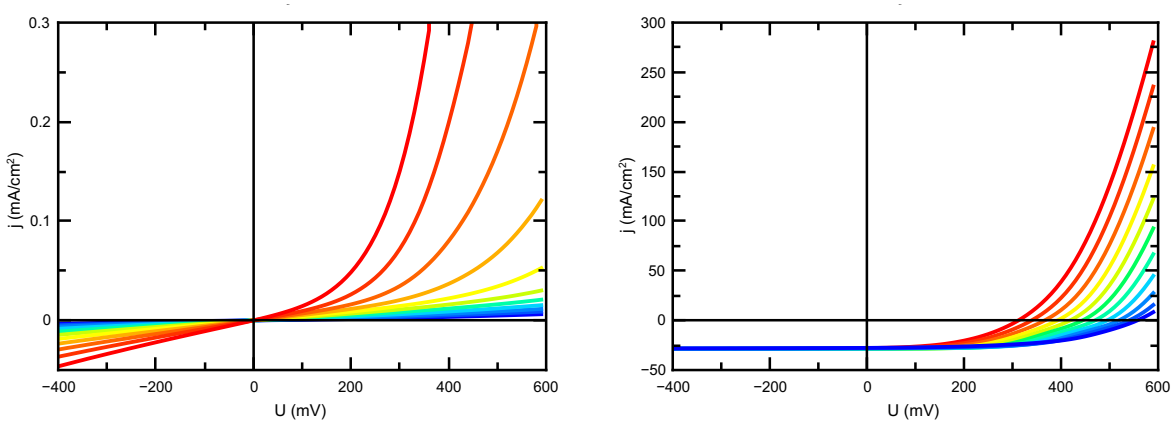

(a) Dark *(b) Illuminated*

Figure 4.11.: ***Temperature dependent IV curves (sample A)*** *- Temperature dependent IV measurements in the dark (left) and under illumination. The measurement ranges from 100K to room temperature. The composition is [Ga]/([Ga]+[In]) = 0.45 and [Cu]/([Ga]+[In]) = 0.94. Note that the scales are different in all IVT measurements.*

Sample A with the copper poorest composition in figure 4.11b exhibits a typical diode behaviour under illumination: with a decreasing temperature, an increasing V_{OC} is observed, while the shunt resistance under illumination remains constant. Also, the series resistance is changes only slightly down to a temperature of $T \approx 170K$ (compare below). In the dark, on the other hand, the shunt resistance does not change significantly down to a temperature of $T \approx 230K$ and is in a comparable order of magnitude. In both cases, under illumination and in the dark, it is $R_{sh} \geq 1000\ \Omega cm^2$ at room temperature. Nevertheless, the series resistance in the dark is higher (at room temperature it is $R_{s,dark} = 68\ \Omega cm^2$ compared to $R_{s,illu} = 0.5\ \Omega cm^2$ under illumination) and increases with a decreasing temperature. This leads to a less typical diode curve until the device is almost ohmic for $T \lesssim 200K$. Additionally, the current in the dark is much lower than under illumination (two orders of magnitude). The best performing device B2 shows a difference of only one order of magnitude, when comparing the currents in the dark and under illumination. Furthermore, the current in the dark is two orders of magnitude higher (figure 4.13a), when compared to sample A. This indicates the presence of an illumination dependent potential barrier in sample A, since the currents under illumination are in the same order of magnitude when compared to the best performing device B2 (figure 4.13b).

Sample B1 (figure 4.12a) exhibits a similar behaviour like sample A, when comparing the shunt resistances in the dark and under illumination. Both exhibit a comparable order of magnitude of $R_{sh,illu} = 200\ \Omega cm^2$ and $R_{sh,dark} = 300\ \Omega cm^2$ at room temperature. The slope in figure 4.12a appears steeper, since the scales of the current axis is different

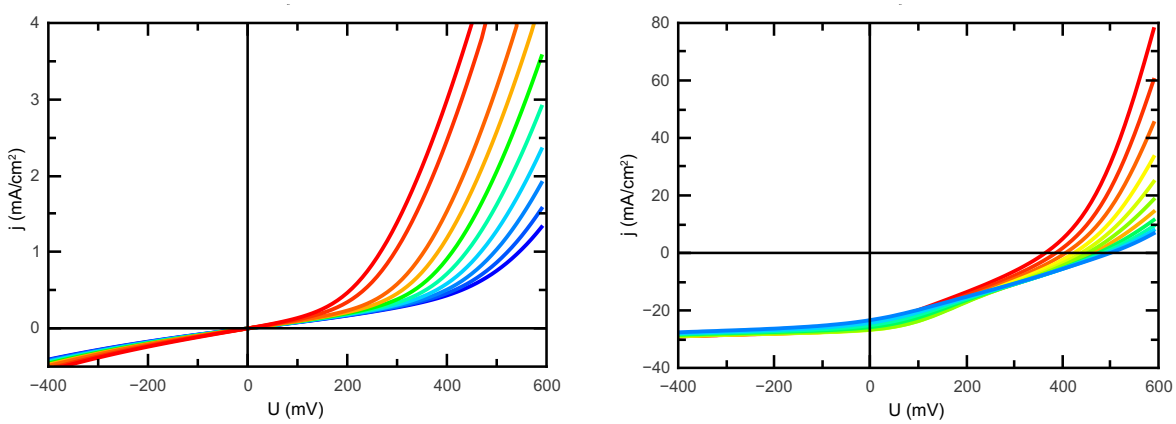

(a) Dark (b) Illuminated

Figure 4.12.: ***Temperature dependent IV curves (sample B1)*** *- Temperature dependent IV measurements in the dark and under illumination. The measurement ranges from 100K to room temperature. The composition is [Ga]/([Ga]+[In]) = 0.48 and [Cu]/([Ga]+[In]) = 0.98. Note that the scales are different in all IVT measurements.*

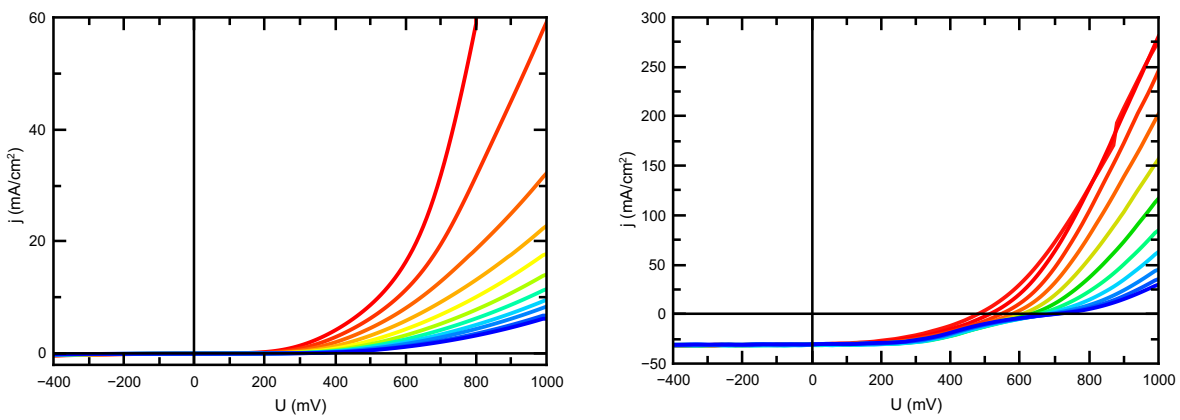

(a) Dark (b) Illuminated

Figure 4.13.: ***Temperature dependent IV curves (sample B2)*** *- Temperature dependent IV measurements in the dark and under illumination. The measurement ranges from 100K to room temperature. The composition is [Ga]/([Ga]+[In]) = 0.48 and [Cu]/([Ga]+[In]) = 0.98. Note that the scales are different in all IVT measurements.*

compared to the illuminated case. With a decreasing temperature, the shunt does not change remarkably. The differences in the current, when comparing the illuminated and the dark case, are similar to sample A albeit it is only in the order of one magnitude. Still, compared to the best performing device, the observed currents in the dark are much lower. The illuminated curve clearly shows a kink around 0.25 V which gets more pronounced for lower temperatures.

Sample B2 with the identical composition (figure 4.13a) shows a similar kink, however, much less noticeable at room temperature. Only for decreasing temperatures, it gets more pronounced. The shunt resistance is reasonable high for the measurement under illumination and in the dark. Similar, the series resistance shows a comparable order of magnitude for both measurement conditions (table 4.3).

The observed kink for sample B1 and B2 is most likely not related to the additional interface to the GaAs. Indications for that are the absence of a pronounced kink for sample A and C. Furthermore, the simulation in section 4.10 suggest, that the additional GaAs layer is not harmful for the device. Therefore, it is very likely, that the kink is related to effects close to the interface between the absorber and the buffer. Even descent $Cu(In,Ga)Se_2$ based solar cells can exhibit kinks under certain illumination conditions [180].

Finally, the fourth device C (figure 4.14a) shows generally a very low shunt resistance. In the dark, it becomes also almost ohmic for lower temperatures. Under illumination, the low shunt resistance is still present and dominates the IV curves. In general, device C behaves very unusual, e.g. the V_{OC} decreases with a decreasing temperature. The device with the highest copper content exhibits the lowest efficiency which makes an interpretation difficult, since it does not behave like a usual diode and is not further discussed.

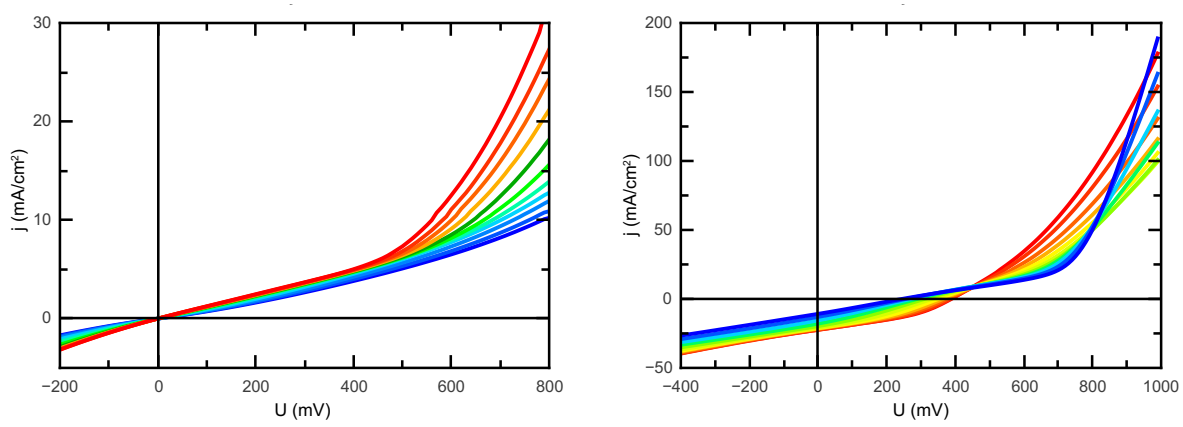

(a) Dark *(b) Illuminated*

Figure 4.14.: *Temperature dependent IV curves (sample C)* - *Temperature dependent IV measurements in the dark and under illumination. The measurement ranges from 100K to room temperature. The composition is [Ga]/([Ga]+[In]) = 0.44 and [Cu]/([Ga]+[In]) = 1.00. Note that the scales are different in all IVT measurements.*

4.6.1. V_{OC} and temperature

Temperature dependent measurements are useful, since they allow the determination of the dominating recombination path by analysing the temperature dependence of the open circuit voltage(compare section 2.6.4). The temperature dependence of the V_{OC} is plotted in figure 4.15a and reveals, that all of the measured devices is dominated by interface recombination (to the buffer layer and/or to the GaAs). The open circuit voltages were extrapolated at zero kelvin to determine the activation energies. These energies are 0.76 eV for the copper poorest and 1.03 eV for the almost stoichiometric device B2. Sample B1 with the identical composition shows an activation energy of 0.71 eV. The comparison with the band gap, which was determined from the EQE measurements (compare table 4.4) reveals up to 0.54 eV lower activation energies compared to the respective band gap. The determination of the band gap is described in section 4.7. The copper richest device (sample C) does not allow a proper analysis, since its behaviour can not be described with common models.

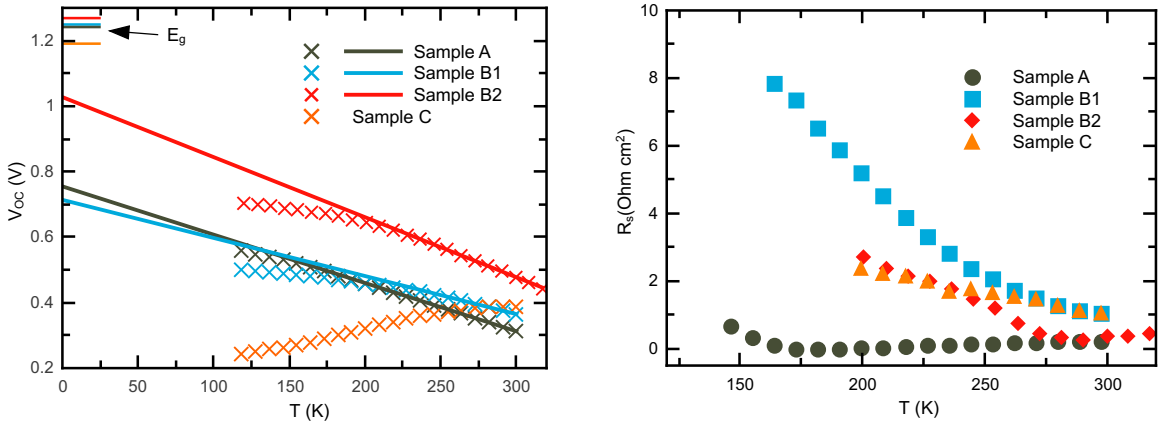

(a) Temperature dependence of the open circuit voltage

(b) Series resistance under illumination

Figure 4.15.: ***Temperature dependence of the open circuit voltage and the series resistance*** *- Left: The open circuit voltage in dependence of the temperature for the four analysed samples. Recombinations at the interface are dominating for all of the samples, since the activation energy is below the band gap. Right: Temperature dependence of the series resistance.*

4.6.2. Resistances

At room temperature, where the devices would be operated, the series is below 2 Ωcm^2 for all devices (table 4.3). Although high efficient cells exhibit lower values in the range of $0.2 - 0.5$ Ωcm^2 [181], the series resistance is not responsible for the low efficiencies. A simulation with the device simulator SCAPS [139] shows an efficiency of $\eta = 16.2\%$ for a series resistance of 0.22 Ωcm^2 and $\eta = 14.6\%$ for 2.0 Ωcm^2. The situation is similar for the shunt resistance of sample A, B1, and B2: Values of 1000 Ωcm^2 (sample A), 200 Ωcm^2 (sample B1), and 400 Ωcm^2 (sample B2) are observed. Although a high efficient device shows values above > 1000 Ωcm^2 [35], even a low value of 200 Ωcm^2 is still acceptable.

A similar simulation as for the series resistance shows also only a minor drop in the efficiency. An efficiency of $\eta = 16.2\%$ is achieved for a shunt resistance of 1000 Ωcm^2 and $\eta = 15.1\%$ for 200 Ωcm^2. Thus, the shunt resistance does not explain the low efficiencies as well. Both simulations were done with the definition file of the "Numos CIGS baseline" included in SCAPS. In both cases, only one resistance was changed, while the other was not accounted for.
When comparing the illuminated and the dark resistances, differences can be observed (table 4.3). The series resistance in the dark is up to ≈ 130 times higher for the lowest copper content (sample A) and still ≈ 3.5 times higher for the best performing device. The differences in the shunt resistance are less pronounced: Apart from the highest copper content (sample C), difference between a factor of 1.5 (sample B1) and 4.5 (sample B2) are observed. Nevertheless, the shunt increases under illumination while the series resistance increases. The differences between the illuminated and the dark case indicate the presence of one or more light dependent conduction paths. For instance, CdS is known to be photoconductive [182] and may open an additional shunt path under illumination. Another possible explanation might be an electron barrier due to a high density of acceptors in the absorber's near surface [35]. The negative charge at the acceptor states may form an electron barrier in the dark. Under illumination, when the absorber acceptors are filled with holes, which are photogenerated in the buffer. This leads to a reduction of the acceptor charge and therefore to a lower electron barrier [35, 179]. This effect may explain an illumination dependent series resistance.
The temperature dependence of the series resistance $R_{s,illu}$ under illumination is shown in figure 4.15b. $R_{s,illu}$ was obtained from the implicit fit explained in the beginning of section 4.5, which is why the values cover different temperature ranges. Due to the kink, which is more pronounced at low temperatures, a reliable evaluation was not possible below a certain temperature.
While the lowest copper content (sample A) exhibits almost constant values below 2 Ωcm^2 within the whole temperature range, the other samples show a slight increase with a decreasing temperature. For the increasing resistances, one can conclude, that a temperature activated barrier is present. An increasing potential barrier, e.g. an electron barrier in the conduction band, can explain an increasing series resistance. Nevertheless, device A does not show the presence of such a barrier.

4.6.3. Diode factor

Next, the diode parameter can reveal further information about the device. The diode factor was determined as described above (beginning of section 4.5) and is shown in figure 4.16a for the dark and in 4.16b for the illuminated case. First, the diode factor is very high, since for decent devices it is found to be $1 < A \lesssim 2$.
The reason was explained in the beginning of this section and is related to the choice of the fitting limits due to the kink, which is particularly visible at lower temperatures for the samples B1 (figure 4.12b) and B2 (figure 4.13b) under illumination. As described above, the region where the kink is pronounced was not considered when fitting the diode equation to the measured data (for samples A, B2, and C). Since the kink is especially pronounced in sample B1, leaving out the involved voltage range hampered the fit. There-

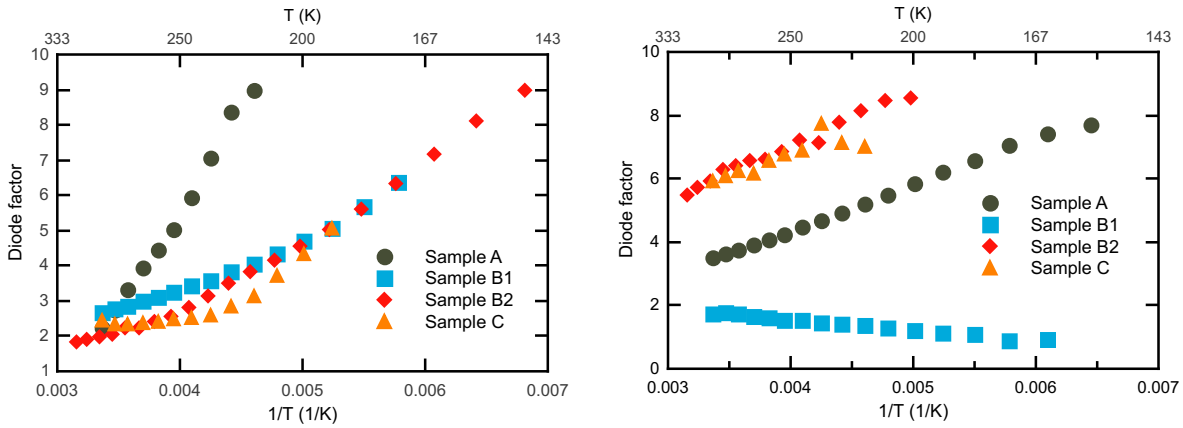

(a) Dark (b) Illuminated

Figure 4.16.: ***Temperature dependence of the diode factor*** *- The diode factor in dependence of the inverse of the temperature is shown. If a diode is dominated by tunneling processes, a straight line is expected in this plot.*

fore, for sample B1 the fit limits where adjusted according to the kink, as shown in the blue curve in figure 4.9 As pointed out above, regardless of the fitting process (adjusting the limits or leaving out the data around the kink), the trends remain the same. Due to the differently pronounced kinks at low temperatures, the diode factors are plotted down to different temperatures for the different samples.
Because of the different fitting ranges for sample B1, the diode factors in figure 4.16b are lower ($A < 2$), when compared to the other samples ($A > 3$). It is to mention, that the values for the samples A, B2, and C are in any case above 2, as exemplary shown in figure 4.9a leading to a diode factor of $A = 3.2$ or $A = 2.6$. Except for sample B1, the diode factors above 2 indicate, that devices are dominated by tunnelling processes (section 2.6.4). The usefulness of plotting the inverse temperature and the diode factor was pointed out in section 2.6.4, since it allows conclusions about the tunnelling behaviour of a device as well. If the change of the diode factor can be extrapolated linearly (with a positive slope), the device is dominated by tunnelling processes. Excluding the cell B1, the other devices show a linear increase with the inverse of a decreasing temperature indicating dominating tunnelling processes. Interestingly, the samples with identical compositions (B1 and B2) differ from each other. While the record device B2 is dominated by tunnelling, the worse performing cell B1 is not.
In the dark, no sample showed the presence of a kink. Therefore, the diode factor of sample B1 is higher in the dark, when compared to the illuminated case (figure 4.16a). In the dark, all devices show a linear increase with an increasing inverse temperature. In combination with the generally high values of $A > 2$, all devices are dominated by tunnelling processes.

4.7. Quantum efficiency

Figure 4.17 depicts the QE spectra for the best performing cells. Photons with shorter wavelengths show an almost identical response of the device. This is not surprising, since this region is determined by the ZnO window layer and the CdS buffer layer which are comparable for all devices.

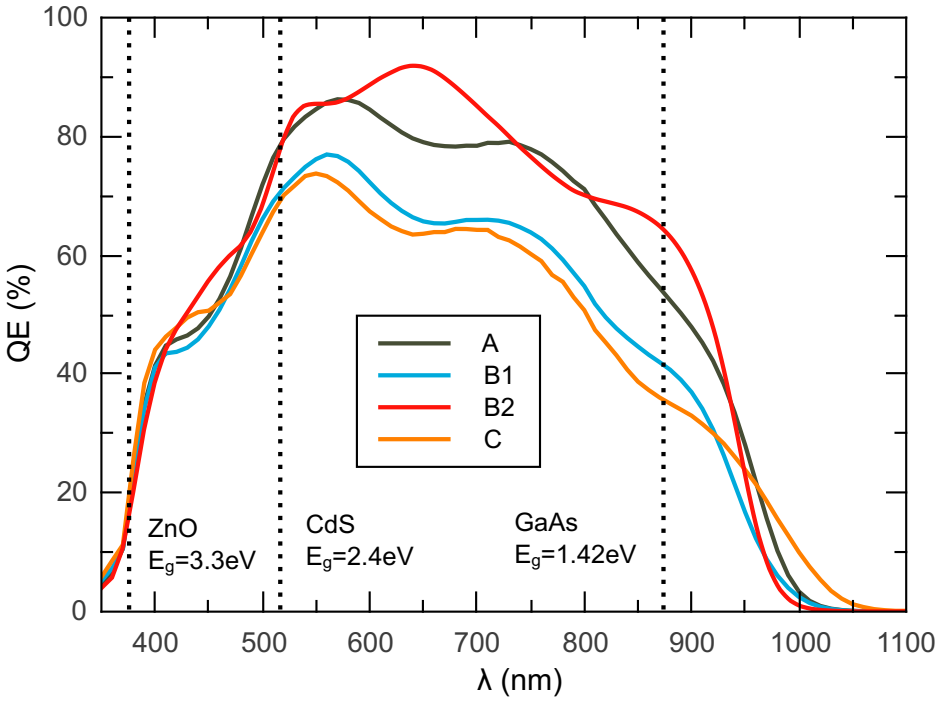

Figure 4.17.: ***Overview of QE measurement*** *- The QE spectra of the analysed samples.*

For increasing wavelengths, between the band gaps of ZnO and CdS, sample B2 (red curve) exhibits slightly higher values, which is most likely related to small deviations in the ZnO, since it was sputtered with a different system in Berlin. Thus, the difference of the red curve when compared to the others between $650 - 800$ nm is most likely related to a different interference behaviour of due to small deviations in the thickness. The shape of the other devices is qualitatively comparable. Only around the absorber's band gap the device with $[Ga]/([Ga] + [In]) = 0.44$ and $[Cu]/([Ga] + [In]) = 1.00$ (sample C) remains the exception. Here, the absorption edges is smeared out. The device with the highest conversion efficiency exhibits a sharp transition around the band gap and the highest EQE reaching values of 90% while the other sample's maxima reaches between 70% and 80%. This is expected, since the area below the curve is proportional to the photo current. The area correlates with the measured short circuit currents (table 4.2).

4.7.1. Band gap and collection length

EQE measurements are suitable to determine the band gap and the effective diffusion length as described in section 2.6.5. Equation (2.50) can be used to determine both values. Nevertheless, the equation requires the knowledge of the absorption coefficient α.

Thus, the EQE spectra were fitted using an optical model for α which was extrapolated from the absorption coefficient obtained from PL measurements at room temperature.

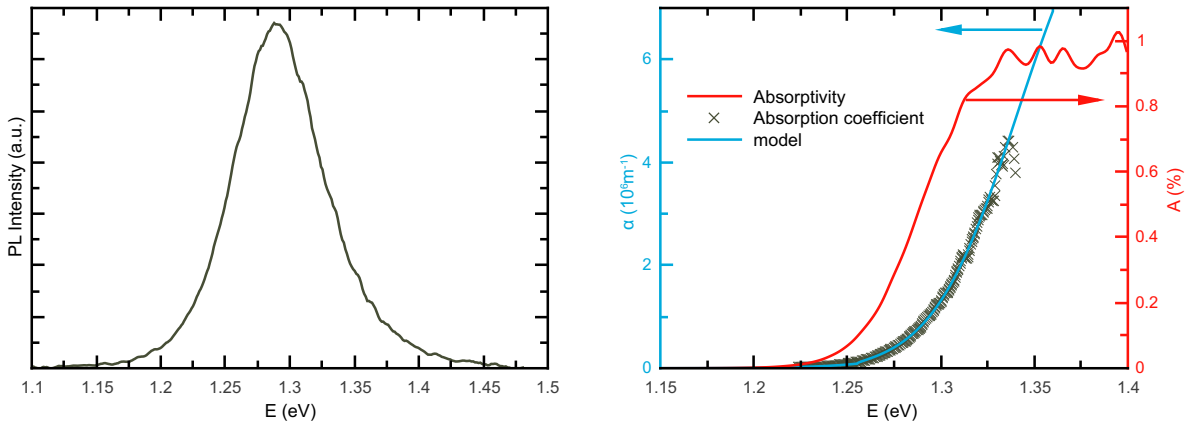

(a) PL spectra used to derive the absorption coefficient

(b) Extracted absorption coefficient

Figure 4.18.: ***Absorption coefficient for the evaluation of the EQE spectra*** *- The PL spectrum of an $CuIn_{1-x}Ga_xSe_2$ absorber with $x = 0.48$ (left) used to extract the absorptivity (right). The absorption coefficient was than fitted with an optical model taking the square root characteristics for band-to-band transitions into account and an exponential term to consider the Urbach tailing (equation (C.3)).*

Figure 4.18a shows the PL spectrum used to determine the absorptivity, which allows the calculation of the absorptivity and thus the absorption coefficient (section 2.5.4). The deduced absorption behaviour is shwon in figure 4.18b. Since no PL measurements at room temperature were available for the absorbers used for the discussed cells, an absorber with a comparable composition of [Ga]/([Ga] + [In]) = 0.48 was used. Figure 4.18b shows the extracted absorptivity and the calculated absorption coefficient using equation (2.12). The reflectivity was assumed to be $R_f = 0$ and the sample thickness d = 1.1 µm (determined from SEM measurements). The calculated absorption coefficient was then fitted with the optical model described in section C.2 (equation (C.3)) to determine the pre factors α_0, α_{Urbach}, the weeding parameter w and the E_0. Important is, that the parameters for an appropriate description of the absorption coefficient can be specified and used in equation (2.50) which describes the EQE spectra around the band gap. In principle, the band gap can be determined without knowing the exact parameters for α_0 and α_{Urbach}, since these parameters determine the steepness of the absorption coefficient curve. The band gap rather determines the position in terms of energy, where the absorption begins[5]. To estimate the effective collection length, the pre factors are important, since both, $\alpha_{0,\mathrm{Urbach}}$ and L_{e0ff} determine the steepness of the EQE (equation (2.46)). For the evaluation, the steepness determining parameters were kept constant and the band gap and the effective collection length were fitted. Thereby, the band gap and the effective collection length can be determined. The data and the respective models are depicted in figure 4.19. An increasing trend with an increasing [Ga]/([Ga] + [In]) ratio is observed: $E_g = 1.19$ eV for

[5]Alternatively, the band gap can be approximately easily by fitting a linear equation to the band gap region on the long wavelength side.

sample C, $E_g = 1.24$ eV for sample A, $E_g = 1.25$ eV for sample B1, and $E_g = 1.27$ eV for sample B2. The values compare reasonable with the excepted ones according to the dependence of the band gap on the [Ga]/([Ga] + [In]) ratio (table 4.4). The resulting effective collection lengths are ≈ 850 nm for sample B2, ≈ 540 nm for sample A, ≈ 400 nm for sample B1, and ≈ 270 nm for sample C. For polycrystalline Cu-poor $CuInSe_2$, the lengths are in the range of ≈ 2 µm [141]. A summary of the band gap and the collection lengths is given in table 4.4.

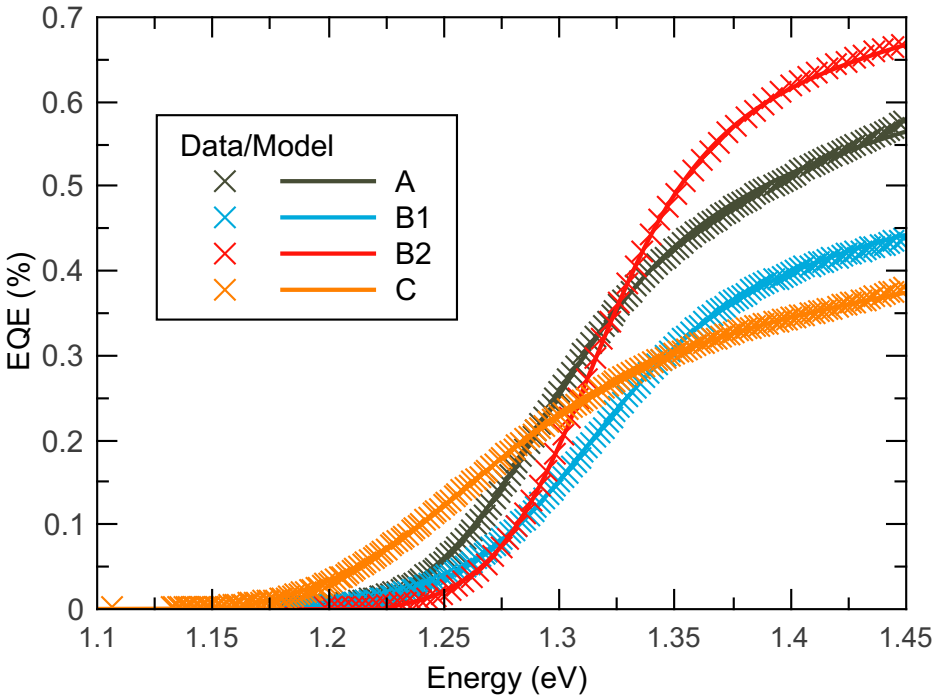

Figure 4.19.: ***Band gap determination from the QE measurement*** *- Data (symbols) and the fitted model (solid lines) according to equation* (2.50) *and* (C.3)*. The determined band gaps are summarized in table 4.4.*

Sample	CGI/GGI	$E_{g,calc}$ [a]	$E_{g,QE}$	$E_{act,IVT}$	L_{eff} (nm)
A	0.94/0.45	1.26	1.24	0.76	540
B1	0.98/0.48	1.28	1.25	0.72	400
B2	0.98/0.48	1.28	1.27	1.03	850
C	1.00/0.44	1.25	1.19	-	270

[a] Determined with the equation given in B.1.

Table 4.4.: ***Summary of solar cell parameters*** *- Summary of the determined band gap and the effective collection length from the EQE measurements (section 4.7). The activation energies were determined by the temperature dependence of the V_{OC} (section4.6.1).*

4.7.2. Bias dependence

Information about an incomplete carrier collection can be gathered by a voltage dependent EQE measurement. Minority carriers generated in the absorber can only be collected if the generation takes place within a distance of $L_{n,a} + w_a(V)$ where $L_{n,a}$ is the diffusion length of electrons in the absorber and w_a the voltage dependent width of the space charge region (section 2.6.5). If the distance is greater, not all minority carriers can be collected and an incomplete collection is observed.
An applied reverse bias can increase the space charge region and more charge carriers can be collected. The bias dependent EQE measurements for the samples B1 and B2 with an identical composition are depicted in figure 4.20a and 4.20b, sample A in 4.21a, and figure 4.21b shows sample C. The top part in the graphs shows the EQE responds for different bias conditions. The bottom plot illustrates the relative change of these spectra compared to the measurement without bias.

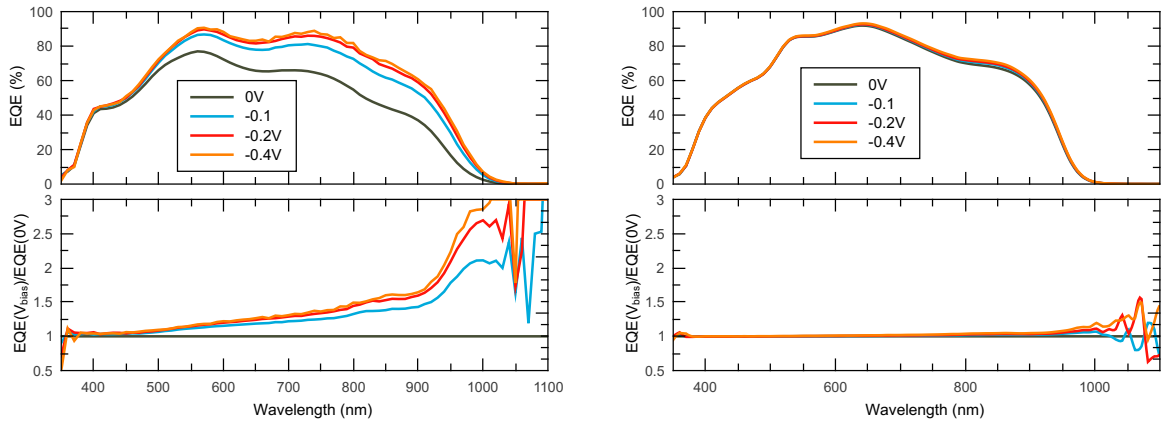

(a) Sample B1 (b) Sample B2

Figure 4.20.: ***Bias dependent EQE for sample B1 and B2*** *- The bias dependent EQE for the samples with an identical composition with [Ga]/([Ga] + [In]) = 0.48 and [Cu]/([Ga] + [In]) = 0.98. In the top the EQE spectra measured for different reverse bias conditions and shown. The bottom illustrates the relative change of different biases compared to the spectra measured without bias.*

Interestingly, the samples B1 and B2 with an identical composition show a very different responds to the revere bias. While the best performing sample B2 does not show significant changes within the whole spectral range, B1 exhibits differences starting below the band gap of the CdS (≈ 500 nm) and increases to a factor of 1.5 in the region of the band gap of GaAs. The highest change - up to 2.5 times more - is observed for higher wavelength, where the absorber dominates the collection. This is expected, since the reverse bias increases the SCR. Therefore, it has the strongest effect on the charge carrier generation towards the back of absorber. Thus, device B1 suffers from an incomplete charge carrier collection either due to small SCR and/or a short diffusion length.
On the other hand, sample B2 shows only minor changes within the whole spectral region. One explanation for this characteristic is fully depleted absorber layer which does not exhibit a SCR (the voltage dependent capacitance measurements in section 4.8 indicate a

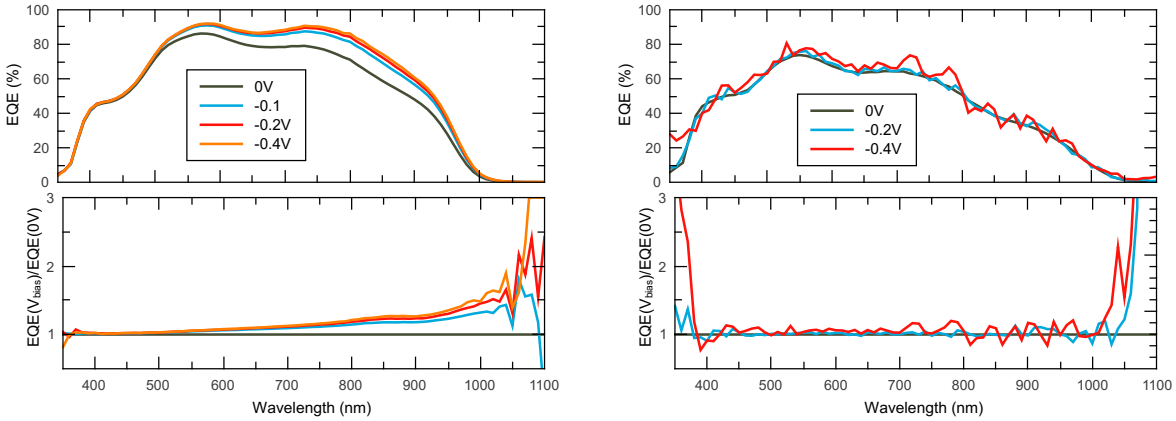

(a) Sample A with [Ga]/([Ga]+[In]) = 0.45 and [Cu]/([Ga]+[In]) = 0.94.

(b) Sample C with [Ga]/([Ga]+[In]) = 0.44 and [Cu]/([Ga]+[In]) = 1.0.

Figure 4.21.: *Bias dependent EQE for sample A and C* *- In the top the EQE spectra measured for different reverse bias conditions and shown. The bottom illustrates the relative change of different biases compared to the spectra measured without bias.*

depleted absorber). For a fully depleted absorber, the electrical field through the whole layer is present and the charge separation of electrons and holes is possible within the whole layer. An applied reverse bias, does not change the electrical field significantly and no change in the effective collection length is expected.
The differences between sample B1 and B2 are in agreement with the different short circuit currents under illumination of 25 $\frac{\text{mA}}{\text{cm}^2}$ for sample B1 and 30 $\frac{\text{mA}}{\text{cm}^2}$ for sample B2 (table 4.2). According to equation (2.47), the photo current is proportional to the integral of the product of the EQE and the photon flux. Since the of the EQE of sample B2 has a bigger area, a higher photo current is expected.
The voltage dependent change of the EQE of sample A (figure 4.21a) exhibits also a voltage dependent current collection albeit less pronounced than sample B1. Again, this indicates an incomplete charge carrier collection within the device.
Device C (figure 4.21b) does not show a voltage dependent change in the EQE. The comparison with the C-V measurements (appendix 4.8) suggest, similar to device B2, a fully depleted absorber layer. However, the carrier collection is much worse compared to the other devices and shorter than the device thickness. The unusual behaviour in the temperature dependent IV measurements already suggested, that this device does not behave like a typical Cu(In,Ga)Se_2 device with a reasonable quality. Thus, the interpretation of the results are very difficult.

4.8. Voltage dependent capacitance measurement

The set-up used for the temperature dependent IV measurements (section 4.6) can be used to perform voltage dependent capacitance measurements without changing the contacts on the sample inside the cryostat. A LCR-bridge allows the measurement of the capacitance within a frequency range of 100Hz to 1MHz and an optional offset voltage. Thus, the set-up allows voltage and or frequency dependent measurments of the capaci-

tance. Admittance measurements (C-f) allow the determination of the density of defect states. The voltage dependent measurement (C-V) extents the possibilities to measure the spatial distribution of defects within a semiconductor. Although both techniques were applied to the devices, the evaluation was not possible. This is why the discussion in the following is limited to the C-V measurements.
By changing the external voltage, the determination of the defect concentration gets possible (section 2.6.6).

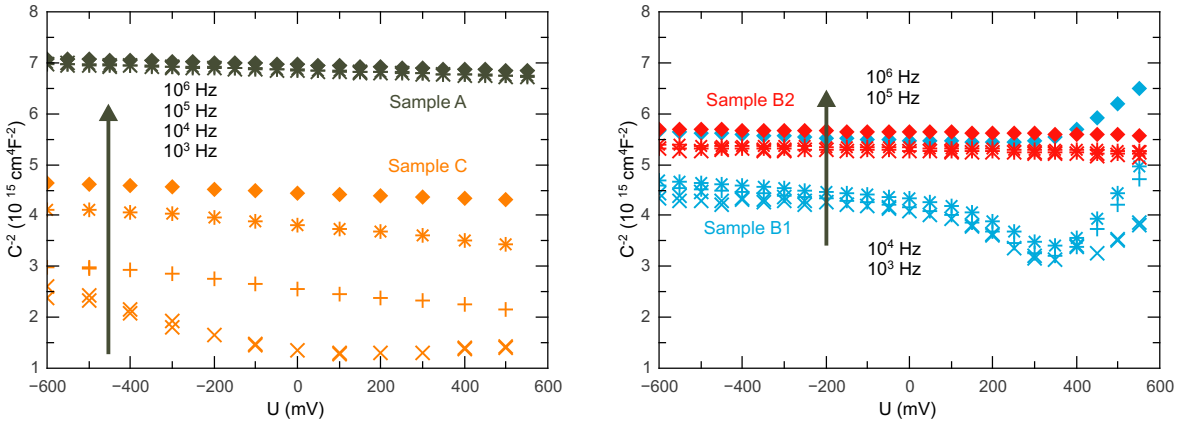

(a) CV profile of Cu-poor (grey) and Cu-rich (orange) composition

(b) CV profile of same composition. The red symbols represent the best performing cell.

Figure 4.22.: ***CV profile*** *- Capacitance in dependence of the applied voltage at 200K. The different colors represent the different samples, the symbols represent measurements with different AC frequencies as indicated in the plots.*

Unfortunately, the slope of the plots in figure 4.22a and 4.22b does not show a typical behaviour known from descent devices. When fitting a linear equation to the data, the intercept with the voltage axis should be the built in voltage of "normal" devices. For the present cells, the built in voltage extrapolates up to $10 - 30$ V, which is impossible. However, the very straight lines can be explained with a fully depleted absorber layer. An approximation of the expected capacitance for a fully depleted layer can be calculated using (2.52). With the dielectric constant of Cu(In,Ga)Se_2 ($\frac{\epsilon}{\epsilon_0} = 13.6$ [183]), an sample area of $A = 0.5\text{cm}^2$, and a width of $w_a = 1000$ nm it follows that $\frac{1}{(C/A)^2} = 6.9c10^{15}\frac{cm^2}{F^2}$. The value is very close to the measured values in figure 4.22. Therefore it is very likely, that the absorber layer is completely depleted.

4.9. Decreasing gallium content

After the interesting first results more absorber were grown. The aim was to decrease the copper and the gallium content to be more comparable to the composition of highly efficient polycrystalline cells [22]. The idea was, to achieve higher efficiencies by following the polycrystalline example: a Cu-poor grown absorber with [Ga]/([Ga] + [In]) ≈ 0.3. The IV curves of these absorbers are plotted in figure 4.23 and exhibit only a very poor

performance. The highest efficiency of 3.0%, with a V_{OC} of 275mVand a short circuit current of 25 $\frac{\text{mA}}{\text{cm}^2}$ was observed. The other absorbers show significantly smaller V_{OC} and accordingly efficiencies below 1%.
One absorber with a [Ga]/([Ga] + [In]) = 0.45 was produced together with the freshly grown absorbers and showed a comparable high efficiency of 6.1%. Thus, neither the CdS nor the ZnO deposition seems to be problematic and the poor performance is more likely related to a low absorber quality. Unfortunately, no further measurements are available to address the problem more in detail.

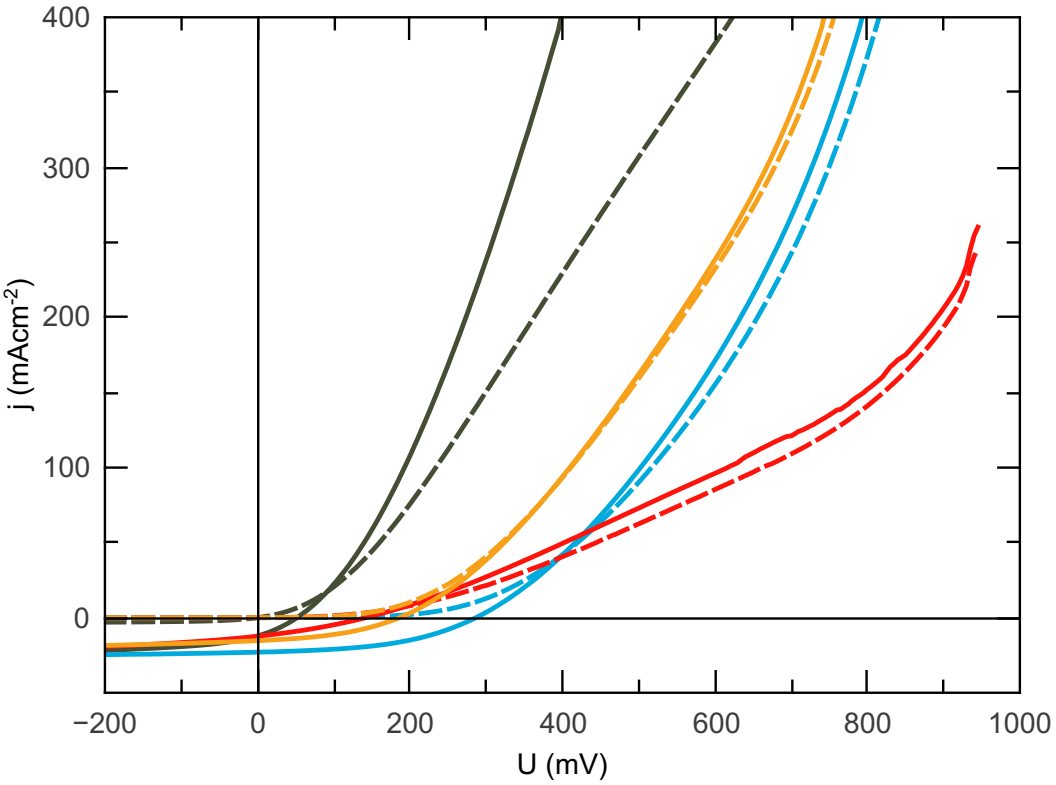

Figure 4.23.: ***IV curves for lower gallium content*** *- Examples of IV curves with a decreasing gallium content. The is [Ga]/([Ga] + [In]) ≈ 0.3 and the copper content was varied. Nevertheless, no trends were observed.*

However, due to the lower GGI, the strain within the film is expected to be higher, compared to a GGI around 0.5 (section 2.2). To release the stress, the formation of dislocation gets more likely and more defects are expected for the GGI of 0.3 coming along with a shorter lifetime for the minority carriers and worse transport properties.

4.10. Simulation

The highest reported efficiency for epitaxial Cu(In,Ga)Se_2 solar cells reach 8.5% for material grown on GaAs (111) and 7.3% for a substrate orientation of (001) [7]. The highest efficiency of $\eta = 6.7\%$ for the epitaxial devices grown on GaAs (0001) in this work (section 4.4) differs only by 0.6% compared to the substrate orientation of (100) used in the record device in literature.
Nevertheless, the efficiencies do not compare to the current polycrystalline record devices showing conversion efficiencies of 20.8% [2]. A fundamental difference is the lack of sodium, when growing the epitaxial devices. The presence of Na, either due to diffusion from the soda lime glass substrate or by an additional Na source, is known to increase the device efficiencies drastically by improving the V_{OC} and the fill factor [164, 165].
However, the first photovoltaic device based on $CuInSe_2$ single crystals did not contain Na and reached a power conversion efficiency of 12% [1] proving that efficiencies above 10% are possible even without Na. In contrast to the solar cells produced by Shay [1] who used a zone-refining technique[6], the later work concentrates on epitaxial Cu(In,Ga)Se_2 grown on a substrate. Here, the absorber is typically grown on GaAs using molecular beam epitaxy [166] or metal organic chemical vapour deposition [7, 11]. To clarify, whether the additional GaAs layer required for the growth process may hamper the performance of these devices, the device simulation program SCAPS [139] (version 3.2.01) was used to simulate the structure with the additional GaAs layer.

4.10.1. Band structure

The basis of any simulation is the definition of the band structure. The crucial properties are the conduction and valence band offsets between two layers of different materials. In SCAPS, the electron affinity has to be adjusted such, that the offsets of the conduction bands correspond to the measured or calculated offsets (see section 2.6.7). The valence band offset is than calculated by means of the respective band gap energies (equation (2.2)).
The valence band offset between GaAs and $CuGaSe_2$ is between -0.4 eV and $+0.1$ eV (table 2.2). For the following discussion of the band structure for Cu(In,Ga)Se_2 on top of GaAs, the electron affinity was tuned such, that the valence band offset is zero. As shown later, the simulated device properties differ only slightly for any valence band offset between $\Delta E_{VB} = \pm 0.4$.
To determine the electron affinity in dependence of the GGI, the valence band maximum was assumed to be independent of the composition [40]. This approximation is valid, since the change of the VB offset $\Delta E_{CB} = 0.7$ eV is much more pronounce compared to $\Delta E_{VB} = 0.04$ eV for the VB offset when comparing the offsets between $CuInSe_2$ and $CuGaSe_2$ [40]. Thus, only the electron affinity has to be adjusted and was calculated according to the band gap energy of the specific composition. The band gap of $CuIn_{1-x}Ga_xSe_2$ in dependence of x is known (section 2.1.2) and was calculated by a quadratic equation given in table B.1 [41]. Therefore, the electron affinity in dependence

[6] To purify the single crystal, a narrow region within the crystal is molten. By pulling the crystal though the heater, the molten zone moves along the crystal. The principle can be used to produce crack free single crystals with a very high purity and quality.

of the composition x can be calculated with

$$\chi(x) = 4.1 + 1.688 - E_g(x) - 0.26 \tag{4.2}$$

where 4.1 is the electron affinity of GaAs, $E_g(x)$ the band gap, and the -0.26 shifts the affinity such, that the valence band offset to the GaAs is zero. The conduction band offset between Cu(In,Ga)Se_2 and the buffer layer was adjusted such, that it is zero for [Ga]/([Ga] + [In]) = 0.3. Further material properties necessary for the simulations are summarized in table 4.5.
The thickness for the Cu(In,Ga)Se_2 was set to 1 µm since the epitaxial films grown in this work were approximately in this range. The used GaAs has a thickness of $d = 0.5$mm. Nevertheless, for the simulation the thickness of the GaAs was assumed to be 1 µm as well, because SCAPS tends to show convergence failures for thicker layers especially for low x values. A stepwise increase in the thickness of the GaAs layer did not change the results, so that the smaller thickness compared to the real substrate does not hamper the discussion.

		$CuIn_{1-x}Ga_xSe_2$ for x						
	GaAs	0	0.3	0.7	1	CdS [a]	i-ZnO [a]	ZnO [a]
χ (eV)	4.1	4.48	4.34	4.08	3.8	4.34	4.55	4.55
E_g (eV)	1.42	1.03	1.17	1.44	1.68	2.4	3.3	3.4
d (µm)	1.0	1.0				0.05	0.05	0.2
ϵ/ϵ_0	12.9	13.6				10	9	9
N_C (cm^{-3})	4.7e17	7.0e17				4e18	4e18	4e18
N_V (cm^{-3})	7.0e18	1.5e19				9e18	9e18	9e18
N_D (cm^{-3})	0	0				4e15	1e18	1e18
N_A (cm^{-3})	1e18	1e16				0	0	0
V_n (cm/s)	1e7	1e7				1e7	1e7	1e7
V_p (cm/s)	1e7	1e7				1e7	1e7	1e7
μ_n ($cm^2/(Vs)$)	800	20				20	20	20
μ_p ($cm^2/(Vs)$)	400	20				20	20	20
E_{defect} (eV)	-	0.515	0.585	0.72	0.845	1.2	1.65	1.7
Type	-	A				D	D	D
N_d (cm^{-3})	-	$5.0x10^{12}$				$1x10^{15}$	$1x10^{18}$	$1x10^{16}$
σ_n (cm/s)	-	$1.0x10^{-13}$				$1x10^{-15}$	$1x10^{-15}$	$1x10^{-15}$
σ_p (cm/s)	-	$1.0x10^{-15}$				$1x10^{-12}$	$1x10^{-12}$	$1x10^{-12}$
α_0 ($10^4$1/cm)	SCAPS	0.98	0.84	0.79	0.84	SCAPS	SCAPS	SCAPS
α_1 ($10^3$1/cm)	-	6.04	6.33	5.35	3.59	-	-	-
E_1 (eV)	-	1.574	1.546	1.621	1.762	-	-	-
B_1 (eV)	-	0.364	0.406	0.403	0.357	-	-	-

[a] Data from [35]

Table 4.5.: *Parameter used for the simulation* - *A summary of the electrical and optical properties used for the simulations.*

Figure 4.24 shows the simulated band structure in the dark for $CuIn_{1-x}Ga_xSe_2$. The top shows the ternaries $CuInSe_2$ (left) and $CuGaSe_2$ (right). The figures in the bottom illustrate the situation for $CuIn_{1-x}Ga_xSe_2$ with $x = 0.3$ (left) and $x = 0.7$ (right). The grey lines describe the conduction band maximum (CBM) and the valence band maximum (VBM), the red line the Fermi level, and the dashed orange line the mid gap defect in dependence of the position. The character of the mid gap defect and the electrical properties follow table 8.4 in [35] and are summarized in table 4.5.
According to the choice of the electron affinity, the valence band maximum (VBM) does not exhibit a discontinuity when going from the GaAs to the absorber layer for any composition x. The slightly higher energy level on the GaAs side is related to the bigger shallow acceptor density of $N_A = 10^{18}\text{cm}^{-3}$ (taken from the data sheet of the bought GaAs wafer) compared to $N_{A,\mathbf{abs}} = 10^{16}\text{cm}^{-3}$ for the absorber layer.
The CBM of the $Cu(In,Ga)Se_2$ increases with an increasing x. For $x \lesssim 0.7$ the conduction band offset decreases and changes its character from a cliff ($\Delta E_{CB} < 0$) to a spike ($\Delta E_{CB} > 0$) for higher compositions. The second difference is the interface to the CdS which forms a spike for $[Ga]/([Ga] + [In]) < 3$ and a cliff for larger band gap energies. The simulated IV and QE curves are discussed in the next section.

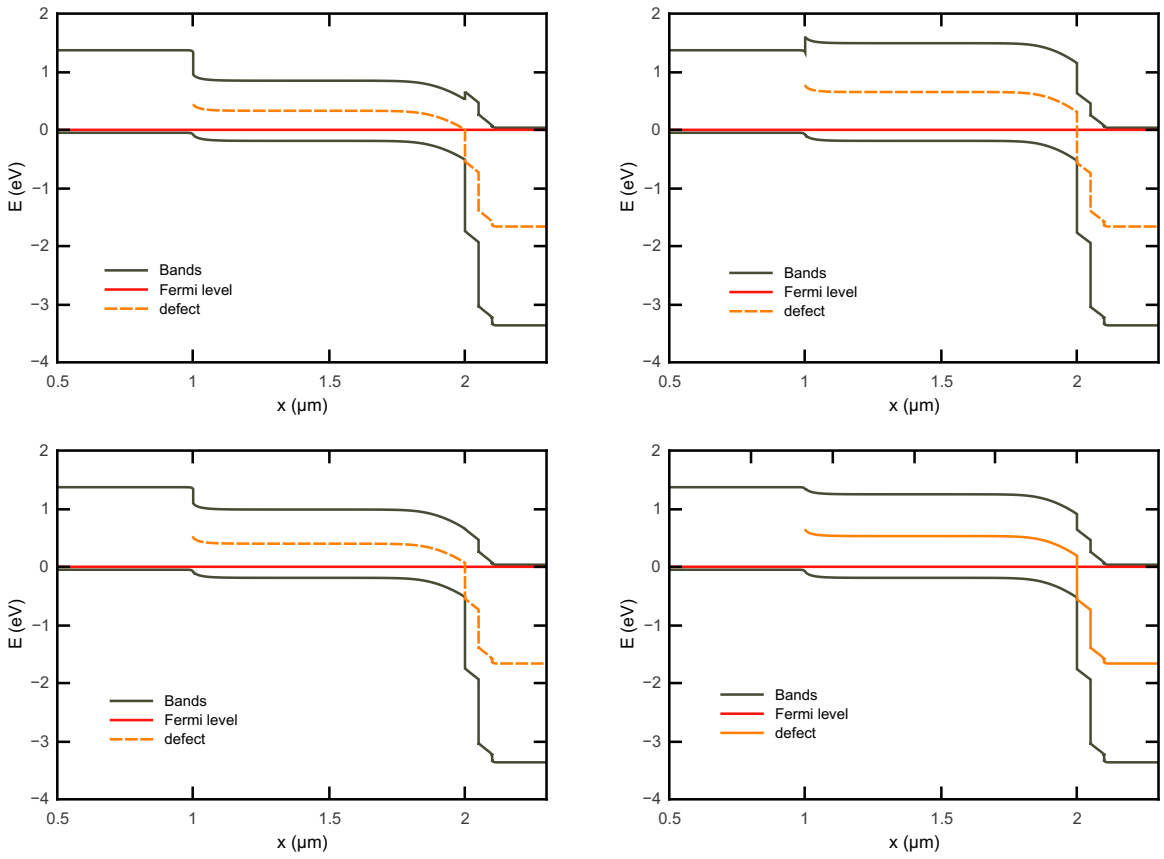

Figure 4.24.: ***Simulated band structure for $CuIn_{1-x}Ga_xSe_2$*** *- Simulated band structure in the dark for $CuIn_{1-x}Ga_xSe_2$. Depicted are the situations for $x = 0$ (top left), $x = 1$ (top right), $x = 0.3$ (bottom left), and $x = 0.3$ (bottom right).*

4.10.2. Simulated IV curves

To simulate the parameter solar cell parameter, the optical parameters have to be defined. For the GaAs, the CdS, and the ZnO layers, the default spectra in SCAPS were used. For the absorber layer, the optical properties were calculated using equation (2.17) to describe the band gap region (the square root) of the absorption coefficient and the shape for higher energies with the exponential function (as described in section 2.4.1 and plotted in figure 2.13). To calculate the composition dependence of the parameters α_0, α_1, $B1$, and $E1$, the literature values in [35] were fitted with a quadratic equation (see table B.1). The values used in the following simulations are given in table 4.5. Note, that the values were calculated and small deviations from the measured ones may occur, e.g. $\alpha_{1,\mathrm{calc}} = 6.04e3\mathrm{cm}^{-1}$ compared to the literature value $\alpha_{1,\mathrm{measured}} = 6.01e3\mathrm{cm}^{-1}$ for $x = 0$. To take the reflection losses into account, the reflectivity of a CdS/i-ZnO/ZnO layer was used. Therefore, CdS was deposited on a glass substrate during the process used for the epitaxial devices and during the following deposition of the window layer. Afterwards, the glass witness was used to determine the transmission and the reflection behaviour of the buffer and the window layer. The optical measurements were performed with a commercially available UVVIS spectrometer by PerkinElmar. Although the growth process on glass is not directly comparable to the growth on epitaxial Cu(In,Ga)Se_2, it gives at least a realistic approximation to the transmission behaviour. In the simulation, the reflection spectrum was accounted for in the optical properties of the front contact.

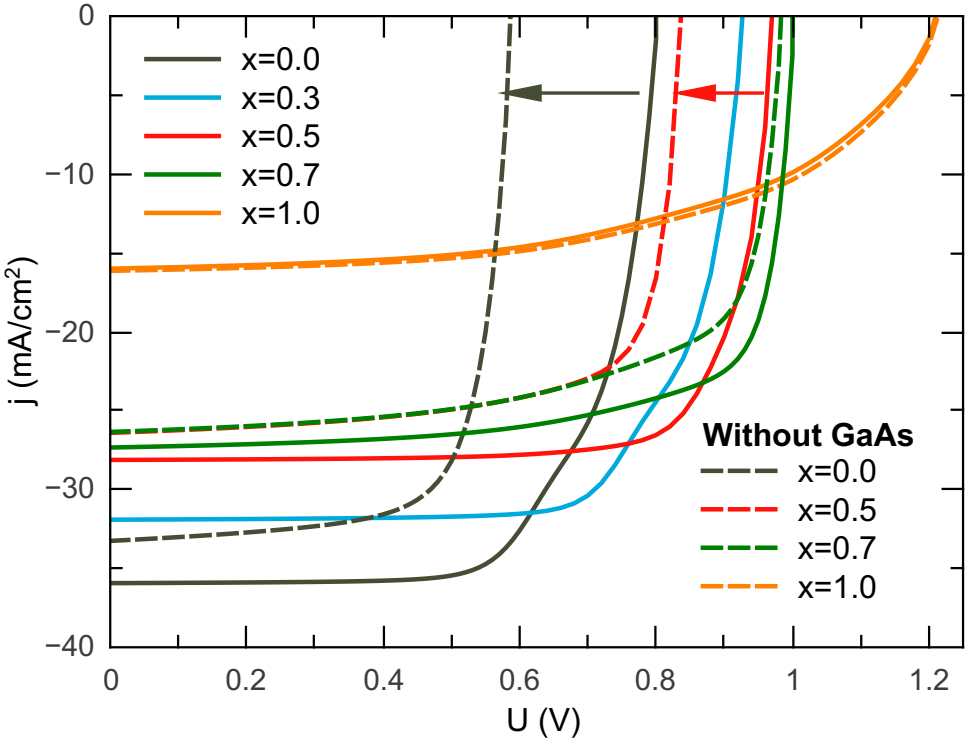

Figure 4.25.: ***Simulated IV curves*** *- Simulated IV curves for $CuIn_{1-x}Ga_xSe_2$ with x=0 (grey), 0.3 (red), 0.5 (blue), and 1.0 (orange) on top of GaAs . The dashed lines were simulations without the GaAs and represent the polycrystalline case directly grown on the back contact.*

Figure 4.25 shows the simulated IV curves at room temperature under illumination using the AM1.5g spectrum included in SCAPS. The solid lines represent the curves for $x = 0$ (grey), $x = 0.3$ (blue), $x = 0.5$ (red), $x = 0.7$ (green), and $x = 1$ (orange). For $x < 0.5$ a kink visible between 0.6V and 0.8V is observed, which disappears for $x > 0.5$. To compare the simulation with solar cells without the additional substrate, the GaAs layer was removed and the simulation was repeated. Exemplary, the simulated curves for $x = 0$, $x = 0.5$, $x = 0.7$, and $x = 1$ are also depicted in figure 4.25 (the dashed lines). While the IV characteristic for $CuGaSe_2$ is comparable for with and without the additional GaAs layer, it differs for smaller values of x. With an decreasing x, the difference gets more pronounced and is visible in the solar cell parameters (table 4.6). As visible in figure 4.25, the difference in the open circuit voltage increases with a decreasing [Ga]/([Ga] + [In]) ratio. Likewise, the difference in the short circuit current increases ($\Delta J_{sc}(x = 0) = 2.63 mA/cm^2$ and $\Delta J_{sc}(x = 0.5) = 1.72 mA/cm^2$) with a decreasing [Ga]/([Ga] + [In]) ratio.

First of all, it can be pointed out, that the additional GaAs layer does not hamper the performance of epitaxial devices. Although the band offsets may be slightly different in reality, since additional effects such as strain (in the $Cu(In,Ga)Se_2$ layer) or slightly different surface compositions of the GaAs can modify the band offsets further. For instance, theoretical tight binding calculations applied to $CuGaSe_2$ predict, that strain can modify the band gap energy by a few 10 meV [43, 48]. An idea of the change due to the surface composition can be found in literature, investigating the valance band offset for ZnSe grown on GaAs [137]. It was shown, that the valance band offset depends on the Ga/As ratio. The VB offset is found to increase ≈ 0.12 eV when the surface composition increases from Ga/As=1.0 to 1.5. Nevertheless, the next section (4.10.3) will show, that an even more pronounced change in the band offsets will not hamper the device performance. Second, the appearance of the kink is related to the conduction band offset to the GaAs. As soon as the CB offset between the substrate and the absorber layer approaches zero and changes its character from a cliff to a spike like offset (compare the band structure in figure 4.24), the kink disappears. In other words, as soon as the band gap of the absorber is comparable or greater compared to the GaAs, the kink disappears. This effect is related with the absorber thickness, as shown in section 4.10.5.

x	V_{OC} (V)		J_{SC} (mA/cm^2)		η (%)		FF	
âĂć	GaAs	Without	GaAs	Without	GaAs	Without	GaAs	Without
0	0.802	0.584	35.89	33.26	19	14	67.4	72.0
0.3	0.928	0.721	31.91	29.72	21	16	72.0	76.0
0.5	0.971	0.838	28.13	26.41	21	16	78.1	73.6
0.7	1.003	0.985	27.34	26.35	20	17.6	73.9	67.8
1	1.213	1.216	16.00	16.14	10	11	53.8	55.0

Table 4.6.: ***Comparison of the solar cell parameter from the simulation with and without GaAs*** *- Comparison of the open circuit voltage, the short circuit current, the efficiency, and the fill factor gained from the simulation with and without GaAs .*

4.10.3. Influence of the conduction band offset

As discussed before, the values for the band offset between GaAs and Cu(In,Ga)Se_2 vary within the literature (section 2.6.7). To verify the influence of a possible different value, the band offsets for GaAs and Cu(In,Ga)Se_2 were varied. Therefore, the electron affinity of the GaAs was varied such, that the valence band offset to Cu(In,Ga)Se_2 was between -0.4 eV and $+0.4$ eV. All other properties were kept constant as summarized in table 4.5. The variation of only GaAs is valid, since the "flat band" option was used in any simulation. Flat band condition means, that a possible band bending at the metal/semiconductor interface is neglected. In this case, the work function of the metal is adjusted before the simulation by SCAPS to ensure flat bands at the interface.
The influence of the different band offsets on the simulated IV curves is depicted in figure 4.26 for $x = 0.0$, $x = 0.3$, and , $x = 0.7$. While the short circuit current does not change for $x < 0.5$ ($x = 0.5$ is not depicted), a small change of $\Delta J_{SC} = 1\ \frac{mA}{cm^2}$ is observed for $x > 0.5$. The V_{OC} for $x = 0$ exhibits almost no change. Small derivation are observed for $x = 0.3$ (10compared meV) and for $x = 0.7$ (20 meV). Due to the very small differences, it is justified to limit the discussion to a valence band offset of 0 eV for Cu(In,Ga)Se_2.
Although the VB offsets found in literature vary between at least -0.4 eV and $+0.1$ eV (table 2.2) it is to say, that the epitaxial devices with the additional GaAs layer are not hampered in any case.

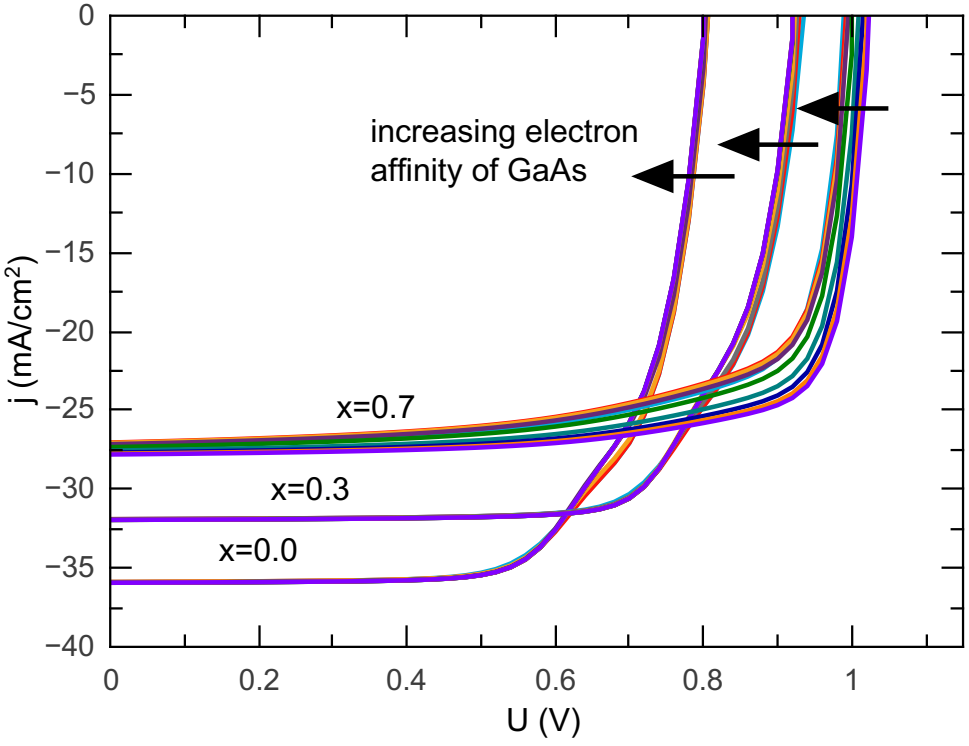

Figure 4.26.: ***Influence of the conduction band offset*** *- The simulated IV curves do not change significantly, if the conduction band offset between GaAs and Cu(In,Ga)Se_2 is varied between -0.4 eV and $+0.4$ eV. The simulated IV curves do not differ significantly for a composition of $x < 0.5$.*

4.10.4. Simulated QE curves

The simulated external quantum efficiency is depicted in figure 4.27. Again, the solid lines represent the solar cell with a GaAs layer and the dashed lines the case without. Similar to the IV curves, the EQE for $CuGaSe_2$ does not differ significantly for both cases. For a decreasing [Ga]/([Ga] + [In]) ratio the differences between with and without GaAs are especially pronounced within the band gap region indicating an effect due to the GaAs. The generally lower values for the simulation without GaAs can be explained with the small thickness of only 1 µm used in the simulation, which is not sufficient for an efficient absorption of all incident photons. Real polycrystalline solar cells are between $2 - 3$ µm thick and show higher values in the long wavelength region around the band gap. This indicates, that the additional GaAs layer acts as an extension of the $Cu(In,Ga)Se_2$ absorber layer, where additional e-h pairs can be generated, as discussed in the next section. The simulated QE does not show any difference when the band offsets between the GaAs and the $Cu(In,Ga)Se_2$ are changed, as described above (section 4.10.3).

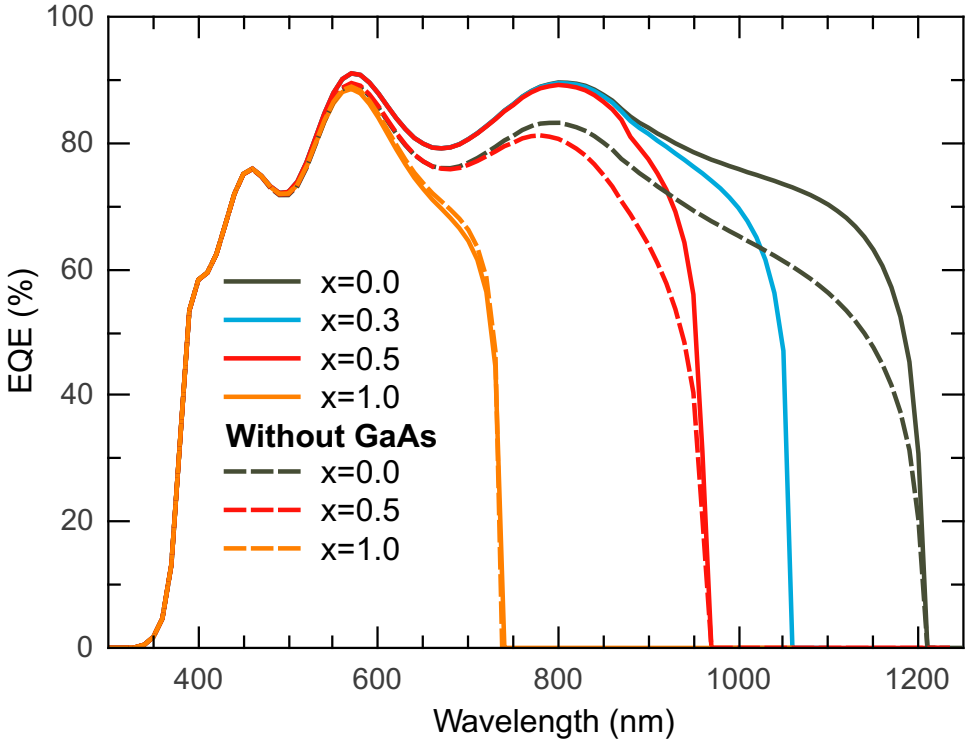

Figure 4.27.: *Simulated QE curves* - *Simulated IV curves for $CuIn_{1-x}Ga_xSe_2$ with x=0 (grey), 0.3 (red), 0.5 (blue), and 1.0 (orange) on top of GaAs. The dashed lines were simulations without the GaAs and represent the polycrystalline case directly grown on the back contact.*

4.10.5. Absorber thickness

Figure 4.28a shows exemplary the influence of the absorber thickness on the simulated EQE spectrum for $x = 0.3$. Compared are the cases with (blue) and without (dashed red line) GaAs. An increasing absorber thickness clearly increases the collection close to the band gap. The previously (figure 4.27) huge differences between with and without GaAs are significantly reduced. Nevertheless, the EQE for the case with GaAs also shows an additional increase even though it is less pronounced. This behaviour is expected, since the number of the absorbed photons increases with the sample thickness. More interesting is the comparison with the corresponding IV curves depicted in figure 4.28b. The dashed line compares again the case without GaAs for a thickness of 1 µm and 3 µm. With the thicker layer, an increase in V_{OC} and J_{SC} is observed. More interesting is the influence with an additional GaAs layer (solid line). While the short circuit current remains unchanged, the V_{OC} decreases closer to the case without GaAs. Additionally, the kink vanishes for an increasing absorber thickness. This indicates, that the GaAs acts as an increased absorber layer and the current beyond the V_{OC} of the devices without the substrate layer is related to the generation of e-h pairs within the GaAs. A further indication is the introduction of a defect at the interface between the substrate and the $Cu(In,Ga)Se_2$ layer.

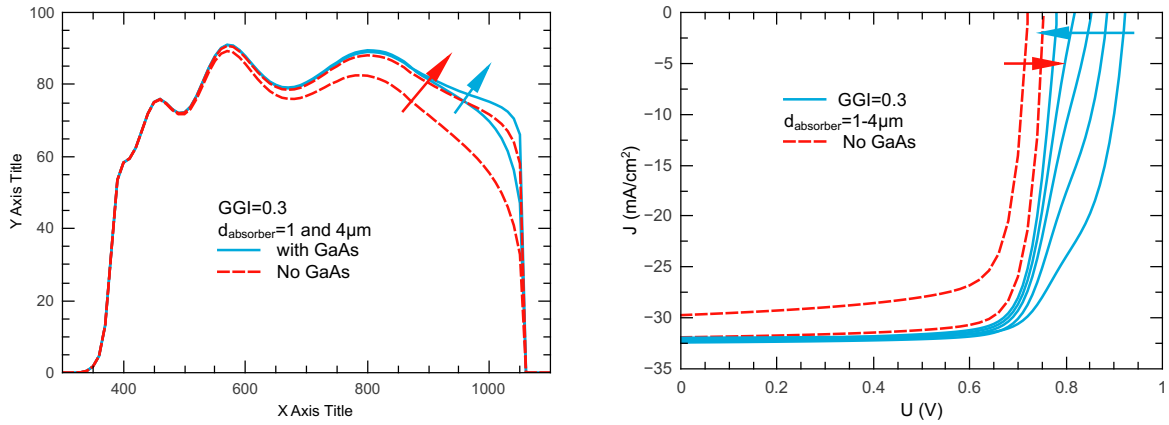

(a) Simulated QE curves for different absorber layer thickness.

(b) Simulated IV curves for different absorber layer thickness.

Figure 4.28.: ***Influence of the absorber thickness*** *- Simulated EQE and IV curves for an increasing thickness in the absorber layer for [Ga]/([Ga]+[In]) = 0.3 with and without GaAs . The arrows indicate the increasing thickness from 1 µm up to 4 µm.*

4.10.6. Influence of the interfaces

Figure 4.29 shows the influence of an additional defect state at the interface between the GaAs and the $Cu(In,Ga)Se_2$ layer with a varying capture cross section for electrons σ_e (blue). For comparison reasons, the same absorber layer without the GaAs substrate is depicted in the red dashed line. The device properties are again as summarized in table 4.5.

The defect type was chosen to be "neutral" with a single energy level 0.7 eV above the

VBM of the GaAs with a total defect density of 10^{12}cm^{-2} and a capture cross section for holes of $\sigma_e = 10^{-15}\text{cm}^2$. The capture cross section for electrons was changed from $\sigma_e = 10^{-20}\text{cm}^2$ to $\sigma_e = 10^{-10}\text{cm}^2$. With an increasing σ_e, the IV curves approach again the reverence curve without GaAs. At the same time, the kink vanishes for $\sigma_e \geq 10^{-17}\text{cm}^2$. The additional electrons created within the GaAs do no longer contribute to the current beyond the V_{OC} of the reference simulation without GaAs, since they recombine at the interface. Therefore, the kink is first suspressed and disappeares when the both curves (with and without GaAs) approach each other.

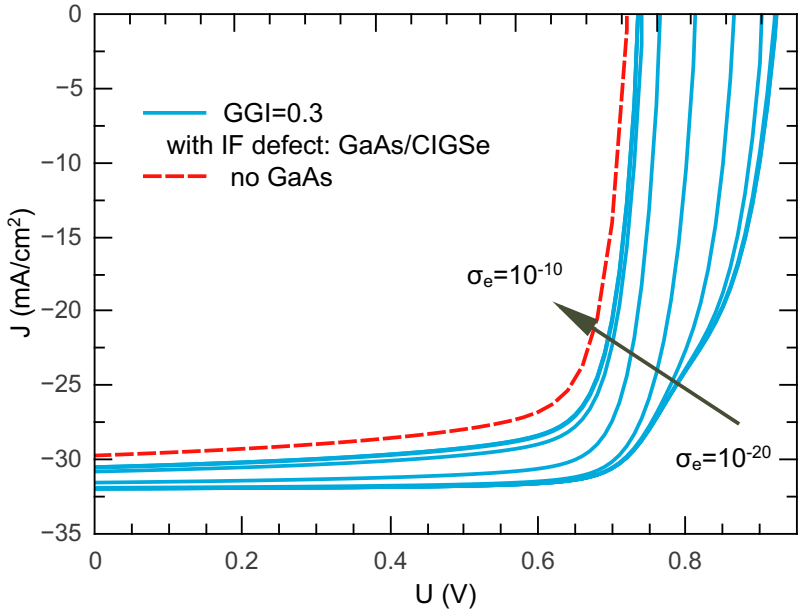

Figure 4.29.: ***Interface defect between GaAs and Cu(In,Ga)Se$_2$*** *- The presence of an interface defect can "decouple" the GaAs from the absorber. The observed kink disappears for an increasing capture cross section of the electrons (arrow). The red dashed line is the equivalent device without a GaAs layer.*

4.11. Summary and Outlook

4.11.1. Summary of the experimental part

For the first time, epitaxial Cu(In,Ga)Se$_2$ solar cells were produced in the home laboratory. The necessary steps were optimized for the epitaxial wafers and can be carried out with the available equipment in the laboratory. The highest efficiency of 6.7% with a V_{OC} of 0.5 V and a short circuit current of 31 $\frac{\text{mA}}{\text{cm}^2}$ showed, that reasonable epitaxial solar cells can now be produced in Luxembourg. It could be shown, that it is possible to produce devices with very acceptable resistances under illumination not hampering the device (compare table 4.4). The measured solar cell parameters are partly (V_{OC} and J_{SC}) even better than the record device, although the record efficiency of 7.3% (grown on the comparable substrate orientation of (001)) [7] is still slightly higher, compared to the cells

in this work.
The temperature dependent analysis of the IV characteristic revealed, that all devices within this work suffer from interface recombinations. Since the usage of a single crystal substrate cannot be avoided and an additional interface to the absorber is introduced. Therefore, a new source of interface recombinations is present. However, due to the minimized strain and an optimized interface between the GaAs and the $Cu(In,Ga)Se_2$, it is very likely, that the critical interface is between the absorber and the CdS buffer. This is most likely related to the relatively high gallium content, leading to a bigger cliff in the conduction band when going from the absorber to the buffer layer. This is not favourable for the solar cell and an increasing gallium content worsen the performance of the device [184].
Additionally, as seen in the bias dependent EQE measurements (section 4.7.2) and supported by the capacitance measurements (section 4.8) two cells were depleted, resulting in a solar cell with a p-i-n structure.
Although the shunt resistances are not responsible for the poor performance, two devices showed a decreased shunt resistance under illumination. Therefore, some illumination dependent shunt paths are present. Possible explanations are the presence of Cu_xSe or conducting dislocations within the absorber.
To decrease the interface recombination, the gallium content should be decreased. However, the decrease will lead to an increased strain and thus to more dislocations, leading to worse performing cells again. An alternative solution to overcome the predicament is given in the outlook in section 4.11.3.
From the obtained results, one cannot conclude, that the reason for the poor performance is the lack of grain boundaries in the epitaxial absorber.

4.11.2. Summary of the simulation

The simulations revealed, that the additional GaAs substrate layer which is necessary to grow epitaxial $Cu(In,Ga)Se_2$ does not hamper the device performance. Although the band offsets between the GaAs and $Cu(In,Ga)Se_2$ is not known exactly, it could be shown that any offset between -0.4 eV and $+0.4$ eV has only a minor effect on the device performance. The simulated IV curves showed the appearance of a kink, which is correlated with the band gap of the absorber material. As soon as E_g is close to the band gap of GaAs, the kink vanishes and the IV curves are comparable to a reference simulation without the additional GaAs layer ($x \approx 0.7$). The extinct kink for $x \lesssim 0.5$ is reduced for an increasing absorber thickness, leading to comparable IV curves, when compared to devices without GaAs. Then, the generation of minority carriers is limited to the $Cu(In,Ga)Se_2$ absorber. Furthermore, the presence of an interface defect between the GaAs and the $Cu(In,Ga)Se_2$ layer has a similar effect. With an increasing capture cross section of electrons, the kink disappears likewise. Both, the increasing thickness and the introduction of an interface defect lead to a "decoupling" of the substrate and the $Cu(In,Ga)Se_2$ absorber layer. Then, the solar cell shows a comparable performance than observed for simulations without GaAs.
The simulated QE curves reveal an influence of the GaAs layer for $x \lesssim 0.5$ as well, if the $Cu(In,Ga)Se_2$ thickness is not sufficient. An increasing absorber thickness leads obviously to an improvement in the collection behaviour and the absorption edge of GaAs is not

visible any more.
The simulation proved, that the epitaxial devices should not behave differently compared to the polycrystalline counter part, if the thickness is sufficient to absorb the incident light within the $Cu(In,Ga)Se_2$ layer.

4.11.3. Outlook

It is necessary, to produce much more samples to allow reliable conclusions about epitaxial devices. The focus should be an a broader range of compositions. Since the composition with $[Ga]/([Ga]+[In]) \approx 0.3$ is comparable to the best performing polycrystalline cells, it is worth to concentrate on the growth conditions between $[Ga]/([Ga]+[In])0-0.5$ and put more effort in Cu-poor devices. The process for compositions of $[Ga]/([Ga]+[In]) \approx 0.3$ may be further optimized by changing the temperature and/or by applying temperature profiles during the process.
To do so, the growth process should be examined more carefully, since the slight decrease in the gallium content lead to very badly performing cells. The optimization of the growth conditions might start with a series of different growth temperatures for varying $[Ga]/([Ga]+[In])$ -ratios. Furthermore, a temperature profile during the growth might further help to an improved crystal quality. Thereby, the influence of the selenium pressure should be studied more carefully. The optimized growth conditions at $[Ga]/([Ga]+[In]) = 0.5$ showed, that the selenium influences the absorber surface (section 4.2). Low selenium pressures seem to lead to the inclusion of polycrystalline material, while too high concentrations do not show the typical facet like structure on the surface (grown under copper poor conditions). The series should be checked with the XRD pattern providing information about the strain and defect densities. Furthermore, the doping densities should be studied directly on the bare absorber with the newly available Hall set-up. By doing so, the observed difficulties while performing C-V measurements can be avoided. Thereby, it is important to keep in mind, that the growth is slightly different, when grown on undoped GaAs, which is necessary to use, when performing Hall measurements.
Because of the very time consuming growth process of 8-12 hours for a film thickness of around 1 µm), it is advisable to limit the new runs within a certain range of GGI-ratios. Since the strain in the absorber increases for $[Ga]/([Ga]+[In]) < 0.4$, these GGI should be avoided in the beginning. On the other hand, to avoid problems at the interface to the CdS buffer for $[Ga]/([Ga]+[In]) > 0.4$, an epitaxial buffer layer should be deposited directly after the absorber layer to form two well defined interfaces to the substrate and to the buffer. As discussed before [136] ZnSe might be suitable for that and can be deposited in the MOVPE system right after the absorber layer. Additional measurements with a TEM system would help to optimize the interface to the buffer layer and can be additionally applied to the GaAs /$Cu(In,Ga)Se_2$ interface. Unfortunately, the ZnO layer cannot be deposited in the MOVPE system, since the usage of oxygen may lead to exothermic reactions in the other precursors. However, further investigations should also consider the usage of $Zn_{1-y}Mg_yO$ instead of the aluminium doped window, because of a tunable band gap which can be adjusted by changing the Mg content [185] and the conduction band offset can be more favourable for the device performance [186]. The band gap can be adjusted between $E_{g,y=0} = 3.3$ eV and $E_{g,y=1} = 7.7$ eV [185]. Therefore, the absorption

within the window layer can be slightly decreased. The conduction band offset between the $Cu(In,Ga)Se_2$ and the $Zn_{1-y}Mg_yO$ changes from a negative (cliff) to a positive (spike) one which is the reason for a probably improved performance.

CHAPTER

FIVE

SUMMARY

The aims of this thesis have been (1) to carry out absolute photoluminescence (PL) measurements which allows the comparison of different samples and (2) the growth and characterisation of epitaxial Cu(In,Ga)Se_2 solar cells. The growth is performed in the MOVPE system in the Laboratory for Photovoltaics in Luxembourg.

The available set-up at LPV was extended and optimized to allow absolute PL measurements. Calibrated PL measurements at room temperature are of interest, since they allow the determination of the quasi-Fermi level splitting inside the absorber layer, and the absorption characteristics near the band edge of a semiconductor. The quasi-Fermi level splitting constitutes an upper limit for the maximum achievable open circuit voltage in a solar cell by only measuring the absorber without having finished the device. Thus, the quasi-Fermi level splitting is interpreted as a measure of the absorber's quality.

The growth of epitaxial Cu(In,Ga)Se_2 is important, since the material does not contain any grain boundaries and is suitable to study fundamental properties of the absorber. Although it was possible to produce epitaxial Cu(In,Ga)Se_2 absorbers with a high quality before, the solar cells show only poor performances. While polycrystalline samples reach energy conversion efficiencies above 20% [2], the epitaxial counterpart reached values below 10% [7, 11]. This is astonishing, since epitaxial material usually exhibits better electrical properties, when compared to the polycrystalline material. To clarify this discrepancy in the device performance the established recipes at LPV for the growth of epitaxial $CuInSe_2$ and $CuGaSe_2$ are optimized to grow $CuIn_{1-x}Ga_xSe_2$ samples with a varying gallium content in the home lab in Luxembourg. Additionally, a route to finish epitaxial devices is established allowing the production of solar cells.

The quasi-Fermi level splitting in $CuInSe_2$

The calibrated set-up allowing the absolute measurements of emitted photons is used to compare epitaxial and polycrystalline $CuInSe_2$ material. The comparison is based on the quasi-Fermi level splitting, the band gap, and the Urbach energy. The series of analysed epitaxial and polycrystalline absorbers cover different [Cu]/[In] ratios and were grown under Cu-poor and Cu-rich conditions. All polycrystalline samples are grown in the home laboratory by a coevaporation process in a vacuum chamber. The epitaxial devices are grown with the MOVPE system.

The comparison of Cu-poor and Cu-rich absorbers reveals higher quasi-Fermi level splitting for the material grown under Cu-rich conditions. Both, epitaxial and polycrystalline absorbers, show a difference of ≈ 150 eV. However, a comparison between the epitaxial and the polycrystalline material shows, that the epitaxial absorbers exhibit generally higher values between $50 - 100$ eV. This indicates that the material quality in the epitaxial case is indeed higher. The worse performance in solar cell devices is not due to inferior quality of the absorber. Indeed, since the quasi-Fermi level splitting is a measure for the maximum achievable open circuit voltage, the device should reach reasonable values for the V_{OC}.

PL measurements at room temperature provide a powerful tool to determine the absorption behaviour near the band gap. The strength of this technique is the measurement of an emission spectrum instead of measuring the absorption spectra directly. The detection of a very low photon flux emitted from a semiconductor is much easier, than the detection of absorbed photons with conventional methods. The absorption spectrum of $CuInSe_2$ was deduced from the PL measurements and used to analyse the dependence of the band gap and the Urbach energy on the [Cu]/[In] ratio.

The band gap of $CuInSe_2$ has been investigated before (e.g. [41, 146]). However, a detailed investigation over a large range of composition extending into the Cu-poor region has never been done before. The determined values of $E_g = 1.02$ eV within this work for the Cu-rich absorbers are in agreement with the previously reported value [41, 146]. The PL measurements revealed, that the band gap decreases linearly with a decreasing [Cu]/[In] ratio below the stoichiometric point. For a composition of [Cu]/[In] = 0.9 a value of $E_g = 0.97$ eV is observed for the polycrystalline absorbers. Most likely because of a slightly strained films, the epitaxial films exhibit slightly higher values of $E_g \leq 1$ eV. It was shown, that in $CuInSe_2$ a clear distinction between the absorption behaviour due to band-to-band transitions and due to an Urbach tailing is possible.

The Urbach energy in dependence of the [Cu]/[In] ratio of $CuInSe_2$ single crystals grown by a freezing method were reported before [104]. Nevertheless, for epitaxial films grown on GaAs, no data are found in literature. Additionally, a direct comparison between epitaxial and polycrystalline material was missing. The determined values of and their dependence on the [Cu]/[In] ratio are in excellent agreement with the reported values measured on the single crystals [104]. The determined value of $E_U = 9$ meV on the Cu-rich side is identical to the value measured on epitaxial samples in this work. Similar to the band gap, the Urbach energy is independent for compositions above the stoichiometric point. However, a linear increase is observed for a decreasing [Cu]/[In] ratio reaching a value of $E_U = \approx 14$ meV for [Cu]/[In] = 0.8. The measured polycrystalline absorbers show an identical trend with slightly higher values in the order of $\Delta E_U = 2$ meV. The lower E_U for the Cu-rich material indicates a lower defect density within the crystal.

Degradation of $CuInSe_2$

While pushing the lab efficiencies beyond 20%, the optimization of each production process was beneficial. By minimizing the time between each step, the performance was increased [22]. Therefore, it is likely, that a degradation processes plays a role during the production. In this work, it is shown, that the degradation of $CuInSe_2$ can be observed quantitatively

and in real time as a decrease in quasi-Fermi level splitting over time. The degree of the degradation depends again on the sample's composition: Cu-poor material degrades much faster than samples grown under Cu-rich conditions. It is shown, that an etch in KCN refreshes aged samples to a degree so that they perform as well as directly after the growth process. As a consequence for the solar cell, the maximum achievable V_{OC} decreases more, the longer the absorbers are exposed to air.

The degradation is more severe, when the samples are constantly illuminated and exhibits the same trend for epitaxial and polycrystalline absorbers. Nevertheless, the loss in the quasi-Fermi level splitting for a freshly grown or a sample with a prior etch in KCN within the first hour is in the order of 15 meV for epitaxial samples and in the order of 55 meV for the polycrystalline ones. Since both material types exhibit the same trend, the ageing behaviour is interpreted to be rather independent of the sodium content. The polycrystalline samples were grown on Na containing soda lime glass leading to a diffusion of sodium into the absorber during the growth process. On the other hand, the GaAs substrate used for the epitaxial sample does not contain sodium. The reason for the degradation is believed to be related with oxygen and the formation of In_2O_3 explaining the faster degradation observed for Cu-poor samples. The refreshing effect of an etch in KCN suggests the removal of indium oxide.

It is shown, that the chemical bath deposition of the CdS buffer layer cleans the surface as well, since the quasi-Fermi level splitting increases for aged samples treated directly with CdS without a prior etch in KCN. The deposition of the CdS layer passivates the surface and no decrease, even after several months, in the quasi-Fermi level splitting is observed. Interestingly, the Cu-poor samples show higher quasi-Fermi level splitting after the deposition of the buffer layer than the Cu-rich ones. This is interpreted to be related with more non-radiative recombination centres between the absorber and the buffer. This indicates that the CdS layer is not beneficial for $CuInSe_2$ grown under Cu-rich conditions. Therefore, the interface to the buffer layer is the problem, and not the surface of the Cu-rich absorbers.

Epitaxial Cu(In,Ga)Se_2

The available recipes for the growth of $CuInSe_2$ and $CuGaSe_2$ in the MOVPE system are modified to allow the growth of $CuIn_{1-x}Ga_xSe_2$. Therefore, the temperature and the selenium flux are adjusted to allow the growth of epitaxial layers with a high quality within the composition range of $0.4 < x < 0.7$. A measure for the quality is the full width half maximum (FWHM) of the peaks in the diffraction pattern of XRD measurements, since it indicates the amount of defects within the film. After the optimization of the growth process, the FWHM shows values below $< 0.1°$ better than any Cu(In,Ga)Se_2 film reported so far.

A route for the preparation of epitaxial solar cells is established and used to produce the first epitaxial Cu(In,Ga)Se_2 based solar cells at LPV. The highest achieved efficiency was 6.7% (for $[Ga]/([Ga]+[In]) = 0.48$) while the record device in the literature [7] grown on a GaAs substrate with the same orientation showed a value of 7.3%. In this context, the highest achieved efficiencies in this work is only 0.6% lower than the world record. However, the devices suffer mostly from interface recombinations, which seemingly is independent of the additionalGaAs layer. Therefore it is most likely that the recombination

is taking place at the buffer/absorber interface. To minimize these interface recombinations, the GGI was reduced to [Ga]/([Ga] + [In]) $\approx$ 0.3 leading to efficiencies of $< 3\%$. The drastic reduction in performance is very likely to be related with an increased strain within the layer and thereby with an increased number of dislocations.

Simulation of the epitaxial device with the GaAs substrate revealed, that the GaAs does not hamper the device performance. As soon as the Cu(In,Ga)Se_2 layer is sufficiently thick to absorb all incident photons, the device behaves like a device without GaAs.

Since this work revealed reasons for the low efficiencies and established the preparation path for epitaxial devices, the future preparation will hopefully lead to higher efficiencies. Thereby, the suggestions (section 4.11.3) given within this work may help. One of the most promising paths is the exchange of the CdS buffer layer. Instead, a ZnSe buffer layer should be deposited in the MOVPE system directly after the absorber layer. By optimizing the growth conditions, the interface should be improved significantly.

APPENDIX

A

ACKNOWLEDGEMENT

First, of all I want to thank Prof. Dr. Susanne Siebentritt who gave me the opportunity to work on the interesting project that involves the usage of various different machines and characterisation techniques. Thank you very much for all your support and advices!

I would like to thank Roland Scheer, Ludger Wirtz, Heinz Kalt, and Alex Redinger for being part of the examination board of my thesis.

Without the help of a various number of people, this work would not have been possible. I am especially grateful for the help of (in alphabetic order):

- Alex Redinger for his very helpful advices and discussions about IVT, UVVIS, semiconductors, and solar cells.
- Daisuke Tanaka for growing one sample used for the degradation study and for helping to remove it "on time".
- Jes Larsen for growing the epitaxial $CuInSe_2$ films.
- Levent Gütay for growing the epitaxial $CuInSe_2$ layers, his patience and helpful advices to perform PL experiments and to highlight the analysis method.
- Maxime Thevenin for the "uncountable" hours he spent at the SEM machine, for his great support by depositing the CdS, and the deposition of the ZnOand the grids of the very special and sensitive epitaxial cells! Thanks a lot, Maximchen, for the great time we spent together - independent of when and where!
- Michael Kirsch from the Helmholtz Zentrum Berlin for depositing some of the ZnO layers as well as the front contact.
- Patricia Ramoa, ma poulette, for all the ordering and especially for sorting out the mass of the invoices.
- Thomas Schuler for all his advices, the hours he spent in, above, or next to the MOVPE, and his fast and "bureaucratic" ways of solving (technical) problems of all kinds. And for everything else, Mon ChiChi!
- Thomas Weiss for prove reading some chapters, his suggestions and for the more or less important things (That's what...).

- Tobias Bertram for his helpful discussions about defects, PL, and the more or less important stuff.
- Valérie Deprédurand for growing one sample used for the degradation study and removing it "on time" from the vacuum chamber.
- Yasuhiro Aida for providing all the other polycrystalline samples used in the PL chapter.

I would like to thank all the members of the LPV and LEM team for the nice time we spend together and especially my officemates for the great atmosphere.
This thesis was funded by the "Fonds National de la Recherche Luxembourg".

Finally, I want to thank my brother Tobias, JoaNdriana, and my parents for the constant support during the last years - in the good and in the bad times!

APPENDIX

B

MATERIAL PROPERTIES

A list of literature values are summarized in the table below. Included are the ternaries $CuInSe_2$ and $CuGaSe_2$ and an approximation for the alloy component $CuIn_{1-x}Ga_xSe_2$ for $x = [0, 1]$.

	$CuInSe_2$	$CuGaSe_2$	$CuIn_{1-x}Ga_xSe_2$
Crystal structure			
a [Å][a]	5.781 [59],5.8512 [53]	5.6 [67],5.619 [64]	-0.1769x+5.7871
c [Å][a]	11.614 [62],11.7268 [53]	11.02 [66],11.03 [68]	-0.3060x+5.8150
α_a 10^{-6} [K^{-1}]	10.3 [187], 11 [188]	13.1 [189]	2.45*x+10.65
α_c 10^{-6} [K^{-1}]	7.9 [187], 8.4 [188]	5.2 [189]	-2.95*x+8.15
Electrical properties			
ϵ/ϵ_0	13.6 [183]	11.0 [190]	$-2.6x + 13.6$
$m_{eff,e}/m_0$	0.09 [191]	0.115 [192]	$0.025x + 0.09$
$m_{eff,h}/m_0$	0.71 [193]	0.64 [192]	$-0.07x + 0.71$
N_C (cm^{-3})[b]	6.77e17	9.79e17	
N_V (cm^{-3})[b]	1.50e19	1.28e19	
E_g [eV]	1.03 [41]	1.69 [41]	$1.035 + 0.389x + 0.264x^2$ [41]
χ [eV][c]	4.48	3.83	$4.1 + 1.69 - E_g - 0.26$
Optical properties [35][d]			
α_0 $10^4[cm^{-1}]$	0.98 [35]	0.84 [35]	$4.53e3x^2 - 5.91e3x + 9.88e3$
α_1 $10^3[cm^{-1}]$	6.01 [35]	3.59 [35]	$4.87e3x^2 + 2.42e3x + 6.04e3$
E_1 [eV]	1.574 [35]	1.765 [35]	$0.403x^2 - 0.215x + 1.574$
B_1 [eV]	0.363 [35]	0.357 [35]	$0.211x^2 + 0.204x + 0.364$

Table B.1.: ***Material properties*** *- A summary of the material properties used in this work.*

[a] The limits of lattice constants found in literature at room temperature. The extrapolation takes more values into account (compare section 2.2.1).

[b] Calculated with $N_{C,V} = 2\left(2\pi m_{eff} k_B T/h^2\right)^{3/2}$ [194]

[c] The derivation is explained in section 4.10.1

[d] Parameter for $\alpha(E) = \alpha_0\sqrt{\frac{E-E_g}{k_B T}} + \alpha_1 \exp\left(\frac{E-E_1}{B_1}\right)$ [35].

APPENDIX

C

EXPERIMENTAL DETAILS

C.1. Details about the excitation for PL measurements

To allow an excitation equivalent to n-times the solar spectrum, the AM1.5g spectrum can be used to calculate the number of photons being absorbed within a semiconductor:

$$\int_{E_g}^{\infty} AM1.5(E)dE. \tag{C.1}$$

The photon flux from a monochromatic laser source can than be tuned to correspond

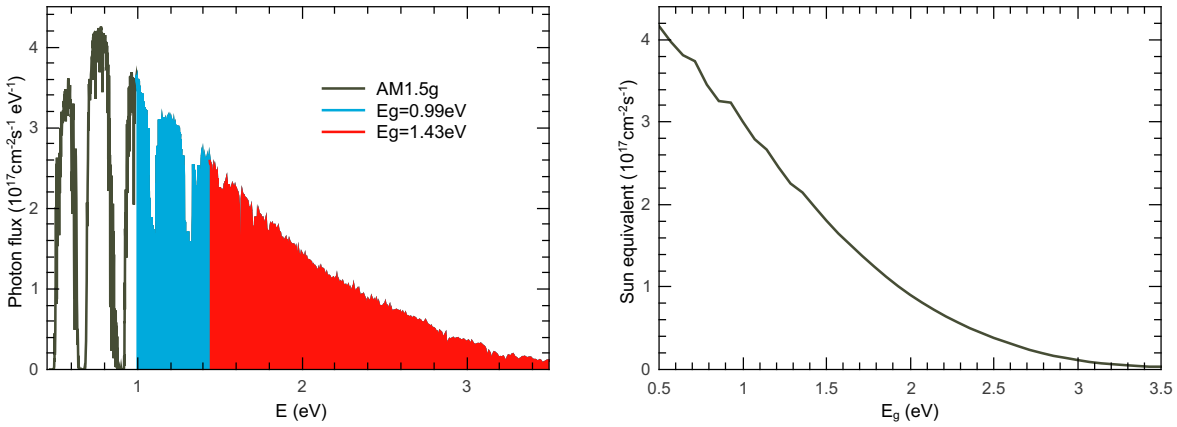

(a) AM1.5 sepctrum [122]. The integration over the coloured area gives the number of absorbable photons for two different semiconductors with a band gap of $\mathrm{E_g} = 0.99$ eV *and* $\mathrm{E_g} = 1.43$ eV.

(b) Excitation equivalent to 1xAM1.5g. The number of photons required to ensure an excitation equivalent to one sun with respect to the band gap of the semiconductor to be measured (calculated with equation (C.1)*).*

Figure C.1.: ***AM1.5g spectrum and the exciation equivalent*** *- By tuning the photon numbers from a monochromatic laser source, measurements with an excitation flux equivalent to one sun are possible.*

to this calculated number. The AM1.5 spectrum is shown in figure C.1a illustrating the area which determines the number of absorbable photons for two semiconductor with a

band gap of $E_g = 0.99$ eV and $E_g = 1.42$ eV (the filled area). The number of photons in dependence of E_g (equation (C.1)) is shown in figure C.1b. The number is important, to control the excitation flux as shown in figure 3.2.

C.2. Modelling the PL spectra at room temperature

The evaluation of the data in chapter 3 is based on Planck's generalised radiation law (section 2.5.3) and equation (2.25) can be used to model the gathered data. In contrast to the ideal case using the square root dependence of the absorption coefficient for an ideal direct semiconductor (section 2.5.3) the reality is more challenging, because of the Urbach tailing.
To achieve a better agreement on the absorption determined side of the PL peak (section 2.5.3), the ideal model has to be extended. One empirical approach, as used in the software Diplot [195], is the sum of the square root dependence of the band-to-band transitions (equation (2.15)) and the exponential tailing (2.16). To correct the dominating exponential Urbach term for energies (far) above the band gap, the sum can be divided by an additional mathematically motivated correction term

$$\alpha_{\text{correction}} = \exp\left(\frac{(w+1)(E_g - E)}{E_u} + E_0\right) + 1 \tag{C.2}$$

where E_g is the band gap (equation (2.15)), E_u the Urbach energy, and E_0 the shift of the Urbach tailing (equation (2.16)). w is a weeding parameter to tune the transition between equation (2.15) and (2.16). In total, the absorption coefficient near the band gap can be approximated with

$$\alpha(E) = \left(\alpha_0\sqrt{\frac{E - E_g}{E}} + \alpha_u \exp\left(-\frac{(E_0 - E)}{E_u}\right)\right) / \alpha_{\text{correction}} \tag{C.3}$$

An example for an epitaxial $CuInSe_2$ sample measured at room temperature is shown in figure C.2. The crosses mark the measured data, the red line shows a fit of the ideal case of a direct semiconductor[1], and the blue line was calculated using the corrected absorption coefficient in equation (C.3). The reflectivity was assumed to be $R_f = 0$ and the absorber thickness to be $d = 1$ µm (equations (2.25) and (2.12)).

The fit of the red curve lead to a temperature of $T = 329.4K$ (due to the laser, the sample is heated and the temperature is slightly above room temperature), which was also used for the blue curve. The other parameters were fitted leading to an Urbach energy of $E_u = 18$ meV and a weeding parameter of $w = 13.2$. The quasi-Fermi level splitting was found to be 743 meV for the ideal model and 734 meV for the extended one.
The advantage of fitting a model to the complete data set is that all data points are taken into account. Nevertheless, the determination of the temperature remains difficult since small changes in the temperature lead to significant changes on the high energy side. Since the exact change of the absorption coefficient is unknown, the low energy side cannot be used to support the determination of the temperature. This is why the

[1] The data were fitted starting slightly above the band gap up to the highest energy point.

approximation described in section 2.5.4 was used, since it gives a more robust method for the determination of the quasi-Fermi level splitting.

Nevertheless, the model can easily reveal the influence of the reflectivity. The corrected absorption model with the previously fitted parameter can be used to keep all determined parameters constant, except the quasi-Fermi level splitting. When modifying the reflectivity, the quasi-Fermi level splitting was fitted and reads 734 meV for $R_f = 0$, 737 meV for $R_f = 0.1$, and 740 meV for $R_f = 0.2$. Thus, the difference between a non reflective surface and a reflectivity of $R_f = 0.2$ is very small and can be neglected.

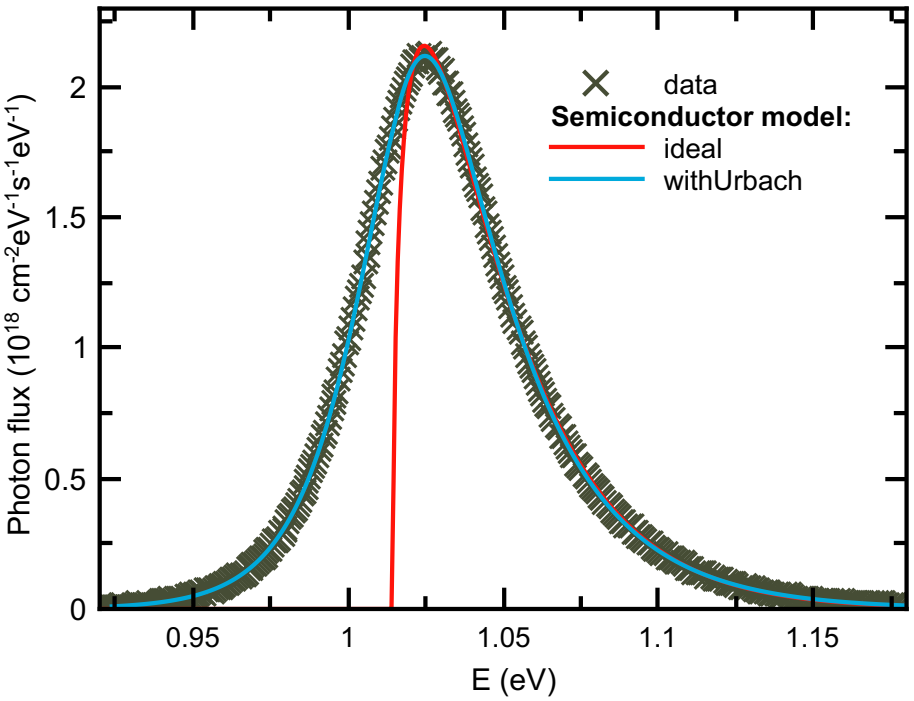

Figure C.2.: ***Example of a possible evaluation model for PL measurements at room temperature*** *- The grey symbols represent the measurement of a Cu-rich $CuInSe_2$ sample. The solid lines illustrate possible ways of an evaluation using Planck's generalized law (equation (2.25). The red line assumes the absorption coefficient of an ideal semiconductor; the blue curve corrects the absorption coefficient with an additional Urbach tailing. Details about the model are described in the text.*

APPENDIX

D

EVALUATION PROGRAM

Most of the evaluations within this work were done with a self made program ("lll") written in python [176]. The program contains several libraries written for different purposes as described below briefly. The library may either be used in any python environment or in the included graphical user interface (GUI). While the GUI allows an intuitive way to solve daily tasks, such as evaluating IV (preferable well behaving ones) or QE curves, the usage within a python environment allows an extremely flexible usage independent of the operation system. For example Spyder [196][1] can be used to perform more complicated operations and combine the library with own functions. The most important features are highlighted in the following.

Basic mathematical operations

The basis of many operations is the python class "Spec" inspired by the program peak-o-mat [197]. The original class provides many convenient features for basic arithmetic operations related to x-y data sets, such as deviations, integrations or operations like a/b where a and b are spectral data. For instance, the calculation of a correction function (section 3.1.2) requires dividing the reference spectrum by the measured reference data. Generally, the reference spectrum covers a larger range with a different step size $\Delta\lambda$ when compared to the data obtained from a PL measurement. The division is automatically performed within the overlapping λ-range and the different step sizes are accounted for by interpolating data point within one data set. The Spec type was extended to support variables allowing very general operations and the usage of complex data.

Curve fitting

A mathematical model can be applied to the "Spec", which can be fitted with the fitting module. The fitting module, which is also inspired by [197], was extended to support the evaluation of implicit functions (e.g the diode equation 2.39) and complex functions (for data such as the admittance mentioned in 2.6.6 or the complex refraction index). The fitting procedure itself uses the ODR library available in the scientific python library

[1] Spyder is a python environment very similar to the commercial MatLab™ by MathWorks®.

scipy [177][2]. Nevertheless, the lll-library supports an abstract way to define any model, by either using an equation (e.g. $\exp((a * x - x0)/T)$) or by combining an arbitrary number of pre defined functions (Gaussian, Voigt, Lorentzian,...). The parameters are determined automatically and transferred in a format which is compatible with the ODR package. Additionally, the fitting parameter can either be "free", "constant", or bounded to specified limits, which cannot be done directly with the ODR package.

GUI

The GUI was developed to ensure proper evaluations of many data sets. It can be used to visualize the properties stored in the "Spec" type, to retrace operations which were done automatically, and to handle own extension for specific evaluation procedures (see below). Figure D.1 shows a screen shot of the GUI. Visible is the toolbox, holding the active data sets and visualizing the available evaluation tools. The data and the model are shown in the "View widget" on the right hand side. In the bottom, the active model and the corresponding parameters are shown. The parameters can be changed manually, or fitted with the least square method or by applying orthogonal distance regression [175, 177].

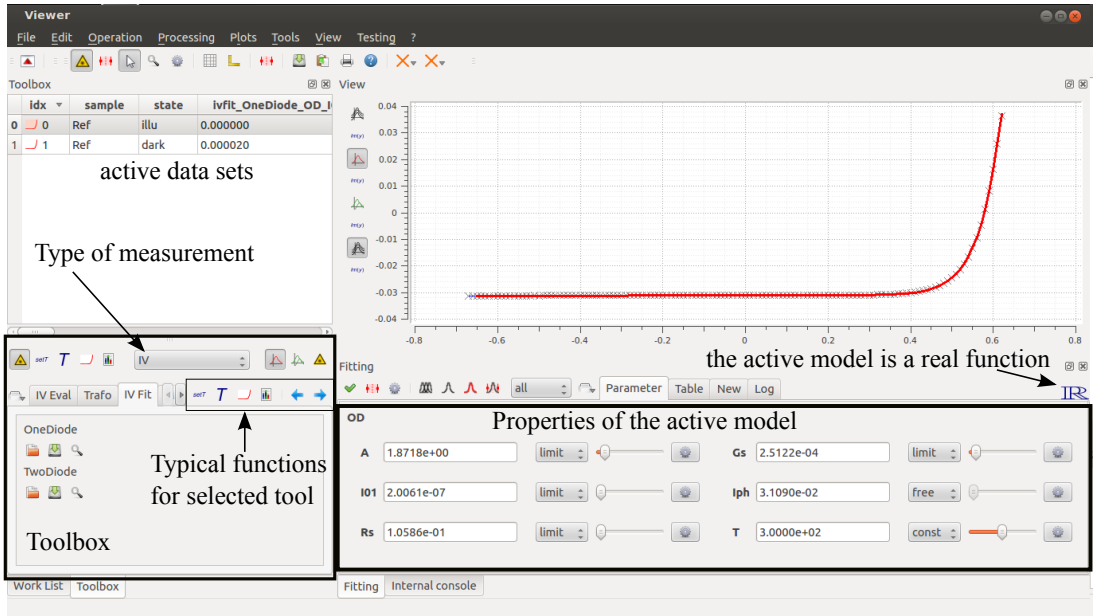

Figure D.1.: *GUI for evaluations* - *The GUI consists of a toolbox where the active data sets are shown (left side). Below the list, the active tool is visible. Depending on the type of measurement, different tools can be selected. Each tool offers several functions, such as attributing variables (e.g. attributing the temperature) or performing calculations. The data are plotted in the "view widget" on the right hand side (the crosses). The red line shows the active model, which can be controlled within the "Fitting widget". The example shows the one-diode model.*

[2]Examples of how to use the library can be found, e.g. under the URL `http://docs.scipy.org/doc/scipy-dev/reference/odr.html`

PL

The library offers plenty of helpful tools for the evaluation of PL data. Figure D.2 shows the ones implemented in the GUI. One important feature is the calculation of correction functions (section 3.1.2). The program calculates correction functions based on reference measurements and stores the data for further measurements. Saved are all data, which are important for the correct assignment of functions, e.g. the date, the used grating, the centre wave length, the exposure time, and the used filter combination. The correction function can be applied automatically (if all parameters are the same) or manually. The GUI provides a very convenient and fast way to correct a huge amount of measurements. Additionally, tools for the evaluation at room temperature (section 2.5.4) and at low temperatures (section 2.5.2) are provided, allowing the fast evaluation of measured data.

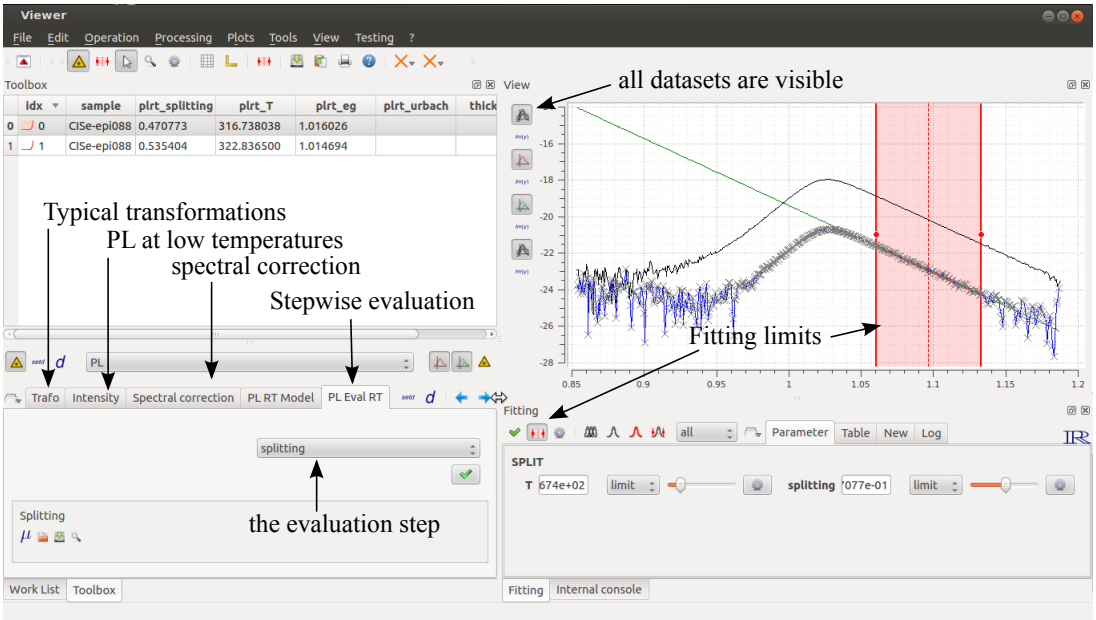

Figure D.2.: ***GUI for PL evaluations*** *- The GUI for daily tasks when performing PL measurements. The active tool allows the stepwise evaluation of the quasi-Fermi level splitting and the determination of the absorption properties. The "Trafo" tool provides typical transformation such as converting wavelengths to energies. The spectral correction tool allows the calculation and the applying of correction functions. The intensity tool can handle the evaluation of intensity dependent PL measurements at low temperature, or temperature dependent measurements. A bunch of measurements can be displayed simultaneously allowing the fast evaluation of many datasets. The applied model and the fitting limits can be copied to the other data.*

APPENDIX

E

LIST OF PUBLICATIONS AND CONFERENCES

Publications

H. Meadows, A. Bhatia, V. Depredurand, J. Guillot, D. Regesch, A. Malyeyev, D. Colombara, M. Scarpulla, S. Siebentritt, P. Dale: Single Second Laser Annealed $CuInSe_2$ Semiconductors from Electrodeposited Precursors as Absorber Layers for Solar Cells, *The Journal of Physical Chemistr*y (accepted) *2013*

J. C. Malaquias, D. Regesch, P. J. Dale, M. Steichen: Tuning the Gallium Content of Metal Precursors for Cu(In,Ga)Se2 Thin Film Solar Cells by Electrodeposition from a Deep Eutectic Solvent, *Physical Chemistry Chemical Physics* (accepted) (2013)

S. Siebentritt, L. Gütay, D. Regesch, Y. Aida 2, V. Depredurand: Why do we make $Cu(In,Ga)Se_2$ solar cells non-stoichiometric?, *Solar Energy Materials and Solar Cells* 119, p18 (2013)

D. Regesch, L Gütay, J. K. Larsen, V. Depredurand, D. Tanaka, Y. Aida, S. Siebentritt: Degradation and passivation of $CuInSe_2$, *Applied Physics Letters* 101(11) p112108 (2012)

L. Gütay, D. Regesch, J. K. Larsen, Y. Aida, V. Depredurand, A. Redingern, S. Caneva, S. Schorr, C. Stephan, J. Vidal, S. Botti, S. Siebentritt: Feedback mechanism for the stability of the band gap of $CuInSe_2$, *Physical Review B* 86(4) p045216 (2012)

L. Gütay, D. Regesch, J. K. Larsen, Y. Aida, V. Depredurand, S. Siebentritt: Influence of copper excess on the absorber quality of CuInSe2, *Applied Physics Letters* 99(15) p151912 (2011)

Conferences

J. Malaquias, M. Steichen, D. Regesch, P. J. Dale, Deep Eutectic Solvents as Electrolytes for Simultaneous Electrodeposition of Indium and Gallium for $Cu(In,Ga)Se_2$ Solar Cells, 28th EUPVSEC, Paris (2013)

D. Regesch: Luminescence Techniques for Defect Spectroscopy, *MRS Spring Meeting: Young Scientist Tutorial*, San Francisco (2013)

D. Regesch, L. Gütay, J. K. Larsen, S. Siebentritt: Temperature Dependent IV Analysis of Epitaxial $CuIn_{1-x}Ga_xSe_2$ Solar Cells, *MRS Spring Meeting*, San Francisco (2013)

D. Regesch, L. Gütay, J. K. Larsen, Y. Aida, V. Depredurand, S. Siebentritt: *Aging and passivation of CuInSe₂*, *E-MRS Spring Meeting*, Strasbourg (2012)

M. Steichen, R. Djemour, D. Regesch, L. Gütay, S. Siebentritt, P. Dale: Synthesis of SnS thin films by electrodeposition from an ionic liquid containing elemental sulphur, *E-MRS Spring Meeting*, Strasbourg (2012)

L. Gütay, D. Regesch, J. K. Larsen, Y. Aida, A. Redinger, S. Caneva, S. Siebentritt: Composition dependence of band gap and opto-electronic quality of $CuInSe_2$, *E-MRS Spring Meeting*, Nice (2011)

LIST OF FIGURES

BIBLIOGRAPHY

[1] J. L. Shay, Sigurd Wagner, and H. M. Kasper. Efficient CuInSe2/CdS solar cells. *Applied Physics Letters*, 27(2):89–90, 1975. 7, 73, 104

[2] ZSW. ZSW produces world record solar cell, 2013. 7, 73, 104, 117

[3] Solibro. Solibro pushes lab CIGS conversion efficiency to 19.6% - PV-Tech, 2013. 7

[4] Martin A. Green, Keith Emery, Yoshihiro Hishikawa, Wilhelm Warta, and Ewan D. Dunlop. Solar cell efficiency tables (version 42). *Progress in Photovoltaics: Research and Applications*, 21(5):827–837, 2013. 7

[5] L.S. Mattos, S.R. Scully, M. Syfu, E. Olson, Linlin Yang, C. Ling, B.M. Kayes, and Gang He. New module efficiency record: 23.5% under 1-sun illumination using thin-film single-junction GaAs solar cells. In *2012 38th IEEE Photovoltaic Specialists Conference (PVSC)*, pages 003187–003190, 2012. 7

[6] M. A. Green. *Solar cells: operating principles, technology, and system applications*. Prentice-Hall series in solid state physical electronics. Prentice-Hall, 1982. 7

[7] D. Liao and A. Rockett. (220)-oriented cu(In,Ga)Se2-evidence that it may improve solar cell performance. In *Photovoltaic Specialists Conference, 2000. Conference Record of the Twenty-Eighth IEEE*, pages 446 –449, 2000. 7, 72, 73, 89, 104, 112, 117, 119

[8] J. C. Mikkelsen. Ternary phase relations of the chalcopyrite compound CuGaSe2. *Journal of Electronic Materials*, 10(3):541–558, 1981. 7

[9] S. Siebentritt and U. Rau, editors. *Wide-Gap Chalcopyrites*. Springer Series in Materials Science. Springer, 2010. DOI: 10.1007/b105644. 7, 32, 33, 47, 49

[10] L. Gütay, D. Regesch, J. K Larsen, Y. Aida, V. Depredurand, and S. Siebentritt. Influence of copper excess on the absorber quality of CuInSe2. *Applied Physics Letters*, 99(15):151912–151912–3, 2011. 7

[11] S Siebentritt, A Bauknecht, A Gerhard, U Fiedeler, T Kampschulte, S Schuler, W Harneit, S Brehme, J Albert, and M.Ch Lux-Steiner. CuGaSe2 solar cells prepared by MOVPE. *Solar Energy Materials and Solar Cells*, 67(1-4):129–136, 2001. 7, 72, 73, 104, 117

[12] S. Siebentritt, A. Gerhard, S. Brehme, and M. Ch. Lux-Steiner. Composition dependent doping and transport properties of CuGaSe2. *MRS Online Proceedings Library*, 668, 2001. 7

[13] J. K Larsen, L. Gütay, and S. Siebentritt. Influence of secondary phase CuxSe on the optoelectronic quality of chalcopyrite thin films. *Applied Physics Letters*, 98(20):201910–201910–3, 2011. 7, 24, 56

[14] H. SchroÌĹcke and K.-L. Weiner. *Mineralogie: ein Lehrbuch auf systematischer Grundlage*. Walter de Gruyter, 1981. 9

[15] S. Wagner, J. L. Shay, P. Migliorato, and H. M. Kasper. CuInSe2/CdS heterojunction photovoltaic detectors. *Applied Physics Letters*, 25:434–435, 1974. 9

[16] W. N. Shafarman, S. Siebentritt, and L. Stolt. *Cu(InGa)Se2 Solar Cells in Handbook of Photovoltaic Science and Engineering*, pages 546–599. John Wiley & Sons, Ltd, 2011. 9

[17] J. K Larsen. *Inhomogeneties in epitaxial chalcopyrites studied by photoluminescence*. PhD thesis, University of Luxembourg, 2011. 10, 18, 22, 23, 24, 32, 34, 60

[18] J. L. Shay. *Ternary chalcopyrite semiconductors: growth, electronic properties, and applications*. International series of monographs in the science of the solid state, v. 7. Pergamon Press, 1st ed. edition, 1975. 9

[19] J. E. Jaffe and A. Zunger. Electronic structure of the ternary chalcopyrite semiconductors $CuAlS_2$, $CuGaS_2$, $CuInS_2$, $CuAlSe_2$, $CuGaSe_2$, and $CuInSe_2$. *Physical Review B*, 28(10):5822–5847, 1983. 9

[20] C.-H. Chang, S.-H. Wei, W. Johnson, R. Bhattacharya, B. Stanbery, T. Anderson, and R. Duran. Long and short range ordering of $CuInSe_2$. *Japanese Journal of Applied Physics*, 39S1(Supplement 39-1):411–412, 2000. 10

[21] J. E. Jaffe and A. Zunger. Anion displacements and the band-gap anomaly in ternary ABC_2 chalcopyrite semiconductors. *Physical Review B*, 27:5176–5179, 1983. 10

[22] P. Jackson, D. Hariskos, E. Lotter, S. Paetel, R. Wuerz, R. Menner, W. Wischmann, and M. Powalla. New world record efficiency for Cu(In,Ga)Se2 thin-film solar cells beyond 20%. *Progress in Photovoltaics: Research and Applications*, 19(7):894–897, 2011. 10, 67, 69, 102, 118

[23] M. I. Alonso, M. Garriga, C. A. Durante RincÃşn, E. HernÃąndez, and M. LeÃşn. Optical functions of chalcopyrite $CuGa_xIn_{1-x}Se_2$ alloys. *Applied Physics A*, 74(5):659–664, 2002. 11, 27

[24] S. Siebentritt, M. Igalson, C. Persson, and S. Lany. The electronic structure of chalcopyritesâĂŤbands, point defects and grain boundaries. *Progress in Photovoltaics: Research and Applications*, 18(6):390–410, 2010. 11, 12, 13

[25] J. L. Shay and H. M. Kasper. Direct observation of Cu d levels in I-III-VI_2 compounds. *Physical Review Letters*, 29(17):1162–1164, 1972. 11

[26] J. L. Shay, B. Tell, H. M. Kasper, and L. M. Schiavone. Electronic structure of $AgInSe_2$ and $CuInSe_2$. *Physical Review B*, 7(10):4485–4490, 1973. 11

[27] J. C. Rife, R. N. Dexter, P. M. Bridenbaugh, and B. W. Veal. Optical properties of the chalcopyrite semiconductors ZnGeP2, ZnGeAs2, CuGaS2, CuAlS2, CuInSe2, and AgInSe2. *Phys. Rev. B*, 16(10):4491–4500, 1977. 11

[28] J. L. Shay, B. Tell, H. M. Kasper, and L. M. Schiavone. p-d hybridization of the valence bands of I–III–VI2 compounds. *Physical Review B*, 5(12):5003–5005, 1972. 11

[29] M. Grundmann. *The Physics of Semiconductors: An Introduction Including Devices and Nanophysics*. Springer, 1 edition, May 2006. 12

[30] S. B. Zhang, S.-H. Wei, A. Zunger, and H. Katayama-Yoshida. Defect physics of the $CuInSe_2$ chalcopyrite semiconductor. *Physical Review B*, 57(16):9642–9656, 1998. 12

[31] T. Irie, S. Endo, and S. Kimura. Electrical properties of p- and n-type CuInSe2 single crystals. *Japanese Journal of Applied Physics*, 18(7):1303–1310, 1979. 12

[32] R. Noufi, R. Axton, C. Herrington, and S. K. Deb. Electronic properties versus composition of thin films of CuInSe2. *Applied Physics Letters*, 45(6):668–670, 1984. 12

[33] C. Persson, Y.-J. Zhao, S. Lany, and A. Zunger. n-type doping of CuInSe2 and CuGaSe2. *Phys. Rev. B*, 72(3):035211, 2005. 12, 13

[34] Y.-J. Zhao, C. Persson, S. Lany, and A. Zunger. Why can CuInSe2 be readily equilibrium-doped n-type but the wider-gap CuGaSe2 cannot? *Applied Physics Letters*, 85(24):5860–5862, 2004. 12

[35] R. Scheer and H.-W. Schock. *Chalcogenide Photovoltaics: Physics, Technologies, and Thin Film Devices*. Wiley-VCH Verlag, 1 edition, 2011. 12, 28, 29, 30, 38, 40, 41, 42, 43, 44, 45, 46, 47, 49, 90, 94, 95, 105, 106, 107, 123

[36] J. Pohl and K. Albe. Thermodynamics and kinetics of the copper vacancy in CuInSe2, CuGaSe2, CuInS2, and CuGaS2 from screened-exchange hybrid density functional theory. *Journal of Applied Physics*, 108(2):023509, 2010. 12

[37] L. E. Oikkonen, M. G. Ganchenkova, A. P. Seitsonen, and R. M. Nieminen. Vacancies in CuInSe2: new insights from hybrid-functional calculations. *Journal of Physics: Condensed Matter*, 23(42):422202, 2011. 12

[38] L. E. Oikkonen, M. G. Ganchenkova, A. P. Seitsonen, and R. M. Nieminen. Redirecting focus in CuInSe2 research towards selenium-related defects. *Physical Review B*, 86(16):165115, 2012. 12

[39] J. Pohl and K. Albe. Intrinsic point defects in CuInSe2 and CuGaSe2 as seen via screened-exchange hybrid density functional theory. *Physical Review B*, 87(24):245203, 2013. 12, 13

[40] M. Turcu, I. M. Kötschau, and U. Rau. Composition dependence of defect energies and band alignments in the $Cu(In_{1-x}Ga_x)(Se_{1-y}S_y)_2$ alloy system. *Journal of Applied Physics*, 91(3):1391–1399, 2002. 13, 49, 104

[41] P. D. Paulson, R. W. Birkmire, and W. N. Shafarman. Optical characterization of CuIn1-xGaxSe2 alloy thin films by spectroscopic ellipsometry. *Journal of Applied Physics*, 94:879–888, 2003. 13, 60, 71, 104, 118, 123

[42] U. W Pohl. *Epitaxy of semiconductors introduction to physical principles*. Springer, Berlin; New York, 2013. 14, 18, 21, 22, 23

[43] A. Bauknecht. *CuGaSe2 für die Anwendung in der Photovoltaik*. PhD thesis, FU Berlin, Berlin, 1999. 15, 17, 18, 22, 60, 75, 108

[44] D. J. Dunstan. Strain and strain relaxation in semiconductors. *Journal of Materials Science: Materials in Electronics*, 8:337–375, 1997. 15

[45] A. W. Stevenson. Thermal vibrations and bonding in GaAs: an extended-face crystal study. *Acta Crystallographica Section A*, 50(5):621–632, 1994. 16, 17

[46] C.-Y. Yeh, Z. W. Lu, S. Froyen, and A. Zunger. Zinc-blende-wurtzite polytypism in semiconductors. *Physical Review B*, 46(16):10086–10097, 1992. 16, 17

[47] T. Soma, J. Satoh, and H. Matsuo. Thermal expansion coefficient of GaAs and InP. *Solid State Communications*, 42(12):889–892, 1982. 16

[48] S. Shirakata and S. Chichibu. Photoreflectance of cuâĂŘbased I–III–VI2 heteroepitaxial layers grown by metalorganic chemical vapor deposition. *Journal of Applied Physics*, 79(4):2043, 1996. 16, 108

[49] E. D. Pierron, D. L. Parker, and J. B. McNeely. Coefficient of expansion of GaAs, GaP, and Ga(As, P) compounds from $-62°$ to 200°C. *Journal of Applied Physics*, 38(12):4669, 1967. 16, 17

[50] N. Rega. *Photolumineszenz von epitaktischen Cu(In,Ga)Se2-Schichten*. PhD thesis, FU Berlin, Berlin, 2004. 17, 22, 24

[51] J. Yao, Z. Wang, J. van Tol, N. S. Dalal, and J. A. Aitken. Site preference of manganese on the copper site in mn-substituted CuInSe2 chalcopyrites revealed by a combined neutron and x-ray powder diffraction study. *Chemistry of Materials*, 22(5):1647–1655, 2010. 17

[52] Leon, M, Merino, J.M., and Van Tendeloo, G. Anãąlisis estructural de CuInSe2, CuInTe2 y CuInSeTe por microscopãŋa electrãşnica y tãľcnica de rayos x. *Acta Microscopica*, 18:128, 2009. 17

[53] S. Schorr and G. Geandier. In-situ investigation of the temperature dependent structural phase transition in $CuInSe_2$ by synchrotron radiation. *Crystal Research and Technology*, 41(5):450–457, 2006. 17, 123

[54] J.M. Merino, M. Di Michiel, and M. LeÃşn. Structural analysis of CuInSe2 and CuIn3Se5 at different temperatures with synchrotron radiation. *Journal of Physics and Chemistry of Solids*, 64(9-10):1649–1652, 2003. 17

[55] L. Kaplan, G. Leitus, V. Lyakhovitskaya, F. Frolow, H. Hallak, ÃĚ. Kvick, and D. Cahen. Synchrotron x-ray diffraction evidence for native defects in the photovoltaic semiconductor CuInSe2. *Advanced Materials*, 12(5):366–370, 2000. 17

[56] L. I. Gladkikh, E. I. Rogacheva, T. V. Tavrina, and L. P. Fomina. X-ray diffraction study of nonstoichiometry in CuInSe(2+x). *Inorg Mater*, 36(11):1098–1100, 2000. 17

[57] J. M Merino, J. L MartÃŋn de Vidales, S. Mahanty, R. DÃŋaz, F. Rueda, and M. LeÃşn. Composition effects on the crystal structure of CuInSe2. *Journal of Applied Physics*, 80(10):5610–5616, 1996. 17

[58] A. Baldus and K.W. Benz. Melt and metallic solution crystal growth of CuInSe2. *Journal of Crystal Growth*, 130(1-2):37–44, 1993. 17

[59] K.S. Knight. The crystal structures of CuInSe2 and CuInTe2. *Materials Research Bulletin*, 27(2):161–167, 1992. 17, 123

[60] U.-C. Boehnke, H. Neumann, and G. Kühn. Phase study of the system Cu1-xLixInSe2. *Journal of Alloys and Compounds*, 190(1):L17–L18, 1992. 17

[61] H. Miyake and K. Sugiyama. THM growth and properties of CuInSe2 single crystals. *Journal of Crystal Growth*, 125(3-4):548–552, 1992. 17

[62] G. Zahn and P. Paufler. Identification of predominant point defects in nonstoichiometric CuInSe2 by x-ray powder diffraction. *Crystal Research and Technology*, 23(4):499–507, 1988. 17, 123

[63] E. J. Friedrich, R. Fernandez-Ruiz, J. M. Merino, and M. Leon. X-ray diffraction data and rietveld refinement of CuGaxIn1-xSe2 (x=0.15 and 0.50). *Powder Diffraction*, 25(03):253–257, 2010. 17

[64] M. Souilah, A. Lafond, C. Guillot-Deudon, S. Harel, and M. Evain. Structural investigation of the Cu2Se-In2Se3-Ga2Se3 phase diagram, x-ray photoemission and optical properties of the Cu1-z(In0.5Ga0.5)1+z/3Se2 compounds. *Journal of Solid State Chemistry*, 183(10):2274–2280, 2010. 17, 123

[65] M. Souilah, X. Rocquefelte, A. Lafond, C. Guillot-Deudon, J.-P. Morniroli, and J. Kessler. Crystal structure re-investigation in wide band gap CIGSe compounds. *Thin Solid Films*, 517(7):2145–2148, 2009. 17

[66] G. MassÃĬ, K. Djessas, and L. Yarzhou. Study of CuGa(Se,Te)2 bulk materials and thin films. *Journal of Applied Physics*, 74(2):1376, 1993. 17, 123

[67] T. Tinoco, C. Rincon, M. Quintero, and G. Sanchez Perez. Phase diagram and optical energy gaps for $CuIn_yGa_{1-y}Se_2$ alloys. *physica status solidi (a)*, 124(2):427–434, 1991. 17, 123

[68] D. K. Suri, K. C. Nagpal, and G. K. Chadha. X-ray study of CuGaxIn1-xSe2 solid solutions. *Journal of Applied Crystallography*, 22(6):578–583, 1989. 17, 123

[69] M. Rabadanov and I.A. Verin. X–ray diffraction study of CuInSe2 single crystals. *Inorganic Materials*, 34(1):14–16, 1998. 17

[70] L. Mandel, R. D. Tomlinson, and M. J. Hampshire. Crystal data for CuGaSe2. *Journal of Applied Crystallography*, 10(2):130–131, 1977. 17

[71] J. E. Ayers. *Heteroepitaxy of Semiconductors: Theory, Growth, And Characterization*. CRC PressINC, 2007. 18, 21, 23

[72] S. Shirakata, S. Isomura, and S. Chichibu. Photoreflectance characterization of lattice strain in wide-gap Cu-III-VI2 epitaxial layers. In *Proceedings of MRS-J Symposium R; Novel Semiconductor Materials*, volume 20, pages 782–785, Makuhari, 1996. Transactions of the Materials Research Society of Japan. 18, 60

[73] K. Durose, Sally E. Asher, W. Jaegermann, D. Levi, B. E. McCandless, W. Metzger, H. Moutinho, P.d. Paulson, C. L. Perkins, J. R. Sites, G. Teeter, and M. Terheggen. Physical characterization of thin-film solar cells. *Progress in Photovoltaics: Research and Applications*, 12(2-3):177–217, 2004. 19, 77

[74] G. B. Stringfellow. *Organometallic vapor-phase epitaxy: theory and practice*. Academic Press, San Diego, 2nd ed edition, 1999. 21, 23

[75] M. Tirtowidjojo and R. Pollard. Elementary processes and rate-limiting factors in MOVPE of GaAs. *Journal of Crystal Growth*, 93(1-4):108–114, 1988. 22

[76] V.M Donnelly and J.A McCaulley. Products of thermal decomposition of triethylgallium and trimethylgallium adsorbed on Ga-stabilized GaAs(100). *Surface Science*, 238(1-3):34–52, 1990. 22

[77] G. Hanna, J. Mattheis, V. Laptev, Y. Yamamoto, U. Rau, and H.W. Schock. Influence of the selenium flux on the growth of cu(In,Ga)Se2 thin films. *Thin Solid Films*, 431-432:31–36, 2003. 23

[78] E. Wallin, T. Jarmar, U. Malm, M. Edoff, and L. Stolt. Influence of the average Se-to-metal overpressure during co-evaporation of Cu(InxGa1âĹŠx)Se2. *Thin Solid Films*, 519(21):7237–7240, 2011. 23

[79] P. Migliorato, J. L. Shay, H. M. Kasper, and Sigurd Wagner. Analysis of the electrical and luminescent properties of CuInSe2. *Journal of Applied Physics*, 46(4):1777–1782, 1975. 23

[80] T. Kampschulte. *MOCVD von ZnSe für Sperrkontakte in Heterosolarzellen auf der Basis von Chalkopyriten*. PhD thesis, FU Berlin, Berlin, 1999. 23

[81] S. Chichibu, S. Shirakata, S. Isomura, and H. Nakanishi. Visible and ultraviolet photoluminescence from Cu-III-VI_2 chalcopyrite semiconductors grown by metalorganic vapor phase epitaxy. *Japanese Journal of Applied Physics*, 36(Part 1, No. 3B):1703–1714, 1997. 24

[82] P. W. Lee, T. R. Omstead, D. R. McKenna, and K. F. Jensen. In situ mass spectroscopy and thermogravimetric studies of GaAs MOCVD gas phase and surface reactions. *Journal of Crystal Growth*, 85(1-2):165–174, November 1987. 24

[83] G.H. Fan, N. Maung, T.L. Ng, P.F. Heelis, J.O. Williams, A.C. Wright, D.F. Foster, and D.J. Cole-Hamilton. Thermal decomposition of di-tertiarybutyl selenide and dimethylzinc in a metalorganic vapour phase epitaxy reactor. *Journal of Crystal Growth*, 170(1-4):485–490, January 1997. 24

[84] L. Gütay, J. K. Larsen, J. Guillot, M. Müller, F. Bertram, J. Christen, and S. Siebentritt. MOVPE of CuGaSe2 on GaAs in the presence of a CuxSe secondary phase. *Journal of Crystal Growth*, 315(1):82–86, 2011. 24, 56

[85] D. J. Schroeder, G. D. Berry, and A. A. Rockett. Gallium diffusion and diffusivity in CuInSe2 epitaxial layers. *Applied Physics Letters*, 69(26):4068–4070, 1996. 24

[86] C.D Thurmond. Phase equilibria in the GaAs and the GaP systems. *Journal of Physics and Chemistry of Solids*, 26(5):785–802, 1965. 24

[87] T. E. Haynes, W. K. Chu, T. L. Aselage, and S. T. Picraux. Initial evaporation rates from GaAs during rapid thermal processing. *Journal of Applied Physics*, 63(4):1168–1176, February 1988. 24

[88] A. Piotrowska, E. KamiÅĎska, S. Kwiatkowski, and A. Turos. Quantitative analysis of arsenic losses during the formation of Au(Zn)/p-GaAs ohmic contacts. *Journal of Applied Physics*, 73(9):4404–4408, 1993. 24

[89] N. Rega, S. Siebentritt, I. Beckers, J. Beckmann, J. Albert, and M. Lux-Steiner. MOVPE of epitaxial CuInSe2 on GaAs. *Journal of Crystal Growth*, 248(0):169–174, 2003. 24, 25

[90] R. Swanepoel. Determination of the thickness and optical constants of amorphous silicon. *Journal of Physics E: Scientific Instruments*, 16(12):1214, 1983. 26

[91] I. P. Herman. *Optical diagnostics for thin film processing.* Academic Press, San Diego, CA, 1996. 26

[92] D. K. Schroder. *Semiconductor Material and Device Characterization.* John Wiley & Sons, 2006. 26

[93] M. O. Manasreh. *Semiconductor heterojunctions and nanostructures.* McGraw-Hill, New York, 2005. 26, 27

[94] P. Spindler, G. Franz J. Meyer, J. H. Meerburg, L. W. Gilbert, J. C. Poggendorff, G. H. Wiedemann, and E. Wiedemann. *Annalen der Physik.* Joh. Ambr. Barth (Leipzig), 1799. 26

[95] N.L. de La Caille and P. Bouguer. *Traite d optique sur la gradation de la lumiere: ouvrage posthume.* de l'imprimerie de H.L . Guerin & L.F. Delatour, 1760. 26

[96] H.B. Bebb and E.W. Williams. Chapter 4 Photoluminescence I: Theory. In R.K. Willardson and Albert C. Beer, editors, *Semiconductors and Semimetals*, volume Volume 8, pages 181–320. Elsevier, 1972. 27, 29, 31, 32, 34

[97] P. Y. Yu and M. Cardona. *Fundamentals of semiconductors: physics and materials properties*. Graduate texts in physics. Springer, Berlin ; New York, 4th ed edition, 2010. 29

[98] M. V. Kurik. Urbach rule. *physica status solidi (a)*, 8(1):9–45, 1971. 29

[99] J. D. Dow and D. Redfield. Toward a unified theory of Urbach's rule and exponential absorption edges. *Phys. Rev. B*, 5(2):594–610, 1972. 29

[100] T. Skettrup. Urbach's rule derived from thermal fluctuations in the band-gap energy. *Physical Review B*, 18(6):2622–2631, 1978. 29

[101] S. John, C. Soukoulis, M. H. Cohen, and E. N. Economou. Theory of electron band tails and the urbach optical-absorption edge. *Phys. Rev. Lett.*, 57(14):1777–1780, 1986. 29

[102] A. P. Levanyuk and V. V. Osipov. Edge luminescence of direct-gap semiconductors. *Sov. Phys. Usp.*, 24(3):187, 1981. 29

[103] C. F. Klingshirn. *Semiconductor optics*. Advanced texts in physics. Springer, Berlin ; New York, 2005. 29

[104] T. Shioda, S. Chichibu, T. Irie, H. Nakanishi, and T. Kariya. Influence of nonstoichiometry on the UrbachâĂŹs tails of absorption spectra for CuInSe2 single crystals. *Journal of Applied Physics*, 80(2):1106, 1996. 29, 61, 71, 118

[105] W. van Roosbroeck and W. Shockley. Photon-radiative recombination of electrons and holes in germanium. *Physical Review*, 94(6):1558–1560, 1954. 29

[106] P. Würfel. *Physics of solar cells: from principles to new concepts*. Wiley-VCH, Weinheim, 2005. 30, 31, 34, 35

[107] N. Rega, S. Siebentritt, J. Albert, S. Nishiwaki, A. Zajogin, M.Ch. Lux-Steiner, R. Kniese, and M.J. Romero. Excitonic luminescence of cu(In,Ga)Se2. *Thin Solid Films*, 480-481:286–290, 2005. 32

[108] J. R. Haynes. Experimental proof of the existence of a new electronic complex in silicon. *Phys. Rev. Lett.*, 4(7):361–363, 1960. 33

[109] H. Atzmüller and U. Schröder. Theoretical investigations of Haynes' rule. *physica status solidi (b)*, 89(2):349–356, 1978. 33

[110] Y. Toyozawa. Theory of line-shapes of the exciton absorption bands. *Progress in Theoretical Physics*, 20(1):53–81, 1958. 33

[111] F. Luckert, M. V. Yakushev, C. Faugeras, A. V. Karotki, A. V. Mudryi, and R. W. Martin. Excitation power and temperature dependence of excitons in CuInSe2. *Journal of Applied Physics*, 111(9):093507–093507–8, 2012. 33

[112] K. Colbow. Free-to-bound and bound-to-bound transitions in CdS. *Physical Review*, 141(2):742–749, 1966. 33

[113] D.M. Eagles. Optical absorption and recombination radiation in semiconductors due to transitions between hydrogen-like acceptor impurity levels and the conduction band. *Journal of Physics and Chemistry of Solids*, 16(1-2):76–83, 1960. 34

[114] P Würfel. The chemical potential of radiation. *Journal of Physics C: Solid State Physics*, 15(18):3967–3985, 1982. 34

[115] M. Planck and M. Masius. *The theory of heat radiation*. Philadelphia, P. Blakiston's Son & Co, 1914. 34

[116] H. Kalt and M. Hetterich. *Optics of semiconductors and their nanostructures*. Number 146 in Springer series in solid-state sciences. Springer, Berlin ; New York, 2004. 35

[117] M. Bass, C. DeCusatis, J. Enoch, V. Lakshminarayanan, G. Li, C. MacDonald, V. Mahajan, and E. Stryland. *Handbook of Optics, Second Edition Volume I: Geometrical and Physical Optics, Polarized Light, Components and Instruments(set)*. McGraw Hill Professional, 2009. 35, 54

[118] J. H. Lambert and E. Anding. *Lamberts Photometrie: Photometria, sive De mensura et gradibus luminus, colorum et umbrae (1760)*. Leipzig : W. Engelmann, 1892. 35, 54

[119] L. Gütay. *Konfokale Photolumineszenz von Cu(In,Ga)Se2*. PhD thesis, Carl von Ossietzky Universität Oldenburg, 2008. 35, 36, 58

[120] K. Schick, E. Daub, S. Finkbeiner, and P. Würfel. Verification of a generalized planck law for luminescence radiation from silicon solar cells. *Applied Physics A: Materials Science & Processing*, 54:109–114, 1992. 35

[121] L. Gütay and G.H. Bauer. Local fluctuations of absorber properties of Cu(In,Ga)Se2 by sub-micron resolved PL towards real life conditions. *Thin Solid Films*, 517:2222–2225, 2009. 36

[122] ASTM: http://rredc.nrel.gov/solar/spectra/am1.5. 43, 52, 124

[123] W. Shockley and Jr. Read, W. T. Statistics of the recombinations of holes and electrons. *Physical Review*, 87(5):835–842, 1952. 44

[124] R. N. Hall. Electron-hole recombination in germanium. *Physical Review*, 87(2):387–387, 1952. 44

[125] U. Rau and H. W. Schock. Electronic properties of cu(In,Ga)Se2 heterojunction solar cells-recent achievements, current understanding, and future challenges. *Applied Physics A*, 69(2):131–147, 1999. 44

[126] A.R. Riben and D.L. Feucht. nGe-pGaAs heterojunctions. *Solid-State Electronics*, 9(11-12):1055–1065, 1966. 45

[127] W. W. Gärtner. Depletion-layer photoeffects in semiconductors. *Phys. Rev.*, 116(1):84–87, 1959. 46

[128] R. Klenk and H.-W. Schock. Photocurrent collection in thin film solar cells - calculation and characterization for CuGaSe2/(Zn,Cd). In *Proceedings of EUPVSEC94*, 1994. 46

[129] S. Schuler. *Transporteigenschaften und Defekte in polykristallinen $CuGaSe_2$-Schichten und Heterostrukturen*. PhDThesis, FU Berlin, Berlin, 2002. 46

[130] Johannes Fischer. *CuInSe2 Thin Film Solar Cells Synthesised From Electrodeposited Binary Selenide Precursors*. PhD thesis, University of Luxembourg, 2012. 46

[131] W. MöÌĹnch. *Electronic properties of semiconductor interfaces*. Number 43 in Springer series in surface sciences. Springer, Berlin ; New York, 2004. 47, 49

[132] M. Rusu, S. Wiesner, R. Würz, S. Lehmann, S. Doka-Yamigno, A. Meeder, D. Fuertes MarrÃşn, M. Bär, V. Koteski, H.-E. Mahnke, E. Arushanov, J. Beckmann, K. Höhn, W. Fritsch, W. Bohne, P. Schubert-Bischoff, M. Heuken, A. Jäger-Waldau, A. Rumberg, and Th. Schedel-Niedrig. CuGaxSey chalcopyrite-related thin films grown by chemical close-spaced vapor transport (CCSVT) for photovoltaic application: Surface- and bulk material properties, oxidation and surface ge-doping. *Solar Energy Materials and Solar Cells*, 95(6):1555–1580, 2011. 48

[133] S. Chichibu, Y. Harada, M. Sugiyama, and H. Nakanishi. Metalorganic vapor phase epitaxy of Cu(AlxGa1-x)(SySe1-y)2 chalcopyrite semiconductors and their band offsets. *Journal of Physics and Chemistry of Solids*, 64(9-10):1481–1489, 2003. 48, 49

[134] A. D Katnani and G. Margaritondo. Empirical rule to predict heterojunction band discontinuities. *Journal of Applied Physics*, 54(5):2522–2525, 1983. 48

[135] A. D. Katnani and R. S. Bauer. Commutativity and transitivity of GaAs-AlAs-Ge(100) band offsets. *Physical Review B*, 33(2):1106–1109, 1986. 48

[136] A. Bauknecht, U. Blieske, T. Kampschulte, J. Albert, H. Sehnert, M. Ch Lux-Steiner, A. Klein, and W. Jaegermann. Band offsets at the ZnSe/CuGaSe2(001) heterointerface. *Applied Physics Letters*, 74(8):1099–1101, 1999. 49, 114

[137] M. Funato and S. Aoki. Tunable bands offsets in ZnSe/GaAs heterovalent heterostructures grown by metalorganic vapor deposition. *Journal of Applied Physics*, 82(6):2984, 1997. 49, 108

[138] A. Hofmann and C. Pettenkofer. Surface orientation dependent band alignment for CuInSe2–ZnSe–ZnO. *Applied Physics Letters*, 98(11):113503–113503–3, 2011. 49

[139] M Burgelman, P Nollet, and S Degrave. Modelling polycrystalline semiconductor solar cells. *Thin Solid Films*, 361-362:527–532, 2000. 49, 94, 104

[140] J. Eichler and H. J. Eichler. Ausbreitung von Lichtwellen. In *Laser*, pages 231–263. Springer Berlin Heidelberg, 2010. 51

[141] V. Depredurand, D. Tanaka, A. Yasuhiro, N. Fevre, and S. Siebentritt. Why are Cu-rich CIS solar cells not yet living up to their promises? (submitted). *Journal of Applied Physics*, 2013. 52, 99

[142] Wikipedia. Electromagnetic absorption by water, 2013. Page Version ID: 580282690. 52

[143] A. M. Gabor, J. R. Tuttle, D. S. Albin, M. A. Contreras, R. Noufi, and A. M. Hermann. High-efficiency CuIn(x)Ga(1-x)Se2 solar cells made from (In (x),Ga (1-x)2 Se3 precursor films. *Appl Phys Lett*, 65(2):198–200, 1994. 56

[144] L. Gütay, D. Regesch, J. K. Larsen, Y. Aida, V. Depredurand, and S. Siebentritt. Influence of copper excess on the absorber quality of $CuInSe_2$. *Appl Phys Lett*, 99(15):151912, 2011. 56

[145] M. Turcu, O. Pakma, and U. Rau. Interdependence of absorber composition and recombination mechanism in Cu(In,Ga)(Se,S)2 heterojunction solar cells. *Applied Physics Letters*, 80:2598–2600, 2002. 58, 67

[146] S. Shirakata, S. Chichibu, S. Isomura, and H. Nakanishi. Electroreflectance of CuInSe2 single crystals. *Japanese Journal of Applied Physics*, 36(Part 2, No. 5A):L543–L546, 1997. 60, 118

[147] M. I Alonso, K. Wakita, J. Pascual, M. Garriga, and N. Yamamoto. Optical functions and electronic structure of CuInSe2, CuGaSe2, CuInS2, and CuGaS2. *arXiv:cond-mat/0112048*, 2001. Phys. Rev. B 63, 075203 (2001). 60, 71

[148] L. Gütay, D. Regesch, J. K. Larsen, Y. Aida, V. Depredurand, A. Redinger, S. Caneva, S. Schorr, C. Stephan, J. Vidal, S. Botti, and S. Siebentritt. Feedback mechanism for the stability of the band gap of $CuInSe_2$. *Physical Review B*, 86(4):045216, 2012. 60, 61

[149] J. Vidal, S. Botti, P. Olsson, J.-F. Guillemoles, and L. Reining. Strong interplay between structure and electronic properties in CuIn(S,Se)2: A first-principles study. *Physical Review Letters*, 104:056401, 2010. 61

[150] D. Guidotti, Eram Hasan, H. J. Hovel, and Marc Albert. Degradation of bandâĂŘgap photoluminescence in GaAs. *Applied Physics Letters*, 50(14):912–914, 1987. 62

[151] D. Shvydka, C. Verzella, V. G. Karpov, and A. D. Compaan. Photoluminescence fatigue and related degradation in thin-film photovoltaics. *Journal of Applied Physics*, 94(6):3901–3906, 2003. 62

[152] W.K. Metzger, I.L. Repins, M. Romero, P. Dippo, M. Contreras, R. Noufi, and D. Levi. Recombination kinetics and stability in polycrystalline cu(in,ga)se2 solar cells. *Thin Solid Films*, 517(7):2360 – 2364, 2009. 62, 72

[153] S. Siebentritt, N. Papathanasiou, J. Albert, and M. C. Lux-Steiner. Stability of surfaces in the chalcopyrite system. *Applied Physics Letters*, 88(15):151919–151919–3, 2006. 66, 79, 80, 81, 82

[154] L. L. Kazmerski, O. Jamjoum, P. J. Ireland, S. K. Deb, R. A. Mickelsen, W. Chen, K. Satyendra, and K. Bachmann. Oxidation-stability studies of CuInSe2. In *15th PVSC*, pages 247–248. IEEE, 1981. 66

[155] A. J. Nelson, S. Gebhard, L. L. Kazmerski, E. Colavita, M. Engelhardt, and H. Höchst. Characterization of the native oxide of CuInSe2 using synchrotron radiation photoemission. *Applied Physical Letter*, 57(14):1428, 1990. 66

[156] Yasuhiro H., Naoki K., Takayuki N., Mikihiko N., and Takahiro W. Surface characterization of chemically treated Cu(In,Ga)Se2 thin films. *Jpn J Appl Phys 1*, 35(Part 1, No. 9A):4760–4764, 1996. 66

[157] B. Canava, J.F. Guillemoles, J. Vigneron, D. Lincot, and A. Etcheberry. Chemical elaboration of well defined Cu(In,Ga)Se2 surfaces after aqueous oxidation etching. *J Phys Chem Solids*, 64(9-10):1791–1796, 2003. 66

[158] R. Würz, A. Meeder, D. Fuertes Marrón, Th. Schedel-Niedrig, A. Knop-Gericke, and K. Lips. Native oxidation of $CuGaSe_2$ crystals and thin films studied by electron paramagnetic resonance and photoelectron spectroscopy. *Physical Review B*, 70:205321, 2004. 66

[159] C. Heske, G. Richter, Zhonghui Chen, R. Fink, E. Umbach, W. Riedl, and F. Karg. Influence of Na and H2O on the surface properties of Cu(In,Ga)Se2 thin films. *Journal of Applied Physics*, 82(5):2411–2420, 1997. 67

[160] A. Chirila, P. Reinhard, F. Pianezzi, P. Bloesch, A. R. Uhl, C. Fella, L. Kranz, D. Keller, C. Gretener, H. Hagendorfer, D. Jaeger, R. Erni, S. Nishiwaki, S. Buecheler, and A. N. Tiwari. Potassium-induced surface modification of Cu(In,Ga)Se2 thin films for high-efficiency solar cells. *Nature Materials*, 2013. 67

[161] V. Nadenau, D. Hariskos, H.-W. Schock, M. Krejci, F.-J. Haug, A. N. Tiwari, H. Zogg, and G. Kostorz. Microstructural study of the CdS/CuGaSe2 interfacial region in CuGaSe2 thin film solar cells. *Journal of Applied Physics*, 85(1):534–542, 1999. 67, 84

[162] C.L. Perkins, F.S. Hasoon, H.A. Al-Thani, S.E. Asher, and P. Sheldon. XPS and UPS investigation of NH4OH-exposed cu(In,Ga)Se2 thin films. In *Photovoltaic Specialists Conference, 2005. Conference Record of the Thirty-first IEEE*, pages 255 – 258, 2005. 68

[163] S. Chichibu, T. Mizutani, K. Murakami, T. Shioda, T. Kurafuji, H. Nakanishi, S. Niki, P. J. Fons, and A. Yamada. Band gap energies of bulk, thin-film, and epitaxial layers of CuInSe2 and CuGaSe2. *Journal of Applied Physics*, 83(7):3678–3689, 1998. 71

[164] J. Hedström, H. Ohlsen, M. Bodegard, A. Kylner, L. Stolt, D. Hariskos, M. Ruckh, and H. Schock. ZnO/CdS/Cu(In,Ga)Se2 thin film solar cells with improved performance. In *, Conference Record of the Twenty Third IEEE Photovoltaic Specialists Conference, 1993*, pages 364–371, 1993. 73, 104

[165] A. Rockett. The effect of Na in polycrystalline and epitaxial single-crystal $CuIn_{1-x}Ga_xSe_2$. *Thin Solid Films*, 480-481:2–7, 2005. 73, 104

[166] S. Niki, Y. Makita, A. Yamada, A. Obara, S. Misawa, O. Igarashi, K. Aoki, and N. Kutsuwada. Molecular beam epitaxial growth and properties of $CuInSe_2$. *Japanese Journal of Applied Physics*, 32S3(Supplement 32-3):161–162, 1993. 73, 104

[167] Bruker. Communication. with technician from Bruker, Nov 2012. 75

[168] A. Rockett, F. Abou-Elfotouh, D. Albin, M. Bode, J. Ermer, R. Klenk, T. Lommasson, T.W.F. Russell, R.D. Tomlinson, J. Tuttle, L. Stolt, T. Walter, and T.M. Peterson. Structure and chemistry of CuInSe2 for solar cell technology: current understanding and recommendations. *Thin Solid Films*, 237(1-2):1–11, 1994. 84

[169] J.R. Tuttle, M. Ruth, D. Albin, A. Mason, and R. Noufi. Experiments on the modification of the bi-layer structure in CdS/CuInSe2 devices. In *, Conference Record of the Twentieth IEEE Photovoltaic Specialists Conference, 1988*, pages 1525–1530 Vol. 2, 1988. 84

[170] R. Klenk, R. Menner, D. Cahen, and H. W Schock. Improvement of Cu(Ga,In)Se2 based solar cells by etching the absorber. In *, Conference Record of the Twenty First IEEE Photovoltaic Specialists Conference, 1990*, pages 481–486 vol.1, 1990. 84

[171] Yasuhiro Hashimoto, Naoki Kohara, Takayuki Negami, Mikihiko Nishitani, and Takahiro Wada. Surface characterization of chemically treated cu(In,Ga)Se2 thin films. *Japanese Journal of Applied Physics*, 35(Part 1, No. 9A):4760–4764, 1996. 84

[172] Kessler, J, Velthaus, K.O., Ruckh, V., Laichinger, R, and Schock, H.W. CdS deposition. In *Proceedings of the International Photovoltaic Science and Engineering Conference*, New Delhi, 1992. 84

[173] Miguel A. Contreras, Manuel J. Romero, Bobby To, F. Hasoon, R. Noufi, S. Ward, and K. Ramanathan. Optimization of CBD CdS process in high-efficiency Cu(In,Ga)Se2-based solar cells. *Thin Solid Films*, 403 âĂŞ404(0):204–211, 2002. 84

[174] Jon Campbell. from: openclipart.org, 2010. 85

[175] P. T. Boggs and J. E. Rogers. Orthogonal distance regression. In *Statistical analysis of measurement error models and applications*, volume 112. Contemporary Mathematics, 1990. 87, 128

[176] Python: http://www.python.org/. 87, 127

[177] Scipy: http://scipy.org, 2013. 87, 128

[178] I. L Eisgruber, J. E Granata, J. R Sites, J Hou, and J Kessler. Blue-photon modification of nonstandard diode barrier in CuInSe2 solar cells. *Solar Energy Materials and Solar Cells*, 53(3-4):367–377, 1998. 90

[179] A. Niemegeers, M. Burgelman, R. Herberholz, U. Rau, D. Hariskos, and H.-W. Schock. Model for electronic transport in Cu(In,Ga)Se2 solar cells. *Progress in Photovoltaics: Research and Applications*, 6(6):407–421, 1998. 90, 95

[180] U. Rau, K. Weinert, Q. Nguyen, M. Mamor, G. Hanna, A. Jasenek, and H. W. Schock. Device analysis of Cu(In,Ga)Se2 heterojunction solar cells - some open questions. In *Materials Research Society Symposium Proceedings*, volume 668, pages H9–1, 2001. 93

[181] I. Repins, M. A. Contreras, B. Egaas, C. DeHart, J. Scharf, C. L. Perkins, B. To, and R. Noufi. 19.9%-efficient ZnO/CdS/CuInGaSe2 solar cell with 81.2% fill factor. *Progress in Photovoltaics: Research and Applications*, 16(3):235–239, 2008. 94

[182] N. R. Pavaskar, C. A. Menezes, and A. P. B. Sinha. Photoconductive CdS films by a chemical bath deposition process. *Journal of The Electrochemical Society*, 124(5):743–748, 1977. 95

[183] P.W. Li, R.A. Anderson, and R.H. Plovnick. Dielectric constant of CuInSe2 by capacitance measurements. *Journal of Physics and Chemistry of Solids*, 40(4):333–334, 1979. 102, 123

[184] R. Herberholz, V. Nadenau, U. Rühle, C. Köble, H.W. Schock, and B. Dimmler. Prospects of wide-gap chalcopyrites for thin film photovoltaic modules. *Solar Energy Materials and Solar Cells*, 49(1-4):227–237, December 1997. 113

[185] T. Törndahl, C. Platzer-Björkman, J. Kessler, and M. Edoff. Atomic layer deposition of $Zn_{1-x}Mg_xO$ buffer layers for Cu(In,Ga)Se2 solar cells. *Progress in Photovoltaics: Research and Applications*, 15(3):225–235, May 2007. 114

[186] T. Minemoto, Y. Hashimoto, T. Satoh, T. Negami, H. Takakura, and Y. Hamakawa. Cu(In,Ga)Se2 solar cells with controlled conduction band offset of window/Cu(In,Ga)Se2 layers. *Journal of Applied Physics*, 89(12):8327, 2001. 114

[187] P. Kistaiah, Y. C. Venudhar, K. Sathyanarayana Murthy, L. Iyengar, and K. V. Krishna Rao. Temperature dependence of tetragonal distortion and thermal expansion of copper indium selenide. *J. Phys. D: Appl. Phys.*, 14(7):1311, 1981. 123

[188] H.-G. Brühl, H. Neumann, T. Pfeiffer, and G. Kühn. Anisotropic thermal expansion of Cu-III-VI2 compounds. *physica status solidi (a)*, 66(2):597–600, 1981. 123

[189] H.-G. Brühl and H. Neumann. Thermal expansion of CuGaSe2. *Solid State Communications*, 34(4):225–227, 1980. 123

[190] N.N. Syrbu, M. Bogdanash, V.E. Tezlevan, and I. Mushcutariu. Lattice vibrations in $CuIn_{1-x}Ga_xSe_2$ crystals. *Physica B: Condensed Matter*, 229(2):199–212, 1997. 123

[191] H. Weinert, H. Neumann, H.-J. Höbler, G. Kühn, and Nguyen van Nam. Infrared faraday effect in n-type CuInSe2. *physica status solidi (b)*, 81(1):K59–K61, 1977. 123

[192] F. Luckert, M. V. Yakushev, C. Faugeras, A. V. Karotki, A. V. Mudryi, and R. W. Martin. Diamagnetic shift of the a free exciton in CuGaSe2 single crystals. *Applied Physics Letters*, 97(16):162101–162101–3, 2010. 123

[193] H. Neumann, W. Kissinger, H. Sobotta, V. Riede, and G. Kühn. Hole effective masses in CuInSe2. *physica status solidi (b)*, 108(2):483–487, 1981. 123

[194] S. M Sze and Ng Kwok. *Physics of semiconductor devices*. Wiley-Interscience, Hoboken, N.J., 2007. 123

[195] E. Lotter. Diplot (www.diplot.de). 125

[196] Spyder: http://code.google.com/p/spyderlib/. 127

[197] peak-o-mat: http://lorentz.sourceforge.net/. 127